Uncertainly analysis : towards more accurate predictions for the synthesis of superheavy nuclei

Bartholomé Cauchois

Normandie Université

THÈSE

Pour obtenir le diplôme de doctorat

Spécialité PHYSIQUE

Préparé au sein de l'Université de Caen Normandie

Uncertainly analysis : Towards more accurate predictions for the synthesis of superheavy nuclei

Présentée et soutenue par
Bartholome CAUCHOIS

Thèse soutenue publiquement le 25/06/2018 devant le jury composé de		
M. MICHAL WARDA	Maître de conférences HDR, Uniwersytet Marii Curie-Sklodowkiej	Rapporteur du jury
M. FENG-SHOU ZHANG	Professeur, Beijing Normal University	Rapporteur du jury
M. DAVID BOILLEY	Maître de conférences, UNIVERSITE CAEN NORMANDIE	Membre du jury
Mme FRANCESCA GULMINELLI	Professeur des universités, UNIVERSITE CAEN NORMANDIE	Président du jury
Mme CHRISTELLE SCHMITT	Chargé de recherche au CNRS, Institut Hubert Curien	Membre du jury
M. MAREK PLOSZAJCZAK	Directeur de recherche au CEA, 14 GANIL de CAEN	Directeur de thèse

Thèse dirigée par MAREK PLOSZAJCZAK, Grand accélérateur national d'ions lourds (Caen)

UNIVERSITÉ CAEN NORMANDIE

ED 591 PSIME

GANIL spiral2

Contents

Acknowledgment

First and foremost, I would like to thank the members of the jury Francesca Gulminelli, Christelle Schmitt, Michał Warda and Feng-Shou Zhang for having accepted the difficult task to read and evaluate the present work.

Here, I would like to praise the guidance of my supervisor David Boilley without whom this work would not have been possible. David always granted me a considerable amount of independence and confidence from which I greatly benefited all along the three years we have worked together. I would like to further extent my thanks to my director Marek Płoszajczak who has helped me a great deal and in particular in the final moments of my PhD. It is thanks to Marek that I really did discover contemporary nuclear physics by taking part in the TALENT school and to the many FUSTIPEN workshops. I would also like to thank Guy Royer for all of the help he provided me with and in particular for his valuable explanations regarding the Thomas-Fermi model.

I would like to express my deepest gratitude to Yasuhisa Abe and Michał Kowal for the wonderful stays in Japan and in Poland. A PhD is filled with ups and downs and working abroad allowed me to change my personal perspective and helped inspire some of the solutions found in the following months. I am deeply indebted to Michał Kowal for his incredible enthusiasm and fantastic dynamism which truly made a difference and helped me get through hard times. I would also like to thank Krystyna Siwek-Wilczyńska and Tomasz Cap for all the fruitful discussions we had.

I would like to thank GANIL's technical staff for making my life so much simpler as a student. For that I thank Sabrina Lecerf-Rossard, Virginie Lefebvre, Guillaume Lalaire and Michel Lion. I also thank GANIL's directors Navin Alahari and Heloise Goutte for encouraging and supporting this work.

During this thesis I had the chance and pleasure to interact with a few members of the physics group at GANIL. More specifically, I would like to thank François De Oliveira Santos, Beyhan Bastin, Piet Van Isacker and Pierre Delahaye for all of the entertaining discussions.

As a first year student, I had the incredible chance to discover GANIL's experimental facilities during the dubnium-257 experiment on LISE and for that I will always be grateful to all of GANIL's experimentalists and more specifically to those specializing in the field of superheavies. In particular, I will always be thankful to Julien Piot, Marija Voštinar, Christelle Stodel and Dieter Ackermann for all of their detailed explanations about the experimental setup and the subtleties of nuclear structure studies.

I would also like to thank Olivier Juillet for his incredible lectures on the n-body quantum problem as well as for the teaching duties he entrusted me with. For me, teaching at the university was a great pleasure and here I would like to thank some of the people that I had the pleasure to meet and teach with Jean-Christophe Poully, Julie Douady, Vu Hung Dao, Julien Gibelin and François-René Lecolley.

Finally, all along this PhD I have met with many PhD students and I must say that all of them have made my life much more cheerful and for that I thank: Hongliang, Marija, Florent, Coralie, Quentin and all the others that were not mentioned here and that were forgotten by mistake. At last, a huge and very special thanks to Alexis, Fabien, Dennis and Aldric without whom everything would have been so much different.

Chapter 1

Introduction

The birth of nuclear physics can be traced back to 1911 with the discovery of the nucleus by Rutherford [1]. It was only later that the proton and neutron were respectively discovered in 1919 and 1932 by Rutherford and Chadwick [2, 3]. After these discoveries, it was realized that nuclei could be classified according to their proton and neutron numbers which lead to the nuclear chart [4]. From that moment on, the mind of nuclear physicists was set on explaining and exploring that new classification. During the last century, both experimental and theoretical improvements have allowed us to expand and explore the nuclear chart, as well as to further increase our understanding of nuclear phenomena. Although decisive progress has been made, there are still many open questions. In this thesis, we shall focus our attention on one of them: What is the limit of existence for heavy nuclei and thus of elements?

The first answer to that question came from Wheeler. At the time fission had already been discovered in 1938 by Hahn and Strassmann and a first theoretical explanation had been given by Meitner and Frisch which was later completed by Bohr and Wheeler [5–7]. The theoretical explanation of fission was based on the liquid drop model, separately introduced by Weizsäcker in 1935 and by Bethe in 1936 [8,9]. Based on that model, Wheeler showed that the fission barriers of very heavy nuclei vanished. This was considered to be the major limiting factor of the existence of heavy nuclei [7, 10]. Shortly after, the term superheavy nuclei appeared for the very first time in a conference proceeding authored by Wheeler [11, 12]. Meanwhile, theories failed to explain the binding energies of some nuclei having special numbers of protons or neutrons, also known as magic numbers. The nuclear shell model was separately introduced in 1949 by Goeppert-Mayer as well as another group formed by Haxel, Jensen and Suess, in order to interpret this empirical observation [13–16]. As superheavy nuclei only owe their stability to shell effects, the shell model gave a possible explanation for the existence of nuclei beyond the limit first set by Wheeler.

The first transuranium elements were discovered during the 1940's. These elements were synthesized using the intense neutron fluxes produced by nuclear reactors and bombs, consequently, large numbers of neutrons could be captured and the subsequent β decay lead to these new elements. However, in order to proceed beyond fermium, neutron capture had to be abandoned since it lead to fission instead of the desired β decay. Thus, during the 1950's, fusion-evaporation reactions became the leading choice to synthesize new elements.

Moreover, there are two kinds of fusion reactions, namely, cold-fusion and hot-fusion. On the one hand, cold-fusion reactions are based on ^{208}Pb and ^{209}Bi targets as well as various projectiles, e.g., ^{48}Ca, ^{50}Ti or ^{54}Cr. In these reactions, the excitation energy of the compound nucleus is rather low and ranges between 10 and 20 MeV. These energies correspond to low nuclear temperatures, hence, these reactions were said to be cold-fusion reactions. Cold-fusion reactions have been mainly used in GSI and RIKEN in order to synthesis the elements from 107 to 113 [17]. Note that because of the low excitation energies, the compound nucleus only needs to evaporate one or two neutrons in order to cool down. On the other hand, hot-fusion reactions are based on the projectile ^{48}Ca as well as various actinides targets, e.g., Pu, Am and Cm. In these reactions the excitation energies extend from 30 to 60 MeV, thus, the cooling of the compound nucleus requires the evaporation of three or more neutrons which reduces its chances of surviving fission. Hot-fusion was mainly used as FLNR in order to produce the elements from 114 to 118 [18].

A summary of measured fusion-evaporation cross-sections is given in Fig. 1.1 [19]. One can see that the heaviest element ever produced in a cold-fusion reaction is nihonium (Z=113) and that the corresponding cross-section is far below the picobarn. Thus, it is clear that we cannot proceed beyond nihonium using cold-fusion reactions because the cross-sections become too low. Then again, we can see that the heaviest element produced in a hot-fusion reaction is oganesson (Z=118) and that the corresponding cross-section is this time closer to the picobarn. Thus, one might think that hot-fusion is a promising way to discover the next new element. However, we have reached the limit of the available long-lived actinides targets in combination with a ^{48}Ca beam. Therefore, we are entering a new era where new combinations of projectiles and targets will have to be used. Now more than ever, precise theoretical predictions are required in order to successfully guide future experimental campaigns. Furthermore, let us emphasize that at GANIL the study of the structural properties of superheavy nuclei has become one of the key topics in the development of SPIRAL2 and S^3 projects. Therefore, improving theoretical predictions is now critical.

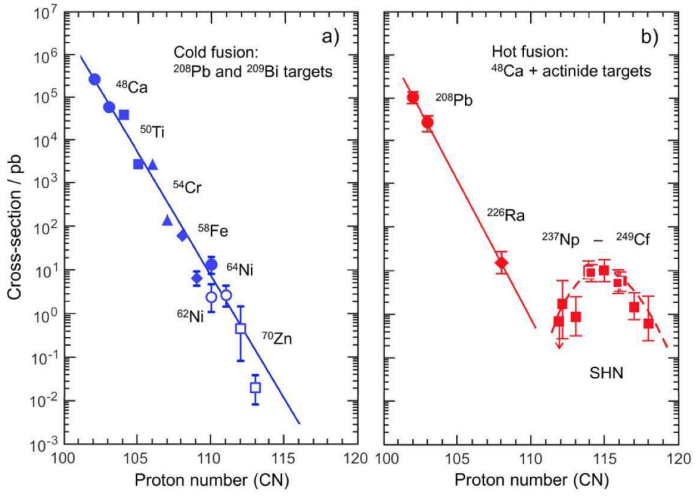

Figure 1.1: Summary of the measured production cross-sections for cold (on the left) and hot-fusion (on the right). Figure reproduced from [19].

The production of superheavy nuclei is important for nuclear structure studies. All elements heavier than lead are unstable and have decreasing binding energies, it is expected that some superheavy nuclei could reverse this general trend and form an island of metastability. As the presence of superheavy nuclei is singularly due to quantum arrangements, they offer an ideal case to inspect and fine-tune nuclear structure theories. In particular, superheavy nuclei accommodate a large number of protons by being overly deformed, and consequently, exhibit extreme Nilsson's level schemes [20]. Moreover, unstable superheavy nuclei have two competing decay modes, α decay and spontaneous fission which is rather uncommon and could improve our understanding of fancier cluster decays [21]. Finally, superheavy elements are also important in chemistry where the extreme relativistic character of the electrons can significantly modify the expected chemical properties [21].

The production of superheavy nuclei is mostly achieved through collisions involving a light nucleus and a heavier one, with the pious hope that the two would fuse together. For fusion to occur, the system needs to overcome the Coulomb barrier. Since both nuclei contain large proton numbers, this requires a large amount of kinetic energy in the entrance channel. Furthermore, fusion is the most inelastic reaction possible, the residual kinetic energy required to pass the Coulomb barrier will be redistributed amongst internal degrees of freedom (heat), thus, leaving the compound nucleus in a delicate and overly excited configuration. In order to survive and reach its ground-state, the compound nucleus must release some of its excitation energy and in doing so, it can either fission or evaporate light particles. Therefore, increasing the kinetic energy in the entrance channel leads to an enhanced fusion probability along with a decrease of the survival probability. As a result, producing superheavy nuclei is an improbable process and the corresponding cross-sections are ultimately low. Consequently, the cross-sections vary promptly with the center-of-mass energy, and so, theoretical studies are needed to choose the energy that will simultaneously maximize fusion and survival.

It has been known for a very long time that fusion of heavy nuclei is hindered with respect to what is observed with lighter systems. However, the precise origin of fusion hindrance was not known before the start of the 1970's where the first calculations [22] showed that in order for heavy systems to fuse they had to cross the conditional saddle in a multidimensional deformation energy landscape. Thus, hindrance was understood as coming from the saddle-point of the compound nucleus which acts as an internal barrier, i.e., a barrier beyond the Coulomb barrier. As we will discuss later, this inner barrier does not appear in the fusion of lighter systems, hence, the absence of hindrance. However, results based only on the existence of an internal barrier underestimated hindrance and it was not before the inclusion of dissipation [23–27] that experimental results [28–30] could be partially explained. Later, fluctuations were also included through the use of Langevin and Smoluchowski equations in order to describe the diffusion over the inner barrier [31–36]. The crossing of this internal barrier requires complex modelling and although fusion hindrance is qualitatively understood, some quantitative ambiguities remain and are still to be clarified.

A preceding investigation proved that, although the various models to calculate fusion-evaporation cross-sections at our disposal, lead to similar final results, i.e., known experimental results, the intermediate steps provide a wide and puzzling range of outcomes, thus, highlighting unre-

solved quantifiable issues [37, 38]. The approach presented here finds its roots in both, the recent emergence of uncertainty analyses in nuclear physics and the necessity to go beyond the qualitative consensus of the fusion-evaporation picture in order to reach a, robust, quantitative description of the synthesis. The object of the current study is to focus on a specific fusion-evaporation model and explore the uncertainties related to each individual step in order to unriddle the predictive power of the model. The prior and present studies are complementary as they are both aimed at the removal of theoretical inconsistencies.

More specifically, this thesis is aimed towards a more profound understanding of models resembling the so-called "fusion-by-diffusion" model which describes the synthesis of superheavy nuclei [36]. Such a family of models all contain three steps. The first step, referred to as *capture*, corresponds to the system overcoming the Coulomb barrier, the second step, known as *formation* amounts to the system overcoming the internal barrier which is responsible for fusion hindrance and the last step, *survival*, characterizes the cooling of the compound nucleus through either evaporation or fission. Previous studies have shown both the lack of constraints and the crucial importance of the formation and survival steps on the cross-section calculations and in particular, on the specific quantities entering those steps, respectively, the internal and the fission barriers [37–39]. The intent of this thesis is therefore twofold: First, to theoretically clarify the diffusion mechanism associated with the formation step and second, to lead off an uncertainty analysis concerning fission barriers calculations.

Formation can be understood as being the inverse process of fission. Therefore, the internal barrier of the fusing system should somehow be related to the fission barrier of the resulting compound nucleus. However, things could not be so simple, for the surface energy landscape seen by the fusing system depends on its center-of-mass energy which alters the height of the internal barrier. This is accounted for through a shift of the initial conditions in the formation step. So far, no theoretical explanation was found for those systematic shifts and these were only included in a phenomenological manner. The origin of these shifts can be found in the reduction of the number of degrees of freedom of the fusing system and are exposed as such in this thesis.

This manuscript is organized in the following way. Chapter 2 is a brief review dedicated to the description of an entire fusion model, i.e., the capture, the formation and the survival steps. Then, chapter 3 discusses fusion hindrance in greater detail and tends to clarify some of the notions phenomenologically introduced in chapter 2. Then, chapter 4 exposes the proper mathematical formalism to treat and propagate uncertainties while chapter 5 focuses on regression analysis which is at the very origin of theoretical uncertainties. Having stressed the importance of masses entering the fusion model, we then proceed to an uncertainty analysis of mass predictions using a simple macroscopic model in chapter 6. The model from chapter 6 is too simple and does not encompass the diversity of nuclear properties, i.e., deformation and shell corrections. Accordingly, a deeper analysis is carried out in chapter 7 where a phenomenological macroscopic-microscopic model is considered. Chapter 8 investigates the predictive power of the naive capture model presented in chapter 2. In chapter 9, we gather all of the results obtained in this thesis in order to constrain the formation step. Finally, a closing conclusion summarizes the important results and discusses future endeavours.

Chapter 2

A model for fusion-evaporation

This chapter contains a detailed description of a fusion-evaporation model which is essentially based on the fusion-by-diffusion model [35, 36, 40, 41]. Note that the two-step model described in Refs. [33, 42] is rather close and shares most of the features of the fusion-by-diffusion model. In all synthesis models the production cross-section is given by

$$\sigma_{\mathrm{ER}} = \frac{\pi}{k^2} \sum_{\ell=0}^{\infty} (2\ell+1) \cdot P_{\mathrm{fus}}(E_{\mathrm{cm}}, \ell) \cdot P_{\mathrm{surv}}(E^*, \ell). \tag{2.1}$$

Here, ℓ stands for the angular momentum, E_{cm} for the center-of-mass energy and E^* for the excitation energy of the compound nucleus. The wavenumber is defined as $k^2 = 2\mu E_{\mathrm{cm}}/\hbar^2$ where μ is the reduced mass. The quantities P_{fus} and P_{surv} are the fusion and survival probabilities, respectively. The subscript ER stands for evaporation residue. According to Bohr's hypothesis, as soon as the compound nucleus is formed, the system no longer remembers how it reached this particular state. Thus, the production cross-section can be expressed as the product of two independent probabilities, i.e., the fusion probability and the survival probability.

The fusion of heavy nuclei is divided into two sequential steps, namely, the capture and formation steps. Thus, the fusion probability can itself be decomposed into the product

$$P_{\mathrm{fus}}(E_{\mathrm{cm}}, \ell) = P_{\mathrm{cap}}(E_{\mathrm{cm}}, \ell) \cdot P_{\mathrm{form}}(E_{\mathrm{cm}}, \ell). \tag{2.2}$$

Since the production cross-section is defined as a product between probabilities, then, these probabilities are considered independent of each other. This is perhaps the strongest assumption in this fusion-evaporation model. Note that the formation step is associated with fusion hindrance which is a unique feature of collisions involving very heavy nuclei.

As a result of the previous decompositions, the production cross-section is the product of three, independent, probabilities. In fact, all the theoretical descriptions of fusion-evaporation contain three models, one for each of these three probabilities. We are now going to describe each and every one of them.

2.1 The capture step

The capture model describes the very first step of the fusion process. More specifically, it details how the dinuclear system overcomes the Coulomb barrier. Here, we are particularly interested in estimating the capture cross-section defined as

$$\sigma_{\text{cap}}\left(E_{\text{cm}}\right) = \frac{\pi}{k^2}\sum_{\ell=0}^{\infty}(2\ell+1)P_{\text{cap}}\left(E_{\text{cm}},\ell\right). \tag{2.3}$$

2.1.1 Classical cross-section

In the center-of-mass frame a 2-body problem reduces to a 1-body problem [43]. In that case, the effective potential felt by the system is

$$V_{\text{eff}}(r) = \frac{L^2}{2\mu r^2} + V(r), \tag{2.4}$$

where r is the relative distance between the two colliding nuclei and $V(r)$ is the interaction potential. Now, let us assume that there is a barrier B, lying between the two nuclei and positioned at R. Then, in order to overcome this barrier the center-of-mass energy must satisfy

$$E_{\text{cm}} \geq \frac{L^2}{2\mu R^2} + B. \tag{2.5}$$

Since angular momentum is conserved, it can be written as $L = \mu b v$ where b is the impact parameter and the initial velocity is given by $v = \sqrt{2E_{\text{cm}}/\mu}$. Therefore, one can show that the previous expression is equivalent to

$$b^2 \leq R^2\left(1 - \frac{B}{E_{\text{cm}}}\right). \tag{2.6}$$

Thus, the classical capture cross-section is given as

$$\sigma_{\text{clas}} = \begin{cases} \pi R^2\left(1 - \frac{B}{E_{\text{cm}}}\right) & E_{\text{cm}} \geq B \\ 0 & E_{\text{cm}} < B. \end{cases} \tag{2.7}$$

It should be noted that a similar quantum mechanical calculation gives the same result.

2.1.2 Barrier distribution

We have just obtained a formula for the classical capture cross-section and it was assumed that the height of the barrier, denoted as B, was well defined. However, it turns out that this description is too simple. Indeed, there are many reasons for the height of the barrier to vary. For instance, if the two colliding nuclei are deformed, their relative orientation will influence the height of the barrier. Tunnelling is another source of "variations" which may be mimic by fluctuations and is not directly accounted for. Thus, barrier fluctuations are required in order to mimic these kinds of aspects. We now expose the barrier distribution formalism which is entirely based on Ref. [44].

Assuming the barrier follows the Gaussian distribution given by

$$P(B) = \frac{1}{\sqrt{2\pi}\sigma_B} \exp\left(-\frac{(B-B_0)^2}{2\sigma_B^2}\right), \tag{2.8}$$

where B_0 and σ_B^2 are, respectively, the mean and the variance of the barrier distribution. From this, it becomes possible to compute the mean capture cross-section as

$$\begin{aligned}\sigma_{\text{cap}}(E_{\text{cm}}) &= \int_0^{E_{\text{cm}}} \sigma_{\text{clas}} P(B)\, \mathrm{d}B \\ &= \frac{\pi R^2 \sigma_B}{\sqrt{2\pi} E_{\text{cm}}} \sqrt{\pi} \frac{(E_{\text{cm}} - B_0)}{\sqrt{2}\sigma_B} \left[\text{erf}\left(\frac{B_0}{\sqrt{2}\sigma_B}\right) + \text{erf}\left(\frac{E_{\text{cm}} - B_0}{\sqrt{2}\sigma_B}\right)\right] \\ &+ \frac{\pi R^2 \sigma_B}{\sqrt{2\pi} E_{\text{cm}}} \left[\exp\left(-\frac{B_0}{2\sigma_B}\right) + \exp\left(-\frac{(B_0 - E_{\text{cm}})^2}{2\sigma_B^2}\right)\right],\end{aligned} \tag{2.9}$$

where the error function is defined as

$$\text{erf}(x) = \frac{2}{\sqrt{\pi}} \int_0^x e^{-t^2} \mathrm{d}t. \tag{2.10}$$

Since the width of the distribution is small with respect to its mean, then, $\frac{B_0}{2\sigma_B} \gg 1$ and the previous relation becomes

$$\sigma_{\text{cap}} = \frac{\pi R^2 \sigma_B}{\sqrt{2\pi} E_{\text{cm}}} \{X\sqrt{\pi}(1 + \text{erf}(X)) + e^{-X^2}\}, \tag{2.11}$$

where

$$X = \frac{E_{\text{cm}} - B_0}{\sqrt{2}\sigma_B}. \tag{2.12}$$

Note that we have used the fact that $\lim_{x\to\infty} \text{erf}(x) = 1$.

2.1.3 Parametrization of the mean barrier

The barrier is in fact nothing else but the Coulomb barrier. Therefore, the resulting potential should have the form

$$V(r) = \frac{e^2 Z_1 Z_2}{r}, \tag{2.13}$$

where r is the relative distance between the two nuclei while Z_1 and Z_2 are their respective proton numbers. Note that Eq. (2.13) is only valid when the charge distributions do not overlap. Based on the liquid drop model the contact point is defined as $r = r_0(A_1^{1/3} + A_2^{1/3})$ where A_1 and A_2 are the respective mass numbers of the two nuclei. Further assuming that the barrier is located close to the contact point, then, a sensible choice of parametrization would be

$$B_0(z) = az \tag{2.14}$$

where a is now considered as an adjustable parameter and the Coulomb parameter is given by

$$z = \frac{Z_1 Z_2}{A_1^{1/3} + A_2^{1/3}}. \tag{2.15}$$

Although incomplete the previous argument is rather correct and resembles the parametrization proposed in Refs. [36, 40, 41] which takes the form

$$B_0(z) = az + bz^2 + cz^3, \tag{2.16}$$

where a, b and c, are adjustable parameters. There has been different sets of values for these parameters. For instance, the values given in Ref. [36] differ from those in Ref. [40]. Here, we reproduce the most recent one given in Ref. [40] as

$$B_0(z) = 0.853315z + 0.0011695z^2 - 0.000001544z^3. \tag{2.17}$$

Is is obvious from this relation that the parameters b and c are negligible with respect to a. This confirms the previous argument regarding the parametrization solely based on a. The regression procedure that allows us to determine a, b and c, will be explored in great detail in chapter 8.

2.1.4 Parametrization of the width of the barrier distribution

Since the width of the distribution must account, effectively, for every possible barrier fluctuation, the width of the barrier distribution is a very subtle quantity. Indeed, the fluctuations have various origins and should encompass: tunnelling, vibrations, the shapes and relative orientations of the colliding nuclei, etc. As proposed in Refs. [36, 40] we shall focus on the latter.

As previously argued, the mean barrier can be approximately expressed as

$$B \approx ar_0 \frac{Z_1 Z_2}{R_1 + R_2}, \tag{2.18}$$

where as before we assume that $R_i = r_0 A_i^{1/3}$. Note that we have neglected the effects of b and c. The total derivative of the previous expression with respect to R_1 and R_2 leads us to

$$dB = -B\,\frac{dR_1 + dR_2}{R_1 + R_2}. \tag{2.19}$$

From this, first, we deduce that the barrier variations (here dB) should be proportional to the barrier itself. Secondly, the variations of the respective radii (here dR_1 and dR_2) also influence the fluctuations of the barrier.

The nuclear shapes can be described by an expansion in spherical harmonics as

$$R(\theta,\phi) = R_0\left[1 + \sum_{\lambda=0}^{\infty}\sum_{\mu=-\lambda}^{\lambda} a^*_{\lambda\mu} Y_{\lambda\mu}(\theta,\phi)\right], \tag{2.20}$$

where $a^*_{\lambda\mu}$ are the parameters defining the deformation [45]. In this expansion, the first relevant deformation corresponds to $\lambda = 2$, also known as the quadrupole deformation. Thus, neglecting higher order as well as non-axiality, the previous expression reduces to

$$R(\theta,\phi) = R_0\left[1 + a^*_{20} Y_{20}(\theta,\phi)\right], \tag{2.21}$$

where a_{20} and Y_{20} are real with $a_{20} = \beta_2$. Only prolate shapes are considered here, i.e., $\gamma = 0$.

The root-mean-square deviation from the spherical radius can characterize any kind of deformation and is defined as

$$\mathrm{RMS} = \left[\int (R(\theta,\phi) - R_0)^2 d\Omega\right]^{\frac{1}{2}} = R_0\beta_2 \left[\int Y_{20}^2 d\Omega\right]^{\frac{1}{2}} = \frac{R_0\beta_2}{\sqrt{4\pi}}. \tag{2.22}$$

Notice various RMS can be combined in order to obtain the total RMS as

$$\mathrm{RMS} = \sqrt{\frac{1}{n}\left(\mathrm{RMS}_1^2 + \mathrm{RMS}_2^2 + \cdots + \mathrm{RMS}_n^2\right)}. \tag{2.23}$$

From all these considerations, we can now appreciate the choice of parametrization proposed in Refs. [36, 40] where the expression for the width of the barrier distribution is taken to be

$$\sigma_B = CB_0\sqrt{W_1^2 + W_2^2 + W_0^2}, \tag{2.24}$$

where

$$W_i^2 = \frac{R_i^2\beta_{2i}^2}{4\pi} \qquad \text{for} \qquad i = 1, 2. \tag{2.25}$$

In Ref. [40], the adjustable parameters are taken to be $C = 0.0421$ fm^{-1}, $R_i = 1.15$ A$_i^{1/3}$ and $W_0 = 0.531$ fm. Later, the regression procedure leading to the values of those parameters will be explored in chapter 8. Fig. 2.1 shows that the mean barrier parametrization reproduces the data much better than the one for the width of the barrier distribution.

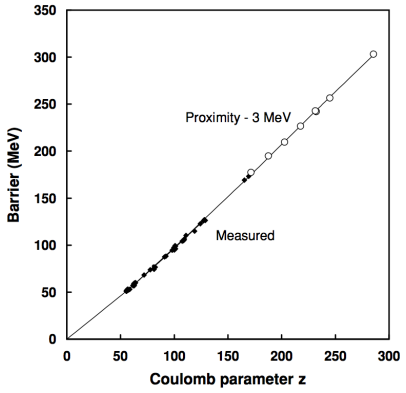

(a) Mean of the barrier height

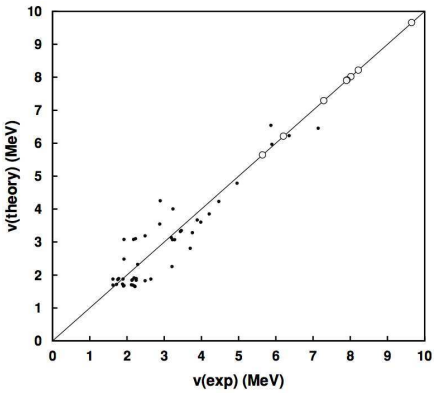

(b) Width of the barrier height

Figure 2.1: The figure on the left shows the great agreement between the measured barriers (black squares) and theoretical mean barrier (solid line) as a function of the Coulomb parameter z. On the right, theoretical and measured widths are plotted against each other. One can see that the agreement between the theoretical and experimental values is rather unsatisfactory. Figure reproduced from [36].

2.2 The formation step

In the present section, we will discuss the second step of the fusion-evaporation model, the formation step. This step takes place right after capture and is a special feature of the fusion leading to superheavy nuclei. Indeed, while the fusion of light nuclei is systematic after capture, the fusion of heavier systems is not. The formation step is a way to account for this particularity known as fusion hindrance that is responsible for the reduction of the fusion probability and in turn for the low production cross-sections.

2.2.1 The origin of fusion hindrance

A simple geometrical explanation for the origin of fusion hindrance can be found in Ref. [36] and is here summarized. On the one hand, when two light systems collide, their elongation at contact is smaller than the one of the saddle-point of the compound nucleus. In those cases fusion always takes place. On the other hand, the total elongation of two heavy colliding systems exceeds the one of the saddle-point configuration. In those cases the system, starting at the contact point, must reach the saddle-point through diffusion. Therefore, the saddle acts as a barrier against fusion. This explanation is illustrated by Fig. 2.2. Moreover, the origin of hindrance comes from the competition between surface tension and Coulomb repulsion. The latter dominates for heavy systems and the dinuclear system does not fuse automatically anymore.

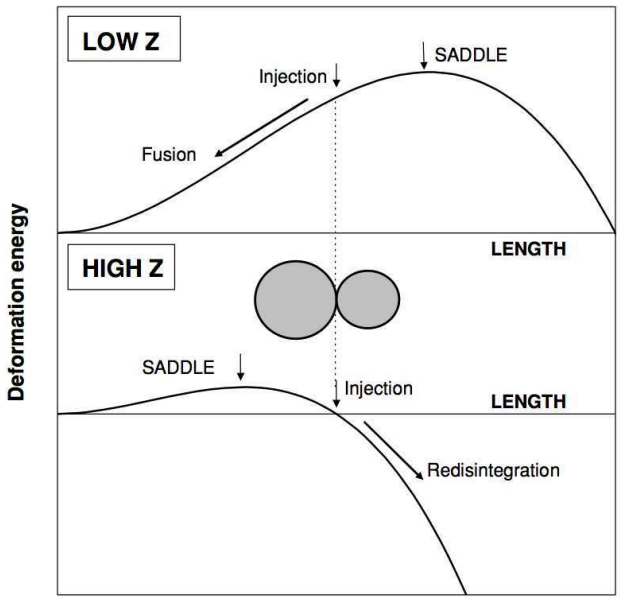

Figure 2.2: Top figure shows that the contact point (or injection point) for light systems is located on the inside of the saddle-point. Bottom figure shows that the contact point (or injection point) for heavy systems is positioned on the outside of the saddle-point. Figure reproduced from [36].

2.2.2 Formation in the fusion-by-diffusion model

We have just given a simple qualitative explanation for the origin of hindrance. Now we would like to theoretically address the diffusion over the conditional saddle and describe how this process is related to the formation probability. In the following, we discuss two theoretical description of hindrance. First, we consider the Smoluchowski approach presented in the fusion-by-diffusion model [35, 36, 40, 41]. Second, we turn to another one, the Langevin description as presented in Ref. [34]. It should be mentioned that the Smoluchowski formulation is nothing but an approximation of the Langevin description where inertia is completely neglected. In both cases, the barrier between the contact point (or injection point) and the saddle is approximated by an inverted parabola. In this thesis, we only consider two simple analytical models. However, it should be mentioned that N-dimensional Langevin equations are also used to study numerically the diffusion process in more elaborate potential landscapes [25, 46].

2.2.2.1 The Smoluchowski equation

In the fusion-by-diffusion model, inertia is assumed to have a negligible influence on the dynamics of diffusion [35,36,40,41]. Consequently, diffusion should be suitably described by a Smoluchowski equation. One can show that the Smoluchowski equation is completely equivalent to the over-damped Langevin equation. Thus, in what follows we solve the over-damped Langevin equation instead. In chapter 3, this will allow us to draw parallels between the Smoluchowski and the Langevin descriptions. In the following, we will indifferently refer to these equations as being over-damped or Smoluchowski descriptions.

Therefore, diffusion is described by the following over-damped (or Smoluchowski) equation

$$\beta\dot{q} - \omega^2 q = r(t) \tag{2.26}$$

where β is the reduced friction and q is a collective variable describing the elongation of the system. The potential felt by the system is taken to be an inverted parabola $V(q) = -\frac{1}{2}m\omega^2 q^2$ which is suppose to mimic the "true" potential between the contact and the saddle points (cf. Fig. 2.2). The Gaussian random force $r(t)$ is a defined by its first two moments as

$$\langle r(t)\rangle = 0, \tag{2.27}$$

$$\langle r(t)r(t')\rangle = \frac{2T\beta}{m}\delta(t-t'), \tag{2.28}$$

in order to satisfy the fluctuation-dissipation theorem [47]. In these expressions, m and T denote the temperature and the mass, respectively. Since the top of the potential is located at the origin, we assume that $q(0) < 0$ so that the compound nucleus is formed when q becomes positive. The three previous equations along with the initial condition $q(0)$ completely specify the problem we need to solve.

Thus, taking the Laplace transform of the over-damped equation yields

$$q(s) = \frac{1}{\beta}\frac{r(s)}{s - \frac{\omega^2}{\beta}} + \frac{q(0)}{s - \frac{\omega^2}{\beta}}. \tag{2.29}$$

The inversion of the previous expression leads us directly to the solution

$$q(t) = q(0)e^{\frac{\omega^2}{\beta}t} + \frac{1}{\beta}\int_0^t r(t')e^{\frac{\omega^2}{\beta}(t-t')}\mathrm{d}t'. \tag{2.30}$$

Then, using the defining moments of the Gaussian random force, we find that the mean trajectory is given by

$$\langle q(t)\rangle = q(0)e^{\frac{\omega^2}{\beta}t}. \tag{2.31}$$

The fluctuations about the mean trajectory are

$$\begin{aligned}\sigma^2(t) &= \langle q^2(t)\rangle - \langle q(t)\rangle^2 \\ &= \int_0^t\int_0^t \langle r(t')r(t'')\rangle e^{\frac{\omega^2}{\beta}(2t-t'-t'')}\mathrm{d}t'\mathrm{d}t'' \\ &= \frac{T}{m\omega^2}\left(e^{2\frac{\omega^2}{\beta}t} - 1\right).\end{aligned} \tag{2.32}$$

Since the random force is Gaussian, the distribution of the trajectories will also follow a Gaussian distribution. As already mentioned, formation is achieved when q becomes positive such that the formation probability can be obtained as

$$P_{\mathrm{form}}(t, q(0)) = \int_0^\infty \frac{1}{\sqrt{2\pi}\sigma}e^{-\frac{(q-\langle q\rangle)^2}{2\sigma^2}}\mathrm{d}q = \frac{1}{\sqrt{\pi}}\int_{-\frac{\langle q\rangle}{\sqrt{2}\sigma}}^\infty e^{-q'^2}\mathrm{d}q' = \frac{1}{2}\,\mathrm{erfc}\left(-\frac{\langle q(t)\rangle}{\sqrt{2}\sigma(t)}\right), \tag{2.33}$$

where an obvious change of variables was made and the complementary error function was introduced as

$$\mathrm{erfc}(x) = \frac{2}{\sqrt{\pi}}\int_x^\infty e^{-t^2}\mathrm{d}t. \tag{2.34}$$

Finally, after a very long time, the formation probability is given by

$$P_{\mathrm{form}}(t\to\infty, q(0)) = \frac{1}{2}\,\mathrm{erfc}\left(\sqrt{\frac{B}{T}}\right), \tag{2.35}$$

where the initial barrier is defined as $B = \frac{1}{2}m\omega^2 q^2(0)$. The last expression is consistent with the one given in Refs. [35, 36, 40, 41]. We have just showed that the formation probability depends on the barrier B and the temperature T. Next, we explain how to determine this barrier and that temperature.

2.2.2.2 The barrier

We have just found a formula for the formation probability as a function of the ratio B/T. We now proceed by providing a way to estimate the barrier B. Close to contact, the system minimizes its surface energy through a very rapid neck growth. In fact, the neck growth is considered to be so fast that other collective degrees of freedom (elongation and asymmetry) are assumed frozen during that process [35]. The neck growth turns the dinuclear system into a mononuclear one.

This is represented schematically in Fig. 2.3. Therefore, it is assumed that, close to contact, the system is injected into an asymmetric fission valley where the deformation energy has been minimized with respect to the neck size while keeping the asymmetry and elongation equal to their initial values [35]. Clearly, injection into the asymmetric fission valley was introduced in order to, starting from a dinuclear system (right after capture) switch to a mononuclear one (right before the start of diffusion) without having to face too many difficulties.

(a) Shape close to contact and before neck growth. (b) Shape after neck growth and at the injection point.

Figure 2.3: The left figure shows the shape of the dinuclear system close to contact and right before the rapid neck growth takes place. The figure on the right shows the shape of the resulting mononucleus after neck growth and in its injection configuration. Thus, one might say that the arrow of time points to the right. Notice that, as mentioned in the text, the rapid neck growth is assumed to occur at constant elongation and asymmetry. Thus, the two shapes presented here have the same elongation and asymmetry. This can be seen from the dashed lines in the rightmost figure.

The shape parametrization consists of two spheres smoothly connected through a hyperboloidal neck. The corresponding macroscopic energy deformation landscapes are available for this particular parametrization as a function of elongation, asymmetry and neck size [48]. By minimizing the energy with respect to the neck parameter while, as previously explained, keeping the asymmetry as well as the elongation equal to their original values, one obtains the deformation energy along the asymmetric fission valley [35]. This deformation energy is given by

$$\xi = a + bS + cS^2, \tag{2.36}$$

where $\xi = E_{\text{def}}/E_{\text{surf}}$ while E_{def} and E_{surf} are, respectively, the deformation energy of the system and the surface energy of corresponding spherical nucleus with radius R. The separation variable is defined as $s = L - 2(R_1 + R_2)$ where L is the total length of the system while R_1 and R_2 are the radii of the two colliding nuclei (the two connected spheres) and $S = s/R$.

The values for a, b and c, can be found in Ref. [35] and are restated here for the sake of completeness. These parameters are functions of the asymmetry and fissility, respectively, defined as

$$\Delta = \frac{R_1 - R_2}{R_1 + R_2}, \tag{2.37}$$

$$x = \frac{E_c}{2E_{\text{surf}}}, \tag{2.38}$$

where E_c and E_{surf} are the Coulomb and surface energy of a sphere, respectively.

Furthermore, a, b and c, are expressed as

$$a = \alpha_a + \beta_a t + \gamma t^2, \tag{2.39}$$
$$b = \alpha_b + \beta_b t, \tag{2.40}$$
$$c = \alpha_c + \beta_c t, \tag{2.41}$$

where

$$\alpha_a = -0.00557 - 0.01929\exp(-D/0.02283), \tag{2.42}$$
$$\beta_a = 0.048 + 0.12151\exp(-D/0.04053), \tag{2.43}$$
$$\gamma = -0.073 + 0.094D, \tag{2.44}$$
$$\alpha_b = -0.01045 - 0.05303\exp(-D/0.03205), \tag{2.45}$$
$$\beta_b = 0.019 + 0.25663\exp(-D/0.07331), \tag{2.46}$$
$$\alpha_c = -0.02137 + 0.1944D, \tag{2.47}$$
$$\beta_c = 0.0214 + 0.6158D, \tag{2.48}$$

with $D = \Delta^2$ and $t = 1 - x$. In the above parametrization, the surface energy and fissility should be taken as

$$E_{\rm surf} = 17.9439\,(1 - 1.7826\,I^2)\,A^{2/3}\ {\rm MeV}, \tag{2.49}$$
$$x = \frac{Z^2/A}{50.883\,(1 - 1.7826\,I^2)}, \tag{2.50}$$

where $I = (N - Z)/A$. Furthermore, all radii are obtained using $R = 1.155A^{1/3}$.

Therefore, given a value of s, corresponding to the injection point, one can deduce the height of the barrier B. Indeed, the barrier can be expressed as

$$B = E_{\rm surf} \cdot \left[\xi(s_{\rm max}) - \xi(s_{\rm inj})\right], \tag{2.51}$$

where $s_{\rm max}$ is the separation for which the deformation energy reaches its maximal value and $s_{\rm inj}$ is the separation at the injection point. In the following, we discuss the injection point parametrization which allows us to determine B using the previous relation, but first let us describe how to determine the temperature appearing in the expression for the formation probability.

2.2.2.3 The temperature

Assuming that, at the injection point, all the collective kinetic energy has been dissipated. Then the thermal excitation energy for the system is equal to

$$E^* = E_{\rm cm} + Q_{\rm fus} - E_{\rm def}(s_{\rm inj}). \tag{2.52}$$

The fusion Q-value is $Q_{\rm fus} = M_T + M_P - M_{CN}$ where M_T, M_P and M_{CN} are the masses of the target, projectile and compound nucleus masses, respectively. The deformation energy at injection is by definition $E_{\rm def}(s_{\rm inj})$.

For a Fermi gas, the excitation energy and the temperature are related through an expression having the form $T = \sqrt{E^*/a}$ where a is the level density parameter. As argued in Refs. [40,41], the temperature changes during diffusion. Thus, one can define the temperature at the injection-point and the temperature at the saddle-point, respectively, as

$$T_{\text{inj}} = \sqrt{E^*_{\text{inj}}/a}, \tag{2.53}$$

$$T_{\text{SP}} = \sqrt{E^*_{\text{SP}}/a}. \tag{2.54}$$

Furthermore, it is assumed as in Refs. [40,41], that during diffusion the temperature is equal to the geometric mean $T = \sqrt{T_{\text{inj}}\, T_{\text{SP}}}$. We will return to the temperatures when we discuss the survival probability and the parametrization of entropy (cf. Sect. 2.3.2).

Again, the compound nucleus mass is experimentally unknown and must be determined by theoretical means. Furthermore, temperature is in some sense also mass dependent, e.g., see Eqs. (2.52) and (2.54). Therefore, this demonstrates the influence of masses and their predictions, on fusion-evaporation models.

2.2.2.4 Injection point parametrization

As previously mentioned, for light systems the formation probability is equal to 1. In those cases, the production cross-section is simply given as the product of the capture and survival probability. Note that we have already explained how to determine the capture cross-section and a method to obtain the survival probability is provided in the next section. Therefore, we are in a position to calculate the production cross-section assuming that hindrance is negligible, i.e., only taking into account the capture and the survival steps. Since some production cross-sections have been measured, it is possible to divide them by the theoretical cross-section obtained neglecting hindrance, thus, an "experimental" formation probability is determined and can be expressed as

$$P^{\text{Exp}}_{\text{form}} = \frac{\sigma^{\text{exp}}_{\text{ER}}}{\sigma_{\text{cap}} \times P_{\text{surv}}}, \tag{2.55}$$

where $\sigma^{\text{exp}}_{\text{ER}}$, σ_{cap} and P_{surv}, are the peak of the measured production cross-section, the calculated capture cross-section and survival probability, respectively. Now, since the "experimental" formation probability and the diffusion temperature are known, it is possible to deduce the barrier B entering the theoretical formation probability and from it, deduce an "experimental" injection-point $s^{\text{Exp}}_{\text{inj}}$.

Based on this empirical evidence, i.e., knowing $s^{\text{Exp}}_{\text{inj}}$, one can construct a parametrization for the injection-points in order to make predictions of the formation probability. As an example, Ref. [40] gives the following parametrization

$$s_{\text{inj}} \approx 2.30\text{fm} - 0.062(E_{\text{cm}} - B_0)\ \text{fm/MeV}, \tag{2.56}$$

where $(E_{\text{cm}} - B_0)$ is the excess of kinetic energy over the mean Coulomb barrier. This expression was obtained based on 27 measured cold-fusion cross-sections and using the mass predictions from Möller [49,50]. Another example taken from Ref. [41] is based on 22 hot-fusion reactions and using the mass predictions from Kowal [51,52], gives

$$s_{\text{inj}} \approx 4.09\text{fm} - 0.192(E_{\text{cm}} - B_0)\ \text{fm/MeV}. \tag{2.57}$$

Both parametrizations are shown in Fig. 2.4. On the one hand, the saddle-point and ground-state masses from Kowal [51, 52] deliver very regular systematics for the injection point. On the other hand, this is not the case when the saddle-point and ground-state masses from Möller [49,50] are used. Note that this regularity may also be inherent to the two different datasets considered in Refs. [40, 41].

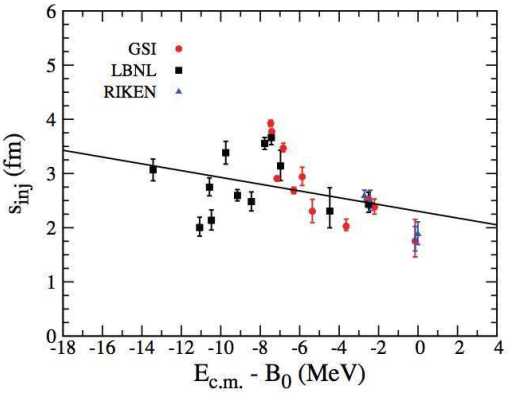

(a) Cold-fusion
$s_{\text{inj}} = 2.30 \text{ fm} - 0.062(E_{cm} - B_0)$ fm/MeV

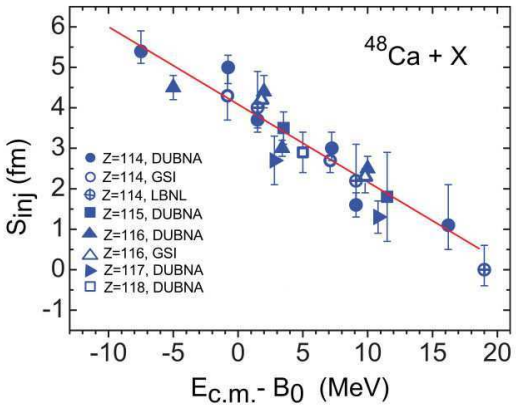

(b) Hot-fusion
$s_{\text{inj}} = 4.09 \text{ fm} - 0.192(E_{cm} - B_0)$ fm/MeV

Figure 2.4: On the left, the injection point parametrization based on 27 cold-fusion excitation functions reproduced from Ref. [40]. On the right, the injection point parametrization based on 22 hot-fusion excitation functions reproduced from Ref. [41].

As the injection point is the only adjustable parameter, its parametrization has great consequences on the predictions of the fusion-by-diffusion model. So far, no clear explanation about the particular form of this parametrization and its energy dependence has been supplied. In the next chapter, an attempt is made to, at least partially, explain the origin of this energy dependent parametrization.

2.2.3 Formation in the Langevin description

We have just finished describing the formation step in the fusion-by-diffusion model where the diffusion is assumed over-damped and inertia is completely neglected. However, there are other descriptions of the diffusion process where inertia is fully considered. Such calculations are based on the Langevin approach. Here, we closely follow the development described in Ref. [34]. The Langevin equation describing the diffusion over an inverted parabola is

$$\ddot{q} + \beta\dot{q} - \omega^2 q = r\,(t)\,, \tag{2.58}$$

where the random force is, as before, defined by

$$\langle r(t)\rangle = 0, \tag{2.59}$$

$$\langle r(t)r(t')\rangle = \frac{2T\beta}{m}\delta(t-t'). \tag{2.60}$$

Taking the Laplace transform leads to

$$q(s)\left[s^2+\beta s-\omega^2\right]=\left[r(s)+q(0)s+(\dot{q}(0)+q(0)\beta)\right]. \tag{2.61}$$

In order to inverse Laplace transform the previous expression, we must use partial fraction decomposition. This is achieved by finding the roots of the left hand side by solving

$$s^2+\beta s-\omega^2=0. \tag{2.62}$$

This is a quadratic equation, consequently, finding the roots, here, is trivial. However, we will see in chapter 3 that this step is critical and bears great physical significance. The roots are, of course, obtained as

$$s_\pm=\frac{-\beta\pm\sqrt{\beta^2+4\omega^2}}{2}. \tag{2.63}$$

From this we deduce that

$$q(s)=\left[\frac{1}{(s-s_+)(s-s_-)}\right]\left[r(s)+q(0)s+(\dot{q}(0)+q(0)\beta)\right]. \tag{2.64}$$

The term by term inverse transformation leads to

$$\begin{aligned}
&\frac{r(s)}{(s-s_+)(s-s_-)}\rightarrow\int_0^t r(t')\left[\frac{e^{s_+(t-t')}-e^{s_-(t-t')}}{s_+-s_-}\right]\mathrm{d}t',\\
&\frac{q(0)s}{(s-s_+)(s-s_-)}\rightarrow[q(0)]\left[\frac{s_+e^{s_+t}-s_-e^{s_-t}}{s_+-s_-}\right],\\
&\frac{\dot{q}(0)+q(0)\beta}{(s-s_+)(s-s_-)}\rightarrow[\dot{q}(0)+q(0)\beta]\left[\frac{e^{s_+t}-e^{s_-t}}{s_+-s_-}\right].
\end{aligned} \tag{2.65}$$

Introducing $x=\beta/2\omega$ the final solution reads

$$\begin{aligned}
q(t)=&\int_0^t r(t')\left[\frac{e^{s_+(t-t')}-e^{s_-(t-t')}}{s_+-s_-}\right]\mathrm{d}t'\\
&+[q(0)]e^{-x\omega t}\left[\cosh\left(\sqrt{1+x^2}\omega t\right)+\frac{x}{\sqrt{1+x^2}}\sinh\left(\sqrt{1+x^2}\omega t\right)\right]\\
&+[\dot{q}(0)]\frac{1}{\omega\sqrt{1+x^2}}e^{-x\omega t}\sinh\left(\sqrt{1+x^2}\omega t\right)
\end{aligned} \tag{2.66}$$

Using $\langle r(t)\rangle=0$, the mean trajectory is obtained as

$$\begin{aligned}
\langle q(t)\rangle=&[q(0)]e^{-x\omega t}\left[\cosh\left(\sqrt{1+x^2}\omega t\right)+\frac{x}{\sqrt{1+x^2}}\sinh\left(\sqrt{1+x^2}\omega t\right)\right]\\
&+[\dot{q}(0)]\frac{1}{\omega\sqrt{1+x^2}}e^{-x\omega t}\sinh\left(\sqrt{1+x^2}\omega t\right).
\end{aligned} \tag{2.67}$$

In a similar way, it is possible to determine the fluctuations about the mean trajectory which are given by

$$\begin{aligned}\sigma^2(t) &= \langle q^2(t)\rangle - \langle q(t)\rangle^2 \\ &= \int_0^t\int_0^t \langle r(t')r(t'')\rangle \left[\frac{e^{s_+(t-t')}-e^{s_-(t-t')}}{s_+-s_-}\right]\left[\frac{e^{s_+(t-t'')}-e^{s_-(t-t'')}}{s_+-s_-}\right]\mathrm{d}t'\mathrm{d}t'' \\ &= \frac{2T\beta}{m(s_+-s_-)^2}\left[\frac{1}{2s_+}\left(e^{2s_+t}-1\right)+\frac{1}{2s_-}\left(e^{2s_-t}-1\right)+\frac{2}{s_++s_-}\left(1-e^{(s_++s_-)t}\right)\right].\end{aligned} \tag{2.68}$$

The introduction of $x=\beta/2\omega$ reduces the previous expression to

$$\begin{aligned}\sigma^2(t) &= \frac{2T\beta}{m(s_+-s_-)^2}\left[e^{-2x\omega t}\left(\frac{1}{2s_+s_-}\left(s_-e^{2\sqrt{1+x^2}}+s_+e^{-2\sqrt{1+x^2}}\right)-\frac{2}{s_++s_-}\right)-\frac{(s_+-s_-)^2}{2s_+s_-\left(s_++s_-\right)}\right] \\ &= \frac{T}{m\omega^2}\left[e^{-2x\omega t}\left(\frac{2x^2}{1+x^2}\sinh^2\left(\sqrt{1+x^2}\omega t\right)+\frac{x}{\sqrt{1+x^2}}\sinh\left(2\sqrt{1+x^2}\omega t\right)+1\right)-1\right].\end{aligned} \tag{2.69}$$

Note that we have used the identity $\cosh(2x)=2\sinh^2(x)+1$. This expression is consistent with the one given in Ref. [34].

As before, the formation probability is given by

$$P_{\text{form}}\left(t,q(0),\dot{q}(0),T\right)=\frac{1}{2}\operatorname{erfc}\left(-\frac{\langle q(t)\rangle}{\sqrt{2}\sigma(t)}\right). \tag{2.70}$$

After a very long time, it becomes

$$P_{\text{form}}\left(t\to\infty,q(0),\dot{q}(0),T\right)=\frac{1}{2}\operatorname{erfc}\left(\sqrt{\frac{B}{T'}}-\frac{1}{(x+\sqrt{1+x^2})}\sqrt{\frac{K}{T'}}\right), \tag{2.71}$$

where the initial kinetic energy $K=m\dot{q}^2(0)/2$ and the initial barrier height $B=m\omega^2q^2(0)/2$ have been introduced and $T'=2Tx(\sqrt{1+x^2}-x)$. Note that this expression is consistent with the one obtained in Ref. [34]. In order for the formation probability to be 1/2, the initial kinetic energy should be

$$K=(x+\sqrt{1+x^2})^2B. \tag{2.72}$$

In turn, the mean trajectory feels an effective barrier expressed as

$$B_{\text{eff}}=(x+\sqrt{1+x^2})^2B. \tag{2.73}$$

Notice that since $x=\beta/2\omega$, the effective barrier accounts for the nuclear viscosity.

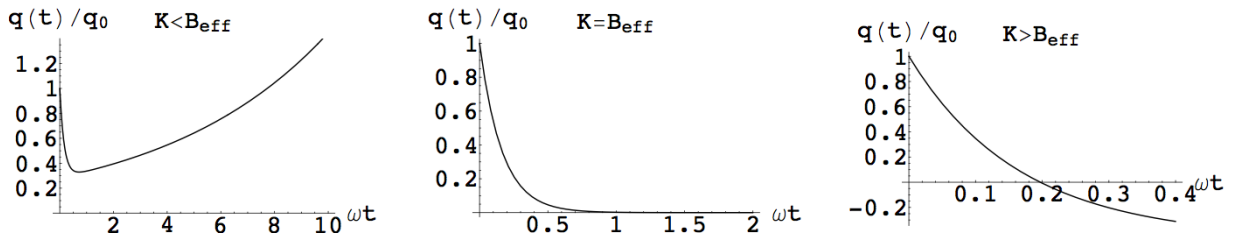

Figure 2.5: The mean trajectory is plotted as a function of time. In the first, second and third columns, we have, respectively, $K = B_{\text{eff}}/2$, $K = B_{\text{eff}}$ and $K = 2B_{\text{eff}}$. These plots are dimensionless. Figure reproduced from [34].

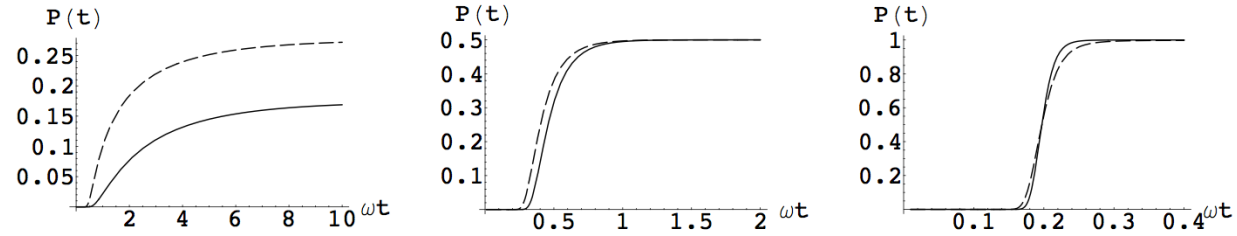

Figure 2.6: The formation probability P_{form} is plotted as a function of time. In the first, second and third column, we have, respectively, $K = B_{\text{eff}}/2$, $K = B_{\text{eff}}$ and $K = 2B_{\text{eff}}$. The solid line corresponds to $T = B/5$ and the dashed line to $T = B/2$. These plots are dimensionless. Figure reproduced from [34].

The mean trajectory and the formation probability are, respectively, shown in Figs. 2.5 and 2.6, as functions of time. Finally, let us mention that with the Smoluchowski equation P_{form} is always lower than 1/2 as no kinetic energy remains at the injection point. With the Langevin formalism, the initial kinetic energy enhances the fusion probability which can then be higher than 1/2 if $K > B_{\text{eff}}$. This can be seen in Fig. 2.6.

From Fig. 2.5, one can see that when $K < B_{\text{eff}}$ the mean trajectory is not able to cross the internal barrier. Therefore, in average the system does not form a compound nucleus but rather disintegrates through quasi-fission. On the other hand, when $K > B_{\text{eff}}$ then the mean trajectory easily crosses the internal barrier. More importantly, Fig. 2.6 shows that even in cases where $K < B_{\text{eff}}$ the formation probability does not vanish. This is due to the thermal fluctuations which allow the system to diffuse over the internal barrier in order to reach the excited compound nucleus configuration. In fusion-evaporation reactions leading to the synthesis of superheavy nuclei, one typically has that $K \ll B_{\text{eff}}$ and in turn the corresponding formation probabilities are extremely small, i.e., $P_{\text{form}} \ll 1$. Thus, fusion is severely hindered.

2.3 The survival step

So far, we have described the fusion cross-section consisting of the capture and formation probabilities. Through these two steps an excited compound nucleus configuration has been reached. We now focus on the de-excitation of this compound nucleus where we assume that it can either evaporate one neutron or fission. In that special case the one neutron survival probability is given by

$$P_{\text{surv}} = \frac{\Gamma_n}{\Gamma_n + \Gamma_f} P_<, \tag{2.74}$$

where Γ_n and Γ_f are, respectively, the neutron emission and fission disintegration widths. Here, $P_<$ is the probability that the excitation energy, after the emission of a single neutron, is below the second chance fission threshold [40]. The first factor on the left hand side is the probability of emitting a first neutron instead of fissioning. Note that generalizations to 2 or more successive neutron emissions and to other particles are easily obtained [53].

The evaporation of light particles and fission are usually described by two different formalisms. On the one hand, evaporation is usually treated within the Weisskopf or Hauser-Feschbach formulations [53]. On the other hand, fission is addressed in the Bohr and Wheeler framework where modern versions include additional corrections by Kramers and Strutinsky [53]. However, it is also possible to treat evaporation and fission on an equal footing by using the transition state theory presented in Ref. [54]. This is what is done in the fusion-by-diffusion model [35,36] which we now present.

2.3.1 The expressions for the widths

After the capture and formation steps a compound nucleus of mass number A is produced in a reaction with an excitation energy $E^* = E_{\text{cm}} + Q_{\text{fus}}$. The fission barrier is defined as,

$$B_f = M_A^{SP} - M_A^{GS}, \tag{2.75}$$

where M_A^{SP} and M_A^{GS} are, respectively, the saddle-point and ground-state masses of the compound nucleus. Notice these two quantities are usually unknown for superheavy nuclei and must be determined through theoretical calculations, i.e., in most cases macroscopic-microscopic calculations Refs. [50–52].

On the other hand, the neutron separation energy is defined as

$$S_n = (M_{A-1}^{GS} + M_n) - M_A^{GS}, \tag{2.76}$$

where M_{A-1}^{GS} and M_n are, respectively, the daughter ground-state mass and the mass of a neutron. As before, M_A^{GS} and M_{A-1}^{GS} must be determined theoretically.

The transition state theory is a statistical calculation and is supported by the equiprobability of all accessible states. Thus, probabilities can be expressed as ratios of numbers of states. The ratio of the neutron emission width to the fission disintegration width is

$$\frac{\Gamma_n}{\Gamma_f} = \frac{N_n}{N_f} = \frac{\int_0^{U_n} \rho_n(\epsilon)\mathrm{d}\epsilon}{\int_0^{U_f} \rho_f(\epsilon)\mathrm{d}\epsilon}. \tag{2.77}$$

In the previous relation, N_n is the number of states, lying between S_n and E^*, the compound nucleus can transition to by emitting a neutron. Similarly, N_f is the number of states, lying between B_f and E^*, the compound nucleus can transition to by fissioning. The notations, $U_n = E^* - S_n$ and $U_f = E^* - B_f$, were introduced in the previous expression for convenience. As usual, ρ_n and ρ_f are the transitional state densities for neutron emission and fission, respectively. In both cases, densities can be expressed as $\rho = \exp(\Sigma)$ where Σ is the corresponding entropy. Therefore, the energies for which the previous integrals yield significant contributions are those close to the upper integration bound, more precisely, U_n and U_f. This allows us to expand the entropies around those values. For the neutron, we have

$$\Sigma_n(\epsilon) \approx \Sigma_n(U_n) + \Sigma_n'(U_n)(\epsilon - U_n). \tag{2.78}$$

Thus, the integral becomes

$$\begin{aligned} N_n &= \int_0^{U_n} \exp(\Sigma(\epsilon))\mathrm{d}\epsilon \\ &\approx \int_0^{U_n} \exp(\Sigma_n(U_n) + \Sigma_n'(U_n)(\epsilon - U_n))\mathrm{d}\epsilon \\ &\approx \frac{1}{\Sigma_n'(U_n)} \exp(\Sigma_n(U_n)). \end{aligned} \tag{2.79}$$

A similar expression can be found for N_f, consequently, one finally has that

$$\frac{\Gamma_n}{\Gamma_f} = \frac{\Sigma_f'(U_f)}{\Sigma_n'(U_n)} \exp(\Sigma_n(U_n) - \Sigma_f(U_f)), \tag{2.80}$$

where Σ_n' and Σ_f' are, as usual, the inverse of the temperatures.

2.3.2 The entropy parametrization

In the literature, formulas for the entropies are available and account for shell corrections, pairing, as well as nuclear deformation. We now simply restate the formulas taken from Refs [55,56] for the sake of completeness. These have been used in the fusion-by-diffusion model [35,36]. The entropy is expressed as

$$\Sigma(U) = 2\sqrt{a(U^* + \Delta_{sh}[1 - \exp(-U^*/k)])} \tag{2.81}$$

where $k = A^{1/3}/0.47$ MeV and Δ_{sh} are the shell corrections also in MeV which can be taken from Refs. [49,57]. The level density parameter is taken to be

$$a = 0.076A + 0.180A^{2/3}F(\alpha) + 0.157A^{1/3}G(\alpha) \quad \mathrm{MeV}^{-1}, \tag{2.82}$$

where the nuclear deformation comes in through the definitions

$$F(\alpha) = 1 + (0.6416\alpha - 0.1421\alpha^2)^2, \tag{2.83}$$

$$G(\alpha) = 1 + (0.6542\alpha - 0.0483\alpha^2)^2, \tag{2.84}$$

with $\alpha = (R_{\max} - R)/R$ where $R_{\max}$ is the semi-major axis in the case of axially symmetric deformation and R is the corresponding spherical radius.

Finally, pairing is taken into account by

$$U^* = \begin{cases} U - 24\ \text{MeV}/\sqrt{A} & \text{even-even nuclei,} \\ U - 12\ \text{MeV}/\sqrt{A} & \text{odd nuclei,} \\ U\ \text{MeV}/\sqrt{A} & \text{odd-odd nuclei.} \end{cases} \tag{2.85}$$

From the previous relation, one can see that U^* can be negative, in those cases the densities are assumed to vanish, i.e., $\rho(U) = 0$, in all other cases, the above formulas for the entropy hold. Note that other approaches include additional effects which might also be important in the calculations of the widths. For instance, some of those effects are the dissipation and collective enhancement factor which, respectively, decrease and increase, the survival probabilities and tend to compensate each other [53]. More importantly, the studies [37, 38] have shown that the survival probabilities are further influenced by the fission barriers than by the moderate differences between the various ways of obtaining the widths.

2.3.3 The survival probability

The probability of emitting a neutron rather than fission is given by

$$\frac{\Gamma_n}{\Gamma_n + \Gamma_f} = \frac{\Gamma_n/\Gamma_f}{1 + \Gamma_n/\Gamma_f} \tag{2.86}$$

where the ratio Γ_n/Γ_f was already obtained. Here, however, we are only interested in survival scenarios where the system emits a single neutron and then neither emits another one nor fissions. For those two processes to be forbidden the remaining energy after emitting one neutron must be smaller than both the neutron emission threshold and the fission threshold. The fission threshold is, of course, the fission barrier of the daughter nucleus given by

$$B_f^{A-1} = (M_{A-1}^{SP} + M_n) - M_A^{GS}. \tag{2.87}$$

This is simply the energy required for fission to take place, after the compound nucleus has emitted one neutron. The remaining energy after a first neutron emission is simply $E^* - K$ where K is the kinetic energy of the emitted neutron. On the one hand, if $E^* < B_f^{A-1}$ then there are no restrictions on K in order to avoid second chance fission. On the other hand, if $E^* > B_f^{A-1}$ then in order to forbid fission K must be larger than $K_1 = E^* - B_f^{A-1}$.

Assuming the kinetic energy of the emitted neutron follows a Maxwell distribution, proportional to $K\exp(-K/T)$, where T is the temperature of the neutron transition state then the probability that $K > K_1$ is given by

$$\frac{\int_{K_1}^{\infty} K\exp(-K/T)\mathrm{d}K}{\int_0^{\infty} K\exp(-K/T)\mathrm{d}K} = \left(1 + \frac{K_1}{T}\right)\exp\left(-\frac{K_1}{T}\right). \tag{2.88}$$

Note that this is not the expression given in Ref. [35] where a mistake was made and corrected in Ref. [36].

Finally, the one neutron survival probability, i.e., the probability to emit a single neutron without emitting a second one or fissioning, is given by

$$\frac{\Gamma_n}{\Gamma_n + \Gamma_f} \qquad \text{if} \qquad E^* < B_f^{A-1}, \tag{2.89}$$

$$\frac{\Gamma_n}{\Gamma_n + \Gamma_f} \left(1 + \frac{K_1}{T}\right) \exp\left(-\frac{K_1}{T}\right) \qquad \text{if} \qquad E^* > B_f^{A-1}. \tag{2.90}$$

2.4 Open questions

We have just finished exposing the three models that, when put together, form the fusion-evaporation model. Now, we would like to precisely explain the global philosophy of this thesis. Our primary goal is to predict, as accurately as possible, the production cross-sections of super-heavy nuclei. This is a very challenging task and up to this day, the precision of these predictions remains unsatisfactory.

As we have seen, the production cross-section is theoretically decomposed into three independent contributions: the capture cross-section, the formation probability and the survival probability. On the one hand, the capture cross-section as well as the survival probability, are theoretically well understood because they are based on our extensive knowledge of collisions between light partners. On the other hand, the formation step, responsible for fusion hindrance, only exists in collisions involving very heavy nuclei. Thus, although qualitatively understood, a precise theoretical description of hindrance is still unavailable. Consequently, this thesis is an attempt to both, clarify and constrain, the formation step.

Typical predictions of the formation probability, obtained with different models, are shown in Fig. 2.7. These predictions span 3 orders of magnitude. This immense gap between existing models clearly demonstrates that the formation step is not properly understood and this motivates the present investigation.

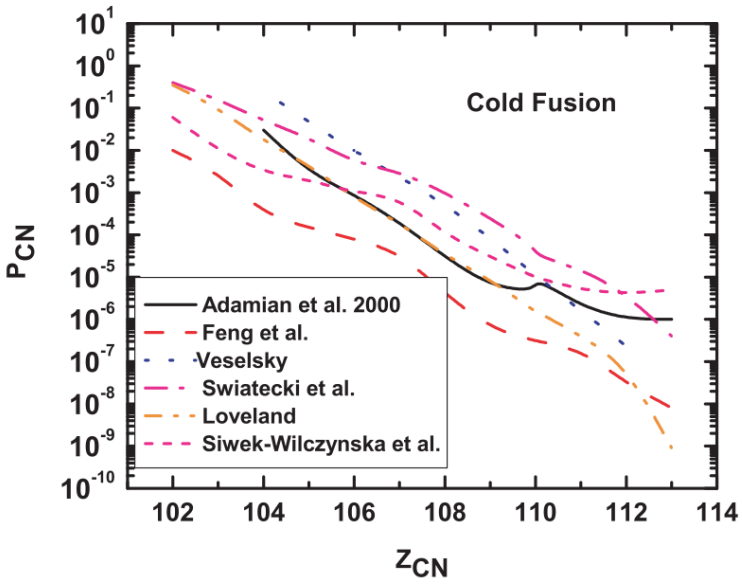

Figure 2.7: Typical predictions for the formation probability in cold-fusion reactions. Figure reproduced from [58].

In collisions between heavy nuclei, the Coulomb repulsion is so intense that, after capture, the composite system often re-separates before the compound nucleus is even formed. This re-separation is usually referred to as quasi-fission and lies at the very heart of fusion hindrance.

Moreover, since the compound nucleus is formed in an excited state, it can disintegrate through fission. It turns out that quasi-fission and fission products are so similar that, experimentally, it is very difficult to distinguish them. Therefore, the formation step cannot be constrained experimentally and one is forced to constrain this step theoretically.

As previously mentioned, some production cross-sections, have been measured. Therefore, the "experimental" formation probability can be expressed as

$$P_{\text{form}}^{\text{exp}} = \frac{\sigma_{\text{ER}}^{\text{exp}}}{\sigma_{\text{cap}} \times P_{\text{surv}}}, \tag{2.91}$$

where $\sigma_{\text{ER}}^{\text{exp}}$ is a measured production cross-section. Thus, our approach goes as follows. First, we will determine the uncertainties in the capture cross-section. Then, we will obtain those in the survival probability. Finally, by propagating these uncertainties onto the formation probability we will constrain this quantity.

We would now like to stress that sensibility as well as uncertainty analyses, such as [37, 38], have shown that the most crucial quantities entering the survival probability calculations are the fission barriers. In the following, we will assume that the uncertainties in the survival probability only come from the fission barriers. The importance of the fission barriers was put forward by comparing the available models. More precisely, by calculating the survival probability through diverse combinations of fission barriers as well as evaporation and fission widths calculations. Here, however, our approach will be different, as we will study the uncertainties within a single fusion-evaporation model. This way it becomes possible to theoretically constrain the formation probability in this particular model.

Constraining the formation probability is certainly not sufficient because this quantity still needs to be calculated in order to make predictions. Therefore, the theoretical description of the formation step is crucial. However, many questions remain unanswered regarding the formation of the compound nucleus. For instance, the influence of inertia, on the diffusion, is not perfectly understood. Therefore, it is unclear whether one should use a Langevin or a Smoluchowski description. Furthermore, the initial conditions required to solve these equations remain unknown. Additionally, the viscosity parameter is not well known. In the next chapter, we will focus on the effects of inertia and on the choice of the dynamical formulation, i.e., Langevin or Smoluchowski.

Chapter 3

New mechanism to the fusion hindrance

In chapter 2, two dynamical formulations of diffusion, considered in the formation step, were exposed. We first saw that, in the fusion-by-diffusion model, the formation step was considered over-damped (Smoluchowski approximation) [35, 36, 40, 41]. Then, we discussed a second model where diffusion was described by a Langevin equation [34]. Remember that the over-damped formulation is nothing but an approximation of the Langevin description where the effects of inertia are completely neglected [59]. The exact quantitative influence of inertia during diffusion is not perfectly understood. As a consequence, it is unclear whether the diffusion process should be described by a Langevin or a Smoluchowski equation.

Furthermore, regardless of the formalism, over-damped or Langevin, the initial conditions required to solve the equations remain unknown. Historically, the initial condition has been chosen at the contact point which defines the border between the dinucleus models and the deformed compound nucleus models. However, it is crucial to remember that the initial condition, entering the Smoluchowski formulation of the fusion-by-diffusion model, is the only adjustable parameter. Thus, for predictions to be made a parametrization of that initial condition is required. Such a parametrization has been proposed, in Refs. [40, 41], as a function of the excess of kinetic energy over the mean Coulomb barrier, i.e., a function of $(E_{\mathrm{cm}} - B_0)$. As stated in Refs. [40, 41], at the moment, there is no clear explanation for this energy dependent parametrization. In other models, the situation is not much clearer and instead of an energy dependent parametrization, the initial condition is arbitrarily chosen to always correspond to the contact point (historical choice) [33, 42].

The purpose of the present chapter is to, first, clarify which description, i.e., the over-damped or the Langevin, should be favoured and second, to provide a parametrization for the initial condition based on first principles. In order to better identify the distinctions between the Smoluchowski and the Langevin descriptions, we start by treating inertia using singular perturbation theory. This can be seen as a third formulation of the diffusion process, falling right between the Langevin and the Smoluchowski approximation. This approach is useful in those cases where inertia cannot be completely neglected nor does it play a dominant role in the dynamics of diffusion. This treatment allows us to formally build a bridge between the Langevin and the Smoluchowski descriptions and to provide a simple explanation for the energy dependence of the initial condition, proposed in [40, 41].

3.1 From Langevin to Smoluchowski

In this section, we discuss solutions to the Langevin equation with a parabolic potential barrier and close to the over-damped regime. This approximation corresponds to the assumption that $\beta \gg \omega$ in the following Langevin equation

$$\ddot{q} + \beta\dot{q} - \omega^2 q = r\left(t\right), \tag{3.1}$$

that was exactly solved in chapter 2. Interestingly enough, it turns out that the Smoluchowksi approximation is equivalent to neglecting the inertia term in this equation, i.e., completely removing the second derivative term. In what follows, we explore in great detail what happens to the solution of the previous expression when this approximation is made. Indeed, dividing the previous relation by ω^2 and making the change of variables $t' = t\omega^2/\beta$, we obtain

$$\epsilon\frac{d^2q\left(t'\right)}{dt'^2} + \frac{dq\left(t'\right)}{dt'} - q\left(t'\right) = R(t), \tag{3.2}$$

where $\epsilon = \omega^2/\beta^2$ and $R(t) = r(t)/\omega^2$. From the last expression, we plainly see that taking the limit $\epsilon \to 0$ is equivalent to the assumption that $\beta \gg \omega$ which is also equivalent to, altogether, neglecting inertia. Here, we discuss cases where this approximation is not valid and inertia must be treated perturbatively. As usual, the random force is statistically defined by

$$\langle R(t)\rangle = 0, \tag{3.3}$$

$$\langle R(t_1)R(t_2)\rangle = \frac{2TB}{\omega^4 m}\delta(t_1 - t_2). \tag{3.4}$$

3.1.1 A perturbative treatment of inertia

We now treat inertia in an approximate way by solving the previous equation using perturbation theory. This approach was strongly influenced by the ideas presented in [60,61] where perturbation theory and asymptotic methods are exposed. Since time was rescaled, we must use the altered Laplace transform formulas

$$\begin{aligned}\epsilon\frac{d^2q\left(t'\right)}{dt'^2} &\to \epsilon\left(\frac{\beta}{\omega^2}\right)^2\left[s^2q(s) - sq(0) - \dot{q}(0)\right],\\ \frac{dq\left(t'\right)}{dt'} &\to \frac{\beta}{\omega^2}\left[sq(s) - q(0)\right].\end{aligned} \tag{3.5}$$

Note that all other transformations remain unchanged. It is also important to mention that, in these transformations, s is the conjugate variable of t and not of t'. In fact, this is the reason why the usual Laplace transforms have been altered. The Laplace transform of (3.2) yields

$$q(s)\left[\epsilon\left(\frac{\beta}{\omega^2}\right)^2 s^2 + \left(\frac{\beta}{\omega^2}\right)s - 1\right] = s\left[\epsilon\left(\frac{\beta}{\omega^2}\right)^2 q(0)\right] + \left[\epsilon\left(\frac{\beta}{\omega^2}\right)^2\dot{q}(0) + \left(\frac{\beta}{\omega^2}\right)q(0)\right] + R(s). \tag{3.6}$$

As usual, we must find the roots of the factor appearing on the left hand side. This is achieved by solving

$$\epsilon s'^2 + s' - 1 = 0, \tag{3.7}$$

where the change of variables $s' = s\beta/\omega^2$ was made. In turn, these roots allow us to use partial fraction decomposition in order to inverse Laplace transform the expression for $q(s)$ and obtain $q(t)$. Notice this is a quadratic equation and the exact roots are easily found. However, since we are interested in the transition between the Langevin and the Smoluchowski description, we will look for approximate roots, expressed as power series in ϵ. The first root is determined using regular perturbation theory, by assuming it has the form

$$s'_+(\epsilon) \approx a_0 + a_1\epsilon, \tag{3.8}$$

when restricting ourselves to a first order expansion. Injecting Eq. (3.8) into Eq. (3.7), we determine that $a_0 = 1$ to zeroth order and $a_1 = -1$ to first order. Gathering these two results, we obtain

$$s'_+ \approx 1 - \epsilon \Longrightarrow \; s_+ \approx \frac{\omega^2}{\beta}(1-\epsilon). \tag{3.9}$$

Looking for the second root is much more subtle. Fortunately, we are solving a quadratic equation, consequently, we know that $\epsilon s'_+ s'_- = -1$. This allows us to directly determine the second root as

$$s'_- \approx \frac{-1}{\epsilon(1-\epsilon)} \approx -(\epsilon^{-1}+1) \Longrightarrow s_- = -\frac{\omega^2}{\beta}(\epsilon^{-1}+1), \tag{3.10}$$

when restricting ourselves to the first two terms. Notice that the second root blows up as $\epsilon \to 0$. This is the reason for this kind of perturbation theory to be known as, singular perturbation theory. It is now possible to rewrite Eq. (3.7) approximately as

$$\epsilon\left(\frac{\beta}{\omega^2}\right)^2 s^2 + \left(\frac{\beta}{\omega^2}\right) s - 1 \approx \epsilon\left(\frac{\beta}{\omega^2}\right)^2 (s-s_+)\,(s-s_-)\,. \tag{3.11}$$

The expression for $q(s)$ then becomes

$$q(s) \approx \underbrace{\frac{s\left[\epsilon\left(\frac{\beta}{\omega^2}\right)^2 q(0)\right]}{\epsilon\left(\frac{\beta}{\omega^2}\right)^2 (s-s_+)\,(s-s_-)}}_{I} + \underbrace{\frac{\left[\epsilon\left(\frac{\beta}{\omega^2}\right)^2 \dot{q}(0) + \left(\frac{\beta}{\omega^2}\right) q(0)\right]}{\epsilon\left(\frac{\beta}{\omega^2}\right)^2 (s-s_+)\,(s-s_-)}}_{II} + \underbrace{\frac{R(s)}{\epsilon\left(\frac{\beta}{\omega^2}\right)^2 (s-s_+)\,(s-s_-)}}_{III}. \tag{3.12}$$

Taking the term by term inverse Laplace transform of the former expression gives

$$\begin{aligned}
I &\to \frac{\epsilon\frac{\beta}{\omega^2}\dot{q}(0) + q(0)}{1+2\epsilon-\epsilon^2}\left[e^{\frac{\omega^2}{\beta}(1-\epsilon)t} - e^{-\frac{\omega^2}{\beta}(\epsilon^{-1}+1)t}\right], \\
II &\to \frac{q(0)}{1+2\epsilon-\epsilon^2}\left[(\epsilon-\epsilon^2)\,e^{\frac{\omega^2}{\beta}(1-\epsilon)t} + (1+\epsilon)\,e^{-\frac{\omega^2}{\beta}(\epsilon^{-1}+1)t}\right], \\
III &\to \frac{\omega^2}{\beta\,(1+2\epsilon-\epsilon^2)}\int_0^t R(t')\left[e^{\frac{\omega^2}{\beta}(1-\epsilon)(t-t')} - e^{-\frac{\omega^2}{\beta}(\epsilon^{-1}+1)(t-t')}\right]\mathrm{d}t'.
\end{aligned} \tag{3.13}$$

Then, the mean solution reads

$$\langle q(t)\rangle \approx \frac{e^{\frac{\omega^2}{\beta}(1-\epsilon)t}}{1+2\epsilon-\epsilon^2}\left[\frac{\dot{q}(0)}{\beta}+q(0)\left(1+\epsilon-\epsilon^2\right)\right]+\frac{e^{-\frac{\omega^2}{\beta}(\epsilon^{-1}+1)t}}{1+2\epsilon-\epsilon^2}\left[-\frac{\dot{q}(0)}{\beta}+q(0)\epsilon\right], \tag{3.14}$$

with the simplification $\epsilon\beta/\omega^2 = 1/\beta$ along with the fact that $\langle R(t)\rangle = 0$. This last expression can be, more conveniently, written as

$$\frac{\langle q(t)\rangle}{q(0)} \approx \frac{e^{\sqrt{\epsilon}(1-\epsilon)\omega t}}{1+2\epsilon-\epsilon^2}\left[-\sqrt{\frac{\epsilon K}{B}}+\left(1+\epsilon-\epsilon^2\right)\right]+\frac{e^{-\sqrt{\epsilon}(\epsilon^{-1}+1)\omega t}}{1+2\epsilon-\epsilon^2}\left[\sqrt{\frac{\epsilon K}{B}}+\epsilon\right], \tag{3.15}$$

by introducing, as in chapter 2, the initial barrier height $B = m\omega^2 q^2(0)/2$, the initial kinetic energy $K = m\dot{q}^2(0)/2$, as well as remembering that $\dot{q}(0) > 0$ while $q(0) < 0$.

So far, we have only spoken about the average solution and now, we would like to address the question of the fluctuations. The latter can be obtained by computing

$$\begin{aligned}\sigma^2(t) &= \langle q^2(t)\rangle - \langle q(t)\rangle^2 \\ &= \left(\frac{\omega^2}{\beta\left(1+2\epsilon-\epsilon^2\right)}\right)^2 \int_0^t\int_0^t \langle R(t')R(t'')\rangle\left[e^{\frac{\omega^2}{\beta}(1-\epsilon)(t-t')}-e^{-\frac{\omega^2}{\beta}(\epsilon^{-1}+1)(t-t')}\right] \\ &\left[e^{\frac{\omega^2}{\beta}(1-\epsilon)(t-t'')}-e^{-\frac{\omega^2}{\beta}(\epsilon^{-1}+1)(t-t'')}\right]\mathrm{d}t'\mathrm{d}t''.\end{aligned} \tag{3.16}$$

Then, using $\langle R(t')R(t'')\rangle = 2T\beta\delta(t'-t'')/(\omega^4 m)$, leads us to

$$\begin{aligned}\sigma^2(t) = \frac{T}{m\omega^2}\frac{1}{\left(1+2\epsilon-\epsilon^2\right)^2}\Bigg[&\frac{1}{(1-\epsilon)}\left(e^{2\frac{\omega^2}{\beta}(1-\epsilon)t}-1\right)+\frac{\epsilon}{(1+\epsilon)}\left(1-e^{-2\frac{\omega^2}{\beta}(\epsilon^{-1}+1)t}\right) \\ &+\frac{4\epsilon}{(1+\epsilon^2)}\left(e^{-\frac{\omega^2}{\beta}(\epsilon^{-1}+\epsilon)t}-1\right)\Bigg].\end{aligned} \tag{3.17}$$

As before, the last expression can be, more conveniently, written as

$$\begin{aligned}\frac{\sigma^2(t)}{q(0)^2} = \frac{T}{2B}\frac{1}{\left(1+2\epsilon-\epsilon^2\right)^2}\Bigg[&\frac{1}{(1-\epsilon)}\left(e^{2\sqrt{\epsilon}(1-\epsilon)\omega t}-1\right)+\frac{\epsilon}{(1+\epsilon)}\left(1-e^{-2\sqrt{\epsilon}(\epsilon^{-1}+1)\omega t}\right) \\ &+\frac{4\epsilon}{(1+\epsilon^2)}\left(e^{-\sqrt{\epsilon}(\epsilon^{-1}+\epsilon)\omega t}-1\right)\Bigg].\end{aligned} \tag{3.18}$$

Finally, the fusion probability is

$$P_{\mathrm{form}}(t, q(0), \dot{q}(0), T) = \frac{1}{2}\,\mathrm{erfc}\left(-\frac{\langle q(t)\rangle}{\sqrt{2}\sigma(t)}\right), \tag{3.19}$$

where the expressions for the mean trajectory and the fluctuations are, respectively, given by Eqs. (3.15) and (3.18).

3.1.2 Comparing the three formulations

We are now in a position to compare the Langevin and Smoluchowski solutions, obtained in chapter 2, to the one we have just reached with our perturbative approach (cf. Eqs. (3.15) and (3.18)). This is shown in Fig. 3.1 where one can see that the three mean trajectories exhibit similar trends. This is also the case for the three formation probabilities. These similarities arise because we have set $\epsilon = 0.1$ such that inertia does not dominate the dynamics. Secondly, the kinetic energy K does not appear in the Smoluchowski solution, thus, we chose to set $K = 0$ such that we could easily compare the three approaches. We will later compare cases where $K \neq 0$ and explain why K does not appear in the Smoluchowski solution. Finally, note that our perturbative calculation is closer to a Langevin description than to a Smoluchowski one. It should also be mentioned that, in this case with $K = 0$, the Smoluchowski description and the perturbative approach overestimate the formation probability with respect to the Langevin formulation.

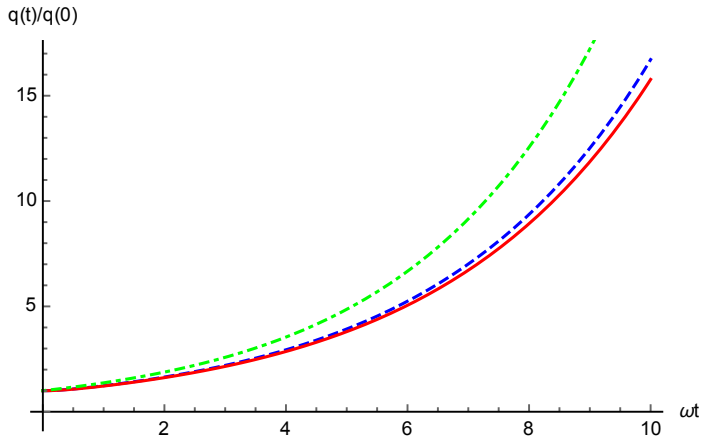

(a)

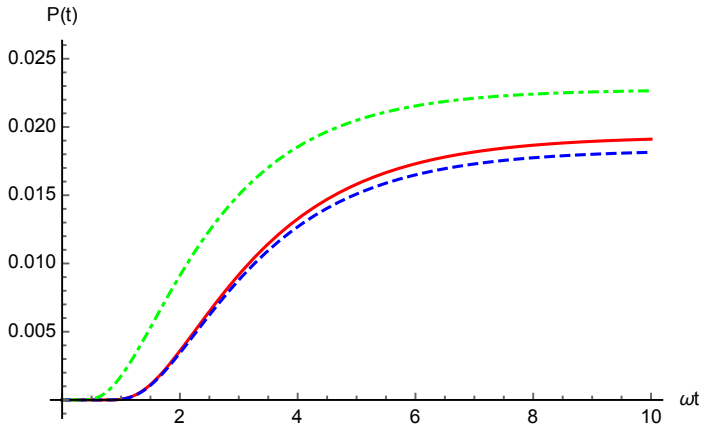

(b)

Figure 3.1: The mean trajectory and formation probability are given as functions of time, respectively, at the top and at the bottom. These are presented for the Smoluchowski (green dot-dashed line), the Langevin (blue dashed line) and our perturbative approach given by Eqs. (3.15) and (3.18) (red solid line). These are dimensionless plots where $\epsilon = 0.1$, $K = 0$ and $T = B/2$.

3.2 The initial conditions

We have, in some sense, reconciled the Langevin and the Smoluchowski descriptions. Let us further examine what happens when we try to recover the Smoluchowski approximation in our perturbative approach.

3.2.1 The shifted Smoluchowski description

We have seen, in chapter 2, that the solution to the Smoluchowski equation was given by

$$\langle q_S(t)\rangle = q_S(0)\, e^{\frac{\omega^2}{\beta}t}, \tag{3.20}$$

$$\sigma_S^2(t) = \frac{T}{m\omega^2}\left[e^{2\frac{\omega^2}{\beta}t} - 1\right], \tag{3.21}$$

where the subscript S stands for Smoluchowski.

In our perturbative approach we have found that

$$\langle q(t)\rangle \approx \frac{e^{\frac{\omega^2}{\beta}(1-\epsilon)t}}{1+2\epsilon-\epsilon^2}\left[\frac{\dot{q}(0)}{\beta} + q(0)\left(1+\epsilon-\epsilon^2\right)\right], \tag{3.22}$$

$$\sigma^2(t) \approx \frac{T}{m\omega^2}\frac{1}{\left(1+2\epsilon-\epsilon^2\right)^2}\left[\frac{1}{1-\epsilon}\left(e^{2\frac{\omega^2}{\beta}(1-\epsilon)t} - 1\right) + \frac{\epsilon}{1+\epsilon} - \frac{4\epsilon}{1+\epsilon^2}\right]. \tag{3.23}$$

Since we are only interested in the end result, i.e., knowing if the compound nucleus was formed, all terms vanishing for long enough times, were suppressed.

Naively, one might think that setting $\epsilon = 0$, our perturbative approach will simply reduce to the Smoluchowski one. This is, indeed, the case for the fluctuations but not for the mean trajectory. In fact, our perturbative solution becomes

$$\langle q(t)\rangle \approx \left[\frac{\dot{q}(0)}{\beta} + q(0)\right] e^{\frac{\omega^2}{\beta}t}. \tag{3.24}$$

This expression only reduces to the Smoluchowski solution by further assuming that $\dot{q}(0) = 0$. The physical interpretation of this assumption is that, before diffusion starts, all the collective kinetic energy has been dissipated.

Clearly, the previous expression has the form of the Smoluchowski solution (cf. Eq. (3.20)) where the initial condition $q_S(0)$ has been replaced by $q(0) + \dot{q}(0)/\beta$. This shift, in the initial condition, does not come from the perturbative treatment of inertia but rather finds its roots in the fact that the Smoluchowski equation is a first order equation and our perturbative approach is, approximately, a second order equation. Thus, the perturbative approach requires two initial conditions, namely $q(0)$ and $\dot{q}(0)$, while the Smoluchowski only requires one, namely $q_S(0)$. Therefore, the Smoluchowski description intrinsically assumes that all the kinetic energy has been dissipated before the diffusion takes place. This is not the case in our perturbative treatment.

More importantly, this shift in the initial condition changes the height of the fusion barrier and, in turn, also has an influence on the formation probability. Since in our case $q(0) < 0$ and $\dot{q}(0) > 0$, the shift in the initial condition should reduce the hindrance to fusion.

Let us mention here that other mechanisms affect the shift in the initial condition, such as the very rapid evolution of the neck with respect to the slow evolution of the elongation, or asymmetry, during fusion [62].

3.2.2 Comparing the shifted Smoluchowski and the Langevin descriptions

Previously, by setting $\epsilon = 0$ in our perturbative approach, we have obtained that

$$\langle q(t) \rangle \approx \left[\frac{\dot{q}(0)}{\beta} + q(0) \right] e^{\frac{\omega^2}{\beta} t}, \tag{3.25}$$

$$\sigma^2(t) \approx \frac{T}{m\omega^2} \left[e^{2\frac{\omega^2}{\beta} t} - 1 \right]. \tag{3.26}$$

From now on, we shall refer to this solution as the shifted Smoluchowski framework. Next, we compare this framework to the Langevin description. As usual, introducing the initial barrier height and the initial kinetic energy, makes the comparison easier.

Assuming, as in Ref. [34], the standard values of nuclear physics $\hbar\omega \sim 1$ MeV and $\beta \sim 5 \times 10^{21}$ s we deduce that $\epsilon \sim 0.1$. From this, it seems reasonable to believe that inertia does not play such a critical role in the dynamics of the diffusion considered here. However, to be on the safe side, we discuss the three values ϵ =0.05, 0.1, 0.2, in order to show that the formation probabilities obtained within the shifted Smoluchowski framework are close to those obtained with a Langevin description.

This can be seen in Figs. 3.2 and 3.3 where the two frameworks are compared. Notice that these two formulations converge to the same formation probability as $\epsilon \to 0$. Also, the formation probability obtained in the Langevin description, always, begins at $P_{\text{form}} = 0$ and then, starts increasing because of the diffusion across the barrier. Notice this is not necessarily the case in the shifted Smoluchowski formulation. Indeed, in Fig. 3.3, we see that the formation probability initially starts at $P_{\text{form}} = 1$ and then, decreases to reach its final value. The explanation for this peculiar result goes as follows. If the kinetic energy is large enough, then, the shifted initial condition $q(0) + \dot{q}(0)/\beta$ will become positive (remember $q(0) < 0$ and $\dot{q}(0) > 0$) and the system will, effectively, start on the other side of the barrier, i.e., when diffusion starts the system has already "fused". It should be mentioned that the Figs. 3.2 and 3.3 were obtained assuming that $K = B_{\text{eff}}/2$ and $K = 3B_{\text{eff}}/2$, respectively. Thus, proving that the previous interpretation was correct. Remember that $K = B_{\text{eff}}$ is the energy required for the formation probability to be 1/2 in the Langevin description (cf. chapter 2 for more details).

As previously argued, we do not expect ϵ to be larger than 0.2. Therefore, this value should lead to the largest possible disagreement between the two approaches. Based on the Figs. 3.2 and 3.3, we do not expect, the changes in the formation probability to exceed 10%.

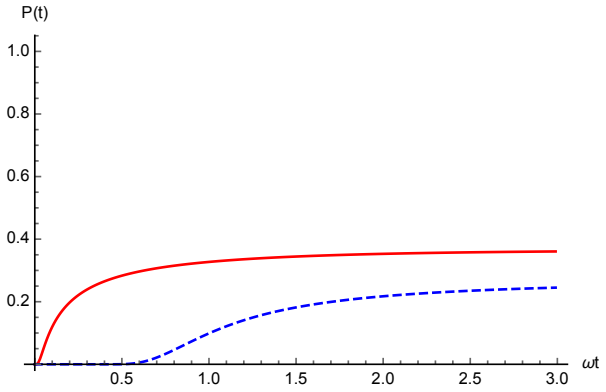

(a) $\epsilon = 0.2$

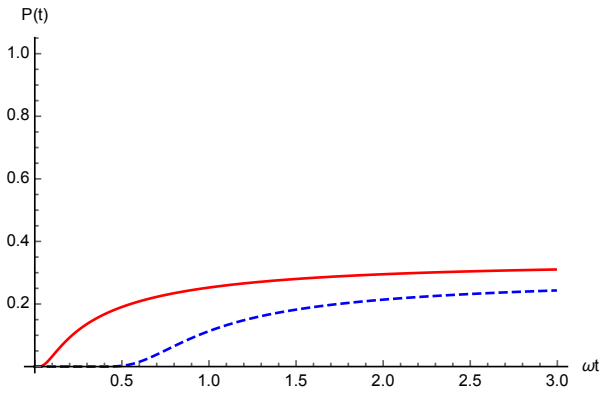

(b) $\epsilon = 0.1$

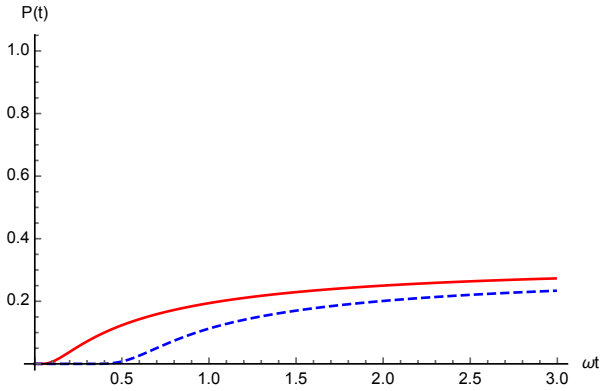

(c) $\epsilon = 0.05$

Figure 3.2: The formation probability is given as a function of time, for the shifted Smoluchowski (red solid line) and Langevin (blue dashed line) formulations. These are dimensionless plots where $K = B_{\text{eff}}/2$ and $T = B/2$. Note that B_{eff} is the kinetic energy required to have a formation probability equal to 1/2 in the Langevin description.

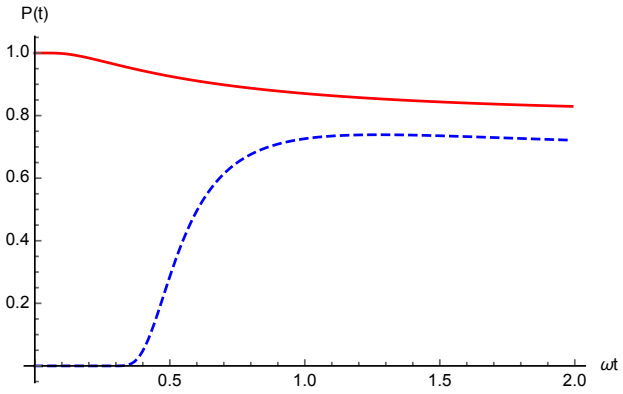

(a) $\epsilon = 0.2$

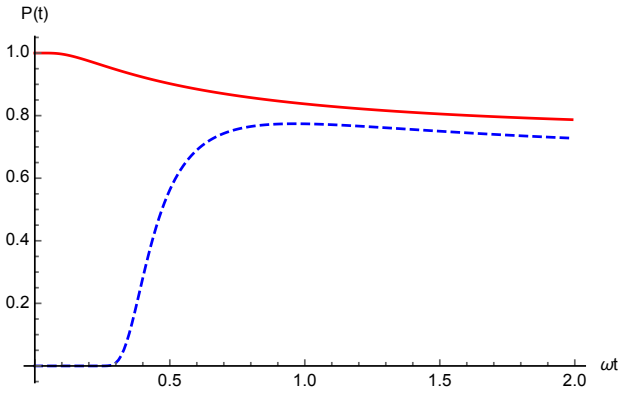

(b) $\epsilon = 0.1$

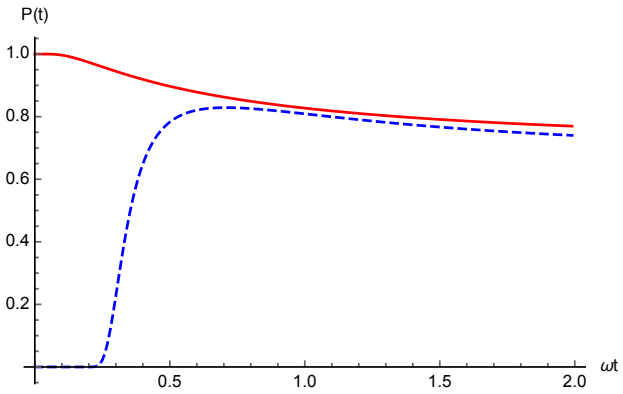

(c) $\epsilon = 0.05$

Figure 3.3: The formation probability is given as a function of time, for the shifted Smoluchowski (red solid line) and Langevin (blue dashed line) formulations. These are dimensionless plots where $K = 3B_{\text{eff}}/2$ and $T = B/2$. Note that B_{eff} is the kinetic energy required to have a formation probability equal to $1/2$ in the Langevin description. Also, an initial condition on the other side of the barrier can be thought of as unphysical and in practice systems never reach contact with suffisent energy for this to happen.

3.3 Link to the phenomenological injection point

We have demonstrated that the initial condition $q_S(0)$ should be interpreted as $q(0) + \dot{q}(0)/\beta$. As already discussed, this is important if the kinetic energy has not been entirely dissipated.

One can show that if $E_{\rm cm} > B_0$, then, after capture, the remaining kinetic energy is simply given by $(E_{\rm cm} - B_0)/2$ [63]. From this we find that the initial velocity is

$$\dot{q}(0) = \sqrt{\frac{E_{\rm cm} - B_0}{\mu}}. \tag{3.27}$$

Therefore, assuming that none of the kinetic energy has been dissipated, one obtains a simple parametrization for the initial condition of the Smoluchowski problem given by

$$q_S(E_{\rm cm}) = K_1 + K_2\sqrt{E_{\rm cm} - B_0} \tag{3.28}$$

where K_1 and K_2 are now adjustable parameters. Note that these parameters could be interpreted as $K_1 = q(0)$ and $K_2 = 1/(\beta\sqrt{\mu})$. However, we absolutely do not know the value for $q(0)$ and the one for β is rather uncertain.

It should be mentioned that we have found an alternative parametrization to one phenomenologically introduced in Refs. [40,41]. Although these two parametrizations differ, both are functions of $(E_{\rm cm} - B_0)$. Furthermore, they follow the same trend, more precisely, as the center-of-mass energy increases the initial condition gets closer and closer to the top of the parabolic barrier. Consequently, both parametrizations reduce fusion hindrance.

This parametrization is based on three main assumptions. First, ϵ should be so small that it can be taken equal to 0. Second, the long term evolution can be reasonably described by the shifted Smoluchowski approach, i.e., the Smoluchowski solution with a shift in the initial condition. Third, no dissipation has taken place before the start of diffusion otherwise Eq. (3.27) would not be valid. In the previous section, we have demonstrated that the first and second were valid.

3.4 Conclusion

In this chapter, the effects of inertia on the formation step were investigated. This was achieved through the use of singular perturbation theory. We have shown that, even when inertia was completely neglected ($\epsilon = 0$), our perturbative approach did not reduce to a Smoluchowski description. The reason for this unexpected turn of events is that the Smoluchowski equation is a first order equation, with a single initial condition, while our treatment is second order and requires two initial conditions. Consequently, complete energy dissipation, before diffusion sets in, is intrinsic to the Smoluchowski framework. However, complete dissipation was never assumed in our perturbative approach and this is what sets these two descriptions apart. Furthermore, we have shown that the remaining kinetic energy (not dissipated) is at the very origin of a shift in the initial condition within the Smoluchowski framework. Indeed, it was proven that the Smoluchowski initial condition $q_S(0)$ became $q(0) + \dot{q}(0)/\beta$ in our perturbative framework. Moreover, this shift offers a natural

parametrization of the initial condition and its energy dependence. We would like to stress that the approach developed in this chapter, allowed us to fundamentally ground the phenomenological parametrization introduced in the fusion-by-diffusion model. This investigation also proved that the effects of inertia which were completely neglected in this parametrization, cannot affect the final formation probability by more than 10% with respect to the Langevin description where inertia is treated exactly.

Chapter 4

Uncertainties and their propagation

4.1 Random variables

This chapter contains a precise presentation of the mathematical concepts required to introduce the notion of uncertainty, which will be used throughout this thesis. Nowadays, uncertainties are still the object of many theoretical developments and, in parallel, a normalization process has been undertaken. This thesis strictly follows the established standards described in the Guide to Uncertainty in Measurements (GUM) [64, 65].

Most physical quantities are not precisely determined, measured or deduced, and cannot be assimilated to a constant. It is, therefore, much more rigorous to view them as random variables rather then specific, clear-cut, values. A random variable X can take any value x_i from the set P=$\{x_i\}$, called the population. In order to properly define a random variable one must specify, all the possible values for x_i and their probability density distribution. The number of existing probability distributions is countless, however, the central limit theorem states that the sum of independent and identically distributed random variables converges to a Gaussian distribution. It turns out that such a distribution is completely defined by its first three moments: the zeroth moment is simply the total probability, the first moment is known as the mathematical expectation and the second moment is called the variance, all higher order moments are exactly zero. In the following, we first focus our attention on the mathematical expectation and then on the variance which, as we will see, is a special case of covariance.

4.2 The expectation, variance and covariance

4.2.1 The mathematical expectation

The mathematical expectation of a random variable is defined as,

$$\mathrm{E}[X] = \lim_{n\to\infty} \frac{1}{n} \sum_{i=1}^{n} x_i, \tag{4.1}$$

where P=$\{x_i\}$ is the set of all possible values for the random variable X. The mathematical expectation, E[X], can also be referred to as expectation, population mean or even simply mean.

In practice, however, n is finite and the set P is never fully explored. Therefore, it is necessary to define the sample mean.

Intuitively, the mathematical expectation of a random variable is the value, we expect to find, on average, if we iterate a measurement a large amount of times. Therefrom, the value of any physical quantity is, generally, identified to its expectation, whenever it is not treated as a random variable. In cases where the distribution is symmetric the expectation can be seen as the central value of a distribution. Accordingly, a random variable is said to be centred if it has a mathematical expectation equal to 0.

However, a thorough description of any physical quantity cannot be achieved by reducing this quantity to a single value (its mean) and the variability of such quantity must be comprised within its description. This leads us to the notion of variance.

4.2.2 The variance

The variance of a random variable is defined as,

$$\mathrm{Var}[X] = \mathrm{E}[(X - \mathrm{E}[X])^2] = \mathrm{E}[X^2] - \mathrm{E}[X]^2, \tag{4.2}$$

where $\mathrm{E}[X]$ is the mathematical expectation of the random variable X. The population variance $\mathrm{Var}[X]$ is more often than not referred to as variance.

The variance characterizes the variability or deviation of a random variable away from its own mathematical expectation. Consequently, it also corresponds to the square of the standard deviation, the standard deviation being synonymous to the term uncertainty, the concept of variance will, in this chapter and the next, draw most of our attention.

The variance is always positive or zero. A constant, not a random variable, has zero variance since all of its realizations are, of course, identical to the constant itself. Therefore, the mathematical expectation of such a constant, a, is naturally given by $\mathrm{E}[a] = a$ and consequently, $\mathrm{Var}[a] = \mathrm{E}[a - \mathrm{E}[a]] = \mathrm{E}[0] = 0$.

4.2.3 The covariance

The covariance of two random variables is defined as,

$$\mathrm{Cov}[X, Y] = \mathrm{E}[(X - \mathrm{E}[X])(Y - \mathrm{E}[Y])] = \mathrm{E}[XY] - \mathrm{E}[X]\,\mathrm{E}[Y] \tag{4.3}$$

where $\mathrm{E}[X]$ and $\mathrm{E}[Y]$ are the mathematical expectations of the random variables X and Y. This last expression, is a straightforward generalization of variance to two random variables.

Intuitively, the covariance characterizes the simultaneous deviations of two random variables: it vanishes when the two variables vary independently and it will be positive when the deviations between these variables and their respective expectation have the same sign and negative otherwise. The covariance is, thus, an extension of the notion of variance to two random variables.

The correlation is a normalized form of the covariance which can be expressed as,

$$\mathrm{Cor}[X, Y] = \frac{\mathrm{Cov}[X, Y]}{\sqrt{\mathrm{Var}[X]\,\mathrm{Var}[Y]}}, \tag{4.4}$$

which is dimensionless and only takes values in the interval [-1,1].

The concept of covariance can be generalized to more than two random variables, this leads to the idea of covariance matrix. For instance, the covariance matrix of a random vector $\mathbf{X} = [X_1, \ldots, X_n]^T$ is given by

$$\mathbf{Cov}[\mathbf{X}] = \begin{bmatrix} \mathrm{Var}[X_1] & \mathrm{Cov}[X_1, X_2] & \ldots & \mathrm{Cov}[X_1, X_n] \\ \mathrm{Cov}[X_2, X_1] & \mathrm{Var}[X_2] & \ldots & \mathrm{Cov}[X_2, X_n] \\ \vdots & \vdots & \ddots & \vdots \\ \mathrm{Cov}[X_n, X_1] & \mathrm{Cov}[X_n, X_2] & \ldots & \mathrm{Var}[X_n] \end{bmatrix}, \tag{4.5}$$

and the corresponding correlation matrix is

$$\mathbf{Cor}[\mathbf{X}] = \begin{bmatrix} 1 & \mathrm{Cor}[X_1, X_2] & \ldots & \mathrm{Cor}[X_1, X_n] \\ \mathrm{Cor}[X_2, X_1] & 1 & \ldots & \mathrm{Cor}[X_2, X_n] \\ \vdots & \vdots & \ddots & \vdots \\ \mathrm{Cor}[X_n, X_1] & \mathrm{Cor}[X_n, X_2] & \ldots & 1 \end{bmatrix}. \tag{4.6}$$

4.3 Properties of the expectation, variance and covariance

In the following chapters, many calculations will be done using some of the properties of the expectation, the variance and the covariance. We shall now prove some of those properties, all of which are based on either the linearity or bilinearity of those operators.

4.3.1 Expectation

From the definition of the mathematical expectation, Eq. (4.1), one can deduce the linearity property below,

$$E[aX + bY] = \lim_{n\to\infty} \frac{1}{n} \sum_{i=1}^{n} (ax_i + by_i) = a \lim_{n\to\infty} \frac{1}{n} \sum_{i=1}^{n} x_i + b \lim_{n\to\infty} \frac{1}{n} \sum_{i=1}^{n} y_i = aE[X] + bE[Y], \tag{4.7}$$

where a and b are constants while X and Y are random variables. This expression can be generalized as follows,

$$\mathrm{E}\left[\sum_{i=1}^{n} a_i X_i\right] = \sum_{i=1}^{n} a_i \,\mathrm{E}[X_i], \tag{4.8}$$

where a_i are constants and X_i are random variables.

4.3.2 Variance

Using successively the definition of variance Eq. (4.2), the linearity of the mathematical expectation Eq. (4.8) and the definition of covariance Eq. (4.3), one can show that

$$\begin{aligned} \mathrm{Var}[aX + bY] &= \mathrm{E}[(aX + bY)^2] - \mathrm{E}[(aX + bY)]^2 \\ &= a^2(\mathrm{E}[X^2] - \mathrm{E}[X]^2) + b^2(\mathrm{E}[Y^2] - \mathrm{E}[Y]^2) + 2ab(\mathrm{E}[XY] - \mathrm{E}[X]\,\mathrm{E}[Y]) \\ &= a^2\,\mathrm{Var}[X] + b^2\,\mathrm{Var}[Y] + 2ab\,\mathrm{Cov}[X, Y], \end{aligned} \tag{4.9}$$

where a and b are constants while X and Y are random variables. This expression can be generalized as follows,

$$\mathrm{Var}\left[\sum_{i=1}^{n} a_i X_i\right] = \sum_{i=1}^{n} a_i^2 \,\mathrm{Var}[X_i] + \sum_{i=1}^{n} \sum_{\substack{j=1 \\ j\neq i}}^{n} a_i a_j \,\mathrm{Cov}[X_i, X_j], \tag{4.10}$$

where a_i are constants and X_i are random variables.

4.3.3 Covariance

Using successively the definition of covariance Eq. (4.3) and the linearity of the mathematical expectation Eq. (4.8), one can show that

$$\begin{aligned}
\mathrm{Cov}[aW + bX, cY + dZ] &= \mathrm{E}[(aW + bX)(cY + dZ)] - \mathrm{E}[aW + bX]\,\mathrm{E}[cY + dZ] \\
&= ac(\mathrm{E}[WY] - \mathrm{E}[W]\,\mathrm{E}[Y]) + ad(\mathrm{E}[WZ] - \mathrm{E}[W]\,\mathrm{E}[YZ]) \\
&\quad + bc(\mathrm{E}[XY] - \mathrm{E}[X]\,\mathrm{E}[Y]) + bd(\mathrm{E}[XZ] - \mathrm{E}[X]\,\mathrm{E}[Z]) \\
&= ac\,\mathrm{Cov}[W, Y] + ad\,\mathrm{Cov}[W, Z] + bc\,\mathrm{Cov}[X, Y] + bd\,\mathrm{Cov}[X, Z],
\end{aligned} \tag{4.11}$$

where a, b, c and d are constants while W, X, Y and Z are random variables. This expression can be generalized as follows,

$$\mathrm{Cov}\left[\sum_{i=1}^{n} a_i X_i, \sum_{j=1}^{m} b_j Y_j\right] = \sum_{i=1}^{n} \sum_{j=1}^{m} a_i b_j \,\mathrm{Cov}[X_i, Y_j], \tag{4.12}$$

where a_i and b_j are constants while X_i and Y_j are random variables.

4.4 Unbiased sample estimates

In practice, samples have a finite size, thus, calculating the mathematical expectation, the variance or the covariance, directly from their definition, is hopeless. Perhaps, a more sensible intent would be providing estimates for these quantities which would be based on finite samples. However, we would also like to insure that, as the size of the samples increase, the resulting estimates get closer and closer to the values one obtains using the original definitions. This naturally leads us to the concept of unbiased sample estimates.

The quantity $\hat{\theta}$ is said to be an unbiased estimator of θ if,

$$\mathrm{E}[\hat{\theta}] = \theta, \tag{4.13}$$

or more explicitly,

$$\mathrm{E}[\hat{\theta}] = \lim_{n\to\infty} \frac{1}{n} \sum_{i=1}^{n} \hat{\theta}_i = \theta, \tag{4.14}$$

where $\hat{\theta}_i$ is the estimator of θ calculated with the ith sample and n is the number of samples. Indeed, although many different samples can be obtained from the same population, they lead to different estimates. An estimator is unbiased if the mathematical expectation, over all possible samples, equals the value, one should obtain, for the whole population.

4.4.1 The sample mean

As previously mentioned, in reality samples have a finite size, therefore, calculating the mathematical expectation from its definition, is desperate. A more practical intent would be providing an estimate for the mathematical expectation based on a finite sample. Having this purpose in mind, one could define the sample mean as,

$$\bar{x} = \frac{1}{n}\sum_{i=1}^{n} x_i, \tag{4.15}$$

where n is the size of the sample and S=$\{x_i\}$ is now a set containing the n values obtained for X, called sample. Of course, the sample set S is a subset of the population set P. The term, sample, is to be understood as, a sample of the population, that is, a portion or a part of the whole population. The sample mean of a set S=$\{x_i\}$ is denoted $\bar{x}$. The $\bar{x}$ gives an estimate of E[X], hence, $\bar{x}$ is said to be an estimator of E[X].

By convention, estimators usually wear hats, for instance, if μ=E[X] then we would write $\hat{\mu}$=$\bar{x}$. It may be more rigorous to write $\hat{\bar{x}}$ rather than simply $\bar{x}$, however, it is customary to implicitly view $\bar{x}$ as an estimator, the hat being dropped in order to lighten the notation.

Let's try to see if the sample mean, $\bar{x}$, is an unbiased estimator of the mathematical expectation, E[X]. Using the definition of $\bar{x}$, the linearity property of E[X] and the fact that all the realizations of X have the same expectation, we find that

$$\mathrm{E}[\bar{x}] = \mathrm{E}\left[\frac{1}{n}\sum_{i=1}^{n} x_i\right] = \frac{1}{n}\sum_{i=1}^{n}\mathrm{E}[x_i] = \frac{1}{n}\sum_{i=1}^{n}\mathrm{E}[X] = \mathrm{E}[X]. \tag{4.16}$$

From this last calculation, one can clearly state that $\bar{x}$ is, indeed, an unbiased estimate of the mathematical expectation.

4.4.2 The sample variance

Let's now try to find an unbiased estimate of the sample variance. From the definition of variance Eq. (4.2), one would define the sample variance as

$$s_x^2 = \frac{1}{n}\sum_{i=1}^{n}(x_i - \bar{x})^2 = \left(\frac{1}{n}\sum_{i=1}^{n} x_i^2\right) - \bar{x}^2. \tag{4.17}$$

The mathematical expectation of the first term leads to

$$\mathrm{E}\left[\frac{1}{n}\sum_{i=1}^{n} x_i^2\right] = \frac{1}{n}\sum_{i=1}^{n} E\left[x_i^2\right] = \frac{n}{n}\mathrm{E}\left[x_i^2\right] = \mathrm{E}\left[X^2\right], \tag{4.18}$$

where we have used the linearity property of the mathematical expectation Eq. (4.8) and since all the realizations have the same mathematical expectation, E[x_i]=E[X]. Then from the definition of variance Eq. (4.2), one obtains

$$\mathrm{E}[x_i^2] = \mathrm{E}[X^2] = \mathrm{E}[X]^2 + \mathrm{Var}[X]. \tag{4.19}$$

Using that same trick, the second term of Eq. (4.17) can be rewritten as

$$\mathrm{E}[\bar{x}^2] = \mathrm{E}[\bar{x}]^2 + \mathrm{Var}[\bar{x}]. \tag{4.20}$$

We have previously shown that $\bar{x}$ was an unbiased estimate of E[X] such that E[$\bar{x}$]=E[X]. From the property of variance Eq. (4.10) and since all the realizations have the same variance Var[x_i]=Var[X], we obtain that

$$\mathrm{Var}[\bar{x}] = \mathrm{Var}\left[\frac{1}{n}\sum_{i=1}^{n} x_i\right] = \frac{1}{n^2}\sum_{i=1}^{n}\mathrm{Var}\left[x_i\right] = \frac{1}{n^2}\sum_{i=1}^{n}\mathrm{Var}\left[X\right] = \frac{\mathrm{Var}\left[X\right]}{n}. \tag{4.21}$$

Such that the expectation of the second term of Eq. (4.17) yields

$$\mathrm{E}[\bar{x}^2] = \frac{\mathrm{Var}[X]}{n} + \mathrm{E}[X]^2, \tag{4.22}$$

and, together with Eq. (4.19), leads us to

$$\mathrm{E}[s_x^2] = \frac{n-1}{n}\,\mathrm{Var}[X]. \tag{4.23}$$

The factor $n/(n-1)$ is better known as Bessel's correction factor. From this last result, one can deduce the following unbiased estimate for the sample variance,

$$s_x^2 = \frac{1}{n-1}\sum_{i=1}^{n}\left(x_i - \bar{x}\right)^2. \tag{4.24}$$

4.4.3 The sample covariance

Based on the definition of the unbiased sample variance Eq. (4.24) along with the definition of covariance Eq. (4.3), we propose the following definition for the sample covariance

$$s_{xy}^2 = \frac{1}{n-1}\sum_{i=1}^{n}\left(x_i y_i - \bar{x}\bar{y}\right), \tag{4.25}$$

or rather,

$$(n-1)s_{xy}^2 = \sum_{i=1}^{n} x_i y_i - n\sum_{i=1}^{n}\frac{x_i}{n}\sum_{i=1}^{n}\frac{y_i}{n}. \tag{4.26}$$

Let's try to establish that this is truly an unbiased estimator of the covariance Cov[X,Y]. By taking the mathematical expectation of Eq. (4.26), one obtains

$$(n-1)\,\mathrm{E}\left[s_{xy}^2\right] = \mathrm{E}\left[\sum_{i=1}^{n} x_i y_i\right] - \mathrm{E}\left[\frac{1}{n}\sum_{i=1}^{n} x_i \sum_{j=1}^{n} y_j\right], \tag{4.27}$$

exploiting the linearity property of the mathematical expectation Eq. (4.8). The first term on the right hand side leads to,

$$\mathrm{E}\left[\sum_{i=1}^{n} x_i y_i\right] = \sum_{i=1}^{n}\mathrm{E}\left[x_i y_i\right] = n\,\mathrm{E}[XY]. \tag{4.28}$$

Since

$$\sum_{i=1}^{n} x_i \sum_{j=1}^{n} y_j = \sum_{i=1}^{n} x_i y_i + \sum_{i=1}^{n} \sum_{\substack{j=1 \\ j \neq i}}^{n} x_i y_j, \tag{4.29}$$

the second term on the right hand side can be computed as follows,

$$\frac{1}{n} \sum_{i=1}^{n} \mathrm{E}\left[x_i y_i\right] + \frac{1}{n} \sum_{i=1}^{n} \mathrm{E}\left[x_i\right] \sum_{\substack{j=1 \\ j \neq i}}^{n} \mathrm{E}\left[y_j\right] = \mathrm{E}\left[XY\right] + (n-1)\,\mathrm{E}\left[X\right]\mathrm{E}\left[Y\right], \tag{4.30}$$

by employing the linearity of the mathematical expectation, Eq. (4.8). Gathering the results from Eq. (4.28) and Eq. (4.30), we obtain that

$$\begin{aligned} (n-1)\,\mathrm{E}\left[s_{xy}^2\right] &= n\,\mathrm{E}[XY] - \mathrm{E}[XY] - (n-1)\,\mathrm{E}[X]\,\mathrm{E}[Y] \\ &= (n-1)(\mathrm{E}[XY] - \mathrm{E}[X]\,\mathrm{E}[Y]) \\ &= (n-1)\,\mathrm{Cov}[X,Y]. \end{aligned} \tag{4.31}$$

This last result clearly shows that the Eq. (4.25) already gives an unbiased estimate of the covariance.

4.5 Formulas for the propagation of uncertainties

Let us assume that the output quantities Y and Z depend upon N correlated input quantities $\beta_1, \ldots, \beta_N$. The relationships are given by the functions $Y{=}f(\beta_1, \ldots, \beta_N)$ and $Z{=}g(\beta_1, \ldots, \beta_N)$. For the sake of simplicity, we will assume, without any loss of generality, that there are only two input quantities. The total derivative of Y, or total variation of Y, is

$$dY = \frac{\partial f}{\partial \beta_1} d\beta_1 + \frac{\partial f}{\partial \beta_2} d\beta_2. \tag{4.32}$$

Noting μ_y the mathematical expectation of Y then one can approximate μ_y as $f(\bar{\beta}_1,\bar{\beta}_2)$ up to first order. As a result, we approximately have,

$$y - \mu_y \simeq \frac{\partial f}{\partial \beta_1}(\beta_1 - \bar{\beta}_1) + \frac{\partial f}{\partial \beta_2}(\beta_2 - \bar{\beta}_2) \tag{4.33}$$

and similarly,

$$z - \mu_z \simeq \frac{\partial g}{\partial \beta_1}(\beta_1 - \bar{\beta}_1) + \frac{\partial g}{\partial \beta_2}(\beta_2 - \bar{\beta}_2). \tag{4.34}$$

The previous results lead to,

$$\begin{aligned} (y - \mu_y)(z - \mu_z) \simeq \frac{\partial f}{\partial \beta_1}\frac{\partial g}{\partial \beta_1}(\beta_1 - \bar{\beta}_1)^2 + \frac{\partial f}{\partial \beta_1}\frac{\partial g}{\partial \beta_2}(\beta_1 - \bar{\beta}_1)(\beta_2 - \bar{\beta}_2) \\ + \frac{\partial f}{\partial \beta_2}\frac{\partial g}{\partial \beta_1}(\beta_2 - \bar{\beta}_2)(\beta_1 - \bar{\beta}_1) + \frac{\partial f}{\partial \beta_2}\frac{\partial g}{\partial \beta_2}(\beta_2 - \bar{\beta}_2)^2. \end{aligned} \tag{4.35}$$

From this last expression, we end up with

$$u(y,z) = \sum_{i=1}^{N}\sum_{j=1}^{N} \frac{\partial Y}{\partial \beta_i}\frac{\partial Z}{\partial \beta_j} u(\beta_i,\beta_j), \tag{4.36}$$

where $u(y,z)$ is the covariance between y and z. We change notations here in order to emphasize the fact that we are now discussing uncertainties. It is interesting to realize that Eq. (4.36) is similar to Eq. (4.12). In fact, Eq. (4.36) is a simple generalization of Eq. (4.12) to those cases where f and g are nonlinear with respect to the input quantities. Since Eq. (4.36) allows us to compute every single covariance, it will also allow us to compute every single variance and standard deviation. As the uncertainty and the standard deviation are identical, this is the most general, as well as the most useful formula for the propagation of uncertainties. As a consequence, we will use it to deduce other useful formulas.

For instance, if the input quantities were uncorrelated, the equation Eq. (4.36) would reduce to

$$u(y,z) = \sum_{i=1}^{N} \frac{\partial Y}{\partial \beta_i}\frac{\partial Z}{\partial \beta_i} u^2(\beta_i). \tag{4.37}$$

Furthermore, it is possible to infer a variance formula from Eq. (4.36), simply by taking Y and Z to be equal,

$$u^2(z) = \sum_{i=1}^{N}\sum_{j=1}^{N} \frac{\partial Z}{\partial \beta_i}\frac{\partial Z}{\partial \beta_j} u(\beta_i,\beta_j), \tag{4.38}$$

which can be rewritten as,

$$u^2(z) = \sum_{i=1}^{N} \left(\frac{\partial Z}{\partial \beta_i}\right)^2 u^2(\beta_i) + 2\sum_{i=1}^{N-1}\sum_{j=i+1}^{N} \frac{\partial Z}{\partial \beta_i}\frac{\partial Z}{\partial \beta_j} u(\beta_i,\beta_j), \tag{4.39}$$

where $u^2(z)$ is the variance of z. Once again, it is interesting to notice the parallel existing between Eq. (4.39) and Eq. (4.10) where Eq. (4.10) is a particular case of Eq. (4.39) if f is linear with respect to the input quantities.

All of these expressions, Eq. (4.36), Eq. (4.37) and Eq. (4.39), can be found in the Guide to the expression of Uncertainty in Measurement (GUM) [65] which sets the international standards for the propagation of uncertainties, or alternatively in Refs. [64, 66].

4.6 Matrix formulation for the propagation of uncertainties

As, Eq. (4.36) is the most general formula for the propagation of uncertainty, it is the only one we actually need. However, for more than two output quantities, it is convenient to introduce a matrix formulation. In the following, we use lower case bold characters for vectors and upper case bold characters for matrices. Thus, we introduce the notations,

$$\mathbf{dy}^T = \left[\frac{\partial Y}{\partial \beta_1}, \ldots, \frac{\partial Y}{\partial \beta_N}\right], \tag{4.40}$$

and

$$\mathbf{dz}^T = \left[\frac{\partial Z}{\partial \beta_1}, \ldots, \frac{\partial Z}{\partial \beta_N}\right], \tag{4.41}$$

as well as

$$\mathbf{U} = \begin{bmatrix} u^2(\beta_1) & u(\beta_1, \beta_2) & \ldots & u(\beta_1, \beta_n) \\ u(\beta_2, \beta_1) & u^2(\beta_2) & \ldots & u(\beta_2, \beta_n) \\ \vdots & \vdots & \ddots & \vdots \\ u(\beta_n, \beta_1) & u(\beta_n, \beta_2) & \ldots & u^2(\beta_n) \end{bmatrix}.$$

We now realize that Eq. (4.36) takes the following simple matrix form:

$$u(y, z) = \mathbf{dy}^T \, \mathbf{U} \, \mathbf{dz}. \tag{4.42}$$

4.7 Conclusion

In this chapter, we argued that physical quantities should be treated as random variables. This approach bears great convenience since it naturally carries on the concepts of expectation, variance and covariance, onto physical quantities which allows for a simple interpretation and propagation of both uncertainties and correlations. Despite all this progress, so far, we did not explain the origin of uncertainties or correlations, this discussion is the central topic of the next chapter which is based on regression analysis.

Chapter 5

Regression analysis

Regression analysis is a set of tools allowing us to understand the very origin of uncertainties. Although all the following formulas have been proven, the length and tedious character of the proofs forbids us to repeat them here. Nevertheless, the main ideas and certainly the key assumptions of regression analysis stand out. The complete set of demonstrations can be found in many excellent texts, for instance Refs. [66–69].

Regression analysis is one of the most widely used statistical tools because it provides simple methods for investigating functional relationships amongst variables. The relationship is expressed in the form of an equation or a model connecting the *response* or *dependent* variable and one or more *explanatory* or *predictor* variables. We denote the response variable by Y and the set of explanatory variables by $X_1, X_2, \ldots, X_p$. The true relationship between Y and $X_1, X_2, \ldots, X_p$ can be approximated by the regression model,

$$Y = f(X_1, X_2, \ldots, X_p) + \epsilon. \tag{5.1}$$

We first discuss linear regression analysis where the previous expression reduces to

$$Y = p_0 + p_1 X_1 + \ldots + p_p X_p + \epsilon \tag{5.2}$$

where $p_0, p_1, \ldots, p_p$ are N_p parameters to be determined from the data and ϵ represents both the error of the model and the part of the variations that is not explained by the variables $X_1, X_2, \ldots, X_p$. It should be noted that in order to use linear regression the model must be linear with respect to the parameters but does not need to be linear with respect to the explanatory variables.

We start this chapter by describing the inner workings of regression analysis in the case of a simple two-parameter model. Then, we proceed by exposing the highly convenient matrix formulation of linear regression which is very useful in cases where the model involves many parameters. Finally, we discuss the case of regression analysis for nonlinear models which turns out to be a simple generalization of the linear case.

5.1 A simple two-parameter model

5.1.1 Deterministic versus stochastic relationships

In some cases, the relationship between the model $(p_0 + p_1 X)$ and the experimental data (Y_{Exp}) is assumed to be exact, even if the coefficients are unknown. Considering the case of a simple linear relationship,

$$Y_{\text{Exp}} = p_0 + p_1 X, \tag{5.3}$$

the intercept p_0 and slope p_1 are determined from a set of N_n points $\{(x_i, y_i), i = 1, \ldots, N_n\}$ by direct use of the least squares method. Notice the only information extracted through this approach are the coefficients themselves and nothing else.

However, there are many cases where the relationship between the model and the experimental data is not considered to be exact. In such cases, we introduce the random variable ϵ as

$$Y_{\text{Exp}} = Y_{\text{Th}} + \epsilon, \tag{5.4}$$

where $Y_{\text{Th}} = p_0 + p_1 X$ and ϵ represents the errors of the model. Clearly, since ϵ is a random variable then Y_{Exp} will be one as well. Of course, the basic idea is to determine the parameters of the model. However, since their determination will be based on the experimental data, which is a random variable, these parameters also become random variables and follow a distribution. The standard deviation of this particular distribution will be taken as their uncertainty. The main goal of regression analysis is to extract the uncertainties of the coefficients in order to propagate them onto the model. Notice regression is, in this sense, much more powerful than least squares.

5.1.2 Coefficient estimation

Based on a sample of experimental data $\{(x_i, y_i), i = 1, \ldots, N_n\}$, we wish to estimate the coefficients p_0 and p_1 where x_i and y_i are related through,

$$y_i = p_0 + p_1 x_i + \epsilon_i. \tag{5.5}$$

These estimates are sample estimates since the population, consisting of all the possible pairs of points (x_i,y_i), is usually infinite and therefore unavailable. As usual in statistics, the estimators of these coefficients are denoted by $\hat{p}_0$ and $\hat{p}_1$. The question regarding whether these estimates are biased or not will be discussed later.

The estimators of the intercept and slope are obtained by minimizing, the sum of the squared errors,

$$S = \sum_{i=1}^{N_n} \epsilon_i^2 = \sum_{i=1}^{N_n} \left[y_i - (p_0 + p_1 x_i) \right]^2, \tag{5.6}$$

with respect to p_0 and p_1. The derivative with respect to p_0 leads us to the estimate

$$\hat{p}_0 = \bar{y} - \hat{p}_1 \bar{x}, \tag{5.7}$$

where $\bar{x}$ and $\bar{y}$ are the sample means, defined in the previous chapter. The derivative with respect to p_1 leads to the other estimate

$$\hat{p}_1 = \frac{\sum_{i=1}^{N_n} x_i y_i - N_n \bar{x}\bar{y}}{\sum_{i=1}^{N_n} x_i^2 - N_n \bar{x}} = \frac{\sum_{i=1}^{N_n} (x_i - \bar{x})(y_i - \bar{y})}{\sum_{i=1}^{N_n} (x_i - \bar{x})^2} = \frac{s_{xy}^2}{s_x^2}. \tag{5.8}$$

The last expression was obtained using $\hat{p}_0 = \bar{y} - \hat{p}_1\bar{x}$ and recognizing, the sample variance s_x^2 and sample covariance s_{xy}^2, respectively, at the denominator and numerator, as defined in the previous chapter. Consequently, if there is no correlation between X and Y, the covariance vanishes and so does the slope $\hat{p}_1$.

The regression line is simply,

$$\hat{y}(x) = \hat{p}_0 + \hat{p}_1 x, \tag{5.9}$$

where, as previously shown, $\hat{p_0}$ and $\hat{p_1}$ depend exclusively on the data $\{(x_i, y_i), i = 1, \ldots, N_n\}$. For each observation in the data, we can compute

$$\hat{y}_i = \hat{p}_0 + \hat{p}_1 x_i, \tag{5.10}$$

allowing us to estimate the errors as

$$\hat{\epsilon}_i = y_i - \hat{y}_i, \tag{5.11}$$

otherwise known as residuals. Notice that the Eq. (5.7) can be rewritten as

$$\sum_{i=1}^{N_n} \hat{\epsilon}_i = 0. \tag{5.12}$$

Let us stress that this relation only holds for models including an intercept, i.e., a constant parameter such as p_0. This will have its importance when we will review the regression hypotheses.

5.1.3 Explained and unexplained deviations

Assuming no prior understanding of the experimental data, the observations $\mathrm{y_{Exp,i}}$ are just a set of distinct scattered values, thus, having a mean and a variance. A model's ambition is, of course, to explain why these values are all so different from each other and to uncover the origin of this variance. Interestingly enough, one can show that the sample variance can be decomposed as

$$\frac{1}{N_n - 1}\sum_{i=1}^{N_n}(y_i - \bar{y})^2 = \frac{1}{N_n - 1}\sum_{i=1}^{N_n}(\hat{y}_i - \bar{y})^2 + \frac{1}{N_n - 1}\sum_{i=1}^{N_n}(y_i - \hat{y}_i)^2 . \tag{5.13}$$

Clearly, the first term on the right hand side, is the deviation away from the mean which is explained by the model whereas the second term, is the residual deviation that remains unexplained. Note that this decomposition only holds for models including an intercept. Moreover, according to our definition of the errors, $\hat{\epsilon}_i = y_i - \hat{y}_i$, the second term is simply,

$$\sum_{i=1}^{N_n}(y_i - \hat{y}_i)^2 = \sum_{i=1}^{N_n}\hat{\epsilon_i}^2, \tag{5.14}$$

which is minimized in order to determine the coefficients in the least squares procedure described above. As a result, the least squares method minimizes the part of the deviation which is unexplained by the model. We will come back to this interpretation when we treat multiple regression.

5.1.4 Predictions and uncertainties

Once the coefficients are obtained, it is possible to make predictions, i.e., for any value x, finding the corresponding $\hat{y}$. Naturally, these predictions depend on the estimated parameters, namely, $\hat{p}_0$ and $\hat{p}_1$. Furthermore, it is possible, through some assumptions, to determine the uncertainties and the correlations existing between those parameters. This allows, using the methods prescribed in the previous chapter, to propagate the uncertainties onto the corresponding $\hat{y}$. Thus, it becomes feasible to study the predictivity of the model.

5.1.4.1 The assumptions behind regression analysis

As mentioned before, sample estimates, such as the coefficients of the regression line, may vary depending on the sample used to obtain them. In order to rigorously determine the standard deviation of the coefficients, we would need to know the set of all possible subsets of the population (the powerset of the population set) or said differently, the set of all possible samples. Of course, as we do not even know the population, this is completely out of reach. Therefore, we must rely on the estimates of these standard deviations.

There are two important hypothesis, or assumptions, behind ordinary regression analysis: the first, deals with the mathematical expectation of the random errors while the second deals with the covariance of those same errors. The first assumption, is that the random errors have a null mathematical expectation,

Hypothesis I:

$$\mathrm{E}\left[\epsilon_i\right] = 0. \tag{5.15}$$

This first assumption is strongly supported by the fact that for models with an intercept $\sum_i \hat{\epsilon}_i = 0$, cf. Eq. (5.12). The second assumption, is that the random errors are assumed independent and are normally distributed with a common variance σ^2,

Hypothesis II:

$$\mathrm{Cov}\left[\epsilon_i, \epsilon_j\right] = \sigma^2\, \delta_{ij}. \tag{5.16}$$

This hypothesis is also known as the homoscedastic assumption.

In regression analysis, it is usual to assume that all the samples are obtained in the exact same conditions. In particular, all samples contain the same values for $\{x_i\}$ but different values for $\{y_i\}$ since $\{\epsilon_i\}$ are random variables, as a result, the samples are all different. Here $\mathrm{E}[\epsilon_i]$ denotes the mathematical expectation over all existing samples and $\mathrm{Cov}[\epsilon_i,\epsilon_j]$ the covariance over the same samples.

The two, previously stated, regression hypotheses are essential in order to make any calculation possible. Since we know that $y_i = p_0 + p_1 x_i + \epsilon_i$, a first important corollary follows, from the linearity of the mathematical expectation along with the first regression hypothesis,

Corollary I:

$$\mathrm{E}\left[y_i\right] = \mathrm{E}\left[p_0 + p_1 x_i + \epsilon_i\right] = \mathrm{E}\left[p_0\right] + \mathrm{E}\left[p_1 x_i\right] + \mathrm{E}\left[\epsilon_i\right] = p_0 + p_1 x_i, \tag{5.17}$$

where p_0, p_1 and x_i are constants, not random variables. Similarly, one can show, using the second regression hypothesis, that

Corollary II:

$$\mathrm{Var}\left[y_i\right] = \mathrm{Var}\left[p_0 + p_1 x_i + \epsilon_i\right] = \mathrm{Var}\left[\epsilon_i\right] = \sigma^2, \tag{5.18}$$

Corollary III:

$$\mathrm{Cov}\left[y_i, y_j\right] = \mathrm{Cov}\left[p_0 + p_1 x_i + \epsilon_i, p_0 + p_1 x_j + \epsilon_j\right] = \mathrm{Cov}\left[\epsilon_i, \epsilon_j\right] = \sigma^2 \delta_{ij}, \tag{5.19}$$

again using the fact that p_0, p_1 and x_i, are constants.

5.1.4.2 Expectation and variance of $\hat{p}_1$

To calculate the mean and the variance of the estimated slope $\hat{p}_1$ over all samples, we shall use the expression,

$$\hat{p}_1 = \frac{\sum_{i=1}^{N_n}(x_i - \bar{x}) y_i}{\sum_{i=1}^{N_n}(x_i - \bar{x})^2}, \tag{5.20}$$

where y_i and $\hat{p}_1$ are random variables. Thus, taking the expectation of the previous expression and using the first corollary procures

$$\mathrm{E}[\hat{p}_1] = \frac{\sum_{i=1}^{N_n}(x_i - \bar{x})\,\mathrm{E}[y_i]}{\sum_{i=1}^{N_n}(x_i - \bar{x})^2} = \frac{\sum_{i=1}^{N_n}(x_i - \bar{x})(p_0 + p_1 x)}{\sum_{i=1}^{N_n}(x_i - \bar{x})^2} = p_1. \tag{5.21}$$

We can now conclude that $\hat{p}_1$ is, indeed, an unbiased estimator of p_1.

Similarly, taking the variance of Eq. (5.20) and exploiting the second corollary yields

$$\mathrm{Var}[\hat{p}_1] = \frac{\sum_{i=1}^{N_n}(x_i - \bar{x})^2\,\mathrm{Var}(y_i)}{\left[\sum_{i=1}^{N_n}(x_i - \bar{x})^2\right]^2} = \frac{\sigma^2}{\sum_{i=1}^{N_n}(x_i - \bar{x})^2}. \tag{5.22}$$

Note that the square root of this variance is adopted as the theoretical uncertainty in $\hat{p}_1$. Therefore, regression analysis provides an explanation for the origin of the uncertainties in the coefficients.

5.1.4.3 Expectation and variance of $\hat{p}_0$

Taking the mathematical expectation of $\hat{p}_0 = \bar{y} - \bar{x}\hat{p}_1$, we gather that

$$\mathrm{E}[\hat{p_0}] = \mathrm{E}[\bar{y}] - \bar{x}p_1. \tag{5.23}$$

Note that in order to obtain the previous expression, we have used the fact that $E[\hat{p}_1] = p_1$. From the first corollary, one can show that

$$\mathrm{E}[\bar{y}] = \frac{1}{N_n}\sum_{i=1}^{N_n}\mathrm{E}[y_i] = \frac{1}{N_n}\sum_{i=1}^{N_n}(p_0 + p_1 x_i) = p_0 + p_1\bar{x}. \tag{5.24}$$

Hence, $\mathrm{E}(\hat{p}_0) = p_0$ and, thus, $\hat{p}_0$ is also an unbiased estimator of p_0.

Similarly, taking the variance of $\hat{p}_0 = \bar{y} - \bar{x}\hat{p}_1$ delivers,

$$\mathrm{Var}[\hat{p}_0] = \mathrm{Var}[\bar{y}] + \bar{x}^2\,\mathrm{Var}[\hat{p}_1] - 2\bar{x}\,\mathrm{Cov}[\bar{y}, \hat{p}_1], \tag{5.25}$$

now using the second corollary, we find that $\mathrm{Var}[\bar{y}] = \sigma^2/n$. From the third corollary, it follows that

$$\begin{aligned}\mathrm{Cov}[\bar{y}, \hat{p}_1] &= \frac{\sum_{i=1}^{N_n}\sum_{j=1}^{N_n}(x_j - \bar{x})\,\mathrm{Cov}[y_i, y_j]}{N_n\sum_{j=1}^{N_n}(x_j - \bar{x})^2} = \frac{\sum_{i=1}^{N_n}\sum_{j=1}^{N_n}(x_j - \bar{x})\,\mathrm{Cov}[\epsilon_i, \epsilon_j]}{N_n\sum_{j=1}^{N_n}(x_j - \bar{x})^2} \\ &= \frac{\sigma^2}{N_n}\frac{\sum_{i=1}^{N_n}(x_i - \bar{x})}{\sum_{j=1}^{N_n}(x_j - \bar{x})^2} = 0.\end{aligned} \tag{5.26}$$

Finally,

$$\mathrm{Var}[\hat{p}_0] = \sigma^2\left(\frac{1}{N_n} + \frac{\bar{x}^2}{\sum_{i=1}^{N_n}(x_i - \bar{x})^2}\right). \tag{5.27}$$

Again, note that the square root of this variance is adopted as the theoretical uncertainty in $\hat{p}_0$. Once more, regression analysis provides an explanation for the origin of the uncertainties in the coefficients.

5.1.4.4 Covariance of $\hat{p}_1$ and $\hat{p}_0$

As the two estimators of the regression coefficients depend on the same input quantity, they should be correlated. Indeed, their covariance reads,

$$\mathrm{Cov}[\hat{p}_1, \hat{p}_0] = -\bar{x}\,\mathrm{Var}[\hat{p}_1] = \frac{-\bar{x}\sigma^2}{\sum_{i=1}^{N_n}(x_i - \bar{x})^2}, \tag{5.28}$$

by cause of Eqs. (5.22) and (5.26).

5.1.4.5 Variance of $\hat{y}$

For any value x, we can predict the value taken by $\hat{y} = \hat{p}_0 + \hat{p}_1 x$. Thus, we have that

$$\mathrm{Var}[\hat{y}] = \mathrm{Var}[\hat{p}_0] + x^2\,\mathrm{Var}[\hat{p}_1] + 2x\,\mathrm{Cov}[\hat{p}_0, \hat{p}_1]. \tag{5.29}$$

By injecting Eq. (5.22), Eq. (5.27) and Eq. (5.28), in the previous expression, we obtain

$$\mathrm{Var}[\hat{y}] = \sigma^2 \left(\frac{1}{N_n} + \frac{(x - \bar{x})^2}{\sum_{i=1}^{N_n} (x_i - \bar{x})^2} \right). \tag{5.30}$$

Note that, the further x is from $\bar{x}$, the larger the uncertainty on $\hat{y}$. Therefore, extrapolations far away from the "mean of the data" have larger uncertainties.

Furthermore, accounting for the errors of the errors leads directly to

$$\mathrm{Var}[\hat{y} + \epsilon] = \sigma^2 \left(1 + \frac{1}{N_n} + \frac{(x - \bar{x})^2}{\sum_{i=1}^{N_n} (x_i - \bar{x})^2} \right), \tag{5.31}$$

since from the second hypothesis, the errors are uncorrelated.

5.1.4.6 Estimation of the variance of the errors

Remarkably, all the previous results are proportional to the variance of the errors σ^2 which is unknown because the errors, themselves, are unknown. One can show, cf. Ref. [67], that the unbiased estimator of σ^2 is given by

$$\hat{\sigma}^2 = \frac{1}{N_n - 2} \sum_{i=1}^{N_n} (y_i - \hat{y}_i)^2 = \frac{S}{N_n - 2}. \tag{5.32}$$

The denominator $(N_n - 2)$ should be understood as the number of degrees of freedom, i.e., the total number of observations minus the number of parameters, namely, $(N_n - N_p)$. We can use this result in all the variances and covariance calculated before. For instance, Eq. (5.22) becomes,

$$\mathrm{Var}[\hat{p}_1] = \frac{\hat{\sigma}^2}{\sum_{i=1}^{N_n} (x_i - \bar{x})^2}. \tag{5.33}$$

5.2 Multiple linear regression

We have just treated the case of a particularly simple two-parameter model. We now move on to models containing many parameters. It is, therefore, convenient to introduce a matrix formulation, then, generalizations from two-parameters to many more become fairly easy to understand.

5.2.1 The matrix formulation

In this section, the mathematical formalism of multiple regression, used throughout this text, is exposed and special attention is directed towards the distinction between the least squares method and regression analysis which is based on additional hypotheses and opens the door to uncertainty analysis. Most of the forthcoming material can be found in Refs. [67, 68].

The model now reads,

$$\mathrm{y_{Th,i}} = p_0 + p_1 x_{1,\mathrm{i}} + p_2 x_{2,\mathrm{i}} + \cdots + p_p x_{p,\mathrm{i}}. \tag{5.34}$$

Consequently, it can be put into the matrix form,

$$\mathbf{y}_{\mathrm{Th}} = \mathbf{X} \cdot \mathbf{p}, \tag{5.35}$$

where $\mathbf{y}_{\mathrm{Th}}$ and $\mathbf{p}$ are column vectors, respectively, containing all the values of $\mathrm{y_{Th,i}}$ and $\mathrm{p_j}$ while the matrix $\mathbf{X}$ is defined as

$$\mathbf{X} = \begin{bmatrix} \frac{\partial \mathrm{y_{Th,1}}}{\partial \mathrm{p_0}} & \frac{\partial \mathrm{y_{Th,1}}}{\partial \mathrm{p_1}} & \cdots & \frac{\partial \mathrm{y_{Th,1}}}{\partial \mathrm{p_{Np}}} \\ \frac{\partial \mathrm{y_{Th,2}}}{\partial \mathrm{p_0}} & \frac{\partial \mathrm{y_{Th,2}}}{\partial \mathrm{p_1}} & \cdots & \frac{\partial \mathrm{y_{Th,2}}}{\partial \mathrm{p_{Np}}} \\ \vdots & \vdots & \ddots & \vdots \\ \frac{\partial \mathrm{y_{Th,Nn}}}{\partial \mathrm{p_0}} & \frac{\partial \mathrm{y_{Th,Nn}}}{\partial \mathrm{p_1}} & \cdots & \frac{\partial \mathrm{y_{Th,Nn}}}{\partial \mathrm{p_{Np}}} \end{bmatrix}, \tag{5.36}$$

where the ith line of $\mathbf{X}$ is associated with the ith datum while the jth column is related to the parameter $\mathrm{p_j}$. Thus, the matrix $\mathbf{X}$ has as many lines as there are points in the data $\mathrm{N_n}$ and as many columns as there are parameters $\mathrm{N_p}$ and naturally, the vector $\mathbf{p}$ has as many lines as there are parameters.

5.2.1.1 The ordinary least squares method

The least squares method is, more often than not, the favoured method to determine the parameters. This method consists in minimizing the sum of the squared errors,

$$\mathrm{S} = \sum_{\mathrm{i}=1}^{\mathrm{N_n}} \left(\mathrm{y_{Exp,i}} - \mathrm{y_{Th,i}}\right)^2, \tag{5.37}$$

with respect to the model parameters entering $\mathrm{y_{Th,i}}$. The previous expression can be put into matrix form as

$$\mathrm{S} = \left(\mathbf{y}_{\mathrm{Exp}} - \mathbf{X} \cdot \mathbf{p}\right)^{\mathrm{T}} \cdot \left(\mathbf{y}_{\mathrm{Exp}} - \mathbf{X} \cdot \mathbf{p}\right), \tag{5.38}$$

and its minimization with respect to the parameters yields the following solution,

$$\mathbf{p} = \left(\mathbf{X}^{\mathrm{T}} \cdot \mathbf{X}\right)^{-1} \cdot \mathbf{X}^{\mathrm{T}} \cdot \mathbf{y}_{\mathrm{Exp}}. \tag{5.39}$$

5.2.1.2 The regression hypotheses

In the least squares method, the model is assumed exact and experimental uncertainties are ignored, therefore, theoretical uncertainties cannot be reached. However, this may be achieved, using regression analysis and in particular, by involving the errors of the model. It is assumed, in regression analysis, that the experimental data can be described by

$$\mathbf{y}_{\mathrm{Exp}} = \mathbf{X} \cdot \mathbf{p} + \boldsymbol{\epsilon}, \tag{5.40}$$

where $\boldsymbol{\epsilon}$ represents the error associated with the model.

As for the two-parameter model, assuming no prior understanding of the experimental data, the observations $y_{\mathrm{Exp,i}}$ are just a set of distinct scattered values, thus, having a mean and a variance. A model's ambition is, of course, to explain why these values are all so different from each other and to uncover the origin of this variance. Thus, on the one hand, the model $\mathbf{X} \cdot \mathbf{p}$ is responsible for the explained variations, i.e., the variations that the model is able to account for. On the other hand, the error $\boldsymbol{\epsilon}$ is accountable for the unexplained variations, i.e., the variations left unexplained by the model and yet present in the experimental data.

In order to determine the uncertainties in the parameters, we shall assume the same assumptions as for the two-parameter model. For the simplest regression analysis, the first hypothesis concerns the mean of the errors which is assumed to vanish, i.e., $\mathrm{E}[\epsilon_{\mathrm{i}}]=0$. The second hypothesis deals with the dispersion and the mutual influence of the errors which are assumed to possess a common variance σ^2 and to be uncorrelated, i.e., $\mathrm{Cov}[\epsilon_{\mathrm{i}},\epsilon_{\mathrm{j}}]=\sigma^2\ \delta_{\mathrm{ij}}$. The errors having the same variance, the second hypothesis is also known as the homoscedastic assumption. Thus, according to these hypotheses, the errors follow a Gaussian distribution with zero mean and variance σ^2. Highly convenient regression corollaries derive from these two prior assumptions:

$$\mathbf{E}\left[\mathbf{y}_{\mathrm{Exp}}\right] = \mathbf{X} \cdot \mathbf{p}, \tag{5.41}$$

$$\mathbf{Cov}\left[\mathbf{y}_{\mathrm{Exp}}\right] = \sigma^2 \mathbf{I}, \tag{5.42}$$

where $\mathbf{I}$ is the identity matrix.

5.2.1.3 Unbiased sample estimates

As usual, it is assumed that only a restricted sample of all existing data is known and an even smaller sample may actually be considered, as a result, all of the quantities upon which any study is based, will be sample estimates. Hence, a more appropriate notation for Eq. (5.39) would be,

$$\hat{\mathbf{p}} = \left(\mathbf{X}^{\mathrm{T}} \cdot \mathbf{X}\right)^{-1} \cdot \mathbf{X}^{\mathrm{T}} \cdot \mathbf{y}_{\mathrm{Exp}}. \tag{5.43}$$

Using the first regression hypothesis, one can indeed show that $\mathrm{E}[\hat{\mathrm{p}}]=\mathrm{p}$, thus, making $\hat{\mathrm{p}}$ an unbiased sample estimate of p.

5.2.1.4 Uncertainty in the parameters

The parameters uncertainties are deduced from the $\mathrm{N_p}\times\mathrm{N_p}$ covariance matrix,

$$\begin{aligned} \mathbf{Cov}\left[\hat{\mathbf{p}}\right] &= \mathbf{Cov}\left[\left(\mathbf{X}^{\mathrm{T}} \cdot \mathbf{X}\right)^{-1} \cdot \mathbf{X}^{\mathrm{T}} \cdot \mathbf{y}_{\mathrm{Exp}}\right] \\ &= \sigma^2\ \left(\mathbf{X}^{\mathrm{T}} \cdot \mathbf{X}\right)^{-1}. \end{aligned} \tag{5.44}$$

In the previous expression $\mathbf{X}$ is a constant matrix while $\mathbf{y}_{\text{Exp}}$ is a random vector, implicitly carrying the variability, or said differently the variance, coming from the errors, cf. Eq. (5.40). The diagonal elements of $\mathbf{Cov}[\hat{\mathbf{p}}]$ are the variances of the parameters, i.e., the square of their uncertainties, while the off-diagonal elements are the covariances between the parameters and characterize their mutual influence. This relation concentrates within a unique formula, uncertainties and covariances which are absolutely essential ingredients to any thorough uncertainty analysis.

The corresponding correlation matrix can always be deduced from the covariance matrix through the ensuing expression,

$$\mathbf{Cor}\left[\hat{\mathbf{p}}\right] = \mathbf{Var}\left[\hat{\mathbf{p}}\right]^{-\frac{1}{2}} \cdot \mathbf{Cov}\left[\hat{\mathbf{p}}\right] \cdot \mathbf{Var}\left[\hat{\mathbf{p}}\right]^{-\frac{1}{2}}, \tag{5.45}$$

where $\mathbf{Var}[\hat{\mathbf{p}}]$ is formed from the diagonal of $\mathbf{Cov}[\hat{\mathbf{p}}]$.

5.2.1.5 Uncertainties in the observables

Once the covariance of the parameters is known, one can determine the uncertainties in $\hat{\mathbf{y}}_{\text{Th}}$ expressed in terms of the $\text{N}_\text{n}\times\text{N}_\text{n}$ covariance matrix,

$$\begin{aligned}\mathbf{Cov}\left[\hat{\mathbf{y}}_{\text{Th}}\right] &= \mathbf{Cov}\left[\mathbf{X}\cdot\hat{\mathbf{p}}\right] \\ &= \mathbf{X}\cdot\mathbf{Cov}\left[\hat{\mathbf{p}}\right]\cdot\mathbf{X}^{\text{T}}.\end{aligned} \tag{5.46}$$

This expression only accounts for the uncertainty in the model. Thus, further including the errors of the model yields the $\text{N}_\text{n}\times\text{N}_\text{n}$ covariance matrix,

$$\mathbf{Cov}\left[\hat{\mathbf{y}}_{\text{Th}} + \boldsymbol{\epsilon}\right] = \mathbf{Cov}\left[\hat{\mathbf{y}}_{\text{Th}}\right] + \sigma^2\mathbf{I}. \tag{5.47}$$

Note that this expression differs from second corollary because it involves the estimates of the parameters, i.e., $\hat{\mathbf{y}}_{\text{Th}} = \mathbf{X}\cdot\hat{\mathbf{p}}$ instead of $\mathbf{y}_{\text{Th}} = \mathbf{X}\cdot\mathbf{p}$ in Eqs. (5.40) and (5.42).

In the following chapters, we will encounter many physical observables defined as differences. Accordingly, differences such as $\hat{\mathbf{D}}_{\text{Th}} = \hat{\mathbf{y}}_{\text{Th},1} - \hat{\mathbf{y}}_{\text{Th},2}$, have the following $\text{N}_\text{n}\times\text{N}_\text{n}$ covariance matrix,

$$\mathbf{Cov}\left[\hat{\mathbf{D}}_{\text{Th}}\right] = \mathbf{X}_{12}\cdot\mathbf{Cov}\left[\hat{\mathbf{p}}\right]\cdot\mathbf{X}_{12}^{\text{T}}, \tag{5.48}$$

where $\mathbf{X}_{12} = \mathbf{X}_1 - \mathbf{X}_2$ and $\mathbf{X}_1$ together with $\mathbf{X}_2$, refer to matrices similar to $\mathbf{X}$, cf. Eq. (5.36).

5.2.1.6 Error estimates

Notice the presence of σ^2, i.e., the variance of the errors, in all of the previous expressions involving $\mathbf{Cov}[\hat{\mathbf{p}}] = \sigma^2(\mathbf{X}^{\text{T}}\mathbf{X})^{-1}$. However, in practice, these relations cannot be applied since we do not dispose of an actual estimate, for either the errors or their variance. Fortunately, intuitive sample estimates for the errors, also known as residuals, can be found to be

$$\hat{\boldsymbol{\epsilon}} = \mathbf{y}_{\text{Exp}} - \mathbf{X}\cdot\hat{\mathbf{p}}. \tag{5.49}$$

Furthermore, one can show that the following expression,

$$\hat{\sigma}^2 = \frac{(\mathbf{y}_{\mathrm{Exp}} - \mathbf{X}\cdot\hat{\mathbf{p}})^{\mathrm{T}}\cdot(\mathbf{y}_{\mathrm{Exp}} - \mathbf{X}\cdot\hat{\mathbf{p}})}{\mathrm{N_n} - \mathrm{N_p}}, \tag{5.50}$$

is an unbiased sample estimate of the variance of these errors and therefore, is a precise measure of the variability left unexplained. It also turns out that this relation is the square of a well-known quantity, the root-mean-square deviation (RMS), usually characterizing the goodness-of-fit.

Replacing the variance of the errors by its estimate, i.e., σ^2 becomes $\hat{\sigma}^2$ in the preceding expressions, we gather a new set of useful formulas for the unbiased sample estimates of the covariance matrices, listed above, and at the heart of the present work.

5.2.2 Weighted regression

At this stage, experimental uncertainties or correlations between experimental data were not taken into account. In the present section, we extend the regression analysis previously exposed to encompass this empirical evidence. Strong support for such an extension can be found in Bayesian inference [70].

5.2.2.1 Generalized regression

The uncertainties in the experimental data were previously disregarded and can be accounted for through a weighting matrix. The formalism developed hereafter can be found in Ref. [67]. In this weighted formulation, the sum of squared errors becomes,

$$\mathrm{S} = (\mathbf{y}_{\mathrm{Exp}} - \mathbf{X}\cdot\mathbf{p})^{\mathrm{T}}\cdot\mathbf{W}\cdot(\mathbf{y}_{\mathrm{Exp}} - \mathbf{X}\cdot\mathbf{p}), \tag{5.51}$$

where $\mathbf{W}$ is referred to as a weight matrix and assigns a weight to each datum or pair of data if they are correlated. Minimizing this expression with respect to the parameters leads to

$$\hat{\mathbf{p}} = (\mathbf{X}^{\mathrm{T}}\cdot\mathbf{W}\cdot\mathbf{X})^{-1}\cdot(\mathbf{X}^{\mathrm{T}}\cdot\mathbf{W}\cdot\mathbf{y}_{\mathrm{Exp}}). \tag{5.52}$$

Note that the regression assumptions are revised in this extension and the corollaries now become:

$$\mathbf{E}[\mathbf{y}_{\mathrm{Exp}}] = \mathbf{y}_{\mathrm{Th}}, \tag{5.53}$$

$$\mathbf{Cov}[\mathbf{y}_{\mathrm{Exp}}] = \sigma^2\mathbf{W}^{-1}. \tag{5.54}$$

As before, the parameters are correlated and the covariance matrix reads,

$$\mathbf{Cov}[\hat{\mathbf{p}}] = \sigma^2\,(\mathbf{X}^{\mathrm{T}}\cdot\mathbf{W}\cdot\mathbf{X})^{-1}. \tag{5.55}$$

The covariance matrix $\mathbf{Cov}[\hat{\mathbf{y}}_{\mathrm{Th}}]$ can be obtained from Eq. (5.46) and accordingly, observables expressed as differences have the covariance matrix given by Eq. (5.48) where in both cases $\mathbf{Cov}[\hat{\mathbf{p}}]$ is now defined by Eq. (5.55) instead of Eq. (5.44).

For all practical purposes, the estimate for the variance of the errors is

$$\hat{\sigma}^2 = \frac{(\mathbf{y}_{\mathrm{Exp}} - \mathbf{X}\cdot\hat{\mathbf{p}})^{\mathrm{T}}\cdot\mathbf{W}\cdot(\mathbf{y}_{\mathrm{Exp}} - \mathbf{X}\cdot\hat{\mathbf{p}})}{\mathrm{N_n} - \mathrm{N_p}}. \tag{5.56}$$

5.3 Multiple nonlinear regression

We have just discussed a convenient matrix formulation for multiple linear regression analysis. Of course, this formalism applies to linear models containing many parameters (here we mean linear with respect to the parameters). However, most models are not linear and, therefore, another approach, multiple nonlinear regression, must be used in those special cases. In fact, nonlinear regression can be viewed as a simple generalization of linear regression. We now summarize the excellent discussion concerning nonlinear regression that was found in Ref. [69]. As usual, when facing nonlinearities, the idea is to use linearization in order to reformulate the problem as a linear one. The solutions are then approached iteratively and through successive approximations, until convergence is reached.

We now assume that we have a current guess for the parameters $\mathbf{p}^*$. Then, it is possible to make an expansion of the model about this guess as

$$\mathbf{y}_{\mathrm{Th}}(\mathbf{p}) \approx \mathbf{y}_{\mathrm{Th}}(\mathbf{p}^*) + \mathbf{J}(\mathbf{p}^*)\,(\mathbf{p} - \mathbf{p}^*), \tag{5.57}$$

where

$$\mathbf{J}(\mathbf{p}) = \begin{bmatrix} \frac{\partial \mathrm{y}_{\mathrm{Th},1}}{\partial \mathrm{p}_0} & \frac{\partial \mathrm{y}_{\mathrm{Th},1}}{\partial \mathrm{p}_1} & \cdots & \frac{\partial \mathrm{y}_{\mathrm{Th},1}}{\partial \mathrm{p}_{\mathrm{Np}}} \\ \frac{\partial \mathrm{y}_{\mathrm{Th},2}}{\partial \mathrm{p}_0} & \frac{\partial \mathrm{y}_{\mathrm{Th},2}}{\partial \mathrm{p}_1} & \cdots & \frac{\partial \mathrm{y}_{\mathrm{Th},2}}{\partial \mathrm{p}_{\mathrm{Np}}} \\ \vdots & \vdots & \ddots & \vdots \\ \frac{\partial \mathrm{y}_{\mathrm{Th,Nn}}}{\partial \mathrm{p}_0} & \frac{\partial \mathrm{y}_{\mathrm{Th,Nn}}}{\partial \mathrm{p}_1} & \cdots & \frac{\partial \mathrm{y}_{\mathrm{Th,Nn}}}{\partial \mathrm{p}_{\mathrm{Np}}} \end{bmatrix}, \tag{5.58}$$

Thus, the matrix $\mathbf{J}(\mathbf{p})$ is constructed from derivatives of the model and clearly plays a role analogous to $\mathbf{X}$ in linear regression. Note, however, that because of the linearity of the model $\mathbf{X}$ does not depend on the parameters while $\mathbf{J}(\mathbf{p})$ usually does, again, because of the nonlinearity of the model.

The current residuals can be obtained as

$$\boldsymbol{\epsilon}^* = \mathbf{y}_{\mathrm{Exp}} - \mathbf{y}_{\mathrm{Th}}(\mathbf{p}^*). \tag{5.59}$$

Then the sum of the squared errors can then be written as

$$\begin{aligned} \mathrm{S} &= [\mathbf{y}_{\mathrm{Exp}} - \mathbf{y}_{\mathrm{Th}}]^{\mathrm{T}} \cdot [\mathbf{y}_{\mathrm{Exp}} - \mathbf{y}_{\mathrm{Th}}] \\ &= [\boldsymbol{\epsilon}^* - \mathbf{J}(\mathbf{p}^*)\,(\mathbf{p} - \mathbf{p}^*)]^{\mathrm{T}} \cdot [\boldsymbol{\epsilon}^* - \mathbf{J}(\mathbf{p}^*)\,(\mathbf{p} - \mathbf{p}^*)]\,, \end{aligned} \tag{5.60}$$

using the expansion from Eq. (5.57). Minimizing S with respect to $\mathbf{p}$ leads to

$$\hat{\mathbf{p}} = \mathbf{p}^* + \left[\mathbf{J}^{\mathrm{T}}(\mathbf{p}^*) \cdot \mathbf{J}(\mathbf{p}^*)\right]^{-1} \cdot \mathbf{J}^{\mathrm{T}}(\mathbf{p}^*) \cdot \hat{\boldsymbol{\epsilon}}^*. \tag{5.61}$$

Now that we have explained how, by starting with an initial guess, we can find an estimate for the parameters. We can now proceed iteratively until convergence is reach and a "true" estimate for the parameters is found.

We now describe the Gauss-Newton algorithm.

1. Iteration j=0. Start with an initial guess for the parameters $\mathbf{p}^{(0)}$ and then compute $\mathrm{S}^{(0)}$.
2. Set the iteration counter at j=0.
3. Compute $\mathbf{J}(\mathbf{p}^{(j)})$ and $\hat{\boldsymbol{\epsilon}}^{(j)}$.
   Then compute $\hat{\mathbf{p}} = \mathbf{p}^* + \left[\mathbf{J}^{\mathrm{T}}(\mathbf{p}^*) \cdot \mathbf{J}(\mathbf{p}^*)\right]^{-1} \cdot \mathbf{J}^{\mathrm{T}}(\mathbf{p}^*) \cdot \hat{\boldsymbol{\epsilon}}^*$.
   Finally, compute $\mathrm{S}^{(j+1)}$.
4. Stop, if $|\mathrm{S}^{(j+1)}\text{-}\mathrm{S}^{(j)}|$ is sufficiently small.
   Otherwise, go back to step 3.

Once this procedure has converged, we know the "true" estimates for the parameters $\hat{\mathbf{p}}$ as well as the "true" errors of the model $\hat{\boldsymbol{\epsilon}}$. If the sample is large enough (cf. Ref. [69]) then one can show using Bayesian inference that

$$\mathbf{Cov}[\hat{\mathbf{p}}] = \hat{\sigma}^2 \cdot [\mathbf{J}^{\mathrm{T}}(\hat{\mathbf{p}}) \cdot \mathbf{J}(\hat{\mathbf{p}})]^{-1}, \tag{5.62}$$

$$\mathbf{Cov}[\hat{\mathbf{y}}] = \mathbf{J}(\hat{\mathbf{p}}) \cdot \mathbf{Cov}[\hat{\mathbf{p}}] \cdot \mathbf{J}^{\mathrm{T}}(\hat{\mathbf{p}}). \tag{5.63}$$

All of the previous expressions for multiple linear regression are in fact valid for nonlinear regression as well. This means that extensions to weighted nonlinear regression can easily be obtained. One only needs to replace $\mathbf{X}$ in the linear case by $\mathbf{J}(\hat{\mathbf{p}})$ in the nonlinear case. Again, we stress that this in only valid in the case of large samples and after the iterative algorithm has converged.

5.4 Conclusion

In this chapter we have laid the ground upon which regression analysis is built. First, we have examined a simple two-parameters model. This allowed us to introduce most of the ingredients required to fully understand the core of regression analysis. In particular, it was shown that regression analysis was based on two hypothesis. The latter should always be verified a posteriori. More specifically, the mean of the errors should be zero for models including an intercept and the errors should follow a Gaussian distribution. In the case of the two-parameter model, the calculations were simple and could be done analytically. However, this approach is to cumbersome to be applied to models involving many parameters. Therefore, a matrix formulation was introduced to treat multiple linear regression. Furthermore, most models are not linear and so the end of this chapter focused on nonlinear regression. It was shown that linearization along with an iterative algorithm allowed to treat these cases in a formulation closely related to linear regression.

Chapter 6

A simple macroscopic model

Remember that the goal of the present work is to constrain the formation probability, expressed as

$$P_{\text{form}}^{\text{exp}} = \frac{\sigma_{\text{ER}}^{\text{exp}}}{\sigma_{\text{cap}} \times P_{\text{surv}}}. \tag{6.1}$$

Therefore, in order to constrain the formation probability, we must first evaluate the uncertainties in all the quantities entering this expression. Since we already know the uncertainty in the measured cross-section, in this thesis, we shall focus on the two remaining quantities, the capture cross-section and the survival probability. Here, we shall start by the latter.

A previous investigation has demonstrated that by far the most influential factor in the calculation of the survival probability is the fission barrier of the compound nucleus [37, 38]. Therefore, in this thesis, we will focus our attention on fission barriers and try to evaluate the accuracy of their predictions.

Fission barriers are defined as the difference between the saddle-point and the ground-state masses. It should also be mentioned that fission barriers are very difficult to calculate and that the disagreement between different available approaches spans few MeV's [39]. Thus, in this chapter, we will begin our investigation with ground-state masses and use a simple macroscopic model in order to determine them. The following uncertainty analysis of the liquid drop model has been submitted for publication [71].

In the two previous chapters, we have described how to determine the uncertainties in the parameters of a model using regression analysis and how to propagate these uncertainties through a model. Therefore, our strategy is to, first, determine the parameters and their uncertainties and second, to propagate these uncertainties onto the ground-state masses. Finally, it should be mentioned that in the spirit of our approach the uncertainties are interpreted as constraints since they provide a range in which a parameter or a mass must lie.

6.1 Uncertainty analysis of the liquid drop model

6.1.1 Introduction

The phenomenological Bethe-Weizsäcker formula, proposed in 1935, can describe the binding energy of a broad range of nuclei, using only few elementary concepts [8, 9]. Since then, many refinements have been introduced allowing for a better description of the ever-expanding nuclear chart. The most significant development, was provided by Strutinsky, as semi-classical corrections, i.e., shell corrections, to the original model [72, 73]. A detailed first application of this method can be found in Ref. [74]. An analogous prescription may be applied to procure pairing corrections. Later, deformation was included, both microscopically, i.e., shell and pairing corrections, and macroscopically, i.e., liquid drop model [49, 57]. Although recent investigations [75, 76] have initiated detailed studies of such family of models, a thorough uncertainty analysis is yet to be provided and the ambition of the present text is to fill the current void.

Note that a few uncertainty analysis of mass models within the mean field formalism are available, e.g., Refs. [77–81]. For instance, in Ref. [77] the uncertainty in a parameter is obtained by varying that parameter until a 10% increase in the root-mean-square deviation is observed. Then the corresponding uncertainties in the masses obtained within the HFB-24 model are discussed. Refs. [78–80] detail the Bayesian approach used to determine the uncertainties in the parameters entering the UNEDF1 directly from experimental masses. More important is the Ref. [81] where a brand-new bootstrap method is introduced in order to account for the correlations between the residuals (errors of the model). It is shown that accounting for these correlations yields a better estimate of the uncertainties in the model parameters. It should be stressed that the existing correlations between the residuals will be disregarded in the following study.

The liquid drop model has tremendous implications when it comes to nuclear physics. In particular, the values of some parameters are directly related to infinite nuclear matter, e.g., the binding energy per nucleon or the symmetry energy, having profound consequences on our understanding of the equation of state and consequently, on precise stellar features. Furthermore, numerous observables can be deduced from binding energies, e.g., Q-values influencing the energies either required or released by nuclear reactions, thus, affecting nucleosynthesis and particularly, the r-process involving overly neutron rich systems. The liquid drop parameters are also used to calculate fission barriers, defined as the difference between the ground-state and the saddle-point energies and are crucial quantities for the synthesis of superheavy nuclei. Moreover, separation energies, as well as pairing effects may also be approached directly through masses. Therefore, one can only recognize the dramatic consequences of binding energies and their predictions upon our deepest understanding of nuclear physics.

Since the last decade, theoretical descriptions are being complemented by uncertainty analysis which aims, is to encompass the unexplained variations of the binding energy. Statistical methods, such as regression analysis, have been introduced to specifically address this question in precise quantitative terms. Regarding the current inquiry, we adopt the regression formalism presented in the previous chapters along with an extended version of weighted regression to simultaneously address experimental and theoretical uncertainties as well as their respective correlations. The parameters in the liquid drop model are determined through standard regression analysis, thus, going beyond least squares by involving the errors of the model, the uncertainties, as well as the mutual influence of the parameters. These uncertainties can then be propagated onto observables to reveal the reliability of the predictions, disprove models or even guide further research.

There are several liquid drop formulas in the scientific literature, however, we shall focus on a single one found in Ref. [82]. Nevertheless, the ideas developed here may be applied to any linear model and can further be extended to account for nonlinearities as exposed in Ref. [76].

6.1.2 Liquid drop model

The liquid drop model considered in the present work is taken from Ref. [82] and gives the following expression, for the theoretical binding energy,

$$\begin{aligned} \mathrm{B'_{Th,i}} = &\left(\mathrm{p_1} + \mathrm{p_2 I_i^2}\right) \mathrm{A_i} + \left(\mathrm{p_3} + \mathrm{p_4 I_i^2}\right) \mathrm{A_i^{\frac{2}{3}}} + \mathrm{p_5} \frac{\mathrm{Z_i^2}}{\mathrm{A_i^{\frac{1}{3}}}} \\ &+ \mathrm{p_6} \frac{\mathrm{Z_i^2}}{\mathrm{A_i}} + \mathrm{p_7} \left|\mathrm{N_i - Z_i}\right| e^{-\left(\frac{\mathrm{A_i}}{50}\right)^2} + \mathrm{p_8} e^{-80\mathrm{I_i^2}}, \end{aligned} \tag{6.2}$$

for the ith nucleus having $\mathrm{N_i}$ neutrons, $\mathrm{Z_i}$ protons, mass number $\mathrm{A_i}$=$\mathrm{N_i}$+$\mathrm{Z_i}$, isospin $\mathrm{I_i}$=($\mathrm{N_i}$-$\mathrm{Z_i}$)/$\mathrm{A_i}$ and where $\mathrm{p_j}$ are the parameters entering the model with $\mathrm{j} = 1, \ldots, 8$.

The parameters in Eq. (6.2) are determined through regression using the following expression for the theoretically corrected experimental binding energies,

$$\mathrm{B'_{Exp,i}} = \mathrm{B_{Exp,i}} + \mathrm{E_{Pair,i}} + \mathrm{E_{Shell,i}}. \tag{6.3}$$

It includes the uncorrected experimental binding energy ($\mathrm{B_{Exp,i}}$), the average pairing energy ($\mathrm{E_{Pair,i}}$) and the shell correction energy ($\mathrm{E_{Shell,i}}$). The uncorrected experimental nuclear binding energy is deduced from the atomic mass excess, found in the 2016 mass evaluation, accounting for the masses of the electrons as well as their binding energy [83, 84]. The pairing energy was directly taken from the Thomas-Fermi model [57], and is restated here for the sake of completeness:

$$\mathrm{E_{Pair,i}} = \begin{cases} \dfrac{4.8}{N_\mathrm{i}^{\frac{1}{3}}} + \dfrac{4.8}{Z_\mathrm{i}^{\frac{1}{3}}} - \dfrac{6.6}{A_\mathrm{i}^{\frac{2}{3}}} - \dfrac{30}{A_\mathrm{i}} & (N_\mathrm{i} = Z_\mathrm{i}, \text{odd}) \\ \dfrac{4.8}{N_\mathrm{i}^{\frac{1}{3}}} + \dfrac{4.8}{Z_\mathrm{i}^{\frac{1}{3}}} - \dfrac{6.6}{A_\mathrm{i}^{\frac{2}{3}}} & (N_\mathrm{i}\,\text{odd}, Z_\mathrm{i}\,\text{odd}) \\ \dfrac{4.8}{Z_\mathrm{i}^{\frac{1}{3}}} & (N_\mathrm{i}\,\text{even}, Z_\mathrm{i}\,\text{odd}) \\ \dfrac{4.8}{N_\mathrm{i}^{\frac{1}{3}}} & (N_\mathrm{i}\,\text{odd}, Z_\mathrm{i}\,\text{even}) \\ 0 & (N_\mathrm{i}\,\text{even}, Z_\mathrm{i}\,\text{even}) \end{cases} \tag{6.4}$$

Notice the minus sign before the term $30/\mathrm{A_i}$ instead of the plus sign appearing in Ref. [57] which seems to be a typographical error. In the following, the Thomas-Fermi shell corrections from Ref. [57] are used.

Note that Eq. (6.2) is linear and can easily be written in the matrix form,

$$\mathbf{B'_{Th}} = \mathbf{X} \cdot \mathbf{p}, \tag{6.5}$$

where $\mathbf{B'_{Th}}$ and $\mathbf{p}$ are column vectors, respectively, containing all the values of $\mathrm{B'_{Th,i}}$ and $\mathrm{p_j}$.

The matrix $\mathbf{X}$ is defined as,

$$\mathbf{X} = \begin{bmatrix} \frac{\partial B'_{Th,1}}{\partial p_1} & \frac{\partial B'_{Th,1}}{\partial p_2} & \cdots & \frac{\partial B'_{Th,1}}{\partial p_{Np}} \\ \frac{\partial B'_{Th,2}}{\partial p_1} & \frac{\partial B'_{Th,2}}{\partial p_2} & \cdots & \frac{\partial B'_{Th,2}}{\partial p_{Np}} \\ \vdots & \vdots & \ddots & \vdots \\ \frac{\partial B'_{Th,Nn}}{\partial p_1} & \frac{\partial B'_{Th,Nn}}{\partial p_2} & \cdots & \frac{\partial B'_{Th,Nn}}{\partial p_{Np}} \end{bmatrix}, \tag{6.6}$$

where the ith line of $\mathbf{X}$ is associated with the ith nucleus while the jth column is related to the parameter p_j. Thus, the matrix $\mathbf{X}$ has as many lines as there are nuclei, N_n and as many columns as there are parameters, N_p and naturally, the vector $\mathbf{p}$ has as many lines as there are parameters.

In order to ease the notations of the following sections, the primes will be dropped while still implicitly referring to the corrected experimental binding energies defined by Eq. (6.3).

6.1.3 Primary results

The formalism presented in chapter 5 is now exploited in order to examine the uncertainties and the correlations of the parameters entering the liquid drop model, cf. Eq. (6.2). A particular emphasis is given to the parameters, their uncertainties and correlations, as well as a diversity of observables.

The following results are based on the nuclear binding energies deduced from the atomic mass excesses found in Refs. [83, 84] for all nuclei satisfying N,Z $\geq$ 8 with uncertainties below 150 keV, thus, a total of 2315 nuclei are considered.

Note that the uncertainties in the experimental binding energies, the shell corrections and the pairing energies are disregarded at this stage. However, uncertainties in the shell corrections will be considered in the next chapter.

6.1.3.1 Parameters

The parameters obtained using Eq. (5.43) are displayed in Table 6.1. The corresponding uncertainties, also appearing in this table, were inferred from the diagonal elements of the covariance matrix, cf. Eq. (5.44), given in the appendix at the end of this section (cf. Sect. 6.1.7). Careful examination of the relative uncertainties establishes that the parameters, p_6, p_8 and to an even greater extent p_7, are loosely constrained with respect to the other parameters. More detailed discussions about constraints on the nuclear matter parameters obtained within the mean field formalism can be found in Refs. [77, 85].

Table 6.1: The parameters along with their uncertainties and relative uncertainties.

	$\hat{p}_1$	$\hat{p}_2$	$\hat{p}_3$	$\hat{p}_4$	$\hat{p}_5$	$\hat{p}_6$	$\hat{p}_7$	$\hat{p}_8$
$\hat{p}$ [MeV]	15.4829	-27.8219	-17.5783	31.1447	-0.7058	0.9251	-0.2942	2.7265
$\hat{u}(\hat{p})$[MeV]	0.0145	0.0843	0.0505	0.3797	0.0008	0.0288	0.0293	0.1693
$\lvert\hat{u}(\hat{p})/\hat{p}\rvert$ [%]	0.1	0.3	0.3	1.2	0.1	3.1	10.0	6.2

From the covariance matrix, cf. Table 6.11, one can deduce the correlation matrix, cf. Eq. (5.45), given in Table 6.2. At first glance, it appears that all the parameters entering the liquid drop model are strongly correlated with one another.
Meticulous inspection of Table 6.2, shows the existence of two correlation groups, i.e., sets of parameters with particularly strong correlations. The first involving p_1, p_3, p_5 and p_7, the second comprising p_2, p_4 and p_8. Notice p_6 is less correlated with the other parameters and the two groups are linked through the partial intrusion of p_1 in the second group and p_8 in the first group. Besides the Wigner term p_7, the first group, contains the historical liquid drop parameters while the second group, consists of isospin dependent corrections. Such an observation may be sufficient to physically explain the emergence of these two groups. Although not referred to as correlation groups, their existence has been studied in Ref. [75] by either removing or adding parameters to the regression and debating the corresponding effects on the remaining parameters. In the current analysis, a similar conclusion is drawn, directly, from a detailed examination of the correlation matrix shown Table 6.2.

Table 6.2: Correlation matrix of the parameters deduced from the covariance matrix, cf. Table 6.11. Notations: **group 1**, *group 2* and intruders.

$\hat{p}_1$	$\hat{p}_2$	$\hat{p}_3$	$\hat{p}_4$	$\hat{p}_5$	$\hat{p}_6$	$\hat{p}_7$	$\hat{p}_8$
1.00	-0.71	**-0.93**	0.47	**-0.87**	-0.32	**0.74**	0.82
-0.71	*1.00*	0.62	*-0.92*	0.39	0.51	-0.24	*-0.87*
-0.93	0.62	**1.00**	-0.48	**0.95**	-0.05	**-0.81**	-0.70
0.47	*-0.92*	-0.48	*1.00*	-0.22	-0.25	0.07	*0.72*
-0.87	0.39	**0.95**	-0.22	**1.00**	-0.15	**-0.85**	-0.52
-0.32	0.51	-0.05	-0.25	-0.15	1.00	0.15	-0.55
0.74	-0.24	**-0.81**	0.07	**-0.85**	0.15	**1.00**	0.40
0.82	*-0.87*	-0.70	*0.72*	-0.52	-0.55	0.40	*1.00*

6.1.3.2 Observables

Theoretical binding energies
Once the parameters are determined, one can easily compute the theoretical binding energy of each nucleus along with its uncertainty.

The root-mean-square deviation associated with the binding energies is $\hat{\sigma}$=602 keV. As already mentioned, it is an estimate of the standard deviation of the errors and quantifies the goodness-of-fit.

The uncertainties in the binding energy predictions, as deduced from Eq. (5.46), range from 21 keV to 124 keV with a mean of 33 keV. Those uncertainties are shown in Fig. 6.1. Notice the increase of uncertainties away from the mean proton number of the sample, i.e., 57.9. This is a well-known feature of regression procedures, even extending beyond the regression interval, thus, making extrapolations further and further away from the known data more and more uncertain.

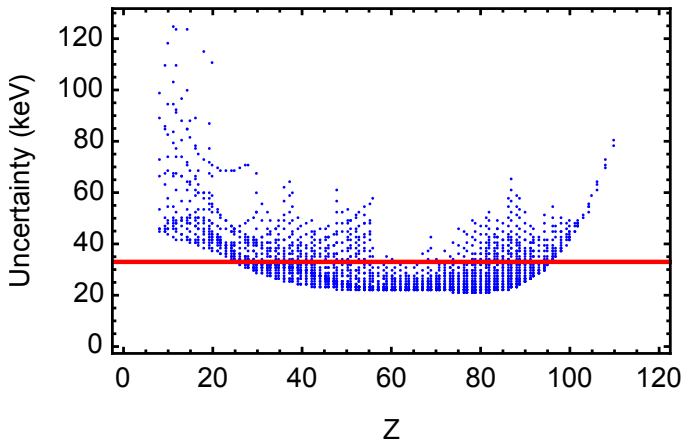

Figure 6.1: Uncertainties in the predicted binding energies (blue dots) as a function of proton number Z along with the mean of the uncertainties (red line). Inferred from the square root of the diagonal elements of the covariance matrix, i.e., the diagonal elements of Eq. (5.46).

Thus, the uncertainties in the predicted binding energies are rather small. This suggests that once the shell corrections and the average pairing have been specified, the liquid drop model is extremely constrained. This could have been foreseen since the parameters, themselves, are firmly constrained. In this work, shell corrections were included in the corrected binding energies, however, they were excluded from the uncertainty analysis. Including the latter should significantly increase the uncertainties in the model constructed from the liquid drop and the shell corrections.

The correlations between the binding energy of ^{208}Pb and the binding energies of the 2315 nuclei is depicted in Fig. 6.2 (including ^{208}Pb). As expected, the correlations with neighbouring nuclei are very strong and fade away from this region.

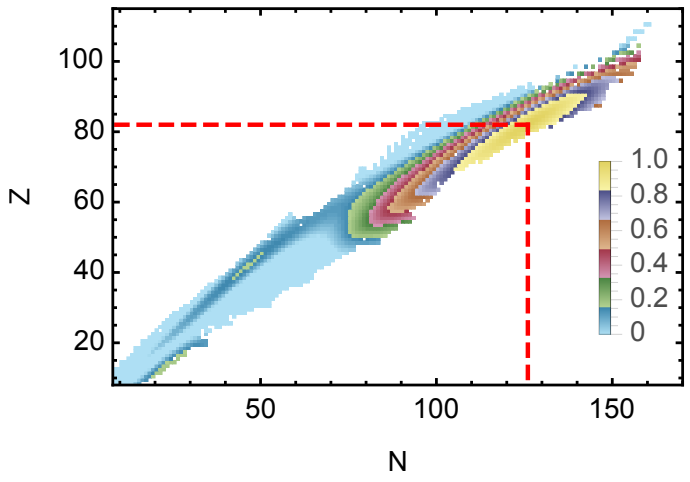

Figure 6.2: Correlations between the theoretical binding energy of ^{208}Pb and the 2315 binding energies. Notice the extreme correlations in the region of ^{208}Pb and their downfall away from this region. The position of ^{208}Pb is indicated by the red dashed lines.

Other observables

Additional observables can be deduced from the binding energies. We have selected here a few mass filters for which experimental values are available over the whole nuclear chart.

For each observable the uncertainties in the predictions of the model were calculated. We present in Table 6.3, the minimum and maximum uncertainties over the nuclear chart, as well as a statistical indicator, the mean of the uncertainties, defined as

$$\mathrm{MU} = \frac{1}{\mathrm{N_n}} \sum_{\mathrm{i}=1}^{\mathrm{N_n}} \mathrm{Var}[\mathrm{O_{Th,i}}]^{\frac{1}{2}}, \tag{6.7}$$

for the observable O. Note that the indicator MU, has no profound statistical significance, and was only introduced, as a substitute for tables of unreasonable length, containing 2315 uncertainties for each observable. It appears that observables based on the difference between binding energies are less uncertain than the binding energies themselves. This is a consequence of the severe correlations existing between binding energies of neighbouring nuclei, cf. Fig. 6.2.

We have also compared the predicted values to the experimental ones. As a statistical indicator, the root-mean-square deviation (RMS) of an observable O, defined as

$$\mathrm{RMS} = \left[\frac{1}{\mathrm{N_n} - \mathrm{N_p}} \sum_{\mathrm{i}=1}^{\mathrm{N_n}} [\mathrm{O_{Th,i}} - \mathrm{O_{Exp,i}}]^2 \right]^{\frac{1}{2}}, \tag{6.8}$$

is presented in Table 6.3. As the model was adjusted to experimental binding energies, it is natural that this quantity possesses the smallest root-mean-square deviation.

Table 6.3: The minimum, mean and maximum of the uncertainties (MinU, MU and MaxU) are presented in the uppermost portion of the table and the root-mean-square deviation (RMS) appears below, for the 2315 nuclei.

	$\hat{\mathrm{B}}_{\mathrm{Th}}$	$\hat{\mathrm{S}}_{\mathrm{n}}$	$\hat{\mathrm{S}}_{\mathrm{2n}}$	$\hat{\mathrm{S}}_{\mathrm{p}}$	$\hat{\mathrm{S}}_{\mathrm{2p}}$	$\hat{\mathrm{Q}}_{\alpha}$	$\hat{\mathrm{Q}}_{\beta}$
MinU [keV]	21	2	3	3	5	2	4
MU [keV]	33	6	11	8	15	5	13
MaxU [keV]	124	72	120	70	120	36	120
RMS [keV]	602	1273	1050	1367	985	1346	1847

The correlations between the theoretical Q_α-value of ^{208}Pb and the 2315 Q_α-values is exposed in Fig. 6.3 (including ^{208}Pb). As formerly argued, the correlations with neighbouring nuclei are very strong and vanish away from this region. However, one can also distinguish more sophisticated patterns which were absent from the correlations between binding energies, cf. Fig. 6.2. Notice these observations can further be extended to the remaining observables considered here. These complex patterns are owed to the involvement of twice as many nuclei. Indeed, binding energy correlations, only, involve two distinct nuclei while those between separation energies, or Q-values, require four, thus, making the structure much more intricate.

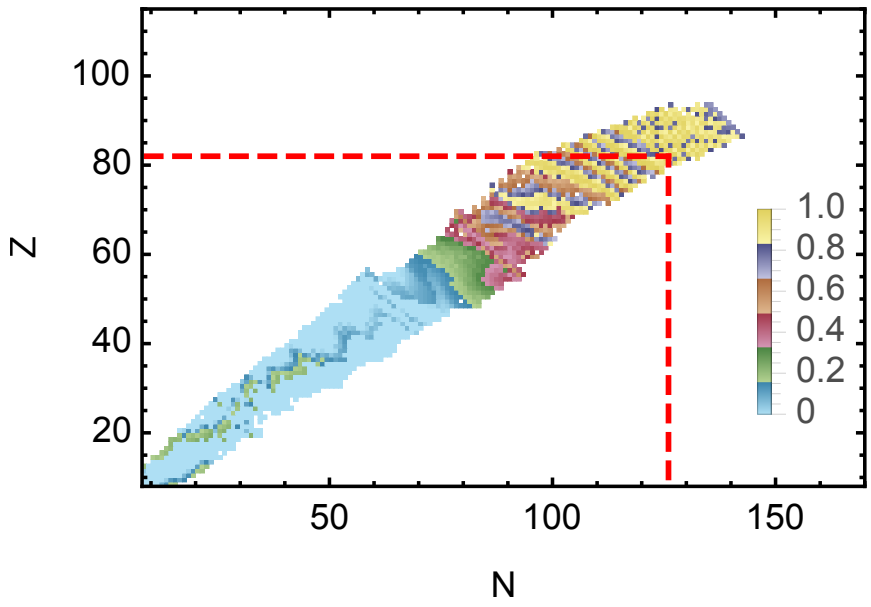

Figure 6.3: Correlations between the theoretical Q_α-value of ^{208}Pb and the 2315 Q_α-values. Notice the extreme correlations in the region of ^{208}Pb and their downfall away from this region, as well as the complex patterns due to the involvement of a greater number of nuclei. The position of ^{208}Pb is indicated by the red dashed lines.

6.1.3.3 Assessment of the regression hypotheses

The results presented beforehand were procured through regression analysis which is based on hypotheses, regarding the distribution of the errors, as described in the previous chapter. This distribution of errors, associated with the binding energies, is shown Fig. 6.4. The corresponding mean and standard deviation are, respectively, 2 keV and $\hat{\sigma} = 602$ keV. These values were used to plot the normal distribution that exhibits a fair agreement with the histogram representing the distribution of the errors.

Other, more elaborate, methods are available to support the normality of the errors. The quantile-quantile plot is a graphical tool used to confirm that a set of data follows a specific probability distribution, e.g., a normal distribution. This is usually done by plotting the quantiles of the observed distribution of errors against the quantiles of the normal distribution having the same mean and variance, i.e., 2 keV and 602 keV. Indeed, if the observed errors do follow a normal distribution, then, the quantiles should be equal and the plot should form a straight line. The corresponding quantile-quantile plot is given Fig. 6.5 and confirms that most of the observed errors follow a normal distribution. However, the plot also makes it clear that the tails of the distribution of the errors do not correspond to those of a normal distribution. Nevertheless, the central part, $\hat{\epsilon} \in$ [-1,1] MeV containing around 95% of the errors, does follow a normal distribution. Thus, the normality assumption, although not perfectly satisfied, should be enough to insure that the outcome of the current endeavour offers serious results.

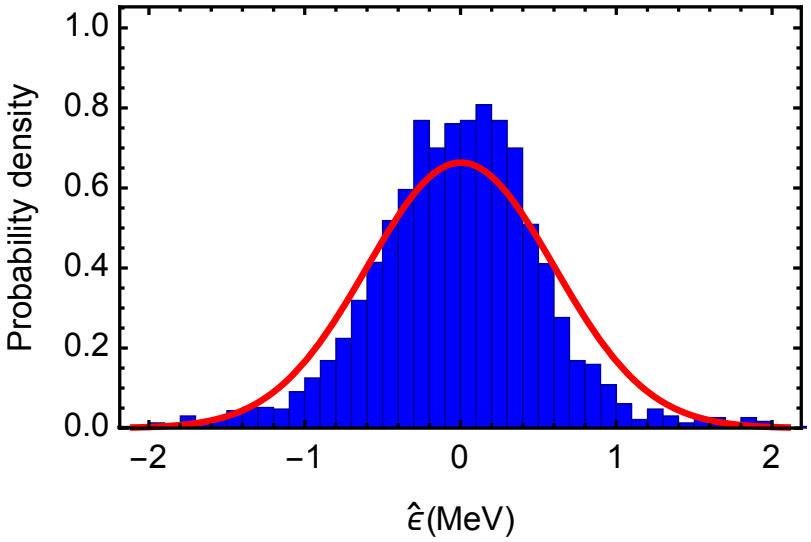

Figure 6.4: Histogram (blue bars) formed of 50 bins restricted to $\hat{\boldsymbol{\epsilon}} \in$ [-2.1;2.1] MeV and representing the distribution of the errors ($\hat{\boldsymbol{\epsilon}} = \mathbf{B}_{\text{Exp}} - \mathbf{X} \cdot \hat{\mathbf{p}}$). The normal distribution constructed from the mean (2 keV) and the standard deviation ($\hat{\sigma}$ = 602 keV) of the errors, is also provided (red line).

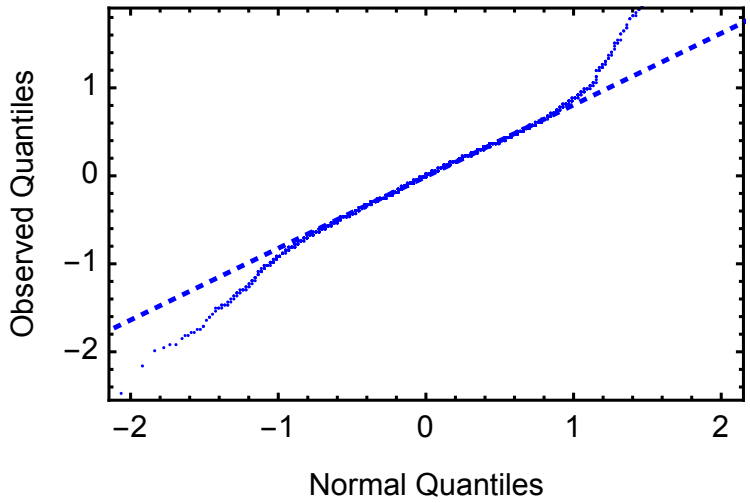

Figure 6.5: Quantile-quantile plot (blue dots) for the distribution of the errors restricted to $\hat{\boldsymbol{\epsilon}} \in$ [-2.1;2.1] MeV and the expected theoretical straight line (dashed blue) in the case where normality is perfectly satisfied.

Notice the mean of these errors does not exactly vanish and one can show that this hypothesis is only strictly satisfied by models including an intercept which macroscopic models do not, in general, contain. We now investigate the impact of adding a constant parameter p_0 to the liquid drop model, Eq. (6.2).

The parameters and their uncertainties were recalculated and the results are reported in Table 6.4. It appears that the additional intercept does not significantly alter the previous outcome, i.e., p_6, p_7 and p_8 are still loosely constrained as well as the intercept p_0.

Table 6.4: The parameters along with their uncertainties and relative uncertainties obtained for the model with intercept.

	$\hat{p}_0$	$\hat{p}_1$	$\hat{p}_2$	$\hat{p}_3$	$\hat{p}_4$	$\hat{p}_5$	$\hat{p}_6$	$\hat{p}_7$	$\hat{p}_8$
$\hat{p}$ [MeV]	1.5896	15.5399	-27.9838	-17.9250	31.8989	-0.7088	1.0017	-0.3448	2.5587
$\hat{u}(\hat{p})$[MeV]	0.3542	0.0193	0.0914	0.0922	0.4138	0.0010	0.0334	0.0313	0.1727
$\lvert\hat{u}(\hat{p})/\hat{p}\rvert$ [%]	22.3	0.1	0.3	0.5	1.3	0.1	3.3	9.1	6.7

Table 6.5 reveals noticeable changes in the correlations, however, the group structure remains quite similar. There are still two correlation groups, a first consisting of p_1, p_3 and p_5, the second involving p_2 and p_4. Parameters, outside these groups, display moderate correlations and there are no intruders in this particular case.

Table 6.5: Correlation matrix obtained for the model with intercept deduced from the covariance matrix, cf. Table 6.12. Notations: **group 1** and *group 2*.

$\hat{p}_0$	$\hat{p}_1$	$\hat{p}_2$	$\hat{p}_3$	$\hat{p}_4$	$\hat{p}_5$	$\hat{p}_6$	$\hat{p}_7$	$\hat{p}_8$
1.00	0.66	-0.39	-0.84	0.41	-0.64	0.51	-0.36	-0.22
0.66	**1.00**	-0.75	**-0.93**	0.59	**-0.93**	0.13	0.28	0.46
-0.39	-0.75	*1.00*	0.64	*-0.93*	0.53	0.20	-0.06	-0.70
-0.84	**-0.93**	0.64	**1.00**	-0.58	**0.94**	-0.45	-0.11	-0.19
0.41	0.59	*-0.93*	-0.58	*1.00*	-0.42	0.01	-0.09	0.55
-0.64	**-0.93**	0.53	**0.94**	-0.42	**1.00**	-0.43	-0.38	-0.25
0.51	0.13	0.20	-0.45	0.01	-0.43	1.00	-0.07	-0.57
-0.36	0.28	-0.06	-0.11	-0.09	-0.38	-0.07	1.00	0.44
-0.22	0.46	-0.70	-0.19	0.55	-0.25	-0.57	0.44	1.00

Regarding the binding energy, the mean uncertainty and root-mean-square deviation, respectively, become MU = 34 keV and $\hat{\sigma}$=600 keV. Thus, the differences between the uncertainties and the predictions obtained with and without an intercept are negligible. Note that, apart from the binding energy, the other observables are not affected by the intercept.

This assessment confirms that, although a more rigorous analysis should include an intercept in order to satisfy the first regression hypothesis, not doing so, does not significantly affect the outcomes of the study.

6.1.3.4 The impact of shell effects

In this study, an attempt was made to examine the impact of shell effects by using both, the Thomas-Fermi [57] and the Nix-Möller [49] microscopic corrections. The results show that the parameters marginally vary with the change of shell corrections, similarly, the absolute and relative uncertainties are barely altered and the correlation matrices are identical. The meagre influence of shell corrections is not surprising since they are identical for nuclei having N, Z $>$ 30 in Refs. [57] and [49]. As only light nuclei contribute to this change, the effects are rather limited. Therefrom, no conclusions could be drawn about the exact impact of shell effects on either the estimation of the parameters, their uncertainties or even their correlations. Nevertheless, the outcome of the study suggested that the parameters could be significantly affected by the microscopic corrections while uncertainties and correlations suffered more minor changes.

6.1.3.5 Primary comments

As mentioned before, other uncertainty analysis of mass models based on SCMF or EDF are available, e.g., Refs. [77,79]. Here we have focused our attention on the liquid drop approach. It should be mentioned that for all observables considered in this work, the uncertainties are insufficiently broad to account for the errors, thus, pointing towards some missing variability, e.g., additional uncertainties should also come from shell corrections and were not included in the present work. Indeed, Fig. 6.6 reveals errors spreading way beyond the bounds of uncertainties which is coherent with prior results and can be understood from the root-mean-square deviation being virtually 20 times larger than the mean uncertainty. Certainly, the scope of our uncertainty analysis, i.e., disregarding pairing and shell corrections, may be too crude and the resulting uncertainties too modest, to properly describe the uncertainties of the entire "macroscopic-microscopic" model. Nevertheless, it serves to distinguish the precision of the predictions from the uncertainties originating from only a limited portion of the model. This suggests that, once the microscopic corrections have been fixed, the experimental data leaves hardly any room for macroscopic variability, i.e., the macroscopic model is extremely constrained. Consequently, any further improvement of such model must be focused on constraining and evaluating uncertainties in the microscopic corrections. Another possibility would be to study models in which there is no distinction between macroscopic and microscopic contributions (e.g. SCMF or EDF type models). To summarize, the errors dominate over the uncertainties. This can be explained because first, the uncertainties in the shell corrections were neglected and second, the correlations between the residuals were not accounted for in the estimation of the uncertainties in the parameters (for more details cf. Ref. [81]).

6.1.4 Empirical weights

At this stage, experimental uncertainties or correlations were not taken into account. Note that these will be accounted for through the weighted regression formalism we have exposed in chapter 5 (cf. Sect. 5.2.2). In the present section, we extend our previous analysis in order to encompass this empirical evidence. Considering both the uncertainties and correlations or only the uncertainties is investigated in the following. Unfortunately, the uncertainties or the correlations regarding microscopic corrections are not currently known, however, when available, these contributions may be included through the extended formalism used here. For now, we shall focus on experimental uncertainties and their correlations.

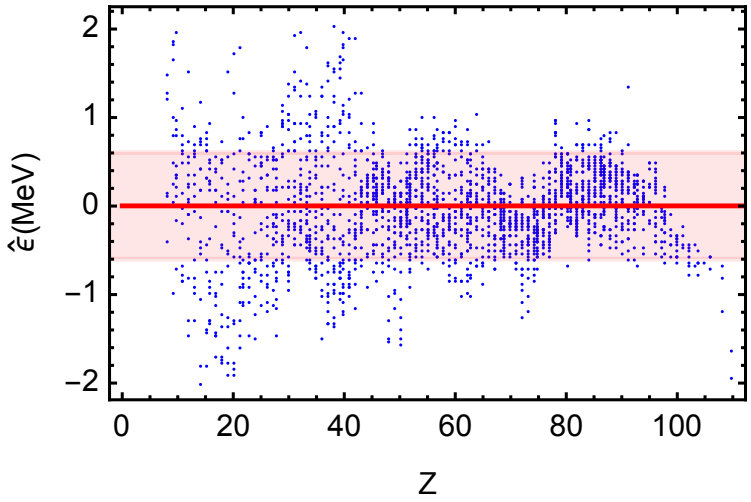

Figure 6.6: The errors ($\hat{\boldsymbol{\epsilon}} = \mathbf{B}_{\rm Exp} - \mathbf{X}\cdot\hat{\mathbf{p}}$) restricted to $\hat{\boldsymbol{\epsilon}} \in$ [-2.1;2.1] MeV are shown (blue dots) as a function of proton number Z. The mean of the errors (red line) and the standard deviation of the errors (red band), i.e., the root-mean-square deviation, are also displayed.

The experimental data are correlated through the specific measurement method that was employed, these correlations are contained in the empirical covariance matrix **ECM** also included in Refs. [83, 84] and having the structure bellow,

$$\mathbf{ECM}\left[\mathbf{y}_{\rm Exp}\right] = \begin{bmatrix} u_1^2 & u_{1,2} & \dots & u_{1,n} \\ u_{1,2} & u_2^2 & \dots & u_{2,n} \\ \vdots & \vdots & \ddots & \vdots \\ u_{1,n} & u_{2,n} & \dots & u_n^2 \end{bmatrix} \tag{6.9}$$

where u_i^2 and $u_{i,j}$ are, respectively, the variance of the ith observation and the covariance between the ith and the jth observations. We hereby describe three possible choices for the weight matrix all of which are constructed from the empirical covariance matrix.

(i) When all data are presumed equivalent, i.e., experimental uncertainties and correlations are ignored, the weight matrix is simply the identity, $\mathbf{W}_1$=**I**. This corresponds to the homoscedastic hypothesis.

(ii) While neglecting correlations and only considering experimental uncertainties, the weight matrix preserves its diagonal form, the ith element being the inverse uncertainty squared associated with the ith binding energy, i.e., u_i^{-2}. Accordingly, the weight matrix is in fact the inverse of the empirical variance matrix, i.e., $\mathbf{W}_2$=**EVM**$[\mathbf{y}_{\rm Exp}]^{-1}$. Thus, in this particular weighing scheme, data having larger uncertainties lose their influence over the regression.

(iii) Finally, the inclusion of correlations along with uncertainties leads to the weight matrix, $\mathbf{W}_3$=**ECM**$[\mathbf{y}_{\rm Exp}]^{-1}$. This weighing scheme incorporates every single empirical evidence at our disposal. Data having larger uncertainties or being correlated, both lose their leverage over the regression. The latter is important such that no over-counting of information occurs.

6.1.5 Secondary results

Here, weighted regression (cf. Sect. 5.2.2) is applied in order to determine the uncertainties and the correlations in the parameters entering the model. A special attention is directed towards the choices of empirical weights and their effects on the outcomes.

The subsequent results are based on the nuclear binding energies deduced from the atomic mass excesses found in Refs. [83, 84] for all nuclei satisfying N,Z $\geq$ 8 with uncertainties below 150 keV and present in the empirical covariance matrix. Thus, a total of 1088 nuclei were considered.

6.1.5.1 The parameters

The parameters obtained using weighted regression are presented in Table 6.6 with the corresponding uncertainties, deduced from the diagonal elements of the covariance matrix, cf. Eq. (5.55), given in the appendix at the end of this section (cf. Sect. 6.1.8).

Table 6.6: The parameters along with their uncertainties and relative uncertainties as determined using the regressions (i), (ii) and (iii).

		$\hat{p}_1$	$\hat{p}_2$	$\hat{p}_3$	$\hat{p}_4$	$\hat{p}_5$	$\hat{p}_6$	$\hat{p}_7$	$\hat{p}_8$
$\hat{p}$ [MeV]	$\mathbf{W}_1$	15.343	-27.034	-16.980	27.423	-0.698	0.840	-0.669	1.365
	$\mathbf{W}_2$	15.651	-44.040	-19.340	118.319	-0.683	1.188	-0.070	12.130
	$\mathbf{W}_3$	15.599	-38.012	-18.540	87.799	-0.690	0.739	-0.445	9.858
$\hat{u}(\hat{p})$ [MeV]	$\mathbf{W}_1$	0.025	0.141	0.087	0.633	0.001	0.045	0.060	0.255
	$\mathbf{W}_2$	0.020	0.635	0.162	3.820	0.002	0.130	0.110	0.401
	$\mathbf{W}_3$	0.016	0.531	0.159	3.488	0.002	0.151	0.117	0.385
$\lvert\hat{u}(\hat{p})/\hat{p}\rvert$ [%]	$\mathbf{W}_1$	0.2	0.5	0.5	2.3	0.2	5.3	8.9	18.7
	$\mathbf{W}_2$	0.1	1.4	0.8	3.2	0.3	11.0	157.6	3.3
	$\mathbf{W}_3$	0.1	1.4	0.9	4.0	0.2	20.4	26.3	3.9

Since the sets of nuclei involved are not identical, the parameters obtained with the regression (i) differ from those obtained in Sect. 6.1.3.1. The inclusion of experimental uncertainties, i.e., regressions (ii) and (iii), changes the weight of each nucleus, thus, influencing the values taken by the parameters. In particular, p_2, p_4, p_7 and p_8 suffer dramatic changes and correspond to isospin dependent terms. On the one hand, exotic nuclei, characterized by larger isospins, have larger uncertainties and therefore, loose their influence over the regression. On the other hand, p_1 and p_5 are quite stable as the volume and Coulomb terms are constrained by larger number of nuclei, i.e., all nuclei independently of their isospin. The prior argument is supported by the Fig. 6.7 proving that exotic nuclei have larger uncertainties. Furthermore, the distribution of the uncertainties presented in Fig. 6.8 is very peaked around the origin where nearly half of the sample is grouped. Combining the conclusions drawn from Figs. 6.7 and 6.8 demonstrates that exotic nuclei should significantly loose their influence over the regressions (ii) and (iii). Also note that the inclusion of experimental covariances seems to reduce the effects of the experimental uncertainties, consequently, the departure away from the results obtained with the homoscedastic regression (i) is diminished.

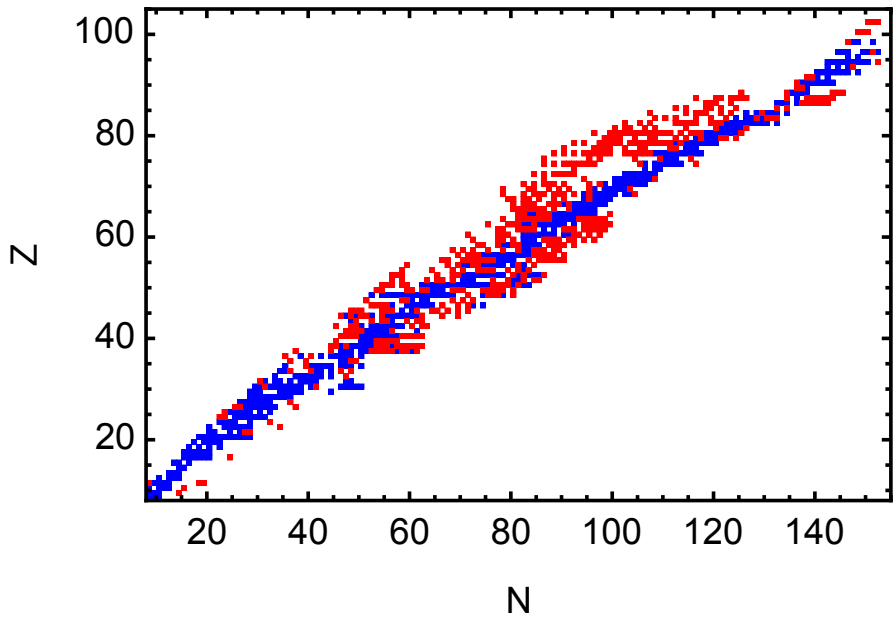

Figure 6.7: The 1088 nuclei involved in the study were divided into two equal groups each containing 544 nuclei. The first group (blue) includes those having a binding energy uncertainty below 2.6 keV while the second (red) contains those having a binding energy uncertainty above 2.6 keV. The second group is composed of more exotic nuclei than the first group.

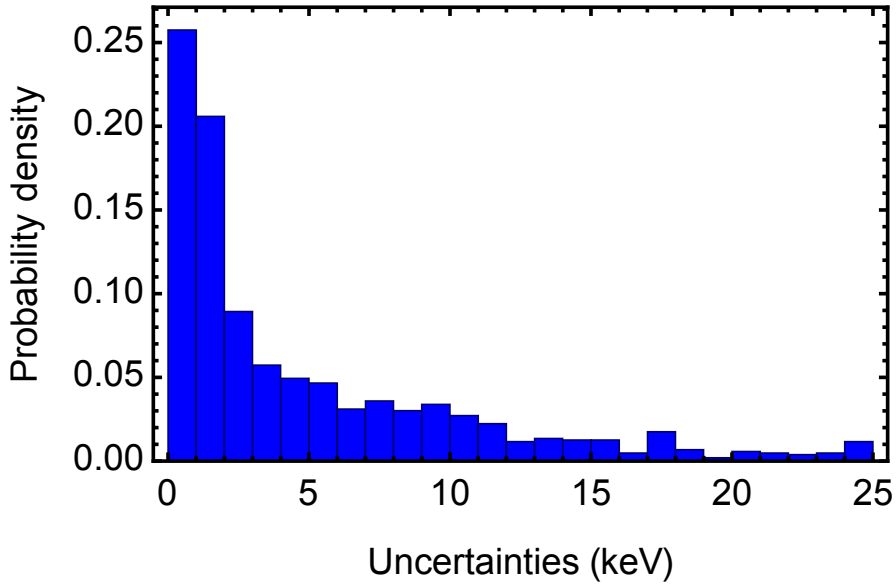

Figure 6.8: Histogram formed of 25 bins, representing distribution of the binding energies uncertainties, restricted to the range [0;25] keV and including 1029 nuclei. A fourth of the 1088 nuclei have uncertainties below 1 keV and half below 2.6 keV.

A cautious analysis of the correlation matrices, given in Tables 6.7, 6.8 and 6.9, shows, in the case of homoscedastic regression (i), the same two correlation groups as in Sect. 6.1.3.1. The first involving p_1, p_3, p_5 and p_7 and the second implicating p_2, p_4 and p_8 while p_6 is almost uncorrelated with the other parameters. These two groups communicate mostly through the incursions of p_1 in the second group and p_8 in the first group. For both regressions (ii) and (iii), two groups can also be distinguished, a weakly correlated first group consisting of p_1, p_5 and a second with stronger correlations containing all of the six remaining parameters. In both cases, the two groups are well separated and are not coupled through decisive correlations, i.e., there are no intruders. Notice regression (i) leads to overall weaker correlations than regression (iii) which, itself, leads to weaker correlations than regression (ii). Thus, the empirical evidence, contained in the weight matrices, seems to globally strengthen the correlations and to change the group structure.

Table 6.7: Correlation matrix deduced from the covariance matrix, cf. Table 6.13, with regression (i). Notations: **group 1**, *group 2* and intruders.

$\hat{p}_1$	$\hat{p}_2$	$\hat{p}_3$	$\hat{p}_4$	$\hat{p}_5$	$\hat{p}_6$	$\hat{p}_7$	$\hat{p}_8$
1.00	-0.75	**-0.94**	0.52	**-0.89**	-0.27	**0.76**	0.88
-0.75	*1.00*	0.67	*-0.92*	0.47	0.44	-0.43	*-0.90*
-0.94	0.67	**1.00**	-0.55	**0.96**	-0.07	**-0.84**	-0.79
0.52	*-0.92*	-0.55	*1.00*	-0.32	-0.18	0.33	*0.74*
-0.89	0.47	**0.96**	-0.32	**1.00**	-0.16	**-0.83**	-0.65
-0.27	0.44	-0.07	-0.18	-0.16	1.00	0.17	-0.44
0.76	-0.43	**-0.84**	0.33	**-0.83**	0.17	**1.00**	0.55
0.88	*-0.90*	-0.79	*0.74*	-0.65	-0.44	0.55	*1.00*

Table 6.8: Correlation matrix deduced from the covariance matrix, cf. Table 6.14, with regression (ii). Notations: **group 1** and *group 2*.

$\hat{p}_1$	$\hat{p}_2$	$\hat{p}_3$	$\hat{p}_4$	$\hat{p}_5$	$\hat{p}_6$	$\hat{p}_7$	$\hat{p}_8$
1.00	-0.42	-0.58	0.37	**-0.76**	0.20	0.44	0.54
-0.42	*1.00*	*0.91*	*-0.99*	0.17	*-0.85*	*-0.88*	*-0.94*
-0.58	*0.91*	*1.00*	*-0.94*	0.47	*-0.91*	*-0.97*	*-0.99*
0.37	*-0.99*	*-0.94*	*1.00*	-0.22	*0.92*	*0.92*	*0.96*
-0.76	0.17	0.47	-0.22	**1.00**	-0.26	-0.33	-0.38
0.20	*-0.85*	*-0.91*	*0.92*	-0.26	*1.00*	*0.94*	*0.90*
0.44	*-0.88*	*-0.97*	*0.92*	-0.33	*0.94*	*1.00*	*0.98*
0.54	*-0.94*	*-0.99*	*0.96*	-0.38	*0.90*	*0.98*	*1.00*

Table 6.9: Correlation matrix deduced from the covariance matrix, cf. Table 6.15, with regression (iii). Notations: **group 1** and *group 2*.

$\hat{p}_1$	$\hat{p}_2$	$\hat{p}_3$	$\hat{p}_4$	$\hat{p}_5$	$\hat{p}_6$	$\hat{p}_7$	$\hat{p}_8$
1.00	-0.37	-0.32	0.25	**-0.71**	-0.00	0.04	0.26
-0.37	*1.00*	*0.90*	*-0.98*	0.39	*-0.79*	*-0.80*	*-0.91*
-0.32	*0.90*	*1.00*	*-0.95*	0.56	*-0.94*	*-0.95*	*-0.99*
0.25	*-0.98*	*-0.95*	*1.00*	-0.41	*0.89*	*0.90*	*0.96*
-0.71	0.39	0.56	-0.41	**1.00**	-0.41	-0.39	-0.48
-0.00	*-0.79*	*-0.94*	*0.89*	-0.41	*1.00*	*0.99*	*0.94*
0.04	*-0.80*	*-0.95*	*0.90*	-0.39	*0.99*	*1.00*	*0.96*
0.26	*-0.91*	*-0.99*	*0.96*	-0.48	*0.94*	*0.96*	*1.00*

6.1.5.2 The observables

The set of observables considered in Sect. 6.1.3.2 is reexamined with special care regarding the impact of empirical weights on predictions as well as uncertainties. The same statistical indicators are summarized in Table 6.10.

In the case of the homoscedastic regression (i), the regression encompasses a reduced number of nuclei and leads to a smaller root-mean-square deviation than in the primary analysis. Since it is no longer the quantity being minimized, the RMS in the heteroscedastics regressions (ii) and (iii) are far larger than in the homoscedastic regression (i). On the other hand, the uncertainties in the predictions of the model are larger for the homoscedastic regression (i). A closer look at Table 6.10 shows a different outcome regarding regressions (ii) and (iii) where the binding energy exhibits the worst predictions as well as the most uncertain ones, i.e., associated with the largest RMS and mean uncertainty.

Analyzing the values obtained for the RMS, shows that regression (iii) yields systematically superior predictions than regression (ii).

Table 6.10: The root-mean-square deviation (RMS) as well as the mean of the uncertainties (MU) are calculated for various observables and for the regressions (i), (ii) and (iii).

		$\hat{B}_{Th}$	$\hat{S}_n$	$\hat{S}_{2n}$	$\hat{S}_p$	$\hat{S}_{2p}$	$\hat{Q}_\alpha$	$\hat{Q}_\beta$
MU [keV]	$\mathbf{W}_1$	42	8	14	11	19	7	17
	$\mathbf{W}_2$	258	35	68	53	106	42	86
	$\mathbf{W}_3$	296	29	55	42	83	33	68
RMS [keV]	$\mathbf{W}_1$	524	1333	1158	1394	986	1371	1758
	$\mathbf{W}_2$	4841	1480	1658	1670	1918	1500	2261
	$\mathbf{W}_3$	2365	1371	1267	1465	1165	1400	1891

6.1.5.3 Secondary comments

Although the weights considered did not improve the adjustment of the model, incoming theoretical developments, leading to enhanced model precision and the future, large scale, mass measurements campaigns, will further increase the importance of empirical uncertainties and correlations, consequently, weighted regression should replace standard regression. Moreover, uncertainties in microscopic corrections are expected to be highly correlated, therefore, when available, their inclusion will require the use of regression (iii). Finally, as the parameters seem to be better constrained and the corresponding predictions are more accurate, the present work seems to suggest that employing regression (iii) may be preferable to using regression (ii).

Note that the weights used in the present study penalize the least precise data which are associated with more exotic nuclei. For a detailed discussion about the importance of exotic nuclei in the adjustment of a relativistic mean field model based on a few selected masses see Ref. [86]. Alternatively, Ref. [80] examines the adjustment of an EDF, based on a larger number of masses and investigates the effects of adding exotic nuclei to the adjustment of the functional.

6.1.6 Conclusion

Standard regression analysis was applied to the liquid drop model which lead us to the covariance of the parameters and more precisely, to their uncertainties and correlations which were then propagated onto observables, thus, providing all of the elements for a thorough uncertainty analysis.

The first part of the present work confirms the presence of strong correlations between the parameters and furthermore, the emergence of correlation groups, i.e., involving many parameters and coupled together through the intrusion of members of other groups. It was also shown that although some parameters are better constrained than others, once the microscopic corrections are fixed, the experimental evidence leaves hardly any room for macroscopic variability, consequently, further research must be focused on constraining microscopic corrections in order to improve the model as a whole.

The second part focuses on the influence of empirical uncertainties and correlations on the results obtained in the first part of the study. The errors being much greater than the empirical variances or covariances, the weights did not improve the adjustment of the model. Nevertheless, it was shown that the inclusion of empirical correlations yields more suitable results than those obtained only accounting for experimental uncertainties. With future experimental and theoretical achievements, weighted regression, involving empirical correlations, will prove to be more attractive than only considering experimental uncertainties. This method opens the doors to the inclusion of uncertainties associated with the microscopic corrections which are expected to be highly correlated.

Independently of the method, uncertainties in the error of the model are far larger than the uncertainties in the liquid drop model. The extent of our uncertainty analysis, i.e., neglecting pairing and shell corrections, may be too coarse to properly describe the uncertainties of the entire “macroscopic-microscopic” model. Moreover, the coherence, between the macroscopic and microscopic contributions, can only be achieved if the same deformation is assumed for both of these components.

In this development, this coherence was lost, as the macroscopic model considered above, bears no deformation while microscopic corrections do, thus making the two contributions inconsistent with one another. Furthermore, the present work disregards any uncertainty or correlation for either the shell or the pairing corrections and are hereby, presumed, independent of the macroscopic component. As such, all of the conclusions drawn from this analysis were reached consciously neglecting these inconsistencies and we will try to correct some of these in following chapter.

6.1.7 Appendix: Covariance of primary results

In this appendix, the covariance between the parameters, obtained from regression analysis using Eq. (5.44), are provided in their matrix form. These results correspond to those contained in the first part of the present study.

In the case of the model without an intercept, the correlations between the parameters, presented in Table 6.2, can be deduced from the covariance matrix given Table 6.11, using Eq. (5.45).

Table 6.11: Covariance matrix between the parameters for the model without intercept.

$\hat{p}_1$	$\hat{p}_2$	$\hat{p}_3$	$\hat{p}_4$	$\hat{p}_5$	$\hat{p}_6$	$\hat{p}_7$	$\hat{p}_8$
0.0002112255	-0.0008757963	-0.0006794524	0.0025757144	-0.0000102194	-0.0001320633	0.0003152269	0.0020147598
-0.0008757963	0.0071133452	0.0026224132	-0.0293433212	0.0000265519	0.0012374354	-0.0005926571	-0.0124508863
-0.0006794524	0.0026224132	0.0025454952	-0.0092533611	0.0000386468	-0.0000681243	-0.0012004781	-0.0059446316
0.0025757144	-0.0293433212	-0.0092533611	0.1441782758	-0.0000678873	-0.0027366304	0.0007282969	0.0460073012
-0.0000102194	0.0000265519	0.0000386468	-0.0000678873	0.0000006481	-0.0000035655	-0.0000200434	-0.0000701814
-0.0001320633	0.0012374354	-0.0000681243	-0.0027366304	-0.0000035655	0.0008284236	0.0001229168	-0.0026805039
0.0003152269	-0.0005926571	-0.0012004781	0.0007282969	-0.0000200434	0.0001229168	0.0008585116	0.0019737292
0.0020147598	-0.0124508863	-0.0059446316	0.0460073012	-0.0000701814	-0.0026805039	0.0019737292	0.0286534371

In the case of the model with an intercept, the correlations between the parameters, presented in Table 6.5, can be deduced from the covariance matrix given Table 6.12, using Eq. (5.45).

Table 6.12: Covariance matrix between the parameters for the model with an intercept.

$\hat{p}_0$	$\hat{p}_1$	$\hat{p}_2$	$\hat{p}_3$	$\hat{p}_4$	$\hat{p}_5$	$\hat{p}_6$	$\hat{p}_7$	$\hat{p}_8$
0.1254667086	0.0044991307	-0.0127792513	-0.0273692844	0.0595335998	-0.0002367796	0.0060480260	-0.0039936493	-0.0132486054
0.0044991307	0.0003708226	-0.0013268437	-0.0016553016	0.0046893470	-0.0000186260	0.0000859004	0.0001694244	0.0015230991
-0.0127792513	-0.0013268437	0.0083564328	0.0053885001	-0.0351656109	0.0000504503	0.0006112401	-0.0001810128	-0.0109990240
-0.0273692844	-0.0016553016	0.0053885001	0.0084948821	-0.0221638752	0.0000899799	-0.0013868790	-0.0003194269	-0.0030056724
0.0595335998	0.0046893470	-0.0351656109	-0.0221638752	0.1712405408	-0.0001796800	0.0001556571	-0.0011726707	0.0393423395
-0.0002367796	-0.0000186260	0.0000504503	0.0000899799	-0.0001796800	0.0000010896	-0.0000149500	-0.0000123417	-0.0000446014
0.0060480259	0.0000859004	0.0006112401	-0.0013868790	0.0001556571	-0.0000149500	0.0011131480	-0.0000706053	-0.0032970883
-0.0039936493	0.0001694244	-0.0001810128	-0.0003194269	-0.0011726707	-0.0000123417	-0.0000706053	0.0009785672	0.0023791976
-0.0132486054	0.0015230991	-0.0109990240	-0.0030056724	0.0393423395	-0.0000446014	-0.0032970883	0.0023791976	0.0298166653

6.1.8 Appendix: Covariance of secondary results

In this appendix, the covariance between the parameters, obtained from weighted regression analysis using Eq. (5.55), are provided in their matrix form. These results correspond to those contained in the second part of the present study, using the regressions i, ii and iii which were defined in Sect. 6.1.4.

The correlations between the parameters, presented in Table 6.7, can be deduced from the covariance matrix given Table 6.13, using Eq. (5.45).

Table 6.13: Covariance matrix between the parameters using regression (i).

$\hat{p}_1$	$\hat{p}_2$	$\hat{p}_3$	$\hat{p}_4$	$\hat{p}_5$	$\hat{p}_6$	$\hat{p}_7$	$\hat{p}_8$
0.0006082522	-0.0025984253	-0.0020193653	0.0081677050	-0.0000304887	-0.0002948485	0.0011131294	0.0055410398
-0.0025984253	0.0199312841	0.0082768795	-0.0824713403	0.0000920849	0.0027833281	-0.0036521942	-0.0322768133
-0.0020193653	0.0082768795	0.0076229685	-0.0306027904	0.0001158646	-0.0002666849	-0.0043696777	-0.0176287206
0.0081677050	-0.0824713403	-0.0306027904	0.4000871096	-0.0002827051	-0.0051879688	0.0123767162	0.1200788307
-0.0000304887	0.0000920849	0.0001158646	-0.0002827051	0.0000019082	-0.0000097643	-0.0000681658	-0.0002287967
-0.0002948485	0.0027833281	-0.0002666849	-0.0051879688	-0.0000097643	0.0019854801	0.0004409849	-0.0050006166
0.0011131294	-0.0036521942	-0.0043696777	0.0123767162	-0.0000681658	0.0004409849	0.0035569094	0.0082877888
0.0055410398	-0.0322768133	-0.0176287206	0.1200788307	-0.0002287967	-0.0050006166	0.0082877888	0.0649826247

The correlations between the parameters, presented in Table 6.8, can be deduced from the covariance matrix given Table 6.14, using Eq. (5.45).

Table 6.14: Covariance matrix between the parameters using regression (ii).

$\hat{p}_1$	$\hat{p}_2$	$\hat{p}_3$	$\hat{p}_4$	$\hat{p}_5$	$\hat{p}_6$	$\hat{p}_7$	$\hat{p}_8$
0.0003819971	-0.0052531624	-0.0018352767	0.0277998983	-0.0000260665	0.0004993266	0.0009365340	0.0042188415
-0.0052531624	0.4034694831	0.0940782882	-2.3921066309	0.0001885700	-0.0699538700	-0.0617906364	-0.2389822932
-0.0018352767	0.0940782882	0.0262915121	-0.5825888711	0.0001329309	-0.0191423309	-0.0173332023	-0.0645221741
0.0277998983	-2.3921066309	-0.5825888711	14.5912280071	-0.0014604903	0.4572853381	0.3881599979	1.4663478275
-0.0000260665	0.0001885700	0.0001329309	-0.0014604903	0.0000030415	-0.0000600708	-0.0000636914	-0.0002641005
0.0004993266	-0.0699538700	-0.0191423309	0.4572853381	-0.0000600708	0.0169847741	0.0134145574	0.0472166671
0.0009365340	-0.0617906364	-0.0173332023	0.3881599979	-0.0000636914	0.0134145574	0.0121098120	0.0431063890
0.0042188415	-0.2389822932	-0.0645221741	1.4663478275	-0.0002641005	0.0472166671	0.0431063890	0.1604514629

The correlations between the parameters, presented in Table 6.9, can be deduced from the covariance matrix given Table 6.15, using Eq. (5.45).

Table 6.15: Covariance matrix between the parameters using regression (iii).

$\hat{p}_1$	$\hat{p}_2$	$\hat{p}_3$	$\hat{p}_4$	$\hat{p}_5$	$\hat{p}_6$	$\hat{p}_7$	$\hat{p}_8$
0.0002444162	-0.0030966569	-0.0007898135	0.0138980286	-0.0000171969	-0.0000074066	0.0000744017	0.0015884903
-0.0030966569	0.2820927098	0.0756541571	-1.8124261615	0.0003224603	-0.0631928071	-0.0495966682	-0.1865929987
-0.0007898135	0.0756541571	0.0252066878	-0.5265266243	0.0001383686	-0.0225791476	-0.0176880512	-0.0607295316
0.0138980286	-1.8124261615	-0.5265266243	12.1680573525	-0.0021906101	0.4706768938	0.3653808853	1.2958749960
-0.0000171969	0.0003224603	0.0001383686	-0.0021906101	0.0000023828	-0.0000955509	-0.0000702254	-0.0002826310
-0.0000074066	-0.0631928071	-0.0225791476	0.4706768938	-0.0000955509	0.0227856426	0.0174302753	0.0548222841
0.0000744017	-0.0495966682	-0.0176880512	0.3653808853	-0.0000702254	0.0174302753	0.0136646136	0.0432448396
0.0015884903	-0.1865929987	-0.0607295316	1.2958749960	-0.0002826310	0.0548222841	0.0432448396	0.1484077708

6.2 Constraining shell correction energies

We have just studied the uncertainties in a simple macroscopic model. In this analysis the uncertainties in the shell corrections were neglected. However, it turns out that these shell corrections are crucial contributions in ground-state masses as well as fission-barrier calculations of superheavy nuclei. Therefore, based on our previous uncertainty analysis of the liquid drop model, we describe a method in to order to constrain the shell corrections of superheavy nuclei. In turn, this provides a test to verify that the macroscopic and microscopic contributions are consistent with one another. The following study has been submitted for publication [87].

6.2.1 Introduction

The existence of superheavy nuclei (SHN) can only be explained by the introduction of stabilizing ground-state shell effects. In addition to ground-state properties, shell effects strongly influence the fission barriers which insure the survival of the compound nucleus. Therefore, shell effects play a crucial role in our understanding of both the structure and the production of SHN.

As discussed in Ref. [88], shell corrections can be obtained from a broad spectrum of models. However, the results are ultimately dispersed, thus proving the compelling need to find suitable experimental constraints. Furthermore, these additional quantum effects are included in various ways within the few theoretical approaches at hand. This leads to discrepancies of few MeVs in the fission barriers calculations [39]. In turn, these discrepancies also result in critical changes of the survival probability, and therefore, on the production cross-section of SHN [38].

Given that masses are very sensitive to structural properties, they contain an impressive amount of insight about shell effects. However, most SHN masses are not precisely known. Nevertheless, assuming that the last mass in an α decay chain is well-established, masses can be deduced from measured Q_α-values of decaying nuclei. In particular, we focus our study on the decay chains:

$$^{291}_{116}\mathrm{Lv} \rightarrow {}^{287}_{114}\mathrm{Fl} \rightarrow {}^{283}_{112}\mathrm{Cn} \rightarrow {}^{279}_{110}\mathrm{Ds} \rightarrow {}^{275}_{108}\mathrm{Hs} \rightarrow {}^{271}_{106}\mathrm{Sg} \rightarrow {}^{267}_{104}\mathrm{Rf}$$

$$^{277}_{112}\mathrm{Cn} \rightarrow {}^{273}_{110}\mathrm{Ds} \rightarrow {}^{269}_{108}\mathrm{Hs} \rightarrow {}^{265}_{106}\mathrm{Sg} \rightarrow {}^{261}_{104}\mathrm{Rf} \rightarrow {}^{257}_{102}\mathrm{No}$$

The first following from a hot-fusion reaction and the second from a cold-fusion one.

On the grounds that macroscopic-microscopic (MM) models incorporate many structure effects, they provide the most accurate mass predictions. The MM masses are the sum of a macroscopic liquid drop (LD) energy contribution and a microscopic shell correction energy (SCE) contribution which are obtained from single-particle spectra using the Strutinsky method [72, 73]. In a similar way, SCE can be inferred by subtracting the LD contribution to the experimental mass. In order to procure realistic results, the LD model should, itself, be fitted using theoretical SCE. From this, it is clear that the SCE deduced from the subtraction of LD contribution to the experimental mass, will depend on both the chosen theoretical SCE and LD model.

In the following, we repeat the study done in Ref. [88] including a detailed uncertainty analysis of the experimental masses and more importantly, of the LD masses [71]. Considering these uncertainties delivers decisive theoretical constraints on SCE. In addition to the SCE and their uncertainties, we provide correlation matrices for experimental and LD masses, as well as for SCE for all nuclei in the studied decay chains. In order to fully comply with international standards, the formulas needed to compute uncertainties, covariances and correlations were taken from Refs. [64, 65].

Table 6.16: Table containing the results concerning the first decay chain along with their uncertainties. The Q_α-values and their uncertainties were taken from Ref. [89] and $\Delta m^{Exp}(^{267}\mathrm{Rf})$ from Refs. [83, 84]. The last column gives the theoretical SCE taken from Refs. [57, 90]. All quantities are given in MeV.

Nuclei	Q_α	Δm^{Exp}	Δm^{LD}	SCE	SCE from refs. [57, 90]
$^{267}_{104}$Rf	-	*113.440±0.580*	117.140±0.059	-3.700±0.583	*-5.08*
$^{271}_{106}$Sg	*8.67±0.08*	124.535±0.585	128.126±0.063	-3.591±0.589	*-5.18*
$^{275}_{108}$Hs	*9.44±0.06*	136.400±0.589	139.725±0.068	-3.325±0.592	*-4.90*
$^{279}_{110}$Ds	*9.84±0.06*	148.665±0.592	151.929±0.074	-3.264±0.596	*-4.91*
$^{283}_{112}$Cn	*9.67±0.06*	160.760±0.595	164.731±0.081	-3.971±0.600	*-6.19*
$^{287}_{114}$Fl	*10.16±0.06*	173.345±0.598	178.124±0.090	-4.779±0.604	*-7.74*
$^{291}_{116}$Lv	*10.89±0.07*	186.659±0.602	192.101±0.099	-5.442±0.610	*-8.07*

Table 6.17: Table containing the results concerning the second decay chain along with their uncertainties. The Q_α-values and their uncertainties were deduced from the α particle's energies presented in Ref. [91] and $\Delta m^{Exp}(^{257}\mathrm{No})$ from Refs. [83, 84]. The last column gives the theoretical SCE taken from Refs. [57, 90]. All quantities are given in MeV.

Nuclei	Q_α	Δm^{Exp}	Δm^{LD}	SCE	SCE from refs. [57, 90]
$^{257}_{102}$No	-	*90.247±0.007*	94.833±0.049	-4.586±0.050	*-5.77*
$^{261}_{104}$Rf	*8.65±0.02*	101.322±0.021	106.075±0.054	-4.753±0.058	*-6.79*
$^{265}_{106}$Sg	*8.84±0.03*	112.587±0.037	117.918±0.061	-5.331±0.071	*-6.38*
$^{269}_{108}$Hs	*9.35±0.02*	124.362±0.042	130.357±0.068	-5.995±0.080	*-5.30*
$^{273}_{110}$Ds	*11.31±0.02*	138.097±0.046	143.383±0.076	-5.286±0.089	*-4.34*
$^{277}_{112}$Cn	*11.42±0.02*	151.942±0.050	156.991±0.085	-5.049±0.099	*-4.11*

6.2.2 Experimental mass excess

Most SHN masses are not precisely known. Nevertheless, assuming the last mass in an α decay chain is known, masses can be deduced from measured Q_α-values:

$$\Delta m^{Exp}(A,Z) = \Delta m^{Exp}(A-4,Z-2) + Q_\alpha(A,Z) + \Delta_\alpha \tag{6.10}$$

where $\Delta m^{Exp}(A,Z)$ and $Q_\alpha(A,Z)$ are respectively the mass excess of the mother nucleus and the Q_α-value of the α decay. The quantity $\Delta m^{Exp}(A-4,Z-2)$ is the mass excess of the daughter nucleus and Δ_α is the α particle's mass excess. In particular, knowing the Q_α-values for all nuclei in the decay chain and the mass excess of the last nucleus, here $\Delta m^{Exp}(^{267}\mathrm{Rf})$ or $\Delta m^{Exp}(^{257}\mathrm{No})$, we can deduce all masses within the decay chain. In the present work, it is assumed that the measured Q_α-values correspond to transitions from the ground-state of the mother nucleus to the ground-state of daughter nucleus.

In the following, $\Delta m^{Exp}(^{267}\mathrm{Rf})$, $\Delta m^{Exp}(^{257}\mathrm{No})$ and Δ_α are taken from the AME2016 table [83, 84] and the Q_α-values were extracted from Refs. [89, 91]. All of these quantities are given in Tables 6.16 and 6.17 alongside their uncertainties and are assumed to be uncorrelated as they were measured independently. They appear in italic to indicate that they were not obtained in the present work.

As the quantities entering Eq. (6.10) are uncorrelated, the variance can be estimated using the familiar uncertainty propagation formula:

$$u^2\left(\Delta m^{Exp}(A,Z)\right) = u^2\left(Q_\alpha(A,Z)\right) + u^2\left(\Delta_\alpha\right) + u^2\left(\Delta m^{Exp}(A-4,Z-2)\right). \tag{6.11}$$

Apart from $\Delta m^{Exp}(^{267}\mathrm{Rf})$ and $\Delta m^{Exp}(^{257}\mathrm{No})$, all Δm^{Exp} and their uncertainties, shown in Tables 6.16 and 6.17, were calculated using Eqs. (6.10) and (6.11), respectively. Clearly, the dominating uncertainty, for the first decay chain, is the one associated with $\Delta m^{Exp}(^{267}\mathrm{Rf})$. This however, is not the case for the second decay chain where the Q_α-values uncertainties are the dominating ones.

From Eq. (6.10), it is clear that the mass of the mother nucleus depends on the mass of the daughter nucleus. Thus, all experimental masses within a decay chain are correlated. The covariance can be easily obtained,

$$u\left(\Delta m^{Exp}(A,Z), \Delta m^{Exp}(A-4,Z-2)\right) = u^2\left(\Delta m^{Exp}(A-4,Z-2)\right). \tag{6.12}$$

Similarly, all other covariances can be calculated and correlation coefficients can be deduced from these. The results are presented in Tables 6.18 and 6.19. The correlation matrix for the first decay chain, cf. Table 6.18, shows strong positive correlations between the experimental masses. This undoubtedly confirms, the influence of the large uncertainty in $\Delta m^{Exp}(^{267}\mathrm{Rf})$ upon all other experimental masses in the decay chain. The outcome for the second decay chain, cf. Table 6.19, is quite different and shows weak positive correlations between the experimental masses, thus, establishing the limited impact of the small uncertainty in $\Delta m^{Exp}(^{257}\mathrm{No})$ on the experimental masses.

Table 6.18: Experimental mass excess correlation matrix for the first decay chain.

^{267}Rf	^{271}Sg	^{275}Hs	^{279}Ds	^{283}Cn	^{287}Fl	^{291}Lv
1.00	0.99	0.98	0.98	0.97	0.97	0.96
0.99	1.00	0.99	0.98	0.98	0.97	0.97
0.98	0.99	1.00	0.99	0.98	0.98	0.97
0.98	0.98	0.99	1.00	0.99	0.98	0.98
0.97	0.98	0.98	0.99	1.00	0.99	0.98
0.97	0.97	0.98	0.98	0.99	1.00	0.99
0.96	0.97	0.97	0.98	0.98	0.99	1.00

Table 6.19: Experimental mass excess correlation matrix for the second decay chain.

^{257}No	^{261}Rf	^{265}Sg	^{269}Hs	^{273}Ds	^{277}Cn
1.00	0.33	0.19	0.16	0.15	0.13
0.33	1.00	0.57	0.50	0.45	0.41
0.19	0.57	1.00	0.87	0.79	0.72
0.16	0.50	0.87	1.00	0.90	0.82
0.15	0.45	0.79	0.90	1.00	0.91
0.13	0.41	0.72	0.82	0.91	1.00

6.2.3 Liquid drop mass excess

The LD contribution to the mass can be deduced from the binding energy using the specific LD model we have previously used in the last section, cf. Eq. (6.2) in Sect. 6.1. However, here the average pairing in also adjusted and reads:

$$E_{pair} = \begin{cases} \frac{p_9}{N^{\frac{1}{3}}} + \frac{p_{10}}{Z^{\frac{1}{3}}} + \frac{p_{11}}{A^{\frac{2}{3}}} + \frac{p_{12}}{A} & \text{N=Z, odd} \\ \frac{p_9}{N^{\frac{1}{3}}} + \frac{p_{10}}{Z^{\frac{1}{3}}} + \frac{p_{11}}{A^{\frac{2}{3}}} & \text{N and Z, odd} \\ \frac{p_{10}}{Z^{\frac{1}{3}}} & \text{N even, Z odd} \\ \frac{p_9}{N^{\frac{1}{3}}} & \text{N odd, Z even} \\ 0 & \text{N even, Z even.} \end{cases} \tag{6.13}$$

In fact, the LD from Eq. (6.2) is fitted upon experimental masses with added theoretical shell corrections. As before, the experimental masses were taken from the AME2016 table [83, 84] and the theoretical SCE from the Thomas-Fermi model [57, 90]. As the sole existence of SHN is based on shell effects, the addition of theoretical SCE to experimental masses is certainly required. The detailed fitting method has been presented in the previous section (cf. Sect. 6.1). In this study, the parameters, their uncertainties and correlation matrix, obtained as in the previous section, are reported in the appendix at the end of this section (cf. Sect. 6.2.6). The LD contributions to the masses of the nuclei entering an α decay chain, are established with the same formula and parameters, consequently, they are very strongly correlated. Results for the two decay chains, are presented in Tables 6.16 and 6.17 while the corresponding correlation matrices are exposed in Tables 6.20 and 6.21, respectively.

Table 6.20: Theoretical LD mass excess correlation matrix for the first decay chain.

^{267}Rf	^{271}Sg	^{275}Hs	^{279}Ds	^{283}Cn	^{287}Fl	^{291}Lv
1.00	0.99	0.97	0.94	0.91	0.88	0.84
0.99	1.00	0.99	0.97	0.95	0.93	0.90
0.97	0.99	1.00	0.99	0.98	0.96	0.94
0.94	0.97	0.99	1.00	0.99	0.98	0.97
0.91	0.95	0.98	0.99	1.00	0.99	0.99
0.88	0.93	0.96	0.98	0.99	1.00	0.99
0.84	0.90	0.94	0.97	0.99	0.99	1.00

Table 6.21: Theoretical LD mass excess correlation matrix for the second decay chain.

^{257}No	^{261}Rf	^{265}Sg	^{269}Hs	^{273}Ds	^{277}Cn
1.00	0.99	0.97	0.95	0.92	0.90
0.99	1.00	0.99	0.98	0.96	0.94
0.97	0.99	1.00	0.99	0.98	0.97
0.95	0.98	0.99	1.00	0.99	0.99
0.92	0.96	0.98	0.99	1.00	0.99
0.90	0.94	0.97	0.99	0.99	1.00

6.2.4 Deduced shell correction energies

In Sect. 6.2.2, informations regarding the α decay chains were used to determine Δm^{Exp} and in Sect. 6.2.3, a specific LD model was used to obtain Δm^{LD}. As mentioned in the introduction, SCE can be inferred by subtracting the LD contribution to the experimental masses:

$$SCE = \Delta m^{Exp} - \Delta m^{LD}. \tag{6.14}$$

Notice the two terms entering the right hand side of Eq. (6.14) are independent, thus, SCE uncertainties simply read:

$$u^2\left(SCE\right) = u^2\left(\Delta m^{Exp}\right) + u^2\left(\Delta m^{LD}\right). \tag{6.15}$$

The SCE are given side by side with their uncertainties in Tables 6.16 and 6.17 and contrasting these tables yields the ensuing conclusion. Since the last masses in decay chains, following from hot-fusion reactions, are not precisely known, the corresponding SCE are loosely constrained and certainly, one could assert the opposite for decay chains subsequent to cold-fusion reactions. Nevertheless, climbing-up the decay chain, the uncertainties in the SCE tend to grow, reaching their maximum for the mother nucleus. This is a direct consequence of the increasing number of Q_α-values involved, along with their uncertainties, and causing the escalation of uncertainties in the SCE.

As discussed in Sects. 6.2.2 and 6.2.3, the values taken by Δm^{Exp} and Δm^{LD} for various nuclei are correlated. Accordingly, this is also the case for SCE of all nuclei in a decay chain. As for the experimental and LD masses, we can construct the SCE correlation matrices given in Tables 6.22 and 6.23. Notice in the case of the first decay chain that the correlations regarding experimental masses, cf. Table 6.18, and those concerning SCE, cf. Table 6.22, are very resemblant. This can be interpreted as coming from the uncertainty in $\Delta m^{Exp}(^{267}\mathrm{Rf})$ which plainly prevails over all other sources of both uncertainties and correlations. However, in the case of the second decay chain, Tables 6.19 and 6.23 do not share this similarity. This can be understood as coming from the minute uncertainty associated with $\Delta m^{Exp}(^{257}\mathrm{No})$. Consequently, the SCE correlations may only be explained by the strong correlations between LD masses.

Table 6.22: SCE correlation matrix for the first decay chain.

^{267}Rf	^{271}Sg	^{275}Hs	^{279}Ds	^{283}Cn	^{287}Fl	^{291}Lv
1.00	0.99	0.98	0.97	0.97	0.96	0.96
0.99	1.00	0.99	0.98	0.98	0.97	0.97
0.98	0.99	1.00	0.99	0.98	0.98	0.97
0.97	0.98	0.99	1.00	0.99	0.98	0.98
0.97	0.98	0.98	0.99	1.00	0.99	0.98
0.96	0.97	0.98	0.98	0.99	1.00	0.99
0.96	0.97	0.97	0.98	0.98	0.99	1.00

Table 6.23: SCE correlation matrix for the second decay chain.

^{257}No	^{261}Rf	^{265}Sg	^{269}Hs	^{273}Ds	^{277}Cn
1.00	0.93	0.83	0.81	0.79	0.77
0.93	1.00	0.90	0.87	0.85	0.83
0.83	0.90	1.00	0.96	0.93	0.90
0.81	0.87	0.96	1.00	0.97	0.94
0.79	0.85	0.93	0.97	1.00	0.97
0.77	0.83	0.90	0.94	0.97	1.00

6.2.5 Discussion and conclusion

In the present work, SCE were inferred by subtracting the LD contributions to their corresponding experimental masses. Assuming the last masses entering the decay chains were known, experimental masses were deduced from measured Q_α-values. The LD contributions to the masses were calculated using a specific LD model which was fitted to experimental masses, corrected by theoretical SCE.

Excluding the correlation matrices, all the results gathered in this work are presented in Tables 6.16 and 6.17. Efforts were made to provide uncertainties for every calculated quantity within the present work. Considering these uncertainties brings decisive theoretical constrains on SCE which play a crucial role in our understanding of both the structure and the production of SHN.

As some of the SHN masses, e.g., $\Delta m^{Exp}(^{267}\mathrm{Rf})$, bear considerable uncertainties which plainly prevail over all other sources of both uncertainties and correlations. This study undeniably shows that improved SHN mass measurements are absolutely necessary in order to better constrain SCE. Following up on this idea, reducing the mass uncertainty of the last nucleus in a decay chain to about 50 keV should be enough and any further reduction would be fruitless as the dominating uncertainties would then be coming from measured Q_α-values and the LDM.

Comparing the two last columns of Table 6.16 or 6.17. We conclude that SCE, deduced in the present work, were, in the case of the first decay chain, 2 MeV higher than the theoretical predictions while being only 0.3 MeV higher in the case of the second decay chain. As follows, deduced SCE indicate that SHN are less bound than what was predicted in Refs. [57,90]. However, one should be cautious as it should be stressed that MM masses are obtained by minimizing the total sum of the LD energy and the theoretical SCE with respect to deformation. Thus, both the macroscopic and microscopic parts of the MM model are coherently glued together through deformation. As the chosen LD model bears no deformation and the theoretical SCE were obtained independently, this coherence is lost in the present study. Once again, it is clear that the SCE deduced in the present work depend on both the chosen theoretical SCE and LD model.

6.2.6 Appendix: Liquid drop parameters

In this appendix, we present the results relative to the regression analysis of the liquid drop model used in this work, cf. Eqs. (6.2) and (6.13). The model is adjusted to the nuclear binding energies deduced from the atomic mass excesses found in Refs. [83,84] for all nuclei satisfying N,Z $\geq$ 8 with uncertainties below 150 keV, thus, a total of 2315 nuclei are considered.

As previously discussed, the uncertainties in the parameters and the correlations between them, are a direct consequence of the regression hypotheses. According to these hypotheses, the errors follow a Gaussian distribution with zero mean and variance σ^2. This variance can then be propagated onto the parameters leading to their covariances, from which, their uncertainties and correlations can be deduced.

Table 6.24 contains the parameters and their uncertainties while Table 6.25 presents the correlations between the parameters. The detailed regression analysis was exposed in the previous section. However, in the present work, the pairing, cf. Eq. (6.13), is adjusted as well which was not previously done. Nevertheless, the method remains unchanged.

Table 6.24: LDM parameters and uncertainties in MeV [71]. Here RMS= 0.602 MeV.

	p_1	p_2	p_3	p_4	p_5	p_6	p_7	p_8	p_9	p_{10}	p_{11}	p_{12}
Parameters	15.4841	-27.8539	-17.5768	31.2893	-0.7056	0.9107	-0.3071	2.8128	-4.75	-4.68	6.63	12.89
Uncertainties	0.0145	0.0850	0.0507	0.3824	0.0008	0.0294	0.0296	0.1726	0.13	0.12	1.00	6.04

Table 6.25: LDM parameters correlation matrix [71].

p_1	p_2	p_3	p_4	p_5	p_6	p_7	p_8	p_9	p_{10}	p_{11}	p_{12}
1.00	-0.71	-0.92	0.47	-0.87	-0.31	0.73	0.80	0.04	0.03	-0.03	-0.02
-0.71	1.00	0.61	-0.92	0.37	0.52	-0.22	-0.87	-0.03	-0.02	0.01	0.12
-0.92	0.61	1.00	-0.48	0.95	-0.06	-0.80	-0.67	-0.08	-0.07	0.05	-0.04
0.47	-0.92	-0.48	1.00	-0.21	-0.26	0.05	0.72	0.03	0.03	-0.01	-0.12
-0.87	0.37	0.95	-0.21	1.00	-0.17	-0.85	-0.48	-0.04	-0.02	0.03	-0.09
-0.31	0.52	-0.06	-0.26	-0.17	1.00	0.16	-0.57	0.05	0.04	-0.02	0.19
0.73	-0.22	-0.80	0.05	-0.85	0.16	1.00	0.37	-0.03	-0.05	-0.01	0.13
0.80	-0.87	-0.67	0.72	-0.48	-0.57	0.37	1.00	-0.03	-0.03	0.02	-0.19
0.04	-0.03	-0.08	0.03	-0.04	0.05	-0.03	-0.03	1.00	0.45	-0.66	0.06
0.03	-0.02	-0.07	0.03	-0.02	0.04	-0.05	-0.03	0.45	1.00	-0.67	0.07
-0.03	0.01	0.05	-0.01	0.03	-0.02	-0.01	0.02	-0.66	-0.67	1.00	-0.24
-0.02	0.12	-0.04	-0.12	-0.09	0.19	0.13	-0.19	0.06	0.07	-0.24	1.00

Chapter 7

Phenomenological macroscopic-microscopic model

In the previous chapter, we have studied the uncertainties in a simple macroscopic model in order to determine the uncertainties in ground-state masses. However, the previous study neglected shell corrections. Remember that these are crucial contributions to the masses as well as the fission barriers of superheavy nuclei. Furthermore, the simple model we have just considered did not contain any deformation degrees of freedom. Therefore, it is impossible with such a model to determine the saddle-point mass and consequently, the fission barrier. In this chapter, we examine the simplest "macroscopic-microscopic" model. This model includes deformation as well as very phenomenological shell corrections. In turn, this allows us to estimate the uncertainties in the fission barriers. Note that there are more advanced and far superior macroscocopic-microscrocopic fission barrier calculations, cf. Refs. [50, 52]. However, in these models the propagation of uncertainties is rather delicate and complex. Thus, we have decided to start with a simpler model. Finally, let us remember that our final goal is to constrain the formation probability. This is achieved by first constraining the survival probability which was shown to be very sensitive to fission barriers. This is the reason why we focus our attention on the fission barriers uncertainties.

7.1 Introduction

The goal of this chapter is to present one of the simplest "macroscopic-microscopic" model which includes a liquid drop model, shell corrections and deformation. The idea is to present the foundations of the macroscopic-microscopic approach without facing too many technical difficulties. Extensions of this simple model then become fairly easy to understand. What follows is merely a summary as well as an uncertainty analysis of the model described in Ref. [74].

This model is largely based on the liquid drop model which is a macroscopic approach. More precisely, it does not account for individual effects of single nucleons, but, only the altogether statistical behaviour of the system as a whole. Later, it was realized that there were ways to add quantum effects to the liquid drop. This idea gave birth to macroscopic-microscopic approaches which are macroscopic because they are based on the liquid drop and microscopic because they also include quantum mechanical corrections. These corrections are referred to as shell corrections because they originate from what can be viewed as, single-particle shells.

It is possible to include quantum effects by forming allowed bands, from the continuous level density, separated by gaps. When filled, the bands correspond to magic closed-shells. The level scheme with bands is said to be *bunched* and the continuous one is said to be *unbunched*.

Another improvement was the introduction of nuclear deformation. This has consequences on both the macroscopic and microscopic contributions. Macroscopically, volume remains unchanged while the surface and Coulomb contributions may be altered, thus, leading to a change in the macroscopic energy. Microscopically, the energy change is related to the breaking of symmetries due to deformation which in turn changes the degeneracies and alters the gaps between the levels. From this, it is obvious that shell corrections and deformation should be intertwined.

7.2 Liquid drop model

The spherical macroscopic mass formula used in [74] is simply,

$$M(N,Z) = M_N N + M_H Z - c_1 A + c_2 A^{\frac{2}{3}} + c_3 \frac{Z^2}{A^{1/3}} - c_4 \frac{Z^2}{A} + \delta, \tag{7.1}$$

where M_N and M_H are, respectively, the mass excess of the neutron and the hydrogen. The parameters appearing in the previous expression can themselves be expressed as

$$c_1 = a_1 \left[1 - k\left(\frac{N-Z}{A}\right)^2\right], \tag{7.2}$$

$$c_2 = a_2 \left[1 - k\left(\frac{N-Z}{A}\right)^2\right], \tag{7.3}$$

$$c_3 = \frac{3}{5}\frac{e^2}{r_0}, \tag{7.4}$$

$$c_4 = \frac{\pi^2}{2}\left(\frac{d}{r_0}\right)^2 \frac{e^2}{r_0}. \tag{7.5}$$

Such that the spherical macroscopic model includes the historical volume, surface, Coulomb and symmetry terms. The model further includes terms corresponding to surface symmetry, charge diffusion and pairing. Surface symmetry term was introduced by analogy to the original symmetry term. Charge diffusion corrects the Coulomb contribution to account for the continuous decline of proton density across the sharp surface. The corresponding surface-thickness parameter $d = 0.5461$ is assumed to be known from electron-scattering experiments. Finally, the pairing term comes from the empirical evidence that even-even nuclei are more bound than odd mass nuclei which are, themselves, more bound than odd-odd nuclei. This term reads,

$$\delta = \begin{cases} \dfrac{11}{\sqrt{A}} & \text{for } N \text{ and } Z \text{ odd} \\ 0 & \text{for } A \text{ odd} \\ -\dfrac{11}{\sqrt{A}} & \text{for } N \text{ and } Z \text{ even.} \end{cases} \tag{7.6}$$

So far, the constants which are assumed to be known are summarized in Table 7.1 while the adjustable parameters are a_1, k, a_2 and r_0.

Table 7.1: The known constants entering the spherical macroscopic model.

M_H (MeV)	M_N (MeV)	e^2 (MeV·fm)	d (fm)
7.28899	8.07144	1.4399764	0.5461

7.3 Shell corrections

We have described the macroscopic part of the model and now follow through with the microscopic one. So far, no quantum effects have been introduced, however, as previously mentioned, these can be accounted for through shell corrections.

7.3.1 Strutinsky's method

The shell corrections are defined as,

$$\begin{aligned}\Delta E &= \sum_i \epsilon_i(\text{Bunched}) - \sum_i \epsilon_i(\text{Unbunched}) \\ &= E_{\text{Bunched}} - E_{\text{Unbunched}},\end{aligned} \tag{7.7}$$

where the ϵ represent the single-particle energies while the E correspond to the total energies. Thus, the shell corrections are the energy difference between a bunched and an unbunched level scheme. On the one hand, the unbunched level scheme is a smooth distribution of single-particle levels which will be taken to be a degenerate Fermi gas for both protons and neutrons. On the other hand, the bunched level scheme will be constructed from the unbunched one. The bunching procedure consists of grouping together levels of the Fermi gas in order to form allowed bands. Each of the bands constructed through that procedure should, when completely filled, contain a magic number of either protons or neutrons. Nothing forbids the bunched level scheme to be different for neutrons and for protons, however, for simplicity, we will assume that they are the same. Of course, a smooth level distribution corresponds to a classical description while a discrete level distribution corresponds to a quantum description. Therefore, shell corrections can be understood as semi-classical corrections.

It should be mentioned that, although this model seems to follow the original ideas introduced by Strutinsky [72,73], it was built a couple of years before. Furthermore, this model starts from an unbunched level scheme, and, from it, forms the bunched spectrum. Consequently, this implies a more phenomenological approach than starting from a Nilsson level scheme and then constructing the unbunched one through a folding procedure which is, truly, at the heart of Strutinsky's method.

7.3.2 The smooth distribution of single-particles levels

As already mentioned, the unbunched level scheme will be a Fermi gas. We, hereby, recall the expression for the energy of nth neutron in such a gas,

$$\epsilon_n = \frac{\hbar^2}{2m}\left(3\pi^2\frac{n}{V}\right)^{\frac{2}{3}}. \tag{7.8}$$

Therefore, the total energy of N neutrons is simply

$$\begin{aligned} E_{\text{Unbunched}} &= \int_0^N \frac{\hbar^2}{2m}\left(3\pi^2\frac{n}{V}\right)^{2/3}\mathrm{d}n \\ &= \frac{\hbar^2}{2mr_0^2}\left(\frac{9\pi}{4A}\right)^{2/3}\int_0^N n^{2/3}\mathrm{d}n \\ &= \frac{t_N}{N^{2/3}}\int_0^N n^{2/3}\mathrm{d}n, \end{aligned} \tag{7.9}$$

where

$$V = \frac{4}{3}\pi r_0^3 A, \tag{7.10}$$

$$t_N = \frac{\hbar^2}{2mr_0^2}\left(\frac{9\pi}{4}\frac{N}{A}\right)^{\frac{2}{3}}. \tag{7.11}$$

The prior expression reduces to

$$t_F = \frac{\hbar^2}{2mr_0^2}\left(\frac{9\pi}{8}\right)^{\frac{2}{3}}, \tag{7.12}$$

in cases where $N = Z$. This quantity is introduced for practical reasons.

Notice all these relations remain unchanged for protons and can simply be obtained by replacing N by Z in the preceding expressions.

7.3.3 The completely bunched spectrum

The bunched level scheme can be constructed from the smooth distribution of single-particle levels. There are many options regarding that matter, however, the simplest one is retained here. The idea is to group together a set of smoothly distributed levels in order to form a unique energy level. By repeating this procedure, one constructs a set of discrete and degenerate levels, i.e., the bunched spectrum. In a sense, this phenomenological approach leads to the discreteness typically found in quantum mechanics and to the degeneracy characteristic of the spherical shell model and associated with angular momentum. Here, only single-particle levels belonging to the smooth distribution, and lying between levels corresponding to two spherical magic numbers will be part of the same group. This way all the particle numbers between two magic numbers will contribute the same energy. Notice this is not the case in the shell model where major shells are not degenerate, only subshells are. The construction of the bunched spectrum is sketched in Fig. 7.1.

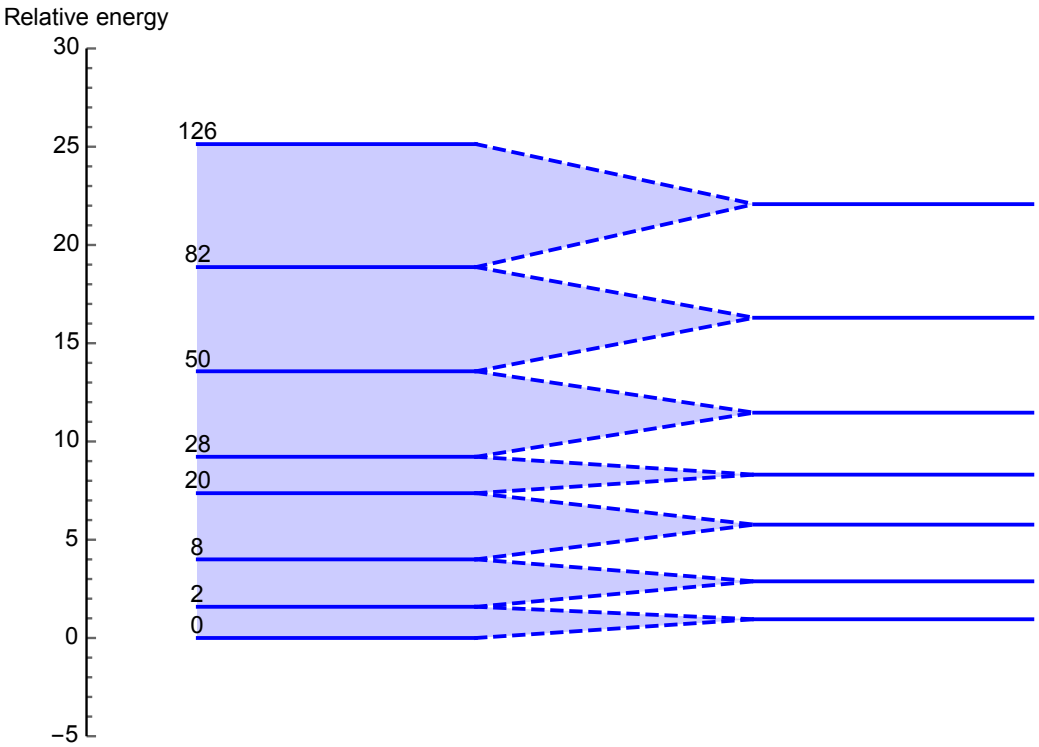

Figure 7.1: On the left, the smooth distribution of single-particle levels along with the corresponding magic numbers. On the right, the discrete and degenerate spectrum resulting from the bunching procedure. In this figure, all energies were divided by $t_N/N^{2/3}$.

Here, these two magic numbers will be labelled, respectively, M_{i-1} and M_i. The resulting single energy will be taken to be the weighted average energy between these two magic numbers. The resulting set of energies can be expressed as

$$t(n) = \frac{t_N}{N^{2/3}} q(n) \quad \text{for} \quad M_{i-1} < n < M_i, \tag{7.13}$$

where $q(n)$, also known as the staircase function, is given by

$$q\,(n) = \frac{\int_{M_{i-1}}^{M_i} n^{2/3} \mathrm{d}n}{\int_{M_{i-1}}^{M_i} \mathrm{d}n} = \frac{3}{5} \frac{M_i^{\frac{5}{3}} - M_{i-1}^{\frac{5}{3}}}{M_i - M_{i-1}} \quad \text{for} \quad M_{i-1} < n < M_i. \tag{7.14}$$

Indeed, this function has the shape of a staircase because it is constant between two magic numbers. Thus, the function $q(n)$ is in fact responsible for the bunching. It is represented Fig 7.2 where it is compared to $n^{2/3}$, describing the smooth distribution of single-particle levels.

Consequently, the total energy of N neutrons in the completely bunched case is simply,

$$E_{\text{Bunched}} = \frac{t_N}{N^{2/3}} \int_0^N q\,(n)\,\mathrm{d}n. \tag{7.15}$$

Again, all these expressions are valid for both protons and neutrons.

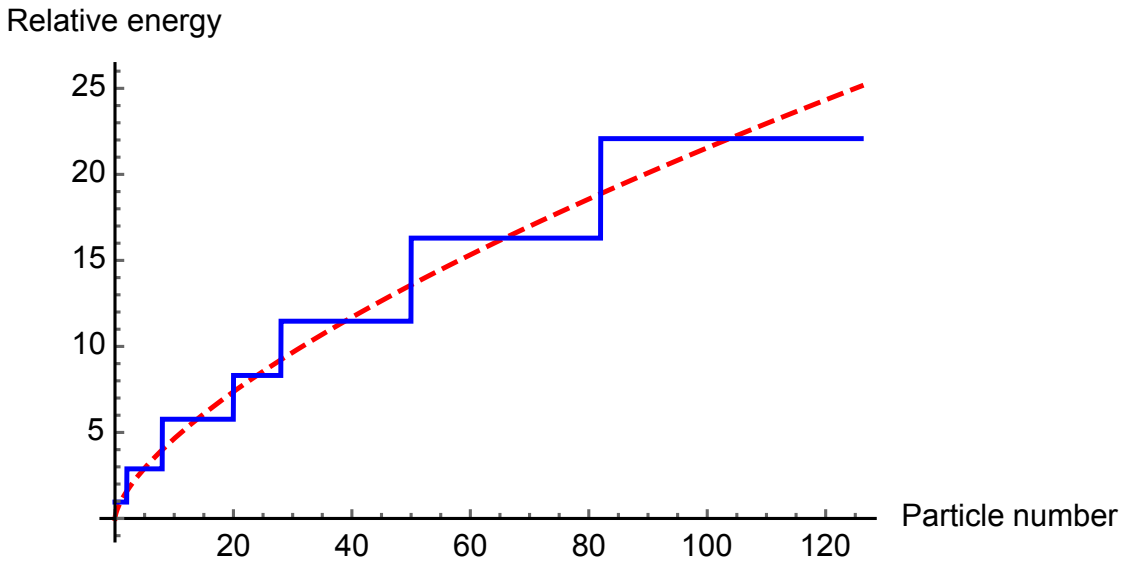

Figure 7.2: The staircase function $q(n)$ (solid blue) and $n^{2/3}$ (dashed red) are plotted against the particle number n. The difference between these two curves is proportional to the shell corrections. In this figure, all energies were divided by $t_N/N^{2/3}$.

7.3.4 Shell correction

From the former discussion, the shell correction energy for the neutrons is

$$\begin{aligned} \Delta E_N &= E_{\text{Bunched}} - E_{\text{Unbunched}} \\ &= \frac{t_N}{N^{2/3}} \int_0^N \left[q(n) - n^{2/3} \right] \mathrm{d}n. \end{aligned} \tag{7.16}$$

The total shell correction is simply the sum of the neutron and proton shell corrections which can be written as

$$\Delta E = t_F \frac{F(N) + F(Z)}{\left(\frac{1}{2}A\right)^{2/3}}, \tag{7.17}$$

where

$$F(N) = \int_0^N \left[q(n) - n^{2/3} \right] \mathrm{d}n. \tag{7.18}$$

7.3.5 Partial bunching

Despite the fact that solving Schrödinger's equation for a bound system yields discrete energy eigenstates, partial bunching of levels rather than complete bunching of the smooth level distribution is sometimes used. In the case of partial bunching, the levels formed from the smooth distribution are no longer discrete nor degenerate but rather bands, having a width $(1 - b)$ times their unbunched width. One can show that in cases where incomplete bunching is considered, t_F is simply replaced by bt_F, in the former expression for the shell corrections. More precisely,

$$\Delta E = bt_F \frac{F(N) + F(Z)}{\left(\frac{1}{2}A\right)^{2/3}}. \tag{7.19}$$

7.3.6 Velocity dependent potentials

In the particular case where the depth of the potential v is assumed to be linearly depend on the kinetic energy of the nucleons, we have that

$$v = v_0 + kt, \tag{7.20}$$

where v_0 and k are constants while t is the kinetic energy. Then, for this velocity-dependent potential and accounting for partial bunching, the t_F should be replaced by $(1 + k/n)bt_F$ in the expression for the completely bunched shell corrections. Here, the variable n is the number of interacting nucleons held responsible for the potential itself. In the following, the product $(1 + k/n)bt_F$ will be taken to be an adjustable parameter, namely C. Concretely, this translates into,

$$\Delta E = C\frac{F(N) + F(Z)}{\left(\frac{1}{2}A\right)^{2/3}}. \tag{7.21}$$

7.3.7 Overall-shift of the bunched energies

It turns out that in order to reproduce experimental data an overall-shift of the bunched energies is also required. This is accounted for by redefining the staircase function as,

$$q\left(n\right) = \frac{3}{5}\frac{M_i^{\frac{5}{3}} - M_{i-1}^{\frac{5}{3}}}{M_i - M_{i-1}} - \frac{c}{2^{2/3}} \text{ for } M_{i-1} < n < M_i, \tag{7.22}$$

where c is an adjustable parameter characterizing the overall-shift and the factor $2^{2/3}$ is introduced for convenience. Thus, the contribution of this shift to the shell corrections is simply

$$-\frac{\int_0^N c\,\mathrm{d}n + \int_0^Z c\,\mathrm{d}n}{2^{2/3}\left(\frac{1}{2}A\right)^{2/3}} = -cA^{1/3}, \tag{7.23}$$

and the shell correction can now be expressed as

$$S\left(N,Z\right) = C\left[\frac{F\left(N\right) + F\left(Z\right)}{\left(\frac{1}{2}A\right)^{\frac{2}{3}}} - cA^{\frac{1}{3}}\right]. \tag{7.24}$$

7.4 Macroscopic deformation

The possible deformations for the nucleus are generally associated with shape degrees of freedom which are incorporated into the spherical liquid drop. The more degrees of freedom are added, the more complex the shape will possibly be. Here, the simplest possible shape parametrization was retained. This parametrization is the one allowing for ellipsoidal deformation. The ellipsoidal shape can be described by the deformation parameter σ and the shape parameter γ, respectively, characterizing quadrupole deformation and non-axiality. Those two parameters define the semi-axes of the ellipsoidal shape through,

$$\begin{aligned} a &= R_0 \exp\left[\sigma \cos\left(\gamma - \frac{2}{3}\pi\right)\right], \\ b &= R_0 \exp\left[\sigma \cos\left(\gamma + \frac{2}{3}\pi\right)\right], \\ c &= R_0 \exp\left[\sigma \cos\left(\gamma\right)\right]. \end{aligned} \tag{7.25}$$

The Jacobian of the transformation from an ellipsoid to a sphere is

$$\begin{aligned} \frac{abc}{R_0^3} &= \exp\left[\sigma\left(\cos\left(\gamma - \frac{2}{3}\pi\right) + \cos\left(\gamma + \frac{2}{3}\pi\right) + \cos\left(\gamma\right)\right)\right] \\ &= \exp\left[\sigma\left(\cos\gamma\cos\frac{2}{3}\pi + \sin\gamma\sin\frac{2}{3}\pi + \cos\gamma\cos\frac{2}{3}\pi - \sin\gamma\sin\frac{2}{3}\pi + \cos\gamma\right)\right] \\ &= \exp\left[\sigma\left(2\cos\left(\gamma\right)\cos\left(\frac{2}{3}\pi\right) + \cos\left(\gamma\right)\right)\right] \\ &= \exp\left[\sigma\cos\left(\gamma\right)\left(2\cos\left(\frac{2}{3}\pi\right) + 1\right)\right] \\ &= 1. \end{aligned} \tag{7.26}$$

From this, we realize that this transformation does not change the volume of the nucleus. Therefore, the volume term will not be affected by deformation. A set of similar computations can be used to show that this is not the case for the surface and Coulomb contributions.

This is the reason for including the macroscopic deformation functions alongside the c_2 and c_3 coefficients in Eq. (7.1). Of course, when no deformation is considered the deformed ellipsoidal liquid drop should reduce to the spherical one. Hence, with deformation, the macroscopic model reads

$$M\left(N,Z\right) = M_N N + M_H Z - c_1 A + c_2\, f(\sigma,\gamma)\, A^{\frac{2}{3}} + c_3\, g(\sigma,\gamma)\, \frac{Z^2}{A^{1/3}} - c_4 \frac{Z^2}{A} + \delta. \tag{7.27}$$

For convenience, one can define another shape parameter α, constructed from σ and γ, through

$$\alpha^2 = \sigma^2\left(1 - \frac{1}{7}\sigma\cos\left(3\gamma\right) + \mathcal{O}\left(\sigma^2\right)\right), \tag{7.28}$$

then, the expressions for the functions f and g become

$$f(\alpha,\gamma) = 1 + \frac{2}{5}\alpha^2 - \frac{4}{105}\alpha^3\cos\left(3\gamma\right) + \mathcal{O}\left(\alpha^4\right), \tag{7.29}$$

$$g(\alpha,\gamma) = 1 - \frac{1}{5}\alpha^2 - \frac{4}{105}\alpha^3\cos\left(3\gamma\right) + \mathcal{O}\left(\alpha^4\right). \tag{7.30}$$

The equation (7.29) is, basically, an expression for the surface ratio between an ellipsoid and a sphere. Therefore, if the ellipsoid's area surpasses that of a sphere the contribution of the surface term grows. The equation (7.30) is the same type of ratio for the Coulomb term. Both (7.29) and (7.30) are third order expansions of integrals which are difficult to compute. Thus, restricting these expansions to third order may limit the range of validity of the model to small ellipsoidal deformations. However, note that as deformation grows higher multipoles become important and the quadrupole approximation breaks down.

7.5 Microscopic deformation

The quantum effects introduced through the shell corrections are also related to the shape of the nucleus. Indeed, solving the Schrödinger equation for differently shaped potentials, all having the same volume, yields, in general, different eigenvalues. As they have different shapes these potentials exhibit different symmetries. The symmetries are at the origin of the degeneracies of the levels, when those symmetries are broken, due to deformation, the degeneracies disappear as well. Thus, deformation causes the degenerate discrete levels to spread into many different energy levels. As the symmetries disappear the degenerate levels scatter away from each other. When this happens, more and more, different energy levels fill the well and resemble, more and more, a continuous smooth distribution of levels. Hence, the disappearing of the shell effects with the deformation away from the spherical shape. Of course, shapes other than the sphere may also display symmetries as well as degeneracies and could result in significant shell effect as well. These, however, are neglected here. From the prior argument the shell corrections must be attenuated by deformation. Thus, the general expression for the shell term is given by

$$S\left(N,Z\right)\cdot\exp\left[-\frac{\overline{\left(\delta R\right)^{2}}}{a^{2}}\right], \tag{7.31}$$

where

$$\overline{\left(\delta R\right)^{2}}=R_{0}^{2}\frac{1}{5}\alpha^{2}, \tag{7.32}$$

is the root-mean-square deviation away from a sphere with an average radius taken as $R_0 = r_0 A^{1/3}$. The variable a is in fact an attenuation factor which is considered to be an adjustable parameter. As it is difficult to know when and how the symmetry breaking occurs through deformation, distortions away from the spherical shapes will be taken to be the root-mean-square deviation noted $\overline{\left(\delta R\right)^{2}}$. Notice the root-mean-square is not sensitive to the kind of deformation which is highly convenient.

7.6 Macroscopic-microscopic model

We hereby summarize the expressions from the previous sections and provide the complete and final version of the model considered in the ensuing analysis. Thus, disregarding non-axiality, the full model reads

$$\begin{aligned} M(N,Z,\alpha) = {} & M_n N + M_H Z \\ & - c_1 A + c_2 A^{\frac{2}{3}} f(\alpha) + c_3 \frac{Z^2}{A^{\frac{1}{3}}} g(\alpha) - c_4 \frac{Z^2}{A} + \delta \\ & + S(N,Z) \exp\left(-\alpha^2/\alpha_0^2\right), \end{aligned} \tag{7.33}$$

where

$$f(\alpha) = 1 + \frac{2}{5}\alpha^2 - \frac{4}{105}\alpha^3, \tag{7.34}$$

$$g(\alpha) = 1 - \frac{1}{5}\alpha^2 - \frac{4}{105}\alpha^3, \tag{7.35}$$

$$\alpha_0^2 = 5\left(\frac{a}{r_0}\right)^2 A^{-2/3}. \tag{7.36}$$

It should be noted that these third order expansions in α only allow for prolate ground-states. The shell correction function is,

$$S(N,Z) = C\left[\frac{F(N)+F(Z)}{\left(\frac{1}{2}A\right)^{\frac{2}{3}}} - cA^{\frac{1}{3}}\right], \tag{7.37}$$

where one can show that

$$F(N) = q(n)\left(N - M_{i-1}\right) - \frac{3}{5}\left(N^{\frac{5}{3}} - M_{i-1}^{\frac{5}{3}}\right) \text{ for } M_{i-1} < n < M_i. \tag{7.38}$$

The model contains 4 macroscopic parameters, namely, a_1 , k, a_2 and r_0, as well as 3 microscopic parameters, specifically, C, c and a. Thus, in total 7 parameters must be adjusted to the experimental data.

7.7 The adjustment of the model

Previously, a simplified "macroscopic-microscopic" model was presented. In this particular description, the mass of a nucleus is assumed to be a function of the number of neutrons, protons, as well as deformation. Consequently, the experimental masses and deformations are required in order to adjust the model. Using the regression analysis exposed in chapter 5, the macroscopic parameters a_1, k, a_2 and r_0, as well as the microscopic parameters, C, c and a, are determined, along with their uncertainties and their correlations.

As usual, empirical data is used in order to adjust the parameters entering the model. The nuclear masses play a central part in this adjustment, however, they do not allow to constrain the deformation. Consequently, another observable must be employed in order to do so, i.e., the electric quadrupole moment.

7.7.1 The masses

The following results are based on the nuclear binding energies deduced from the atomic mass excesses found in Refs. [83, 84] for all nuclei satisfying N,Z $\geq$ 8 and with uncertainties below 150 keV. Furthermore, only selecting those nuclei for which the ground-state electric quadrupole moment was measured, a total of 457 nuclei were considered.

7.7.2 Electric quadrupole moments

The deformation parameter α can be extracted from electric quadrupole moments. Indeed, the following expression for the theoretical electric quadrupole moment can be found in Ref. [92],

$$Q_0 = \frac{3}{\sqrt{5\pi}} ZR^2\beta \left[1 + \frac{2}{7}\sqrt{\frac{5}{\pi}}\beta\right] \tag{7.39}$$

where β is the quadrupole deformation parameter and the average radius was taken to be R=1.19$A^{1/3}$. In order to obtain β, from the prior relation, one has to solve a quadratic equation. It turns out, the only physical solution is

$$\beta = \frac{-a_1 + \sqrt{a_1^2 + 4a_0}}{2}, \tag{7.40}$$

where

$$a_1 = \frac{7}{2}\sqrt{\frac{\pi}{5}}, \tag{7.41}$$

$$a_0 = \frac{7\pi Q_0}{6ZR^2}. \tag{7.42}$$

Finally, the tie between α and β is taken to be

$$\alpha = \sqrt{\frac{5}{4\pi}}\beta. \tag{7.43}$$

In the case of axially symmetric nuclei, the theoretical electric quadrupole moment is related to the measured one through

$$Q_0 = \frac{(I+1)(2I+3)}{3K^2 - I(I+1)} Q_s, \tag{7.44}$$

where I and K are, respectively, the total spin and the spin projection onto the symmetry-axis. However, in most cases, it is not possible to know the exact value for K. Here, it was assumed, as in the original work, that K=I. Thus, the previous expression reduces to,

$$Q_0 = \frac{(I+1)(2I+3)}{I(2I-1)} Q_s. \tag{7.45}$$

The total spins I and measured electric quadrupole moments Q_s were taken from Ref. [93]. From them, the values for Q_0 were deduced, then, β and α were inferred.

7.7.3 The regression

In the original work [74], the adjustment of the parameters was achieved separately for the macroscopic and microscopic contributions. On the one hand, it was realized that the effects described by the liquid drop were, in some sense, universal, and described the whole nuclear chart. On the other hand, deformation and shell corrections were specific to regions of the chart and could vary rapidly, i.e., neighbouring nuclei could have distinct deformations and shell corrections. Consequently, the macroscopic and microscopic parameters could be considered independent. Thus, an initial guess for the macroscopic parameters was made, then, using both the experimental masses and the liquid drop parameters, the microscopic parameters were determined. In the second step, the microscopic parameters were fixed and the macroscopic ones were adjusted. By repeating these steps the spherical macroscopic and microscopic parameters were determined. The remaining parameter a was adjusted afterwards by using the quadrupole moments. In our approach, after an initial guess of all parameters both macroscopic and microscopic parameters are determined at one fell swoop. Here, the initial guess was taken to be the converged result from the original work [74].

7.8 The parameters

The root-mean-square deviation is $\hat{\sigma}$=1.53 MeV. Adjusting only the macroscopic model while keeping the same deformation and disregarding the shell corrections leads to a root-mean-square deviation of $\hat{\sigma}$=2.53 MeV. Thus, the inclusion of the shell corrections does, indeed, yield a significant improvement in the description of nuclear masses. However, it should be mentioned that more accurate shell corrections such as those from the Thomas-Fermi model [57], lead to $\hat{\sigma} \approx$ 600 keV, as shown in the previous chapter. Nevertheless, this model is very simple and yet, the improvement is rather serious.

The parameters along with their uncertainties and relative uncertainties are presented in Table 7.2. As usual, the uncertainties were inferred from the diagonal of the covariance matrix given in Table 7.4. When examining the relative uncertainties, the macroscopic parameters are firmly determined while those describing the shell corrections are more loosely constrained. More specifically, the overall-shift parameter and the attenuating parameter, i.e., respectively c and a, are not precisely known.

Table 7.2: The parameters along with their uncertainties and relative uncertainties. The parameters obtained in the original work are presented in the last line [74].

	a_1	k	a_2	r_0	C	c	a
$\hat{\mathrm{p}}$ [MeV]	15.63695	1.78798	18.40844	1.21103	3.69404	0.22215	0.28959
$\hat{u}(\hat{\mathrm{p}})$[MeV]	0.03529	0.00495	0.13072	0.00434	0.14356	0.02965	0.03597
$\hat{u}(\hat{\mathrm{p}})/\hat{\mathrm{p}}$ [%]	0.23	0.28	0.71	0.36	3.89	13.35	12.42
$\hat{\mathrm{p}}$ [MeV] from Ref. [74]	15.677	1.79	18.56	1.2049	5.8	0.26	0.325

The correlations between the parameters are exposed in Table 7.3 as deduced from the covariances given in Table 7.4. Again, it is clear that the volume, surface and Coulomb parameters exhibit strong correlations and form a correlation group. These three parameters are also correlated, to a lesser extent, with the parameter describing isospin dependence, i.e., the volume and surface symmetry parameter k, which is part of that first group. Furthermore, the shell correction parameter C is almost uncorrelated with any other parameter. Remember, this was an assumption made in the original work which is now confirmed by the present analysis. More interesting, are the existing correlations between the overall-shift parameter c and the attenuating parameter a. These parameters form the second correlation group. Both c and a were introduced in order to moderate the shell corrections. Thus, shell effects can be altered by, indifferently, changing c or a, this is the reason for their correlation. Notice this correlation is negative, clearly showing that if c is too large to properly determine the shell corrections then a will decrease in order to compensate the change in c and vice-versa.

Table 7.3: Correlation matrix deduced from the covariance matrix Table 7.4.
Notations: **group 1** and *group 2*.

a_1	k	a_2	r_0	C	c	a
1.00	**0.73**	**0.97**	**-0.97**	0.15	0.27	-0.18
0.73	**1.00**	**0.74**	**-0.60**	0.21	0.31	-0.22
0.97	**0.74**	**1.00**	**-0.90**	0.18	0.46	-0.31
-0.97	**-0.60**	**-0.90**	**1.00**	-0.12	-0.12	0.09
0.15	0.21	0.18	-0.12	1.00	0.26	-0.39
0.27	0.31	0.46	-0.12	0.26	1.00	*-0.71*
-0.18	-0.22	-0.31	0.09	-0.39	*-0.71*	1.00

Table 7.4: Covariance matrix for the parameters.

a_1	k	a_2	r_0	C	c	a
0.0012450119	0.0001273946	0.0044954844	-0.0001482834	0.0007801377	0.0002802700	-0.0002276940
0.0001273946	0.0000244730	0.0004767682	-0.0000129862	0.0001483606	0.0000459051	-0.0000394312
0.0044954844	0.0004767682	0.0170887151	-0.0005115828	0.0032982450	0.0017919812	-0.0014759566
-0.0001482834	-0.0000129862	-0.0005115828	0.0000188338	-0.0000756432	-0.0000157301	0.0000145733
0.0007801377	0.0001483606	0.0032982450	-0.0000756432	0.0206094480	0.0011127571	-0.0020027538
0.0002802700	0.0000459051	0.0017919812	-0.0000157301	0.0011127571	0.0008791023	-0.0007569549
-0.0002276940	-0.0000394312	-0.0014759566	0.0000145733	-0.0020027538	-0.0007569549	0.0012938005

7.9 The theoretical ground-state masses

In the last section, the parameters, their uncertainties and correlations were presented and commented. We now follow through with their propagation onto the theoretical binding energies. Naturally, this leads us to the ground-state masses along with their uncertainties and correlations.

As in the study focusing on the liquid drop (cf. chapter 6), the uncertainties differs from one nucleus to the other. Indeed, this is made obvious by looking at Fig. 7.3 which shows these uncertainties for the 457 masses entering the adjustment of the model. The values range from 104 keV to 637 keV with a mean of 178 keV. Notice also the growth of uncertainties away from the mean proton number of the sample, i.e., 54.9.

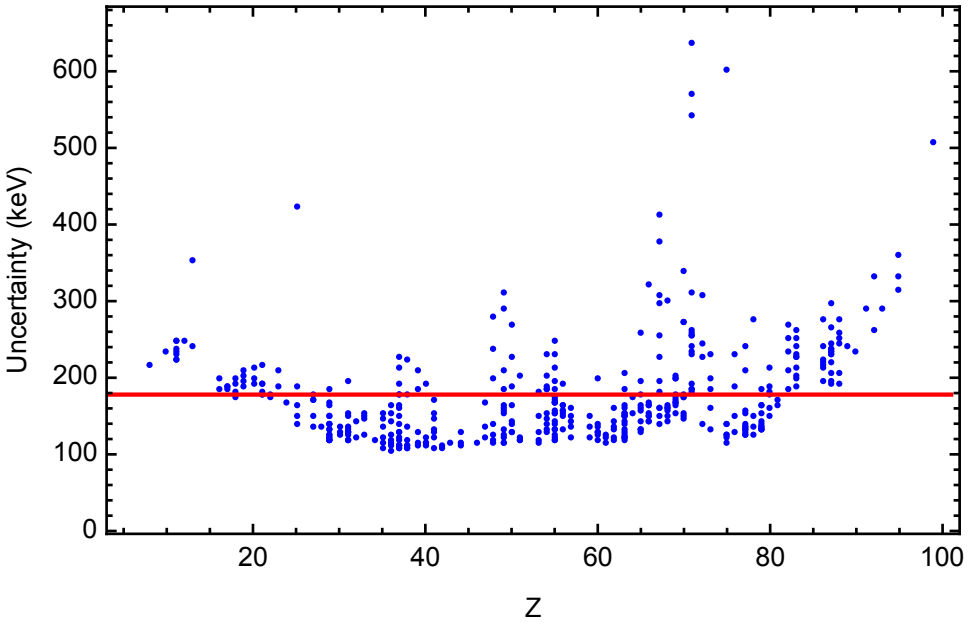

Figure 7.3: Uncertainties in the predicted binding energies (blue dots) as a function of proton number Z along with the mean of the uncertainties (red line). Inferred from the square root of the diagonal elements of the covariance matrix, i.e., the diagonal elements of Eq. (5.46).

Furthermore, the theoretical masses are all obtained using the same model with the same parameters, therefore, it is obvious that all masses should be correlated together. This is illustrated in Fig. 7.4 where the correlations between the mass of ^{235}U and the 457 other masses are shown (including ^{235}U). In the case of the liquid drop model, the correlations were shown to be very strong with neighbouring nuclei and to quickly fade away from this region. Likewise, this is also the case for this phenomenological model. Much more surprising is the fact that correlations between the mass of ^{235}U and distant nuclei, are not that negligible. For instance, the masses of heavy nuclei in the region of $65 < Z < 80$ and $90 < N < 110$ or those of light nuclei in the region of $8 < Z < 20$ and $8 < N < 25$ are quite correlated with the mass of ^{235}U. Note that these regions are in between magic numbers. Moreover, the global structure of the correlations between the masses is more difficult to comprehend. This is related to local effects due to both deformation and shell effects which were disregarded in the liquid drop analysis.

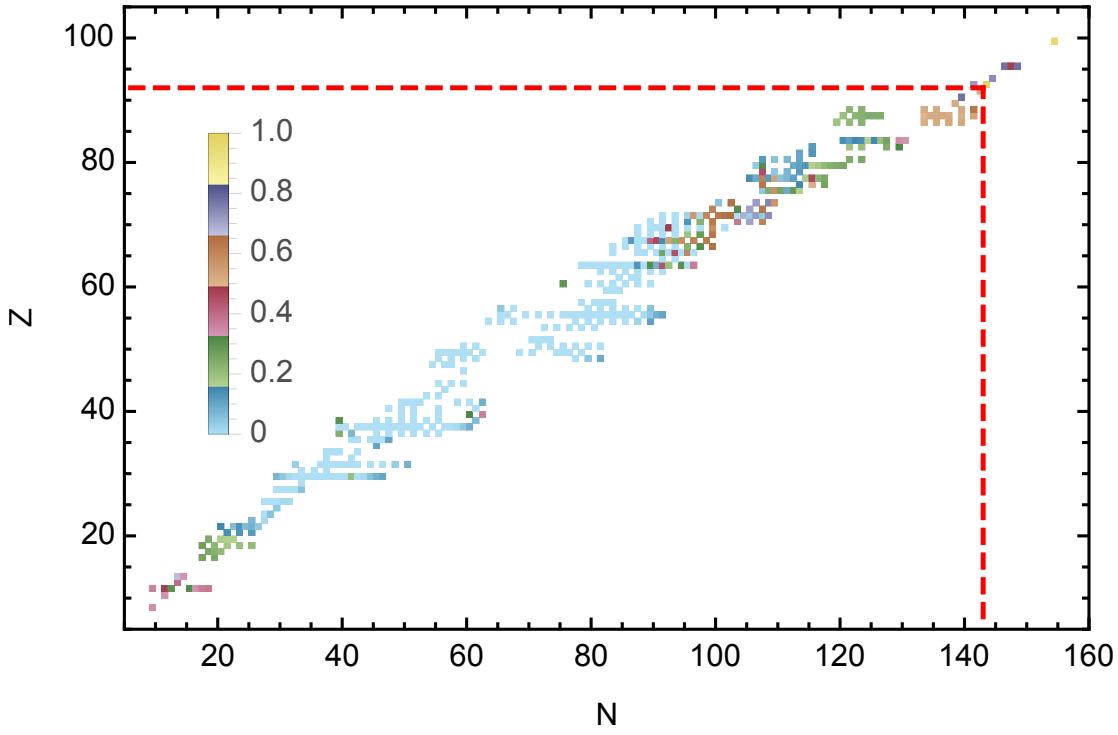

Figure 7.4: Correlations between the theoretical binding energy of ^{235}U and the other 457 binding energies. Notice the correlations in the region of ^{235}U and their downfall away from this region with the exceptions of heavy nuclei in the region $65 < Z < 80$ and $90 < N < 110$, as well as light nuclei in the region $8 < Z < 20$ and $8 < N < 25$.

Comparing the results of this study to the ones obtained in the previous chapter, we see that the uncertainties have significantly increased with the inclusion of quadrupole deformation and shell corrections. This can be partially explained by the increase in $\hat{\sigma}$. However, these uncertainties are still insufficient to include the errors of the model. This is shown Fig. 7.5 where the errors are depicted and compared with the mean uncertainty. Since the shell corrections were not included in the study concerning the liquid drop model, we were lead to believe that their inclusion should result in a significant growth of the uncertainties and that the latter should reach, more or less, the magnitude of the errors. Here, however, the shell corrections were included and yet the issue remains unresolved, i.e., the root-mean-square (RMS) is still 9 times larger than the mean of the uncertainties (MU). Only 30% of the 457 experimental masses, entering the regression, fall within the theoretical uncertainties when assuming a 99.7% level of confidence. Thus, the analysis disproves the model and shows that most masses do in fact require a more complex theoretical treatment in order to be properly described.

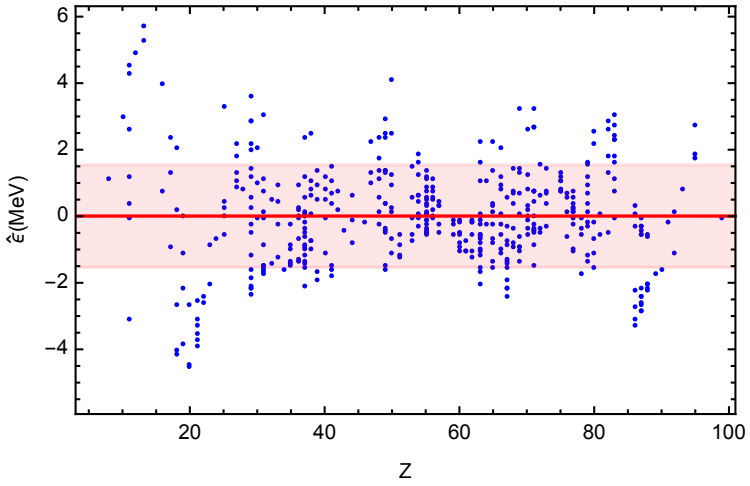

Figure 7.5: The errors ($\hat{\boldsymbol{\epsilon}} = \mathbf{B}_{\mathrm{Exp}} - \mathbf{X} \cdot \hat{\mathbf{p}}$) restricted to $\hat{\boldsymbol{\epsilon}} \in$ [-5.7;5.7] MeV are shown (blue dots) as a function of proton number Z. The mean error (red line) as well as the standard deviation of the errors (red band) are also displayed.

Table 7.5 contains the best and the worst examples the model can provide. The lower-half of the table, containing the worst examples, consists mostly of light nuclei while the upper-half consists of mid-mass nuclei. This confirms the fact that although capable of describing heavier systems, the liquid drop model struggles with the description of light nuclei where the structural effects prevail over the statistical mechanical ones. More importantly, the uncertainties are relatively constant and, because of their statistical nature, struggle to reflect the predictive capabilities of the model.

Table 7.5: Comparison of experimental and theoretical binding energies in MeV. The table is divided in two by a horizontal line. Above, the 5 binding energies which are best reproduced by the model, below, the 5 binding energies which are worst reproduced by the model. All nuclei in the table were part of the regression.

N	Z	B^{Exp}	B^{Th}
100	71	1382.095517	1382.096801 ± 0.261098
65	54	996.841874	996.844858 ± 0.138962
30	25	482.049012	482.045308 ± 0.149996
52	37	771.039232	771.043621 ± 0.112122
41	36	663.426617	663.418327 ± 0.143238
25	20	388.359672	392.862662 ± 0.193628
11	11	174.141948	169.610653 ± 0.247345
13	12	205.584076	200.675385 ± 0.246627
13	13	211.889292	206.602533 ± 0.355101
14	13	224.947442	219.232098 ± 0.242517

Up to now, it was assumed that the ground-state deformation was known. Of course, as previously discussed, this is the case for the nuclei entering the adjustment of the model. However, there are many nuclei for which this deformation remains unknown and must be determined theoretically in order to predict their masses. In those prevailing cases, this is achieved by minimizing the potential energy, i.e., the mass, with respect to deformation. An example of such a minimization is illustrated in Fig. 7.6 where the mass excess of ^{208}Pb is presented as function of deformation. Of course, this nucleus is known to be spherical and consequently, its energy minimum corresponds to the case where there is no deformation, i.e., α=0. Another example may be found in Fig. 7.7 where the mass excess of ^{238}U is given as function of deformation. As can be seen from this figure, nuclei may also be deformed in their ground-state and need not be spherical. More precisely, the minimization yields a prolate ground-state with α=0.152.

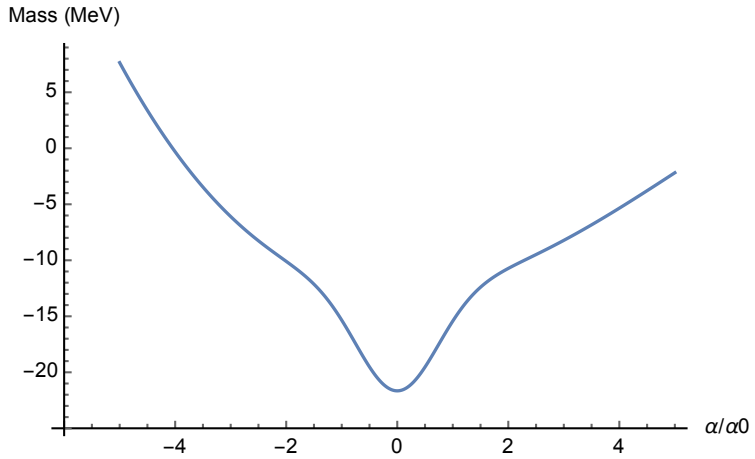

Figure 7.6: The mass excess of ^{208}Pb as a function of deformation. The minimization yields a mass excess of -21.654 MeV at α/α_0=0.

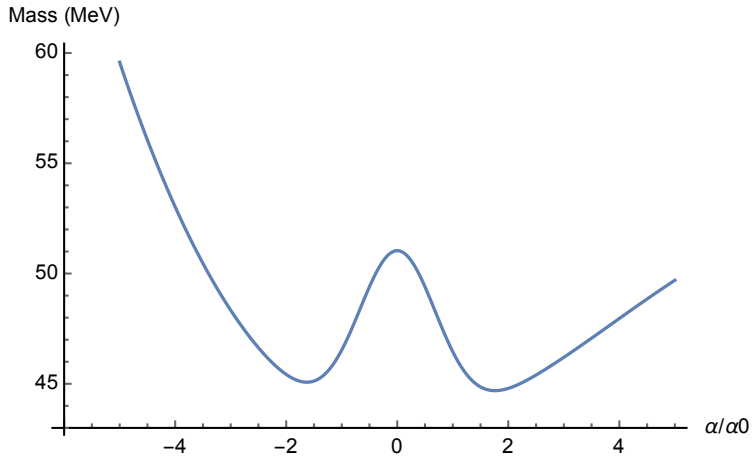

Figure 7.7: The mass excess of ^{238}U as a function of deformation. The minimization yields a mass excess of 44.691 MeV at α/α_0=1.7607.

7.10 The assessment of the regression hypothesis

As in the liquid drop study, the analysis is based on regression assumptions regarding the distribution of the errors. More precisely, the errors should follow a Gaussian distribution with zero mean. This distribution is depicted Fig. 7.8 where the corresponding mean and standard deviation are, respectively, 6 keV and $\hat{\sigma} = 1.53$ MeV. These values were employed to plot the normal distribution that exhibits a decent agreement with the histogram representing the distribution of the errors.

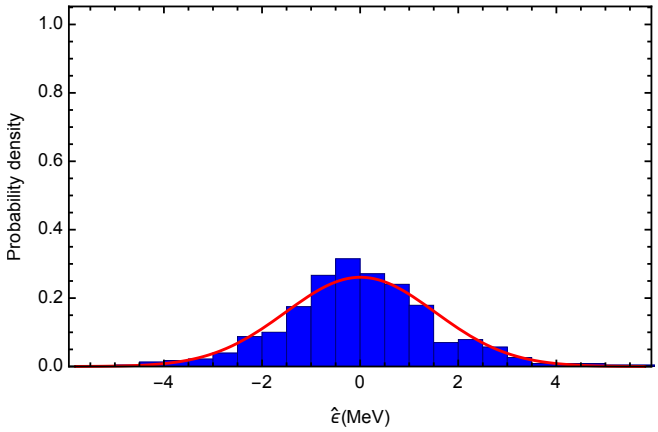

Figure 7.8: Histogram (blue bars) formed of 25 bins restricted to $\hat{\boldsymbol{\epsilon}} \in$ [-5.7;5.7] MeV and representing the distribution of the errors ($\hat{\boldsymbol{\epsilon}} = \mathbf{B}_{\mathrm{Exp}} - \mathbf{X} \cdot \hat{\mathbf{p}}$). The normal distribution constructed from the mean (6 keV) and the standard deviation ($\hat{\sigma} = 1.53$ MeV) of the errors, is also provided (red line).

The quantile-quantile plot, presented in Fig. 7.9, confirms the normality of the errors. Once more, the tails of the distribution of the errors do not, strictly, correspond to those of a normal distribution. Nonetheless, the region around the mean, $\hat{\boldsymbol{\epsilon}} \in$ [-2,2] MeV, containing around 90% of the errors, does follow a normal distribution. Again, this should be enough to insure that the outcome of this analysis delivers dependable results.

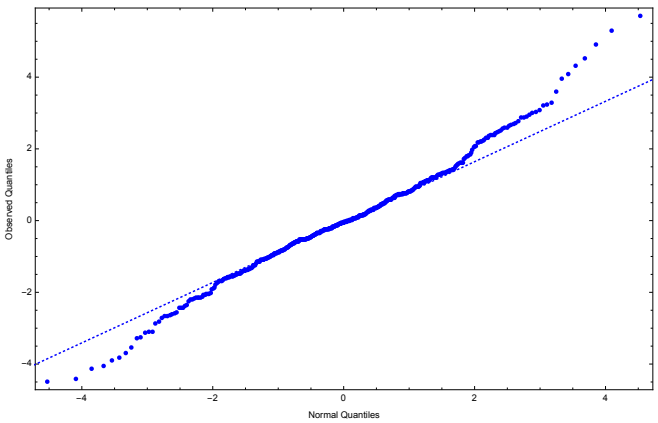

Figure 7.9: Quantile-quantile plot (blue dots) for the distribution of the errors and the expected theoretical straight line (dashed blue) in the case where normality is perfectly satisfied.

Again, since the model does not include an intercept, the mean of these errors does not exactly vanish. As for the liquid drop model, we now consider the impact of an additional constant parameter c_0 on the previous analysis. A look at Table 7.6 reveals that the parameters are affected by the additional intercept, not to mention, the parameters c and a are still loosely constrained and, to an even greater extent, c_0 as well.

Table 7.6: The parameters along with their uncertainties and relative uncertainties for the model with an intercept.

	c_0	a_1	k	a_2	r_0	C	c	a
$\hat{\mathrm{p}}$ [MeV]	5.24442	15.89887	1.81075	19.63452	1.19013	3.66316	0.17900	0.33129
$\hat{u}(\hat{\mathrm{p}})$[MeV]	2.13978	0.11305	0.01060	0.52277	0.00938	0.13974	0.03848	0.04278
$\hat{u}(\hat{\mathrm{p}})/\hat{\mathrm{p}}$ [%]	40.80	0.71	0.59	2.66	0.79	3.82	21.49	12.91

Naturally, the parameters undergoing the most change should be those strongly correlated with the intercept, i.e., the macroscopic parameters. A look at the correlation matrix given Table 7.7 confirms this naive intuition. The correlations are altered by the inclusion of the intercept. In particular, the inclusion of an intercept increases the correlations between all macroscopic parameters, i.e., the volume, the surface, Coulomb and symmetry parameters, all of which are very strongly correlated with the intercept. Nevertheless, the correlation group structure remains unchanged. The four macroscopic parameters form a correlation group along with the intercept. As before, the second group consists of the overall-shift and attenuation parameters. Although they are not directly correlated with the intercept, the overall-shift and attenuation parameters, also change. This is a consequence of the deformation which enters both the macroscopic and the microscopic contributions. Recall that in this analysis, deformation is assumed known from electric quadrupole moments, and therefore, is not an adjustable parameter. Thus, if the macroscopic parameters are correlated to the intercept they will change and in turn, since deformation is fixed, the microscopic parameter a responsible for the description of microscopic deformation will change as well. Finally, as already mentioned, a and c are responsible for the moderation of shell corrections and as such are correlated, therefore, the change in a will, definitely, induce a change in c.

With the additional intercept, the standard deviation of the errors remains unchanged, i.e., $\hat{\sigma} = 1.53$ MeV, while the mean uncertainty increases and becomes MU=187 keV. Again, only 30% of the experimental masses, entering the regression, are correctly reproduced and fall within the theoretical uncertainties when assuming a 99.7% level of confidence. Although the inclusion of the intercept does change the previous results, these effects are not significant.

Table 7.7: Correlation matrix deduced from the covariance matrix Table 7.8 for the model with an intercept. Notations: **group 1** and *group 2*.

c_0	a_1	k	a_2	r_0	C	c	a
1.00	**0.94**	**0.88**	**0.96**	**-0.90**	-0.02	-0.39	0.24
0.94	**1.00**	**0.94**	**0.99**	**-0.99**	0.04	-0.28	0.16
0.88	**0.94**	**1.00**	**0.94**	**-0.92**	0.08	-0.20	0.10
0.96	**0.99**	**0.94**	**1.00**	**-0.97**	0.03	-0.25	0.14
-0.90	**-0.99**	**-0.92**	**-0.97**	**1.00**	-0.05	0.28	-0.17
-0.02	0.04	0.08	0.03	-0.05	1.00	0.27	-0.37
-0.39	-0.28	-0.20	-0.25	0.28	0.27	1.00	*-0.76*
0.24	0.16	0.10	0.14	-0.17	-0.37	*-0.76*	1.00

Table 7.8: Covariance matrix for the parameters for the model with an intercept.

c_0	a_1	k	a_2	r_0	C	c	a
4.5786805061	0.2296977834	0.0200871148	1.0803260309	-0.0179590060	-0.0032911282	-0.0315007617	0.0223479780
0.2296977834	0.0127810949	0.0011351442	0.0588536712	-0.0010438759	0.0006604539	-0.0011849194	0.0007925102
0.0200871148	0.0011351442	0.0001122817	0.0052305823	-0.0000911112	0.0001309628	-0.0000778973	0.0000479548
1.0803260309	0.0588536712	0.0052305823	0.2732892658	-0.0047377677	0.0028439207	-0.0048865862	0.0031375015
-0.0179590060	-0.0010438759	-0.0000911112	-0.0047377677	0.0000878918	-0.0000625250	0.0001018073	-0.0000674291
-0.0032911282	0.0006604539	0.0001309628	0.0028439207	-0.0000625250	0.0195277012	0.0014920870	-0.0022118866
-0.0315007617	-0.0011849194	-0.0000778973	-0.0048865862	0.0001018073	0.0014920870	0.0014802894	-0.0012499882
0.0223479780	0.0007925102	0.0000479548	0.0031375015	-0.0000674291	-0.0022118866	-0.0012499882	0.0018303145

7.11 The theoretical saddle-point masses

As opposed to the model used in the previous chapter, the macroscopic contribution considered here does contain a deformation degree of freedom, i.e., the variable α. Therefore, it becomes possible to exploit this, in order to make symmetric fission barriers calculations accompanied by their uncertainties. Of course, the third order expansions in the deformation may restrict the accuracy of the predictions in a significant manner. Another limiting factor comes from the fact that the saddle-point corresponds, in most cases, to large values of α, consequently, the attenuating exponential completely kills the shell corrections at the saddle. Thus, the saddle-point shell corrections are simply neglected in this theoretical description. It should be mentioned that today's fission barrier calculations involve many deformation degrees of freedom, thus, allowing the system to follow extremely intricate fission paths, going way beyond the range of capabilities of the model considered here.

The fission barrier is defined as,

$$B_f = M_{SP} - M_{GS}, \tag{7.46}$$

where M_{SP} and M_{GS} are, respectively, the saddle-point and ground-state masses.

As described earlier on, the ground-state mass is obtained by minimizing the energy with respect to deformation. The saddle-point mass is obtained by finding the smallest energy peak that restricts deformation and forbids fission. Extending the Figs. 7.6 and 7.7 to account for larger deformations, saddle-points naturally appear. This is illustrated in Figs. 7.10 and 7.11 where the ground-state, the saddle-point and the corresponding fission barrier are shown.

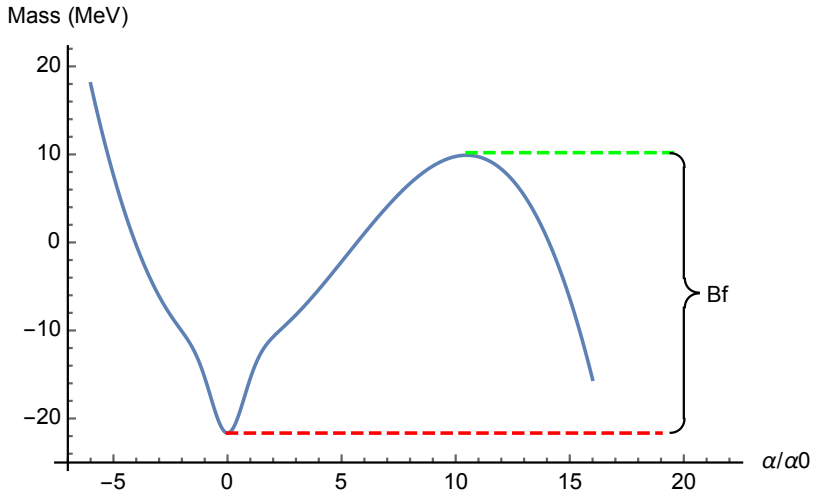

Figure 7.10: The mass excess of ^{208}Pb as a function of deformation. The ground-state mass (red dashed line) is -21.654 MeV at α/α_0=0. The saddle-point mass (green dashed line) is 10.483 MeV at α/α_0=9.9054. The resulting fission barrier (black brace) is 32.137 MeV which is to be compared with Möller's calculation 24.95 MeV [50].

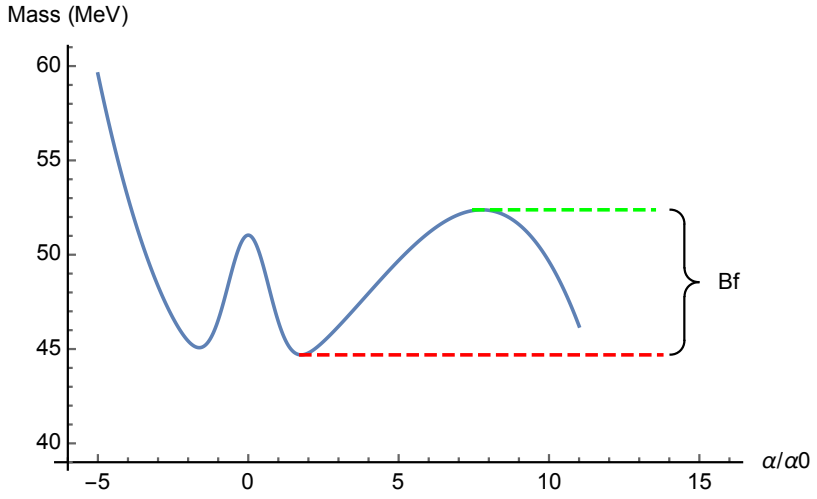

Figure 7.11: The mass excess of ^{238}U as a function of deformation. The ground-state mass (red dashed line) is 44.691 MeV at α/α_0=1.7607. The saddle-point mass (green dashed line) is 52.381 MeV at α/α_0=7.7718. The resulting fission barrier (black brace) is 7.69 MeV which is to be compared with Möller's calculation 5.63 MeV [50].

The uncertainties in the fission barrier can be decomposed into

$$u^2\left(B_F\right) = u^2\left(M_{SP}\right) + u^2\left(M_{GS}\right) - 2\,u\left(M_{SP}, M_{GS}\right), \tag{7.47}$$

where

$$\begin{aligned} u^2\left(M_{SP}\right) &= \mathbf{J}_{SP}\cdot\mathbf{Cov}[\mathbf{p}]\cdot\mathbf{J}_{SP}^T, & (7.48)\\ u^2\left(M_{GS}\right) &= \mathbf{J}_{GS}\cdot\mathbf{Cov}[\mathbf{p}]\cdot\mathbf{J}_{GS}^T, & (7.49)\\ u\left(M_{SP}, M_{GS}\right) &= \mathbf{J}_{SP}\cdot\mathbf{Cov}[\mathbf{p}]\cdot\mathbf{J}_{GS}^T, & (7.50) \end{aligned}$$

with

$$\begin{aligned} \mathbf{J}_{SP} &= \left[\frac{\partial M}{\partial a_1}, \frac{\partial M}{\partial k}, \ldots, \frac{\partial M}{\partial a}\right], & (7.51)\\ \mathbf{J}_{GS} &= \left[\frac{\partial M}{\partial a_1}, \frac{\partial M}{\partial k}, \ldots, \frac{\partial M}{\partial a}\right], & (7.52) \end{aligned}$$

which are, respectively, evaluated at the saddle-point and ground-state deformations. Furthermore, the parameters also take their final estimated value, i.e., after their convergence has been insured by the nonlinear regression procedure [67, 68].

From the previous explanations we know how to determine both the fission barriers and their uncertainties. An illustration of such calculations is given Table 7.9 where the fission barriers and their associated uncertainties are listed for the plutonium isotopes. The results obtained here are compared with Möller's calculations [50]. These two outcomes differ, on average, by a little less than 1 MeV and the uncertainties seem to demonstrate the incompatibility of the two outcomes when assuming the barriers from Ref. [50] have no uncertainties. Since subtracting both results does not yield a constant, the models appear to follow different trends.

This analysis based on plutonium isotopes allows us to give a rough estimate of the uncertainties in the fission barriers. Here, we shall retain that the overall uncertainty in the fission barrier is of the order of 0.5 MeV.

Table 7.9: Fission barriers for plutonium isotopes, extending from ^{228}Pu to ^{247}Pu, are reported and compared with those obtained in Ref. [50].

A	Z	B_f	B_f^M from Ref. [50]	$B_f - B_f^M$
228	94	4.31 ± 0.44	2.93	1.38
229	94	4.40 ± 0.44	2.95	1.45
230	94	4.50 ± 0.44	3.07	1.43
231	94	4.60 ± 0.44	3.05	1.55
232	94	4.70 ± 0.45	3.23	1.47
233	94	4.81 ± 0.45	3.50	1.31
234	94	4.92 ± 0.46	3.83	1.09
235	94	5.03 ± 0.46	4.09	0.94
236	94	5.13 ± 0.46	4.49	0.64
237	94	5.24 ± 0.47	5.00	0.24
238	94	5.35 ± 0.47	5.26	0.09
239	94	5.45 ± 0.48	5.74	-0.29
240	94	5.56 ± 0.48	5.98	-0.42
241	94	5.66 ± 0.48	6.35	-0.69
242	94	5.77 ± 0.49	6.41	-0.64
243	94	5.87 ± 0.49	6.66	-0.79
244	94	5.97 ± 0.50	6.59	-0.62
245	94	6.07 ± 0.50	6.93	-0.86
246	94	6.17 ± 0.50	7.07	-0.90
247	94	6.26 ± 0.51	7.12	-0.86

7.12 Constraining shell correction energies

Previously, in chapter 6, we deduced empirical constraints on the shell corrections. This was achieved by assuming that the last mass in an α decay chain was know and then extracting the experimental masses along with their uncertainties from measured Q_α-values. Just before that an uncertainty analysis of the liquid drop model was provided. In turn, this allowed us to predict the nuclear masses with their corresponding uncertainties. Shell corrections were then inferred by subtracting the liquid drop contribution to the experimental mass. The uncertainty propagation from both, the experimental masses and the liquid drop masses, lead us to decisive theoretical constraints on the shell corrections. In this section, we repeat this study for the phenomenological "macroscopic-microscopic" model considered in this chapter. The same two α decay chain are considered here and every single step of the study is done in the exact same way it was described in chapter 6. The respective outcomes for the two decay chains are reported in Tables 7.10 and 7.11.

The uncertainties obtained here are far larger than those obtained with the liquid drop model. On can now see that in the case of the first decay chain (cf. Table 7.10) the theoretical uncertainty is about the size of the experimental one. In the case of the second decay chain (cf. Table 7.11) the dominating uncertainty comes from the model.

Nevertheless, the constraints on the shell corrections range from 0.5 MeV to 1 MeV. Thus, the conclusions of the two outcomes are rather different. Notice also that the theoretical shell corrections are smaller than the experimental ones. This is due to the fact that superheavy nuclei are known to be strongly deformed and in the model considered here the shell corrections vanish with increasing deformation.

Table 7.10: Table containing the results concerning the first decay chain along with their uncertainties. The Q_α-values and their uncertainties were taken from Ref. [89] and $\Delta m^{Exp}(^{267}\mathrm{Rf})$ from Refs. [83,84]. The last column gives the theoretical SCE^{Th} obtained with the "macroscopic-microscopic" model considered here. All quantities are given in MeV. Results are obtained in the quadratic approximation otherwise it is well known that fission barriers vanish for superheavy elements. Since the microscopic parameters and the macroscopic ones are correlated, it is not possible to give separate uncertainties for both contributions. Thus, the uncertainties in Δm^{LD} are those of the entire model, including the shell corrections.

Nuclei	Q_α	Δm^{Exp}	Δm^{LD}	SCE	SCE^{Th}
$^{267}_{104}$Rf	-	*113.440±0.580*	110.735±0.526	2.705±0.783	0.269
$^{271}_{106}$Sg	*8.67±0.08*	124.535±0.585	121.575±0.565	2.960±0.813	0.236
$^{275}_{108}$Hs	*9.44±0.06*	136.400±0.589	133.023±0.611	3.377±0.849	0.202
$^{279}_{110}$Ds	*9.84±0.06*	148.665±0.592	145.071±0.662	3.594±0.888	0.168
$^{283}_{112}$Cn	*9.67±0.06*	160.760±0.595	157.714±0.718	3.046±0.933	0.133
$^{287}_{114}$Fl	*10.16±0.06*	173.345±0.598	170.942±0.773	2.403±0.977	0.099
$^{291}_{116}$Lv	*10.89±0.07*	186.659±0.602	184.727±0.772	1.932±0.979	0.064

Table 7.11: Table containing the results concerning the second decay chain along with their uncertainties. The Q_α-values and their uncertainties were deduced from the α particle's energies presented in Ref. [91] and $\Delta m^{Exp}(^{257}\mathrm{No})$ from Refs. [83,84]. The last column gives the theoretical SCE^{Th} obtained with the "macroscopic-microscopic" model considered here. All quantities are given in MeV. Results are obtained in the quadratic approximation otherwise it is well known that fission barriers vanish for superheavy elements. Since the microscopic parameters and the macroscopic ones are correlated, it is not possible to give separate uncertainties for both contributions. Thus, the uncertainties in Δm^{LD} are those of the entire model, including the shell corrections.

Nuclei	Q_α	Δm^{Exp}	Δm^{LD}	SCE	SCE^{Th}
$^{257}_{102}$No	-	*90.247±0.007*	89.163±0.449	1.084±0.449	0.294
$^{261}_{104}$Rf	*8.65±0.02*	101.322±0.021	100.268±0.491	1.054±0.492	0.259
$^{265}_{106}$Sg	*8.84±0.03*	112.587±0.037	111.968±0.538	0.619±0.539	0.225
$^{269}_{108}$Hs	*9.35±0.02*	124.362±0.042	124.257±0.592	0.105±0.594	0.190
$^{273}_{110}$Ds	*11.31±0.02*	138.097±0.046	137.131±0.654	0.966±0.656	0.155
$^{277}_{112}$Cn	*11.42±0.02*	151.942±0.050	150.584±0.724	1.358±0.726	0.120

7.13 Modern macroscopic-microscopic model

As already mentioned, there are other available models which are far superior to the one we have considered here. With this idea in mind, we started investigating the uncertainties in Warsaw's macroscopic-microscopic model described in Ref. [51]. The differences between Warsaw's model and the one considered in this chapter are significant to say the least. Indeed, the macroscopic part of the model examined here only includes one deformation degree of freedom while Warsaw's model considers ten. Furthermore, the impact of these complex deformations on the surface and Coulomb contributions are obtained through the explicit calculations of integrals whereas here they were simply expressed as third order expansions. On the one hand, Warsaw's model is based on a microscopic potential and from this potential shell corrections are deduced using Strutinsky's method. On the other hand, the model from this chapter does not contain a microscopic potential and the shell corrections are obtained by bunching levels of a Fermi gas. Finally, Warsaw's model includes pairing correlations within the Bardeen-Cooper-Schrieffer theory while there is no microscopic pairing in the phenomenological model we have studied. It should be noted that the macroscopic and microscopic parts of Warsaw's model were adjusted separately. The microscopic part was fitted on a few selected nuclei for which the single-particle spectra is particularly well-known while the macroscopic part was adjusted on the masses of heavy nuclei, i.e., $Z \geq 84$ [51].

As already mentioned, we started to investigate the uncertainties in Warsaw's macroscopic-microscopic model. Up to now, we have concentrated our efforts on the macroscopic part of this model. However, the analysis is more complicated than for the models we have examined so far. Notice that in all of our previous analyses, experimental data was required in order to adjust the model. Our preliminary tests on a few macroscopic parameters, have shown that Warsaw's model is so finely tuned that minor changes in the experimental data used in the adjustment may have important consequences on the outcome of our analysis. Furthermore, since this model was adjusted many years ago, knowing precisely what data was used is very difficult. So far, we did not manage to reach satisfying results, i.e., the parameters obtained were not compatible (up to uncertainties) with those currently used. However, this analysis is still underway and we hope that the issues we have encountered will quickly be resolved by finding a suitable set of data for the adjustment of this realistic model.

7.14 Conclusion

In this chapter, we have studied the uncertainties in a simple phenomenological "macroscopic-microscopic" model. Although the model we have considered here is very simple it allowed us to account for some of the effects that were previously neglected in our analysis of the liquid drop model. More specifically, this model included shell corrections as well as a single deformation degree of freedom that described quadrupole deformations. Thus, we were able to determine the uncertainties in the ground-state and saddle-point masses which were then propagated onto the fission barriers. Note that the correlations between the ground-state and saddle-point masses are important and that they were accounted for in this analysis. Finally, we have seen that within this model, the uncertainties in the fission barriers were rather stable and about 0.5 MeV. Although in this thesis we have only presented the results for the plutonium isotopes, it should be mentioned that other similar results were obtained in the actinide region.

Chapter 8

Uncertainties in the capture step

As mentioned in chapter 2, fusion of heavy nuclei is divided into two steps, the first of which is known as the capture phase and essentially describes how the system overcomes the Coulomb barrier. The present chapter consists of an uncertainty analysis of the capture model presented in chapter 2. It is crucial to remember that our goal is to constrain the formation step and the analysis presented in this chapter plays an important part in our strategy. As in the previous chapters, this uncertainty analysis is based on regression analysis presented in chapters 4 and 5. Before jumping into this investigation and without duplicating all of the content formerly discussed in chapter 2, a brief summary of the major equations and of the way they enter the following study, may come in handy.

8.1 Equations and methodology

8.1.1 Summary of the major equations

As seen in chapter 2, the capture cross-section is expressed as

$$\sigma_{\rm cap} = \frac{\pi R^2 \sigma_B}{\sqrt{2\pi} E_{\rm cm}} \left[X\sqrt{\pi}(1+\mathrm{erf}(X)) + e^{-X^2} \right], \tag{8.1}$$

where

$$X = \frac{E_{\rm cm} - B_0}{\sqrt{2}\sigma_B}. \tag{8.2}$$

The cross-section normalization parameter, the mean barrier and the width of barrier distribution are, respectively, given by

$$\begin{aligned} R &= r_0(A_1^{1/3} + A_2^{1/3}), & (8.3)\\ B_0 &= az + bz^2 + cz^3, & (8.4)\\ \sigma_B &= CB_0\sqrt{W_1^2 + W_2^2 + W_0^2}. & (8.5) \end{aligned}$$

The Coulomb parameter is defined as $z = Z_1 Z_2/(A_1^{1/3} + A_2^{1/3})$ and $W_i^2 = R_i^2 \beta_{2i}^2/(4\pi)$ with $R_i = 1.15A^{1/3}$ and $i = 1, 2$. Thus, the parameters that have to be determined in order to make capture cross-section predictions are: r_0, a, b, c, C, W_0.

8.1.2 The methodology of the analysis

In order to determine the parameters entering the capture model, one must rely on experimental data. It is possible to extract the "experimental" barrier distribution by directly fitting Eq. (8.1) to well measured capture cross-sections. Consequently, for each reaction, one ends up with three values for R^{exp}, B_0^{exp} and σ_B^{exp}. It should be stressed that these values are specific to a single reaction. This extraction has been done in Ref. [94] where 48 reactions have been analysed in this way. The values obtained in Ref. [94] are reproduced in Table 8.1. It should be noted that the quadrupole deformations of the two colliding nuclei enter the expression for the width of the barrier distribution σ_B. These were taken from the tables of Möller [49] and are reproduced in Table 8.1.

These two sets of data, i.e., the "experimental" barrier distributions and quadrupole deformations, are at the heart of the forthcoming uncertainty analysis. It is important to notice that both, the "experimental" barrier distributions as well as the quadrupole deformations, should be accompanied by their respective uncertainties. However, these uncertainties are, at the moment, unavailable. Therefore, in our analysis we consider these quantities to be perfectly well defined and so, we neglect the fact that they could have uncertainties.

Now that we have described the data that we are about to use, we would like to explain how the next analysis is structured. The analysis is divided into three regressions:

1. The parameter r_0 is determined based on the "experimental" values for R^{exp}.
2. The parameters a, b and c are obtained using the "experimental" values for B_0^{exp}.
3. The parameters C and W_0 are determined using the "experimental" values for σ_B^{exp}.

It is important to realize that the mean barrier enters the expression of the width of the distribution, cf. Eq. (8.5). Therefore, the results from step 2 must be used in step 3. We would like to stress that in step 2 the uncertainties in a, b and c, are obtained. However, in our analysis, these are not propagated onto step 3. Thus, only the parameters a, b and c, are used in step 3 but not their uncertainties. In all three regressions, the uncertainties as well as the correlations between the parameters are obtained through regression analysis, as explained in chapter 5.

Once the uncertainties in the parameters have been determined, then, one can propagate them onto the parameters describing the theoretical barrier distribution, i.e., R, B_0 and σ_B. Finally, these uncertainties are, themselves, propagated onto σ_{cap}. In turn, this allows us to predict capture cross-sections accompanied by their uncertainties. Let us mention that, in the coming analysis, the propagation of uncertainties is done according to chapter 4 and in particular, using Eq. (4.42).

In this chapter, we investigate the uncertainties in the capture cross-section in three different ways. Thus, this chapter is composed of three parts. Part I, is based on linear regression. In this first part, only the "experimental" barrier distributions and the quadrupole deformations are used. Part II is also based on linear regression and on the same quadrupole deformations. However, the "experimental" barrier distributions will be supplemented by theoretical mean barriers. The reasons for including this additional data will be discussed later. Finally, in part III, we use the same set of data that in part II. However, in this third part, we use nonlinear regression instead. This allows us to quantify the effects of nonlinearity on the previous results.

8.2 Part I
Linear regression with "experimental" data

We now present the first part of our analysis, based on linear regression and on the data contained in Table 8.1. This table contains the "experimental" barrier distribution parameters from Ref. [94] as well as the quadrupole deformations from Ref. [49].

Reaction Number (i,j)	A_1	Z_1	A_2	Z_2	$B_0^{\rm exp}$ (MeV)	$\sigma_B^{\rm exp}$ (MeV)	$R^{\rm exp}$ (fm)	β_1	β_2
1	48	20	48	20	51.2	1.11	11.2	0	0
2	30	14	64	28	51.4	1.38	9.6	0	-0.087
3	30	14	62	28	52.1	1.55	9.7	0	-0.096
4	28	14	64	28	50.4	1.12	7.6	-0.478	-0.087
5	28	14	62	28	51.3	1.20	7.7	-0.478	-0.096
6	30	14	58	28	52.8	1.59	8.8	0	0
7	40	20	48	20	51.8	1.78	11.5	0	0
8	28	14	58	28	52.9	1.32	8.1	-0.478	0
9	40	20	44	20	51.8	1.59	7.9	0	0
10	40	20	40	20	53.6	1.60	9.5	0	0
11	36	16	64	28	56.8	1.17	8.5	0	-0.087
12	34	16	64	28	56.9	1.25	8.5	0	-0.087
13	40	20	50	22	57.3	1.72	9.4	0	0
14	40	20	48	22	57.1	1.50	9.4	0	0
15	32	16	64	28	57.3	1.57	8.1	0	-0.087
16	36	16	58	28	58.4	1.53	7.7	0	0
17	40	20	46	22	57.3	1.45	9.4	0	0
18	16	8	154	62	58.4	2.25	9.6	0.021	0.270
19	34	16	58	28	58.5	1.25	7.6	0	0
20	17	8	144	62	60.6	2.06	10.8	0.107	0
21	16	8	148	62	59.4	1.98	10.2	0.021	0.161
22	32	16	58	28	59.6	1.35	8.3	0	0
23	16	8	144	62	60.5	1.45	10.3	0.021	0
24	16	8	186	74	68.3	2.29	10.6	0.021	0.230
25	16	8	208	82	73.6	1.57	10.5	0.021	0
26	36	16	96	40	74.9	1.34	11.0	0	0.217
27	36	16	90	40	77.0	1.24	10.8	0	0.035
28	36	16	110	46	85.5	1.91	8.2	0	0.218
29	32	16	110	46	86.3	2.63	8.0	0	0.218
30	64	28	64	28	92.7	1.58	7.8	-0.087	-0.087
31	58	28	64	28	94.6	2.18	6.5	0	-0.087
32	40	20	96	40	93.6	2.65	9.3	0	0.217
33	58	28	60	28	96.6	1.93	7.5	0	0.027
34	40	20	90	40	96.1	1.53	10.0	0	0.035
35	58	28	58	28	95.8	1.18	6.0	0	0
36	40	18	122	50	103.6	2.58	9.8	0	0
37	40	18	116	50	103.3	2.23	8.7	0	0
38	40	18	112	50	104.0	2.26	8.9	0	0.018
39	64	28	74	32	103.2	1.97	6.5	-0.087	-0.224
40	58	28	74	32	106.8	2.96	7.0	0	-0.224
41	40	20	124	50	113.4	2.75	9.6	0	0
42	28	14	198	78	120.9	3.41	9.8	-0.478	-0.139
43	34	16	168	68	121.5	4.21	10.3	0	0.294
44	40	18	154	62	121.0	3.40	7.3	0	0.270
45	40	18	148	62	124.7	3.15	8.5	0	0.161
46	40	18	144	62	124.4	2.19	8.3	0	0
47	40	20	192	76	167.9	5.46	10.7	0	0.155
48	40	20	194	78	171.0	4.12	9.6	0	-0.148

Table 8.1: The "experimental" barrier distribution parameters obtained in Ref. [94] from 48 measured cross-sections are reproduced. The respective quadrupole deformations come from Ref. [49].

8.2.1 Parameters

Since the relationship between r_0 and R is linear, then, r_0 and its uncertainty are easily determined using multiple regression (cf. chapter 5). Similarly, a, b and c, are linearly related to B_0, so they can also be obtained in this way. The parameters along with their uncertainties and relative uncertainties are presented in Table 8.2. Examining the relative uncertainties, we see that r_0 and a are firmly determined while b and c are more loosely constrained.

	r_0		a		b		c	
$\hat{p}$	1.147	fm	0.918436	MeV	-0.0000963	MeV	0.000003898	MeV
$\hat{u}(\hat{p})$	0.027	fm	0.013668	MeV	0.0002567	MeV	0.000001136	MeV
$\lvert\hat{u}(\hat{p})/\hat{p}\rvert$	2.3	%	1.5	%	37.5	%	29.1	%

Table 8.2: Values and uncertainties of the parameters obtained through multiple regression using exclusively the "experimental" data from Table 8.1.

The correlations between the parameters a, b and c, are presented in Table 8.3 as deduced from the covariance matrix given in Table 8.4. It is clear that all three parameters are strongly correlated. Notice that parameters can only be correlated if they were determined from a common set of data. For instance, a, b and c, are correlated because they were all determined from the "experimental" mean barriers. This also explains why there are no correlations between r_0 and a, for instance.

a	b	c
1.00	-0.98	0.93
-0.98	1.00	-0.99
0.93	-0.99	1.00

Table 8.3: Correlation matrix between the coefficients a, b and c, obtained through multiple regression using exclusively the "experimental" data from Table 8.1. In dimensionless units.

a	b	c
1.8683e-04	-3.4333e-06	1.4518e-08
-3.4333e-06	6.5913e-08	-2.8766e-10
1.4518e-08	-2.8766e-10	1.2924e-12

Table 8.4: Covariance matrix between the coefficients a, b and c, obtained through multiple regression using exclusively the "experimental" data from Table 8.1. In MeV^2 units.

Notice that the relationship between W_0 and σ_B is not linear. Consequently, in order to use linear regression, we must rewrite Eq. (8.5) as

$$y = p_1 x_1 + p_2 x_2, \tag{8.6}$$

where $y = (\sigma_B^{\text{exp}})^2$ with the new parameters defined as $p_1 = C^2$ and $p_2 = C^2 W_0^2$ while the new variables are given by $X_1 = B_0^2(W_1^2 + W_2^2)$ and $X_2 = B_0^2$. This transformed expression enables us to use linear regression. Notice that through this method, we determine the uncertainties in p_1 and p_2, instead of those in C and W_0. Therefore, we must propagate the uncertainties in p_1 and p_2 onto C and W_0. Doing so, leads to the following expressions for the variances,

$$u^2(C) = \frac{u^2(p_1)}{4p_1}, \tag{8.7}$$

$$u^2(W_0) = \begin{bmatrix} -\frac{\sqrt{p_2}}{2(\beta_1)^{3/2}} & \frac{1}{2\sqrt{p_1 p_2}} \end{bmatrix} \begin{bmatrix} u^2(p_1) & u(p_1,p_2) \\ u(p_1,p_2) & u^2(p_2) \end{bmatrix} \begin{bmatrix} -\frac{\sqrt{p_2}}{2(p_1)^{3/2}} & \frac{1}{2\sqrt{p_1 p_2}} \end{bmatrix}^T, \tag{8.8}$$

where $u^2(p_1)$, $u^2(p_2)$ and $u(p_1, p_2)$, were directly obtained from multiple regression.

The parameters, their uncertainties and relative uncertainties are presented in Table 8.5. Inspecting the relative uncertainties, we identify that both C and W_0 are not precisely determined. As mentioned in Ref. [94], the widths of the barrier distributions are not very well reproduced by the model. Thus, the fact that the width parameters are not tightly constrained should not be a surprise (cf. chapter 2).

	C		W_0	
$\hat{p}$	0.0432	fm^{-1}	0.531	fm
$\hat{u}(\hat{p})$	0.0048	fm^{-1}	0.079	fm
$\lvert\hat{u}(\hat{p})/\hat{p}\rvert$	11.1	%	14.9	%

Table 8.5: Values and uncertainties of the parameters obtained through multiple regression using exclusively the "experimental" data from Table 8.1.

The covariance is given by

$$u(C, W_0) = \begin{bmatrix} \frac{1}{2\sqrt{p_1}} & 0 \end{bmatrix} \begin{bmatrix} u^2(p_1) & u(p_1,p_2) \\ u(p_1,p_2) & u^2(p_2) \end{bmatrix} \begin{bmatrix} -\frac{\sqrt{p_2}}{2(p_1)^{3/2}} & \frac{1}{2\sqrt{p_1 p_2}} \end{bmatrix}^T. \tag{8.9}$$

From the previous expression, we find that the covariance is $u(C, W_0) = -3.7190 \times 10^{-4}$ and the correlation coefficient is equal to -0.98. Therefore, the width parameters are extremely correlated.

8.2.2 Predictions of R, B_0 and σ_B for a given reaction

We have previously determined all the parameters entering the capture model along with their uncertainties and their correlations. Therefore, we can now propagate these uncertainties onto R, B_0 and σ_B. The propagation of these uncertainties leads us to

$$u^2(R) = \left[(A_1^{\frac{1}{3}} + A_2^{\frac{1}{3}})\right] u^2(r) \left[(A_1^{\frac{1}{3}} + A_2^{\frac{1}{3}})\right]^T, \tag{8.10}$$

$$u^2(B_0) = \begin{bmatrix} z & z^2 & z^3 \end{bmatrix} \begin{bmatrix} u^2(a) & u(a,b) & u(a,c) \\ u(a,b) & u^2(b) & u(b,c) \\ u(a,c) & u(b,c) & u^2(c) \end{bmatrix} \begin{bmatrix} z & z^2 & z^3 \end{bmatrix}^T, \tag{8.11}$$

$$u^2(\sigma_B) = \begin{bmatrix} C\sqrt{W_1^2+W_2^2+W_0^2} \\ B_0\sqrt{W_1^2+W_2^2+W_0^2} \\ \frac{CB_0W_0}{\sqrt{W_1^2+W_2^2+W_0^2}} \end{bmatrix}^T \begin{bmatrix} u^2(B_0) & 0 & 0 \\ 0 & u^2(C) & u(C,W_0) \\ 0 & u(C,W_0) & u^2(W_0) \end{bmatrix} \begin{bmatrix} C\sqrt{W_1^2+W_2^2+W_0^2} \\ B_0\sqrt{W_1^2+W_2^2+W_0^2} \\ \frac{CB_0W_0}{\sqrt{W_1^2+W_2^2+W_0^2}} \end{bmatrix}. \tag{8.12}$$

The theoretical values for R, B_0 and σ_B, are reported in Table 8.6 with their uncertainties and for every reaction in Table 8.1. Notice that most of these predictions are incompatible with their corresponding "experimental" values. Nevertheless, it should be noted that the distance between theory and "experiment" is rather significant for σ_B while being much more minor for R and B_0. This was already noticed in Ref. [94] where it was graphically shown that the model is capable of accurately reproducing the mean barriers and that the widths of the distributions are not so finely reproduced (cf. Figs. 2.1a and 2.1b in chapter 2). Additionally, one may argue that, although R^{exp}, B_0^{exp} and σ_B^{exp}, are not perfectly reproduced, it does not imply that the cross-section will suffer from the same imperfections. Indeed, all three quantities enter the cross-section prediction and the correlations, involving the mean barrier and the width of the barrier distribution, may resolve part of these issues.

The covariance between the mean barrier and the width of the barrier distribution is given by

$$u(B_0, \sigma_B) = C\sqrt{W_1^2 + W_2^2 + W_0^2}\, u^2(B_0). \tag{8.13}$$

It turns out that this quantity enters the variance of the capture cross-section as

$$u^2(\sigma_{\text{cap}}) = \begin{bmatrix} \frac{\partial\sigma_{\text{cap}}}{\partial R} & \frac{\partial\sigma_{\text{cap}}}{\partial B_0} & \frac{\partial\sigma_{\text{cap}}}{\partial\sigma_B} \end{bmatrix} \begin{bmatrix} u^2(R) & 0 & 0 \\ 0 & u^2(B_0) & u(B_0,\sigma_B) \\ 0 & u(B_0,\sigma_B) & u^2(\sigma_B) \end{bmatrix} \begin{bmatrix} \frac{\partial\sigma_{\text{cap}}}{\partial R} & \frac{\partial\sigma_{\text{cap}}}{\partial B_0} & \frac{\partial\sigma_{\text{cap}}}{\partial\sigma_B} \end{bmatrix}^T, \tag{8.14}$$

where

$$\frac{\partial\sigma_{\text{cap}}}{\partial R} = \frac{\sqrt{2\pi}R\sigma_B}{E_{\text{cm}}}\left[X\sqrt{\pi}(1+\text{erf}(X)) + e^{-X^2}\right], \tag{8.15}$$

$$\frac{\partial\sigma_{\text{cap}}}{\partial B_0} = -\frac{\pi R^2}{2E_{\text{cm}}}(1+\text{erf}(X)), \tag{8.16}$$

$$\frac{\partial\sigma_{\text{cap}}}{\partial\sigma_B} = \frac{\pi R^2}{\sqrt{2\pi}E_{\text{cm}}}e^{-X^2}. \tag{8.17}$$

With the previous expression, it is now possible to predict the capture cross-section with its uncertainty for any given center-of-mass energy.

Reaction Number (i,j)	B_0 (MeV)	σ_B (MeV)	R (fm)	$B_0^{\rm exp}$ (MeV)	$\sigma_B^{\rm exp}$ (MeV)	$R^{\rm exp}$ (fm)
1	50.90 ± 0.19	1.17 ± 0.06	8.34 ± 0.20	51.2	1.11	11.2
2	51.02 ± 0.19	1.20 ± 0.05	8.16 ± 0.19	51.4	1.38	9.6
3	51.33 ± 0.19	1.21 ± 0.05	8.11 ± 0.19	52.1	1.55	9.7
4	51.54 ± 0.19	1.60 ± 0.06	8.07 ± 0.19	50.4	1.12	7.6
5	51.86 ± 0.19	1.62 ± 0.06	8.03 ± 0.19	51.3	1.20	7.7
6	51.98 ± 0.19	1.19 ± 0.06	8.01 ± 0.19	52.8	1.59	8.8
7	52.48 ± 0.19	1.21 ± 0.06	8.09 ± 0.19	51.8	1.78	11.5
8	52.52 ± 0.19	1.61 ± 0.06	7.93 ± 0.19	52.9	1.32	8.1
9	53.28 ± 0.19	1.22 ± 0.06	7.98 ± 0.19	51.8	1.59	7.9
10	54.16 ± 0.19	1.24 ± 0.06	7.85 ± 0.19	53.6	1.60	9.5
11	56.89 ± 0.18	1.34 ± 0.06	8.38 ± 0.20	56.8	1.17	8.5
12	57.39 ± 0.18	1.35 ± 0.06	8.31 ± 0.20	56.9	1.25	8.5
13	57.44 ± 0.18	1.32 ± 0.06	8.15 ± 0.19	57.3	1.72	9.4
14	57.86 ± 0.18	1.33 ± 0.06	8.09 ± 0.19	57.1	1.50	9.4
15	57.92 ± 0.17	1.36 ± 0.06	8.23 ± 0.19	57.3	1.57	8.1
16	57.94 ± 0.17	1.33 ± 0.06	8.23 ± 0.19	58.4	1.53	7.7
17	58.29 ± 0.17	1.34 ± 0.06	8.04 ± 0.19	57.3	1.45	9.4
18	58.40 ± 0.17	1.79 ± 0.06	9.04 ± 0.21	58.4	2.25	9.6
19	58.46 ± 0.17	1.34 ± 0.06	8.16 ± 0.19	58.5	1.25	7.6
20	58.92 ± 0.17	1.37 ± 0.06	8.97 ± 0.21	60.6	2.06	10.8
21	58.94 ± 0.17	1.53 ± 0.04	8.96 ± 0.21	59.4	1.98	10.2
22	59.01 ± 0.17	1.36 ± 0.06	8.08 ± 0.19	59.6	1.35	8.3
23	59.32 ± 0.17	1.36 ± 0.06	8.91 ± 0.21	60.5	1.45	10.3
24	67.03 ± 0.16	1.98 ± 0.06	9.44 ± 0.22	68.3	2.29	10.6
25	72.59 ± 0.15	1.67 ± 0.08	9.69 ± 0.23	73.6	1.57	10.5
26	76.04 ± 0.15	2.04 ± 0.05	9.04 ± 0.21	74.9	1.34	11.0
27	77.04 ± 0.15	1.78 ± 0.08	8.93 ± 0.21	77.0	1.24	10.8
28	85.66 ± 0.17	2.34 ± 0.06	9.29 ± 0.22	85.5	1.91	8.2
29	87.11 ± 0.17	2.37 ± 0.06	9.14 ± 0.22	86.3	2.63	8.0
30	92.75 ± 0.18	2.23 ± 0.08	9.18 ± 0.22	92.7	1.58	7.8
31	94.38 ± 0.19	2.22 ± 0.09	9.03 ± 0.21	94.6	2.18	6.5
32	94.79 ± 0.19	2.55 ± 0.06	9.18 ± 0.22	93.6	2.65	9.3
33	95.49 ± 0.19	2.20 ± 0.10	8.93 ± 0.21	96.6	1.93	7.5
34	96.05 ± 0.19	2.22 ± 0.10	9.07 ± 0.21	96.1	1.53	10.0
35	96.07 ± 0.19	2.21 ± 0.10	8.88 ± 0.21	95.8	1.18	6.0
36	102.36 ± 0.21	2.35 ± 0.11	9.62 ± 0.23	103.6	2.58	9.8
37	103.47 ± 0.21	2.38 ± 0.11	9.52 ± 0.22	103.3	2.23	8.7
38	104.24 ± 0.21	2.40 ± 0.11	9.46 ± 0.22	104.0	2.26	8.9
39	104.31 ± 0.21	2.81 ± 0.07	9.41 ± 0.22	103.2	1.97	6.5
40	106.13 ± 0.22	2.81 ± 0.07	9.26 ± 0.22	106.8	2.96	7.0
41	114.45 ± 0.23	2.63 ± 0.12	9.65 ± 0.23	113.4	2.75	9.6
42	118.96 ± 0.24	3.90 ± 0.17	10.17 ± 0.24	120.9	3.41	9.8
43	120.09 ± 0.24	3.89 ± 0.16	10.05 ± 0.24	121.5	4.21	10.3
44	123.19 ± 0.25	3.78 ± 0.13	10.08 ± 0.24	121.0	3.40	7.3
45	124.30 ± 0.25	3.22 ± 0.08	9.99 ± 0.24	124.7	3.15	8.5
46	125.08 ± 0.25	2.87 ± 0.14	9.94 ± 0.23	124.4	2.19	8.3
47	166.93 ± 0.58	4.37 ± 0.11	10.54 ± 0.25	167.9	5.46	10.7
48	171.77 ± 0.67	4.46 ± 0.12	10.57 ± 0.25	171.0	4.12	9.6
RMS	0.92	0.44	1.47			

Table 8.6: Predictions and their uncertainties, obtained through multiple linear regression using exclusively the "experimental" data given in Table 8.1. The last line shows the root-mean-square deviation between the "experimental" data and the corresponding predictions. The three rightmost columns reproduce the "experimental" data used in order to adjust the model.

8.2.3 Examples solely based on "experimental" data

Thus far, we have determined the parameters, their uncertainties and their correlations which were then propagated onto the capture cross-section. We now present a few examples where the theoretical capture cross-sections are presented and accompanied by their uncertainties.

The capture cross-section for the reaction ^{36}S+^{90}Zr→^{126}Ba* is displayed in Fig. 8.1a. This is one of the reactions that we have used in order to adjust the model (cf. Table 8.1). Note that for energies away from the barrier energy, the model is not able to reproduce the data. More specifically, the cross-section is too large at low energy and too small at high energy. This type of behaviour is typical of an overestimated width of the barrier distribution. As mentioned several times before, the width of the barrier distribution is, in general, not very well reproduced by this model.

However, the purpose of this model is to make capture cross-section predictions for the synthesis of superheavy nuclei. Therefore, we now take a look at a reaction outside the scope of the "experimental" data used to adjust the model. The capture cross-section for the reaction ^{48}Ca+^{238}U→^{286}Cn* is given in Fig. 8.1b. The results suggest that the model reproduces the data even better than in the previous case. Nevertheless, the energy range where the finest agreement can be found is close to the barrier energy. It should be mentioned that for the synthesis of superheavy nuclei, near barrier energies are of the outmost importance, since they, certainly, maximize the probability of overcoming the Coulomb barrier while keeping the system at low excitation energy, thus improving the chances of survival.

Furthermore, predictions in regions where no measurements have ever been made are also possible. For instance, Fig. 8.2a shows the estimated capture cross-section for the reaction ^{51}V+^{248}Cm→^{299}119* which is currently used at RIKEN as a first attempt to produce the element 119. Similarly, Fig. 8.2b shows the capture cross-section for the reaction ^{54}Cr+^{248}Cm→^{302}120* which will be used in Dubna to synthesize the element 120 for the first time. Notice Fig. 8.1 display thinner uncertainty bands than Fig. 8.2. The former describes reactions closely resembling the data used to adjust the model while the latter shows extrapolations way beyond this data, consequently, the associated uncertainties are significantly larger.

The Figs. 8.1 and 8.2 exhibit a bottleneck shape associated with the apparent reduction of uncertainties with increasing center-of-mass energy. This however, is only owed to the logarithmic scale and switching scales disproofs this interpretation. To illustrate this remark, Fig. 8.2b was transformed to a linear scale. The result, displayed in Fig. 8.3, clearly shows the growth of uncertainties with increasing center-of-mass energy.

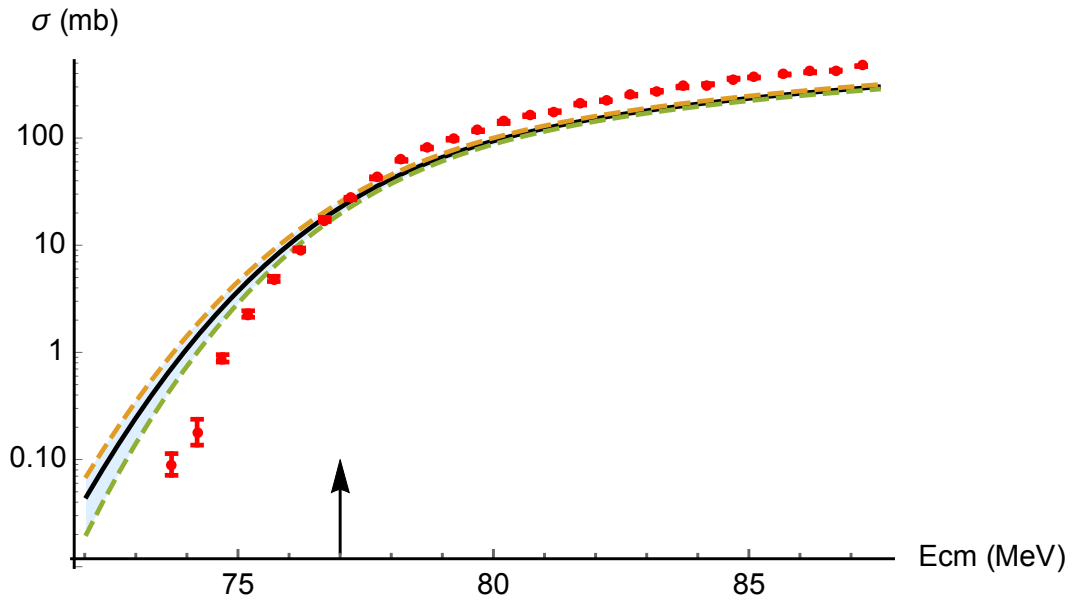

(a) ^{36}S+^{90}Zr→^{126}Ba*

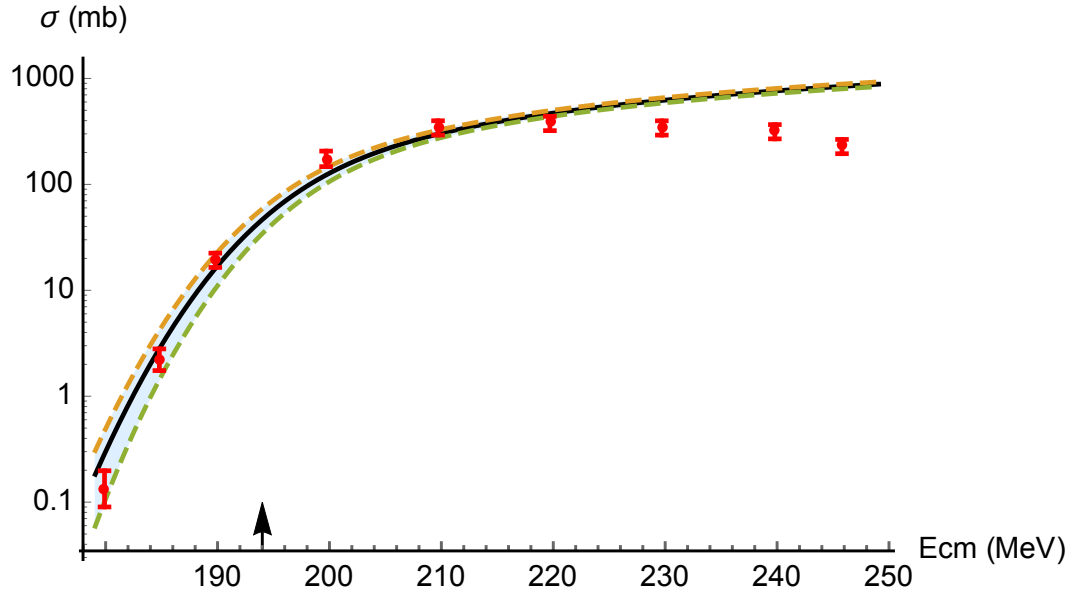

(b) ^{48}Ca+^{238}U→^{286}Cn*

Figure 8.1: Capture cross-section as a function of center-of-mass energy. Theoretical capture cross-section (black line) with lower uncertainty bound (green dashed line) and upper uncertainty bound (orange dashed line). The arrow represents the barrier energy. Fig. 8.1a presents the results for the reaction ^{36}S+^{90}Zr→^{126}Ba* along with the experimental data (red dots) which were taken from Ref. [95]. Fig. 8.1b presents the results for the reaction ^{48}Ca+^{238}U→^{286}Cn* along with the experimental data (red dots) which were taken from Ref. [96].

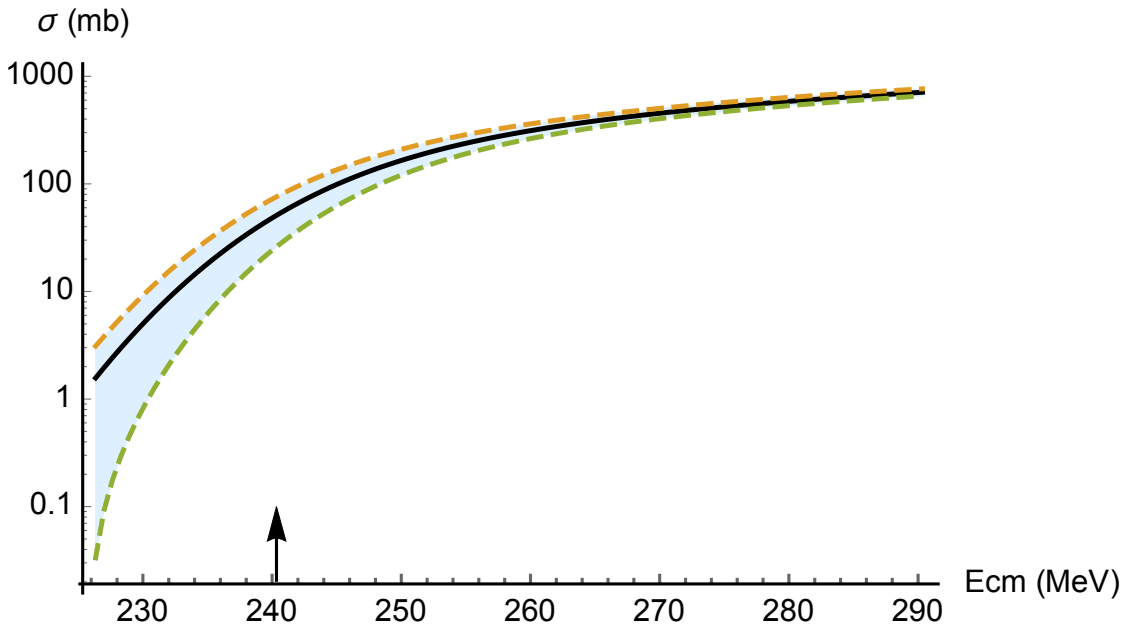

(a) ^{51}V+^{248}Cm→^{299}119*

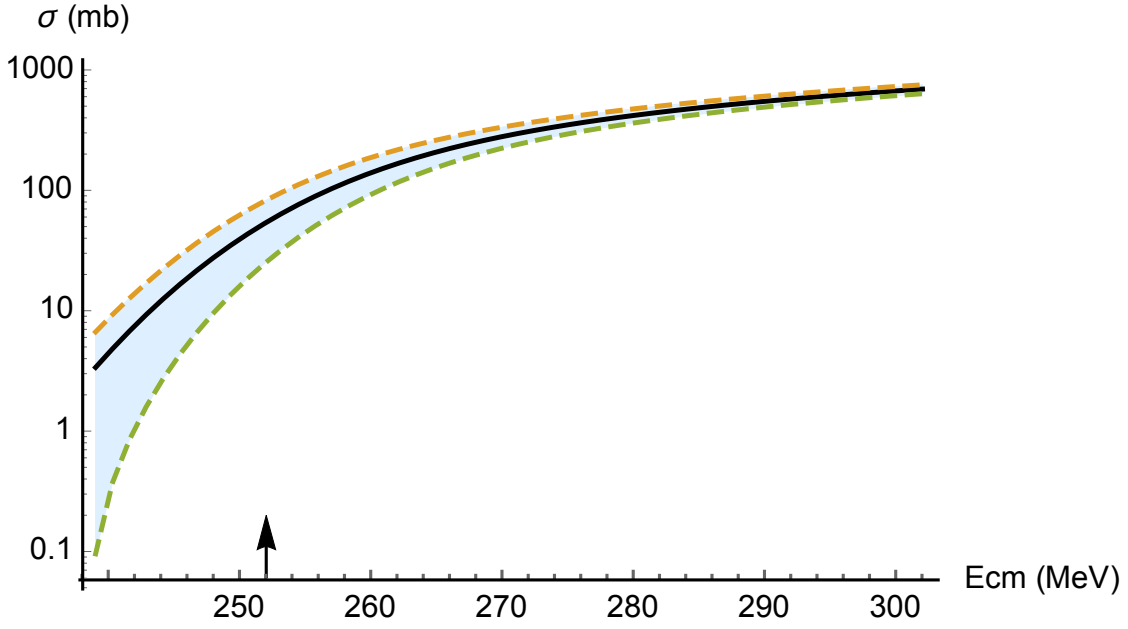

(b) ^{54}Cr+^{248}Cm→^{302}120*

Figure 8.2: Capture cross-section as a function of center-of-mass energy. Theoretical capture cross-section (black line) with lower uncertainty bound (green dashed) and upper uncertainty bound (orange dashed). The arrow represents the barrier energy. Fig. 8.2a represents the capture cross-section prediction for the reaction ^{51}V+^{248}Cm→^{299}119*. Fig. 8.2b represents the capture cross-section prediction for the reaction ^{54}Cr+^{248}Cm→^{302}120*.

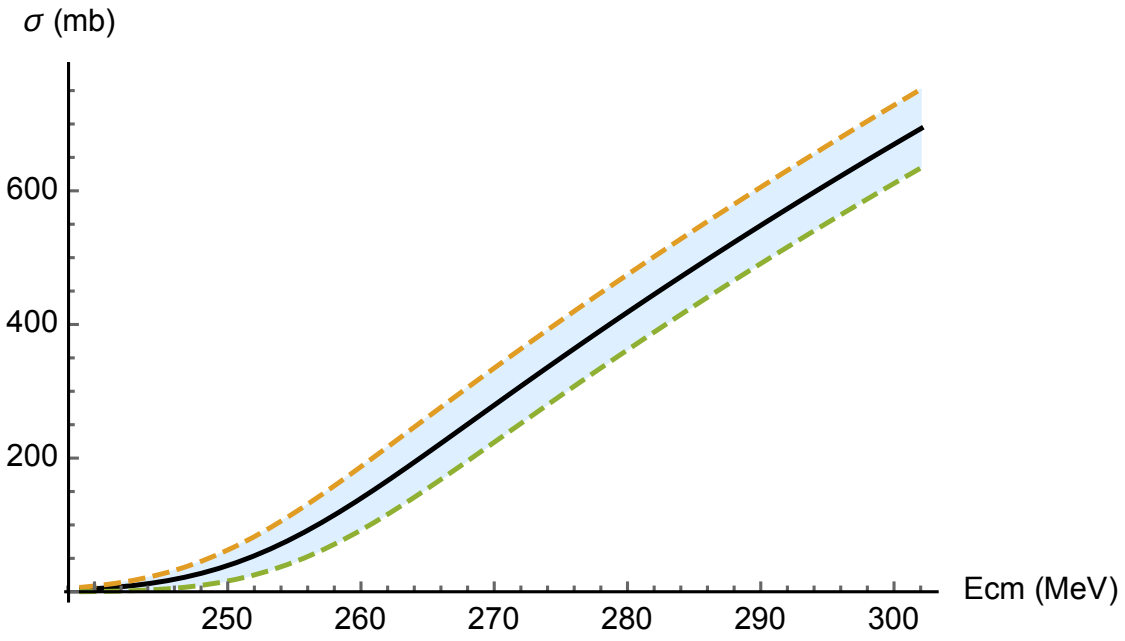

Figure 8.3: Capture cross-section as a function of center-of-mass energy for the reaction ^{54}Cr+^{248}Cm$\rightarrow^{302}$120* in linear scale. Theoretical capture cross-section (black line) with lower uncertainty bound (green dashed line) and upper uncertainty bound (orange dashed line).

8.3 Part II
Linear regression with "experimental" and theoretical data

The capture model we are currently investigating is based on Refs. [36,40]. In those references, the model is adjusted with the same data that we have used the in previous section (cf. Table 8.1). However, in addition to this "experimental" data, a handful of theoretical values for the mean barriers are also used. In Refs. [36, 40] the supplementary mean barriers are calculated using the nucleus-nucleus potential from the proximity theory [97]. Then, as explained in Ref. [36], these mean barriers are systematically lowered by several MeVs in order to better reproduce the measured mean barriers of lighter systems. Here instead, we have chosen to use the empirical nucleus-nucleus potential taken from Ref. [94]. Using this potential, we do not systematically lower the theoretical mean barriers. It should be mentioned that, although we use a different nucleus-nucleus potential, our results are very close to those presented in [40]. Next, we present the empirical nucleus-nucleus potential and then, return to our uncertainty analysis.

8.3.1 The empirical nucleus-nucleus potential

In the following, the additional mean barriers are obtained from the empirical nucleus-nucleus potential [94]. Let us now describe how this potential is constructed. Note that our presentation follows very closely the one of the original work [94].

The empirical nucleus-nucleus potential V is built as the sum of two independent components, the attractive nuclear interaction V_n and the repulsive Coulomb interaction, V_c. Thus, the nucleus-nucleus potential reads

$$V(r) = V_n(r) + V_c(r), \tag{8.18}$$

where r is the relative distance between the two colliding nuclei.

The Coulomb nucleus-nucleus interaction, prior to contact, takes its usual form

$$V_c(r) = \frac{Z_1 Z_2 e^2}{r} \quad \text{when} \quad r \geq R_1 + R_2, \tag{8.19}$$

where Z_1 and Z_2 are the respective proton numbers of the two colliding nuclei. Similarly, R_1 and R_2 are the respective radii of the two nuclei engaged in the collision. As usual, $R_i = r_0 A_i^{1/3}$ and for heavy systems, it was found that $r_0 = 1.11$ fm [94]. Although the notations are identical, the above r_0 is different from the one entering the capture model.

The nuclear interaction is given by the following Woods-Saxon contribution,

$$V_n(r) = \frac{-V_0}{1 + \exp[(r - (R_1 + R_2))/a]}, \tag{8.20}$$

where a is the nuclear diffuseness parameter and for heavy systems, it was found that $a = 0.895$ fm [94].

Unlike r_0 and a, the value for V_0 is specific to every reaction. The maximal depth of the nuclear contribution is reached at $r = 0$ when the system has completely fused. Therefore, V_0 will be a property of the compound nucleus and of the two colliding nuclei. Excluding shell effects, the depth of the nuclear contribution to the nucleus-nucleus interaction, denoted V_0', is the difference between the binding energies resulting from the nuclear interaction before and after fusion, respectively, $N_1 + N_2$ and N_{CN}, thus

$$V_0' = N_{CN} - N_1 - N_2. \tag{8.21}$$

Assuming that the total binding energy B is increased by an attractive nuclear contribution N and reduced by a repulsive Coulomb contribution C, then, $B = N - C$. From this, it follows that

$$V_0' = (B_{CN} - B_1 - B_2) + (C_{CN} - C_1 - C_2), \tag{8.22}$$

where CN stands for compound nucleus and the numeral indices stand for either one of the two colliding nuclei. From the relationship connecting binding energies to masses ($M = ZM_P + NM_N - B$, in units where $c = 1$) we gather,

$$V_0' = (M_1 + M_2 - M_{CN}) + (C_{CN} - C_1 - C_2). \tag{8.23}$$

We recognize, in the last expression, the fusion Q-value,

$$Q_{\rm fus} = M_1 + M_2 - M_{CN}. \tag{8.24}$$

We also identify the Coulomb contribution

$$C_0 = C_{CN} - C_1 - C_2 = 0.7054 \left[\frac{(Z_1+Z_2)^2}{(A_1+A_2)^{1/3}} - \frac{Z_1^2}{A_1^{1/3}} - \frac{Z_2^2}{A_2^{1/3}} \right] \tag{8.25}$$

where the pre-factor has been obtained through a liquid drop model and is given in MeV (cf. Ref. [94] for more details).

In some cases, the mass of the compound nucleus, appearing in the above relationships, has never been measured, consequently, it has to be determined from theoretical calculations. Here, we have used Möller's table [49]. In this table macroscopic masses are corrected in order to account for shell effects. Strong shell effects are a consequence of special nuclear shapes, giving rise to degeneracy, that stabilize the system. The nuclear potential is valid over a wide range of values of r, all of which, correspond to different shapes of the dinuclear system. Most of these shapes may not give rise to significant shell effects. Consequently, for the nuclear potential to be valid over a broad range of relative distances, the shell corrections must be removed from the theoretical estimate of M_{CN}. Finally, we gather from all prior arguments that the expression for the depth of the nuclear contribution is

$$V_0 = Q_{\rm fus} + C_0 + S_{CN}, \tag{8.26}$$

where S_{CN} is the shell correction energy of the compound nucleus taken directly from Ref. [49]. Note that for the sake of consistency, all other masses will also be taken from Möller's table [49].

Since the Coulomb barrier is positioned prior to contact, going beyond the point-charge approximation of Eq. (8.19) seems fruitless, nevertheless, it is possible to construct a potential extending beyond the contact point. Consequently, the Coulomb contribution is expressed as

$$V_c(r) = k_1 + \frac{k_2}{1+\exp\left[(r-R_1-R_2)/a_c\right]} \quad \text{when} \quad r \leq R_1 + R_2. \tag{8.27}$$

A pair of equations, for the parameters k_1, k_2 and a_c, can be obtained by enforcing the continuity of the potential and its first derivative, at contact. A third equation is given by the fact that $V_c(r=0) = C_0$. The system can then be solved which leads to

$$\begin{aligned} k_1 &= 2C_{R0} - C_0, & (8.28)\\ k_2 &= 2C_0 - 2C_{R0}, & (8.29)\\ a_c &= R_0(C_0 - C_{R0})/(2C_{R0}), & (8.30)\\ C_{R0} &= Z_1 Z_2 e^2/R_0. & (8.31) \end{aligned}$$

The various contributions of the empirical nucleus-nucleus potential are depicted in Fig. 8.4, for the reaction ^{54}Cr + ^{208}Pb $\longrightarrow$ ^{266}Sg*.

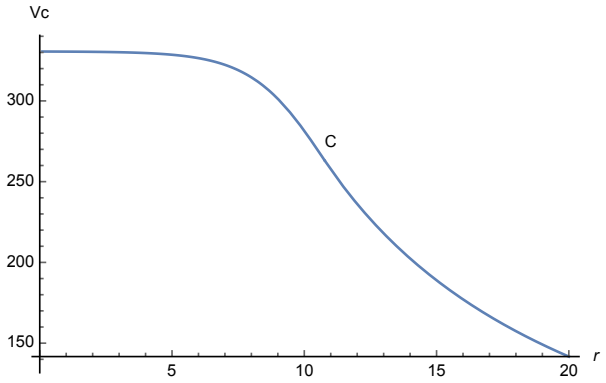

(a) Coulomb potential

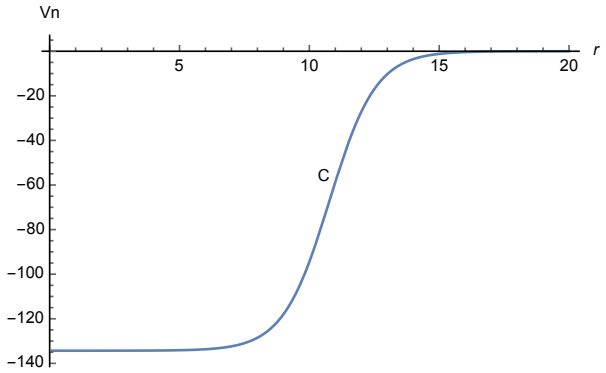

(b) Nuclear potential

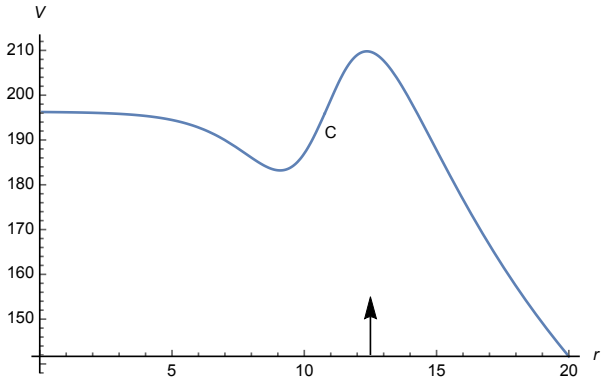

(c) Total potential

Figure 8.4: The empirical nucleus-nucleus potential is shown as a function of the relative distance between the two colliding nuclei. The Coulomb, nuclear and total potentials are, respectively, placed at the top, middle and bottom of this figure. The reaction considered here is ^{54}Cr + ^{208}Pb $\longrightarrow$ ^{266}Sg*. The arrow pinpoints the energy of the Coulomb barrier and C labels the position of the contact point.

8.3.2 Additional theoretical mean barriers

Using the empirical nucleus-nucleus potential, we have deduced the theoretical mean barriers B_0^{Th}. This additional data is presented in Table 8.7 where only lead targets have been considered as well as typical projectiles. Note that the differences between B_0^{Th} and B_0^{PartI} are important. Consequently, we expect that the additional data will strongly influence the results of our extended analysis. The inclusion of bismuth targets while keeping the same projectiles, does not, significantly alter the following results.

Reaction Number (i,j)	A_1	Z_1	A_2	Z_2	ME_1 (MeV)	ME_2 (MeV)	ME_{CN} (MeV)	S_{CN} (MeV)	B_0^{Th} (MeV)	B_0^{PartI} (MeV)
49	48	20	208	82	-43.79	-21.15	87.42	-4.19	176.1	174.4 ± 0.7
50	46	22	208	82	-45.10	-21.15	92.39	-4.12	193.0	197.4 ± 1.3
51	50	22	208	82	-52.30	-21.15	95.80	-4.49	193.0	194.8 ± 1.2
52	56	26	208	82	-60.72	-21.15	118.73	-4.86	225.4	237.0 ± 2.8
53	64	28	208	82	-66.96	-21.15	113.82	-6.55	237.9	255.6 ± 3.7
54	58	28	208	82	-60.84	-21.15	131.78	-4.53	241.4	260.2 ± 4.0
55	74	32	208	82	-73.34	-21.15	165.00	-6.57	271.6	299.5 ± 6.4
56	86	36	208	82	-83.00	-21.15	195.88	-7.67	302.1	345.1 ± 9.7
57	54	24	208	82	-57.47	-21.15	107.83	-4.63	209.1	214.8 ± 1.9
58	62	28	208	82	-66.44	-21.15	132.68	-5.85	240.9	257.1 ± 3.8
59	70	30	208	82	-69.92	-21.15	151.01	-5.06	255.7	276.4 ± 4.9

Table 8.7: Supplement of theoretical data for the mean barrier parametrization. The theoretical barriers, denoted B_0^{Th}, were obtained from the empirical nucleus-nucleus potential [94]. The mass excess of the projectile, the target and compound nucleus, respectively, ME_1, ME_2 and ME_{CN}, along with the shell correction energy of the compound nucleus S_{CN}, were taken from Ref. [49]. The rightmost column contains the predictions and their uncertainties obtained using the results of part I.

8.3.3 Analysis based on theoretically supplemented "experimental" data

Now that we have obtained a set of supplementary theoretical mean barriers, we return to our uncertainty analysis regarding the capture model. What follows is a repetition of the previous uncertainty analysis, based on the "experimental" data (cf. Table 8.1). However, here the additional theoretical mean barriers are included in the regression (cf. Table 8.7).

Of course, as can be seen in Table 8.8, the parameter r_0 is left unchanged by the additional data and obviously, the coefficients a, b and c, are those that suffer the most change. Less expected, are the variations of C and W_0, coming from the mean barrier entering the expression of the width of the barrier distribution. It should be mentioned that all the coefficients are compatible with those obtained in Ref. [40]. Let us stress that the additional mean barriers used in Ref. [40] are provided by the proximity theory [97] which is different from the empirical nucleus-nucleus potential [94], used in the present work. Although the additional reactions considered here are typical, they may also differ from those considered in Ref. [40]. Since our results are compatible with those of the original work [40], it seems that these differences are not too important.

	r_0		a		b		c		C		W_0	
$\hat{p}$ from [40]	1.16	fm	0.853315	MeV	0.0011695	MeV	-0.000001544	MeV	0.0421	fm^{-1}	0.531	fm
$\hat{p}$	1.147	fm	0.857638	MeV	0.0011158	MeV	-0.000001467	MeV	0.0428	fm^{-1}	0.535	fm
$\hat{u}(\hat{p})$	0.027	fm	0.008285	MeV	0.0001067	MeV	0.000000306	MeV	0.0048	fm^{-1}	0.081	fm
$\lvert\hat{u}(\hat{p})/\hat{p}\rvert$	2.3	%	1.0	%	9.6	%	21.1	%	11.2	%	15.1	%

Table 8.8: Values and uncertainties of the parameters obtained through multiple regression using the "experimental" data from Table 8.1 and the theoretical supplement from Table 8.7. All the coefficients are compatible with those obtained in Ref. [40], presented in the first row.

The covariances and correlations of a, b and c, are scaled down by the addition of theoretical data. This can be seen by confronting the results in Table 8.3 to those in Table 8.9.

Again using Eq. (8.9), we find that the covariance is $u(C, W_0) = -3.8799 \times 10^{-4}$ and the correlation coefficient is equal to -0.98 which is the value we had previously found in part I. As before, the width parameters are extremely correlated.

a	b	c
1.00	-0.96	0.91
-0.96	1.00	-0.99
0.91	-0.99	1.00

Table 8.9: Correlation matrix between the coefficients a, b and c, obtained through multiple regression using the "experimental" data from Table 8.1 and the theoretical supplement from Table 8.7. In dimensionless units.

a	b	c
6.8657e-05	-8.4854e-07	2.2979e-09
-8.4854e-07	1.1395e-08	-3.2236e-11
2.2979e-09	-3.2236e-11	9.3918e-14

Table 8.10: Covariance matrix between the coefficients a, b and c, obtained through multiple regression using the "experimental" data from Table 8.1 and the theoretical supplement from Table 8.7. In MeV^2 units.

The predictions for R, B_0 and σ_B are provided with their uncertainties, for every reaction considered, either experimentally or theoretically, in Table 8.11.

Reaction Number (i,j)	B_0 (MeV)	σ_B (MeV)	R (fm)	$B_0^{\exp}$ (MeV)	$\sigma_B^{\exp}$ (MeV)	$R^{\exp}$ (fm)
1	50.33 ± 0.20	1.16 ± 0.06	8.34 ± 0.20	51.2	1.11	11.2
2	50.45 ± 0.20	1.19 ± 0.05	8.16 ± 0.19	51.4	1.38	9.6
3	50.77 ± 0.20	1.20 ± 0.05	8.11 ± 0.19	52.1	1.55	9.7
4	50.99 ± 0.20	1.58 ± 0.06	8.07 ± 0.19	50.4	1.12	7.6
5	51.31 ± 0.20	1.59 ± 0.06	8.03 ± 0.19	51.3	1.20	7.7
6	51.44 ± 0.20	1.18 ± 0.06	8.01 ± 0.19	52.8	1.59	8.8
7	51.95 ± 0.20	1.19 ± 0.06	8.09 ± 0.19	51.8	1.78	11.5
8	52.00 ± 0.20	1.59 ± 0.06	7.93 ± 0.19	52.9	1.32	8.1
9	52.77 ± 0.21	1.21 ± 0.06	7.98 ± 0.19	51.8	1.59	7.9
10	53.68 ± 0.21	1.23 ± 0.06	7.85 ± 0.19	53.6	1.60	9.5
11	56.48 ± 0.21	1.33 ± 0.06	8.38 ± 0.20	56.8	1.17	8.5
12	57.00 ± 0.21	1.34 ± 0.06	8.31 ± 0.20	56.9	1.25	8.5
13	57.05 ± 0.21	1.31 ± 0.06	8.15 ± 0.19	57.3	1.72	9.4
14	57.48 ± 0.20	1.32 ± 0.06	8.09 ± 0.19	57.1	1.50	9.4
15	57.54 ± 0.20	1.35 ± 0.06	8.23 ± 0.19	57.3	1.57	8.1
16	57.56 ± 0.20	1.32 ± 0.06	8.23 ± 0.19	58.4	1.53	7.7
17	57.93 ± 0.20	1.33 ± 0.06	8.04 ± 0.19	57.3	1.45	9.4
18	58.04 ± 0.20	1.77 ± 0.06	9.04 ± 0.21	58.4	2.25	9.6
19	58.10 ± 0.20	1.34 ± 0.06	8.16 ± 0.19	58.5	1.25	7.6
20	58.57 ± 0.20	1.36 ± 0.06	8.97 ± 0.21	60.6	2.06	10.8
21	58.60 ± 0.20	1.52 ± 0.04	8.96 ± 0.21	59.4	1.98	10.2
22	58.67 ± 0.20	1.35 ± 0.06	8.08 ± 0.19	59.6	1.35	8.3
23	58.98 ± 0.20	1.36 ± 0.06	8.91 ± 0.21	60.5	1.45	10.3
24	66.94 ± 0.20	1.97 ± 0.06	9.44 ± 0.22	68.3	2.29	10.6
25	72.67 ± 0.20	1.67 ± 0.08	9.69 ± 0.23	73.6	1.57	10.5
26	76.22 ± 0.20	2.04 ± 0.05	9.04 ± 0.21	74.9	1.34	11.0
27	77.25 ± 0.20	1.78 ± 0.08	8.93 ± 0.21	77.0	1.24	10.8
28	86.12 ± 0.19	2.34 ± 0.06	9.29 ± 0.22	85.5	1.91	8.2
29	87.60 ± 0.19	2.38 ± 0.06	9.14 ± 0.22	86.3	2.63	8.0
30	93.38 ± 0.19	2.24 ± 0.08	9.18 ± 0.22	92.7	1.58	7.8
31	95.05 ± 0.19	2.23 ± 0.09	9.03 ± 0.21	94.6	2.18	6.5
32	95.47 ± 0.19	2.56 ± 0.06	9.18 ± 0.22	93.6	2.65	9.3
33	96.18 ± 0.20	2.22 ± 0.10	8.93 ± 0.21	96.6	1.93	7.5
34	96.75 ± 0.20	2.23 ± 0.10	9.07 ± 0.21	96.1	1.53	10.0
35	96.77 ± 0.20	2.22 ± 0.11	8.88 ± 0.21	95.8	1.18	6.0
36	103.17 ± 0.20	2.37 ± 0.11	9.62 ± 0.23	103.6	2.58	9.8
37	104.29 ± 0.20	2.40 ± 0.11	9.52 ± 0.22	103.3	2.23	8.7
38	105.07 ± 0.20	2.42 ± 0.11	9.46 ± 0.22	104.0	2.26	8.9
39	105.14 ± 0.20	2.83 ± 0.07	9.41 ± 0.22	103.2	1.97	6.5
40	106.98 ± 0.20	2.83 ± 0.07	9.26 ± 0.22	106.8	2.96	7.0
41	115.34 ± 0.22	2.65 ± 0.13	9.65 ± 0.23	113.4	2.75	9.6
42	119.83 ± 0.23	3.91 ± 0.17	10.17 ± 0.24	120.9	3.41	9.8
43	120.96 ± 0.23	3.90 ± 0.16	10.05 ± 0.24	121.5	4.21	10.3
44	124.02 ± 0.24	3.79 ± 0.14	10.08 ± 0.24	121.0	3.40	7.3
45	125.13 ± 0.24	3.24 ± 0.09	9.99 ± 0.24	124.7	3.15	8.5
46	125.89 ± 0.24	2.89 ± 0.14	9.94 ± 0.23	124.4	2.19	8.3
47	165.76 ± 0.33	4.33 ± 0.11	10.54 ± 0.25	167.9	5.46	10.7
48	170.17 ± 0.34	4.41 ± 0.12	10.57 ± 0.25	171.0	4.12	9.6
49	172.57 ± 0.35	3.97 ± 0.19	10.97 ± 0.26	176.1	-	-
50	192.87 ± 0.37	4.43 ± 0.21	10.91 ± 0.26	193.0	-	-
51	190.63 ± 0.37	4.38 ± 0.21	11.03 ± 0.26	193.0	-	-
52	225.52 ± 0.38	5.18 ± 0.25	11.19 ± 0.26	225.4	-	-
53	239.95 ± 0.39	5.51 ± 0.26	11.39 ± 0.27	237.9	-	-
54	243.42 ± 0.40	5.59 ± 0.27	11.24 ± 0.27	241.4	-	-
55	271.71 ± 0.56	6.24 ± 0.30	11.62 ± 0.27	271.6	-	-
56	301.68 ± 0.98	6.93 ± 0.33	11.86 ± 0.28	302.1	-	-
57	207.57 ± 0.38	4.77 ± 0.23	11.14 ± 0.26	209.1	-	-
58	241.07 ± 0.40	5.54 ± 0.26	11.34 ± 0.27	240.9	-	-
59	255.37 ± 0.44	5.87 ± 0.28	11.53 ± 0.27	255.7	-	-
RMS	1.24	0.45	1.47	-	-	-

Table 8.11: Predictions and their uncertainties, obtained through multiple linear regression using the "experimental" data from Table 8.1 and the theoretical supplement from Table 8.7. The table is divided in two by a double horizontal line. The reactions appearing above this line, are part of the "experimental" set of data from Table 8.1, those below, are part of the supplementary set of data from Table 8.7. The last line shows the root-mean-square deviation between the data and the corresponding predictions. Below the double horizontal line the $5th$ column (B_0^{exp}) contains the values for B_0^{Th} taken from Table 8.7.

8.3.4 Examples based on theoretically supplemented "experimental" data

Using the supplemented set of data, we have, as before, determined the parameters, their uncertainties and their correlations which were then propagated onto the capture cross-section. We now revisit some of the examples that were previously discussed in part I, with the exception that we now consider the reaction ^{58}Ni+^{74}Ge$\rightarrow^{132}$Nd* instead of ^{36}S+^{90}Zr$\rightarrow^{126}$Ba*. As the former reaction corresponds to an enhanced barrier and leads to a heavier compound nucleus it is much more representative of the supplemented set of data.

Fig. 8.5a displays the capture cross-section for the reaction ^{58}Ni+^{74}Ge$\rightarrow^{132}$Nd* which is part of the original set of reactions (cf. Table 8.1). The experimental cross-section is well reproduced at sub-barrier energies. However, for energies higher than the barrier, the model struggles to reproduce the data, although the overestimation of the width of the barrier distribution does not seem to be the issue in this particular case.

Again, the sole purpose of this capture model is to make predictions extending beyond the data employed to tune the model. With this idea in mind, we return to the reaction ^{48}Ca+^{238}U$\rightarrow^{286}$Cn* whose capture cross-section is provided in Fig. 8.5b. The outcome suggests that the model reproduces the data rather poorly, except in a limited region right above the Coulomb barrier. A comparison of Figs. 8.1b and 8.5b shows that the predictions do not benefit from the supplementary data.

Once more, it is possible to make predictions in regions where no measurements are available. We revisit the predictions leading to the synthesis of elements 119 and 120, respectively, shown in Figs. 8.6a and 8.6b. Comparing the results of part I (smaller figure) with those obtained here (larger figure), makes the changes in mean barrier estimates very clear, respectively, going from 240.34 MeV to 228.19 MeV. A similar conclusion can be drawn by contrasting Figs. 8.2b and 8.6b. Thus, including the theoretical data significantly reduces the mean barriers. This change in mean barrier predictions is almost exclusively due to the modification of the value of the parameter a.

Notice that the uncertainties obtained here are narrower than those obtained in part I. In part I, the adjustment of the model was based on lighter systems, while here, heavier systems are considered in the additional theoretical data. Thus, leading to a shrinkage of the uncertainties.

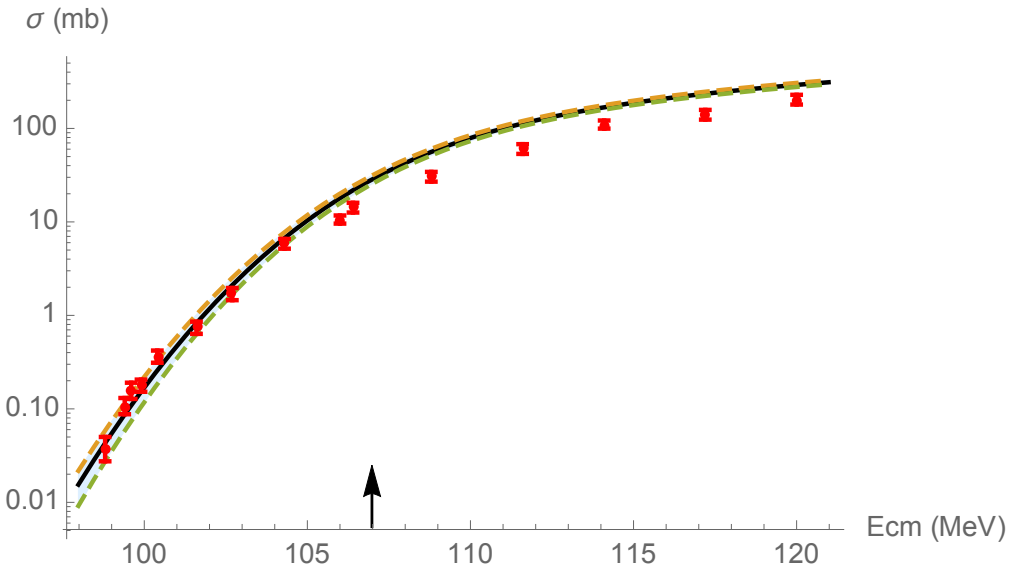

(a) ^{58}Ni+^{74}Ge→^{132}Nd*

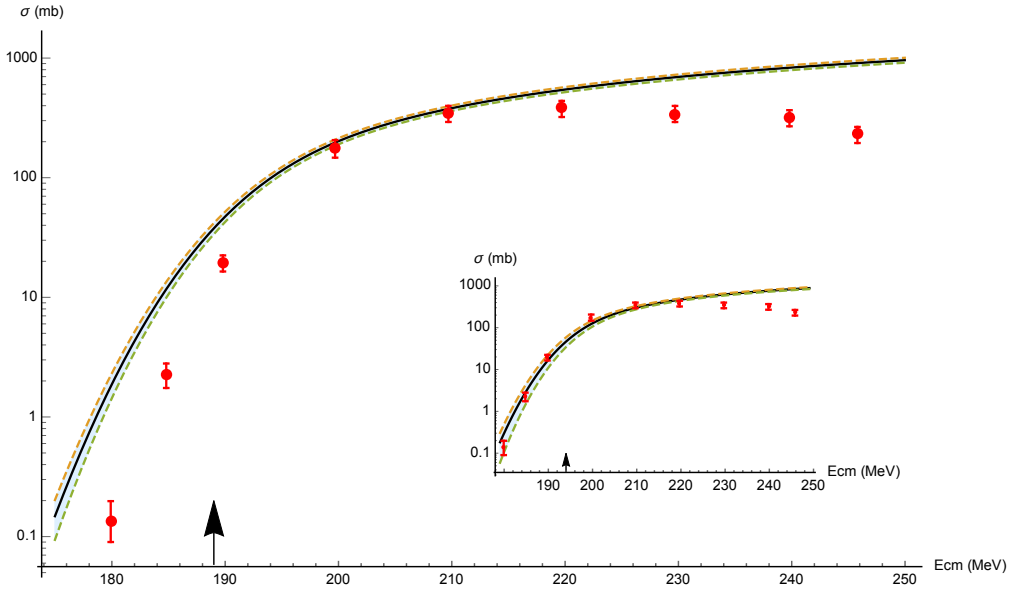

(b) ^{48}Ca+^{238}U→^{286}Cn*

Figure 8.5: Capture cross-section as a function of center-of-mass energy. Theoretical capture cross-section (black line) with lower uncertainty bound (green dashed) and upper uncertainty bound (orange dashed). The arrow represents the barrier energy. The small figure is a reproduction of the result obtained in part I. Fig. 8.5a presents the results for the reaction ^{58}Ni+^{74}Ge→^{132}Nd* along with the experimental data (red dots) which were taken from Ref. [98]. Fig. 8.5b presents the results for the reaction ^{48}Ca+^{238}U→^{286}Cn* along with the experimental data (red dots) which were taken from Ref. [96].

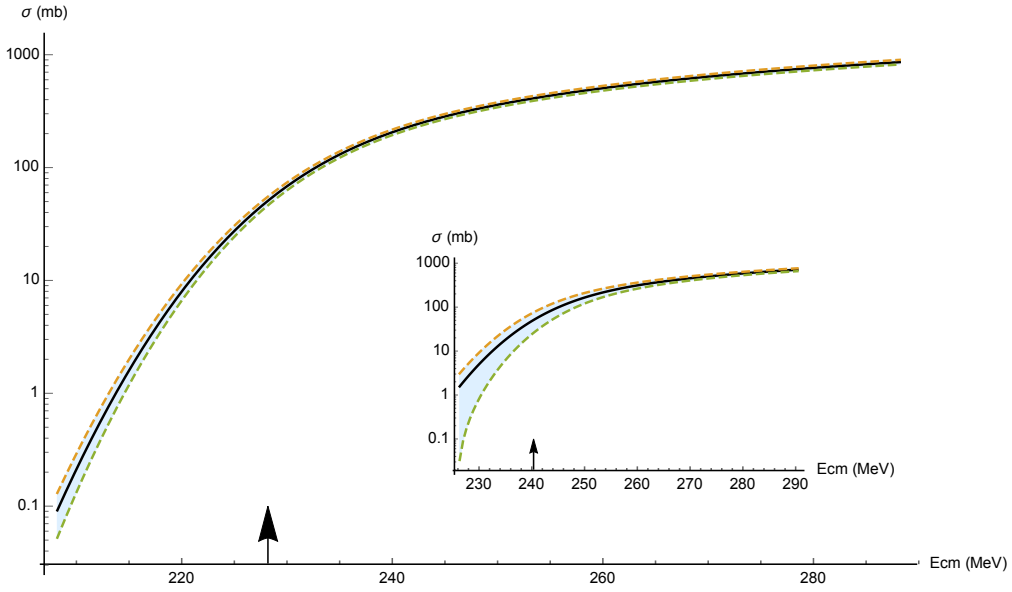

(a) ^{51}V+^{248}Cm→^{299}119*

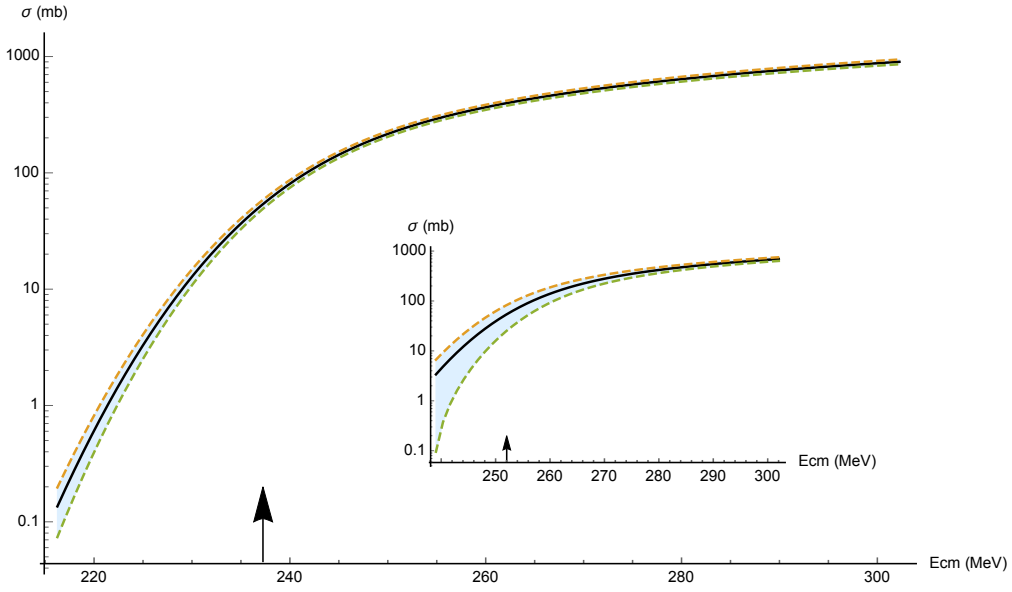

(b) ^{54}Cr+^{248}Cm→^{302}120*

Figure 8.6: Capture cross-section as a function of center-of-mass energy. Capture cross-section (black line), lower uncertainty bound (green dashed) and upper uncertainty bound (orange dashed). The arrow represents the barrier energy. The small figures are reproductions of the results obtained in part I. Fig. 8.6a represents the capture cross-section prediction for the reaction ^{51}V+^{248}Cm→^{299}119*. Fig. 8.6b represents the capture cross-section prediction for the reaction ^{54}Cr+^{248}Cm→^{302}120*.

8.4 Part III
Nonlinear regression with "experimental" and theoretical data

As formerly mentioned, the linearity that made the adjustment of R and B_0 so simple, cannot be exploited in the case of σ_B. Therefore, we had to rewrite the expression for σ_B into a linear form in order to determine C and W_0 using linear regression, cf. Eq. (8.6). This section presents another set of results obtained using nonlinear regression and based on the data contained in Tables. 8.1 and 8.7.

Here, nonlinear regression is only applied in order to estimate C and W_0, thus, the values, the uncertainties and correlations of, R and B_0, are left unaltered by this change of methods. The novel estimates, for the coefficients C and W_0, are provided with their uncertainties in Table 8.12. These results are identical to those obtained using multiple regression, Table 8.8.

	C		W_0	
$\hat{p}$ from [40]	0.0421	fm^{-1}	0.531	fm
$\hat{p}$	0.0428	fm^{-1}	0.535	fm
$\hat{u}(\hat{p})$	0.0048	fm^{-1}	0.081	fm
$\lvert\hat{u}(\hat{p})/\hat{p}\rvert$	11.2	%	15.1	%

Table 8.12: Values and uncertainties of the parameters obtained through nonlinear regression using the "experimental" data from Table 8.1, as well as the theoretical supplement from Table 8.7.

From Eq. (8.9), we obtain that $u(C, W_0) = -4.7110 \times 10^{-4}$ and once more, the correlation coefficient is equal to -0.98. Therefore, the effects of nonlinearity, on the covariances and correlations between C and B_0, are meagre. In fact, we have verified that the results obtained using nonlinear regression are so close to those obtained with linear regression (cf. part II) that the resulting capture cross-sections can be considered identical. We have compared the results obtained with linear and nonlinear regression because the available samples are rather limited and remember that, as mentioned in chapter 5, nonlinear regression only holds for large samples. This explains the motivation behind this comparison.

8.5 Conclusion

In this chapter, we have studied the uncertainties in the capture model using both linear and nonlinear regression as well as "experimental" and theoretical data. Our first step was to determine the uncertainties in the parameters (r_0, a, b, c, C and W_0), then, as an intermediate step we have propagated these uncertainties onto the barrier distributions (R, B_0 and σ_b) and finally, we have obtained the uncertainties in the capture cross-sections. In part I, the regression was based on a set of 48 "experimental" barrier distributions which were taken from the original work [94]. In the second part, we have simply followed the ideas of the original work where the "experimental" data was complemented by theoretical mean barriers. Note that despite the differences between the nucleus-nucleus potentials and the reactions that were considered the parameters obtained here were fully compatible with those given in the original work [94]. Let us note that based on the small samples of data at our disposal, we have chosen to use linear regression which we felt was more robust than nonlinear regression (cf. chapter 5 or Ref. [69] for more details). In the third part, we have simply quantified the effects of nonlinearities on the results obtained in part II and have shown that these were negligible. Finally, let us again recall that the motivation behind the uncertainty analysis of the capture step is to reach better constraints on the formation step.

Chapter 9

Wrap-up

From the very beginning, our goal was to constrain the formation probability. In general, this cannot be done experimentally because we are not able to distinguish quasi-fission from fission products. However, this can be achieved, theoretically, by expressing the "experimental" formation probability as

$$P_{\text{form}}^{\text{exp}} = \frac{\sigma_{\text{ER}}^{\text{exp}}}{\sigma_{\text{cap}} \times P_{\text{surv}}}, \tag{9.1}$$

where $\sigma_{\text{ER}}^{\text{exp}}$, σ_{cap} and P_{surv}, are the measured production cross-section, the capture cross-section and the survival probability, respectively. All along this thesis, we have tried to determine the uncertainties in σ_{cap} and P_{surv}, in order to reach this final step and constrain $P_{\text{form}}^{\text{exp}}$. Note that we did not directly constrain P_{surv}, rather we have directed our efforts towards the fission barriers. This choice was made based on a previous analysis showing that the most influential quantities in the survival probability calculations are the fission barriers [37, 38].

In order to illustrate the philosophy of our approach, we now examine the reaction:

$$^{208}\text{Pb} + {}^{50}\text{Ti} \longrightarrow {}^{257}\text{Rf} + 1\text{n}.$$

For this reaction the one-neutron evaporation residue cross-section is

$$\sigma_{\text{ER}}^{\text{exp}} = 10419 \pm 1284 \text{ pb}. \tag{9.2}$$

It should be mentioned that this value was taken from Ref. [99] and that it corresponds to the peak of the one-neutron excitation function located at E_{cm} =185.02 MeV. Note that all the following results were determined at this center-of-mass energy.

In the previous chapter, we have studied the uncertainties in the capture model described in chapter 2. From this analysis, we are now able to provide capture cross-section predictions along with their uncertainties. For this particular reaction, we have found

$$\sigma_{\text{cap}} = 0.4291 \pm 0.1073 \text{ mb}. \tag{9.3}$$

This value was obtained using Möller's ground-state deformations [49]. Note that here the capture model was adjusted using linear regression (cf. part II of chapter 8).

In chapter 7, we have investigated the uncertainties in the fission barriers with a very simple macroscopic-microscopic model. There, we have seen that the uncertainties in the fission barriers were about 0.5 MeV. However, since this model is really too simple to properly reproduce fission barriers and especially those of superheavy nuclei, here, we will use Möller's fission barrier [50]. Thus, the compound nucleus fission barrier is given by

$$B_f = 5.65 \pm 0.5 \text{ MeV}. \tag{9.4}$$

As mentioned before, the fission barriers are the most important input parameters in the calculations of survival probabilities [37, 38]. Therefore, we shall assume that the only source of uncertainty in the survival probability is the fission barrier of the compound nucleus. Then, the survival probability is obtained using the transition state theory of reaction rates, presented in chapter 2. Recall that in this theory, the survival probability is defined as

$$P_{\text{surv}} = \frac{\Gamma_n}{\Gamma_n + \Gamma_f}, \tag{9.5}$$

where we have neglected the possibility for second chance fission. In order to obtain the uncertainty in P_{surv}, we have propagated the fission barrier uncertainty (± 0.5 MeV) through the transition state theory. In doing so, we gather that

$$P_{\text{surv}} = 0.089 \pm 0.072. \tag{9.6}$$

The previous result can be expressed as

$$\frac{P_{\text{surv}}^{\max}}{P_{\text{surv}}^{\min}} = \frac{0.089 + 0.072}{0.089 - 0.072} \approx 9.5. \tag{9.7}$$

This allows us to appreciate the fact that an uncertainty of 0.5 MeV in the fission barrier roughly corresponds to an order of magnitude difference in the survival probability which is not negligible.

From the prior considerations, we are now in a position to give constraints on the formation probability since one can easily show that

$$\left[\frac{u(P_{\text{form}}^{\text{exp}})}{P_{\text{form}}^{\text{exp}}}\right]^2 = \left[\frac{u(\sigma_{\text{ER}}^{\text{exp}})}{\sigma_{\text{ER}}^{\text{exp}}}\right]^2 + \left[\frac{u(\sigma_{\text{cap}})}{\sigma_{\text{cap}}}\right]^2 + \left[\frac{u(P_{\text{surv}})}{P_{\text{surv}}}\right]^2. \tag{9.8}$$

From the previous expression, we deduce our final result

$$P_{\text{form}}^{\text{exp}} = 0.00025 \pm 0.00021. \tag{9.9}$$

Therefore, we have managed to constrain the formation probability. Applying this strategy to other reactions will helps us unravel part of the remaining mysteries of fusion hindrance. Note that the survival and formation probabilities have large uncertainties and that they become negative if we extend the confidence interval to twice the standard uncertainty. Therefore, in order to be completely rigorous the uncertainties in the survival and formation probabilities should be confirmed by Bayesian inference where the impossibility for the probabilities to become negative should be included in the prior.

Chapter 10

Conclusion and perspectives

In this thesis, we investigated the uncertainties in a fusion-evaporation model describing the synthesis of superheavy nuclei. As previously mentioned, although the basic qualitative features of fusion-evaporation have reached a consensus, the quantitative outcomes of the available models are still unsatisfactory. One should remember that the production cross-sections of superheavy nuclei are ultimately low and therefore, having accurate predictions is necessary in order to guide experimental campaigns. The inaccuracy of the current descriptions can be explained as follows. Theoretically, the production cross-section is assumed to be the product of three independent quantities, i.e., the capture cross-section, the formation probability and the survival probability. Therefore, one should be able to constrain each of these three quantities by relying on experimental data. However, the formation probability cannot be constrained experimentally because it is, in general, not possible to discriminate between quasi-fission and fission products. Furthermore, fission barriers have a strong influence on the survival probability and only very few measurements have been made in the superheavy region. Thus, one must rely on theoretical calculations in order to estimate them. Finally, even though the capture cross-section is well established, both experimentally and theoretically, extrapolations to heavier systems may be doubtful. Here, we should clearly state that the lack of constraints on the formation probability is known to be the leading cause of unreliable predictions. Therefore, in this thesis we have decided to theoretically constrain this quantity and in order to do so, we have investigated the uncertainties in the capture cross-section and the survival probability.

We started out by studying the uncertainties in the survival probability. Since the fission barrier is known to be the most important factor in the calculation of the survival probability, we have assumed that it was the only source of uncertainty. Seeing that the fission barrier is defined as the difference between the saddle-point and the ground-state masses, we started by investigating the uncertainties in masses. The first model we considered was a simple liquid drop model. It should be mentioned that in this analysis we had neglected the uncertainties in the shell correction energies. This allowed us to get familiar with regression analysis. More importantly, we have seen that the macroscopic parameters were extremely constrained once the shell correction energies were specified. As a consequence, the uncertainties in the masses were much smaller than the errors of the model. This lead us to believe that a significant part of these errors came from the shell correction energies and that these should be part of the uncertainty analysis. Here, we should emphasize that the existence of superheavy nuclei is due shell effects, thus, it was also natural to include shell

corrections from a physical point of view as well. Furthermore, in order to assess the uncertainties in the fission barriers we also had to include, at least partially, deformation. Then, as a way to include both shell corrections and deformation, we have investigated a simple phenomenological macroscopic-microscopic model. There, we were able to determine the uncertainties in the ground-state and saddle-point masses and in turn, those in fission barriers which were about 0.5 MeV. As before the uncertainties in the masses were much smaller than the errors of the model. This may be explained by the simplicity of the model but also by the method used in order to extract the theoretical uncertainties. Here, we would like to stress that the phenomenological model that was considered is really too simple to properly describe the fission barriers. Clearly, future investigations should focus on realistic fission barrier calculations involving many deformation degrees of freedom and shell corrections obtained from a microscopic potential using Strutinsky's method. This way the fission barrier uncertainties will perfectly suit the predictions of the model. Finally, by propagating the uncertainties in the fission barrier through an evaporation model we were able to deduce the uncertainties in the survival probability.

Based on our studies of ground-state masses, we have refined a method in order to constrain the shell correction energies of superheavy nuclei. In this method, the shell corrections were defined as the difference between the experimental and the macroscopic masses while the experimental masses were deduced from measured Q_α-values. As we have already mentioned, the stability of superheavy nuclei is only due to shell effects and therefore, being able to constrain them should be seen as an important step. Furthermore, this method also offers a robust way to test the consistency between the macroscopic and microscopic contributions to the masses. Again, as the models we have considered were too simple, it would be very interesting to repeat this study using more realistic models in order to verify their internal coherence. Systematically applying this method to many α decay chains would certainly help us better understand the stability of superheavy nuclei. However, it should be stressed that in order to truly constrain the shell corrections, the mass of the last nucleus in the decay chain must be well established. Therefore, precise mass measurements of "light" superheavy nuclei are really essential if we want to constrain shell corrections.

After, having investigated the uncertainties in the fission barriers, we have turned our attention to the uncertainties in the capture cross-section which is the second quantity required in order to constrain the formation probability. In this thesis, we have considered a phenomenological model based on a simple parametrization of the barrier distribution. In particular, we have seen that the description of the width of the barrier distribution was unsatisfactory and that this was the main cause of miscalculations. It is expected that the better part of the barrier fluctuations comes from the respective shapes of the colliding nuclei. In our analysis, we have used theoretical values for the quadrupole deformations which are provided without their corresponding uncertainties. This is the reason why our study does not include the uncertainties in the quadrupole deformations. Here, instead it may be more suitable to use (when possible) the measured values of the electric quadrupole moments which are provided with their uncertainties. However, let us not forget that the uncertainties in the deformations can also be obtained from the uncertainty analysis of a realistic macroscopic-microscopic model. Finally, we would also like to stress that the model we have considered is only valid close to the barrier.

However, sub-barrier energies are also relevant to the fusion leading to superheavy nuclei and were only accounted for effectively in the model we have studied. Therefore, it could be interesting to compare the uncertainties of the model that was considered here with another model, for instance a semi-classical approach where the description at sub-barrier energies is expected to be much more reliable.

From the prior investigations on the uncertainties in the capture and survival probabilities we were able to constrain the formation probability. This was achieved by propagating the uncertainties in the fission barriers through the transition state theory of reaction rates. First, we should recall that we have used an estimate of the uncertainty in the fission barriers which we have obtained with a simple model and that we have used a reasonable value for the fission barrier itself which was taken from a more realistic model. This method is only partially satisfying and this is the reason why we are currently investigating the uncertainties in Warsaw's macroscopic-microscopic model. Secondly, it should be noted that other approaches can be used in order to calculate the evaporation widths, for instance the Weisskopf-Ewing model or the Hauser-Feshbach formalism. An interesting next step would be to verify that changing the way the evaporation width is calculated does not affect significantly our results.

We have also tried to improve our understanding of fusion hindrance by examining the effects of inertia on the dynamics of diffusion. This was achieved by using singular perturbation theory. Thanks to this approach we were able to build a formal bridge between the Langevin and the Smoluchowski descriptions. More precisely, we have demonstrated that (at zeroth order) the difference between these to approaches came from a shift in the initial condition which is responsible for the reduction of fusion hindrance. In turn, this allowed us to give a simple explanation to the energy dependence of the initial condition within the Smoluchowski framework. The origin of this shift in the initial condition can be traced back to the reduction of the number degrees of freedom due to the fast time evolution of some of them. For instance, it is known that during the fusion process, the evolution of the neck is much faster than the changes in the elongation of the system. As a consequence, completely removing the neck degree of freedom from the description should result in a shift in the initial conditions. Thus, studies to come should include additional dimensions in order to systematically investigate these effects.

Therefore, this thesis has demonstrated that the use of uncertainty analysis can help us constrain quantities which simply cannot be constrained experimentally. However, let us not forget the fact that uncertainty analysis is only a tool in order to better constrain models and will never allow us to discover new mechanisms such as those regarding the shift in the initial conditions we have previously discussed.

Let us emphasize that although we have managed to constrain the formation probability, the constraints we have obtained depend on our ability to properly describe the other steps of the fusion-evaporation model, i.e., the capture and survival steps. Therefore, we will always be limited by our knowledge of these two other steps and we will not be capable to reach satisfactory predictions, say below an order of magnitude inaccuracy.

Let us stress that because the production cross-sections of superheavy nuclei are so low, a single order of magnitude is what separates a successful experiment from no measurements at all. Thus, every step towards more accurate predictions will be highly rewarded by entirely new and exciting experimental evidence. Therefore, the question that comes to mind is: How can we proceed any further in order to reach more accurate predictions ?

A possibility would be to improve our descriptions of the capture cross-section and the survival probability, such as to reduce the uncertainties in those quantities and to more firmly constrain the formation probability. This could be done in three complementary ways. The first strategy would be to use more sophisticated models. For instance, the capture model we have used is extremely simple, however, as a consequence its predictive power may be restricted. An example of studies going in that direction can be found in Ref. [100] where the deformation of the target is better described and its consequences on the production cross-section are explored. Note that, although more difficult to achieve, improving fission barrier calculations may also be possible. The second strategy would be to look for observables that could help us experimentally constrain the capture or survival steps independently. For instance by making fission barrier measurements of a few selected superheavy nuclei. This was shown to be possible in Ref. [101] where the fission barrier of nobelium was deduced from gamma-ray multiplicities. However hard this may be, directly constraining the formation probability by studying quasi-fission should also be considered [102]. All along we have assumed that the production cross-section could be expressed as a product of three independent quantities. This clearly is only approximately true. Thus, our third strategy would be to examine the correlations between the three steps of the fusion-evaporation model. The basic idea behind this strategy is that correlations usually restrict the freedom of the parameters and so, this will help us to more firmly constrain the formation probability. For instance, in order to study the correlations between the formation and survival probabilities, one could try to determine the internal and fission barriers within the same model. Note that this is very promising but has never been attempted within the macroscopic-microscopic formalism. Another possibility would be to use more microscopic models, e.g., SCMF or EDF.

Thus, many open questions remain and we would like here to name a few. What sophisticated models should we use instead? How can we improve fission barrier calculations? How can we experimentally determine the fission barrier of superheavy nuclei? What observables should be used in order to better constrain the capture cross-section and the survival probability? How can we study and constrain the correlations between the three steps and what observables should be used in order to do so? How can we simultaneously constrain the formation and survival steps? How can we distinguish quasi-fission and fission products and what would be the relevant observables to do so? Finally, we would like to stress that these are only some of the unanswered questions and that there are many more calling for answers.

Bibliography

[1] E. Rutherford. *Philosophical Magazine Series 6* ***21****, 669 (1911).*

[2] E. Rutherford. *Philosophical Magazine Series 6* ***37****, 537 (1919).*

[3] J. Chadwick. *Nature* ***129****, 312 (1932).*

[4] G. Fea. *Il Nuovo Cimento* ***2****, 368 (1935).*

[5] O. Hahn and F. Strassmann. *Naturwissenschaften* ***27****, 11 (1939).*

[6] O. Hahn and F. Strassmann. *Naturwissenschaften* ***27****, 89 (1939).*

[7] N. Bohr and J.A. Wheeler. *Phys. Rev.* ***56****, 426 (1939).*

[8] C.F. von Weiszäcker. *Z. Phys.* ***96****, 431 (1935).*

[9] H.A. Bethe and R.F. Backer. *Rev. Mod. Phys.* ***8****, 82 (1936).*

[10] J.A. Wheeler. *Niels Bohr and the Development of Physics (Pergamon Press, London, 1955).*

[11] J.A. Wheeler. *in Proceedings of the International Conference on the Peaceful Uses of Atomic Energy, Geneva, 1955 (United Nations, New York, 1955).*

[12] F.G. Werner and J.A. Wheeler. *Phys. Rev.* ***109****, 126 (1958).*

[13] M.G. Mayer. *Phys. Rev.* ***75****, 1969 (1949).*

[14] M.G. Mayer. *Phys. Rev.* ***78****, 22 (1950).*

[15] O. Haxel, J.H.D. Jensen, and H.E. Suess. *Phys. Rev.* ***75****, 1766 (1949).*

[16] M.G. Mayer and J.H.D. Jensen. *Elementary Theory of Nuclear Shell Structure.* Wiley, 1955.

[17] S. Hofmann and G. Münzenberg. *Rev. Mod. Phys.* ***72****, 733 (2000).*

[18] Yu.Ts. Oganessian, F.Sh. Abdullin, C. Alexander, J. Binder, R.A. Boll, S.N. Dmitriev, J. Ezold, K. Felker, J.M. Gostic, R.K. Grzywacz, J.H. Hamilton, R.A. Henderson, M.G. Itkis, K. Miernik, D. Miller, K.J. Moody, A.N. Polyakov, A.V. Ramayya, J.B. Roberto, M.A. Ryabinin, K.P. Rykaczewski, R.N. Sagaidak, D.A. Shaughnessy, I.V. Shirokovsky, M.V. Shumeiko, M.A. Stoyer, N.J. Stoyer, V.G. Subbotin, A.M. Sukhov, Yu.S. Tsyganov, V.K. Utyonkov, A.A. Voinov, and G.K. Vostokin. *Phys. Rev. Lett.* ***109****, 162501 (2012).*

[19] S. Hofmann. *J. Phys. G: Nucl. Part. Phys* ***42****, 114001 (2015).*

[20] S.G. Nilsson. *Mat. Fys. Medd. Dan. Vid. Selsk.* ***29****, 16 (1955).*

[21] W. Nazarewicz. *Nature Physics* ***14****, 537-541 (2018).*

[22] J. Rayford Nix and Arnold J. Sierk. *Phys. Rev. C* ***15****, 14 (1977).*

[23] W.J. Świątecki. *Physica Scripta* ***24****, 113 (1981).*

[24] W.J. Świątecki. *Nucl. Phys. A* ***376****, 275 (1982).*

[25] G. Royer and B. Remaud. *Nucl. Phys. A* ***444****, 477 (1985).*

[26] K.-H. Schmidt and W. Morawek. *Rep. Prog. Phys.* ***54****, 949 (1991).*

[27] J.P. Błocki, H. Feldmeier, and W.J. Świątecki. *Nucl. Phys. A* ***459****, 145 (1986).*

[28] H. Sann, R. Bock, Y.T. Chu, A. Gobbi, A. Olmi, U. Lynen, W. Müller, S. Bjørnholm, and H. Esbensen. *Phys. Rev. Lett.* ***47****, 1248 (1981).*

[29] R. Bock, Y.T. Chu, M. Dakowski, A. Gobbi, E. Grosse, A. Olmi, H. Sann, U. Lynen, W. Müller, S. Bjørnholm, H. Esbensen, W. Wölfli, and E. Morenzoni. *Nucl. Phys. A* ***388****, 334 (1982).*

[30] W. Westmeier, R.A. Esterlund, A. Rox, and P. Patzelt. *Phys. Lett.* ***117****, 163 (1982).*

[31] Y. Abe, S. Ayik, P.-G. Reinhard, and E. Suraud. *Phys. Rep.* ***275****, 49 (1996).*

[32] Y. Abe, D. Boilley, B.G. Giraud, and T. Wada. *Phys. Rev. E* ***61****, 1125 (2000).*

[33] C. Shen, G. Kosenko, and Y. Abe. *Phys. Rev. C* ***66****, 061602 (2002).*

[34] D. Boilley, Y. Abe, and J.-D. Bao. *Eur. Phys. J. A* ***18****, 627 (2003).*

[35] W.J. Świątecki, K. Siwek-Wilczyńska, and J. Wilczyński. *Acta Physica Polonica B* ***34****, 4 (2003).*

[36] W.J. Świątecki, K. Siwek-Wilczyńska, and J. Wilczyński. *Phys. Rev. C* ***71****, 014602 (2005).*

[37] H. Lü. *Synthesis of Super-Heavy Elements : Role of Uncertainty Analysis in Theoretical Modelling, Thesis, Université de Caen (2015).*

[38] H. Lü, D. Boilley, Y. Abe, and C. Shen. *Phys. Rev. C* ***94****, 034616 (2016).*

[39] A. Baran, M. Kowal, L. M. Robledo P. G. Reinhard, A. Staszczak, and M. Warda. *Nucl. Phys. A* ***944****, 442 (2015).*

[40] T. Cap, K. Siwek-Wilczyńska, and J. Wilczyński. *Phys. Rev. C* ***83****, 054602 (2011).*

[41] K. Siwek-Wilczyńska, T. Cap, M. Kowal, A. Sobiczewski, and J. Wilczyński. *Phys. Rev. C* ***86****, 014611 (2012).*

[42] C. Shen, Y. Abe, D. Boilley, G. Kosenko, and E. Zhao. *Int. J. Phys. E* ***17****, 66 (2008).*

[43] H. Goldstein. *Classical Mechanics.* Pearson, 2001.

[44] K. Siwek-Wilczyńska, E. Siemiaszko, and J. Wilczyński. *Acta Phys. Pol. B* ***33****, 451 (2002).*

[45] W. Greiner and J.A. Maruhn. *Nuclear models.* Springer, 1996.

[46] V. Zagrebaev and W. Greiner. *J. Phys. G: Nucl. Part. Phys.* ***31****, 825 (2005).*

[47] R. Kubo. *Rep. Prog. Phys.* ***29****, 255 (1966).*

[48] J. Błocki and W.J. Świątecki. *Nuclear Deformation Energies.* Lawrence Berkeley Laboratory preprint LBL-12811, 1982.

[49] W.D. Myers, W.J. Świątecki, P. Möller, and J.R Nix. *At. Data Nucl. Data Tables* ***59****, 185 (1995).*

[50] P. Möller, A.J. Sierk, T. Ichikawa, A. Iwamoto, R. Bengtsson, H. Uhrenholt, and S. Åberg. *Phys. Rev. C* ***79****, 064304 (2009).*

[51] M. Kowal, P. Jachimowicz, and J. Skalski. *arXiv:1203.5013.*

[52] M. Kowal, P. Jachimowicz, and A. Sobiczewski. *Phys. Rev. C* ***82****, 014303 (2010).*

[53] H. Lü, A. Marchix, Y. Abe, and D. Boilley. *KEWPIE2: A cascade code for the study of dynamical decay of excited nuclei. Computer Physics Communications, Elsevier, 2016, 200, pp.381-399.*

[54] W.J. Świątecki. *Aust. J. Phys.* ***36****, 641 (1983).*

[55] A.V. Ignatyuk, G.N. Smirenkin, and A.S. Tishin. *Sov. J. Nucl. Phys.* ***21****, 255 (1975).*

[56] S.F. Mughabghab and C. Dunford. *Phys. Rev. Lett.* ***81****, 4083 (1998).*

[57] W.D. Myers and W.J. Świątecki. LBL report 36803, December 1994. UC-413.

[58] R.S. Naik, W. Loveland, P.H. Sprunger, A.M. Vinodkumar, D. Peterson, C.L. Jiang, S. Zhu, X. Tang, E.F. Moore, and P. Chowdhury. *Phys. Rev. C* ***76****, 054604 (2007).*

[59] N. Pottier. *Physique statistique hors de l'équilibre : Processus irréversibles linéaires.* EDP Sciences, 2007.

[60] Kristen Jakobsen. *arXiv:1312.3652.*

[61] C.M. Bender and S.A. Orszag. *Advanced Mathematical Methods for Scientists and Engineers I: Asymptotic Methods and Perturbation Theory.* Springer, 2010.

[62] D. Boilley, H. Lü, C. Shen, Y. Abe, and B.G. Giraud. *Phys. Rev. C* ***84****, 054608 (2011).*

[63] D. Boilley. *Private Communication.*

[64] L. Kirkup and B. Frenkel. *An Introduction to Uncertainty in Measurements: Using the GUM*. Cambridge University Press, 2006.

[65] IFCC ILAC ISO IUPAC BIPM, IEC. *GUM 1995 with minor corrections. Evaluation of measurement data - Guide to the expression of uncertainty in measurement*. 2008.

[66] David Boilley. *Introduction to metrology*. 2017.

[67] Yadolah Dodge. *Analyse de régression appliquée*. Dunod, 1999.

[68] S. Chatterjee and A.S. Hadi. *Regression analysis by example*. Wiley, 2006.

[69] S. Weisberg. *Applied Linear Regression*. Wiley, 2005.

[70] D. Sivia and J. Skilling. *Data analysis: A Bayesian Tutorial*. Oxford University Press, 2006.

[71] B. Cauchois, H. Lü, D. Boilley, and G. Royer. *Submitted to Phys. Rev. C*.

[72] V.M. Strutinski. *Nucl. Phys. A* ***3****, 420 (1967)*.

[73] V.M. Strutinski. *Nucl. Phys. A* ***122****, 1 (1968)*.

[74] W.D. Myers and W.J. Świątecki. *Nucl. Phys.* ***81****, 1 (1966)*.

[75] M. Kirson. *Nucl. Phys. A* ***798****, 29 (2008)*.

[76] J. Toivanen, J. Dobaczewski, M. Kortelainen, and K. Mizuyama. *Phys. Rev. C* ***78****, 426 (2008)*.

[77] S. Goriely and R. Capote. *Phys. Rev. C* ***89****, 054318 (2014)*.

[78] N. Schunk, J.D. McDonnell, J. Sarich, S.M. Wild, and D. Higdon. *J. Phys. G: Nucl. Part. Phys.* ***42****, 034024 (2015)*.

[79] D. Higdon, J.D. McDonnell, N. Schunk, J. Sarich, and S.M. Wild. *J. Phys. G: Nucl. Part. Phys.* ***42****, 034009 (2015)*.

[80] J.D. McDonnell, N. Schunk, D. Higdon, J. Sarich, S.M. Wild, and W. Nazarewicz. *Phys. Rev. Lett.* ***114****, 122501 (2015)*.

[81] G.F. Bertsch and D. Bingham. *Phys. Rev. Lett.* ***119****, 252501 (2017)*.

[82] G. Royer and A. Subercaze. *Nucl. Phys. A* ***917****, 1 (2013)*.

[83] W.J. Huang, G. Audi, M. Wang, F.G. Kondev, S. Naimi, and X. Xu. *Chin. Phys. C* ***41****, 030002 (2017)*.

[84] M. Wang, G. Audi, F.G. Kondev, W.J. Huang, S. Naimi, and X. Xu. *Chin. Phys. C* ***41****, 030003 (2017)*.

[85] J. Margueron, R.H. Casali, and F. Gulminelli. *Phys. Rev. C* ***97****, 025806 (2018)*.

[86] C. Mondal, B.K. Agrawal, J.N. De, and S.K. Samaddar. *Phys. Rev. C* ***93****, 044328 (2016)*.

[87] B. Cauchois and D. Boilley. *Submitted to Eur. Phys. J. A.*

[88] S. Hofmann, S. Heinz, R. Mann, J. Maurer, G. Münzenberg, S. Antalic, W. Barth, H.G. Burkhard, L. Dahl, K. Eberhardt, R. Grzywacz, J.H. Hamilton, R.A. Henderson, J.M. Kenneally, B. Kindler, I. Kojouharov, R. Lang, B. Lommel, K. Miernik, D. Miller, K.J. Moody, K. Morita, K. Nishio, A.G. Popeko, J.B. Roberto, J. Runke, K.P. Rykaczewski, S. Saro, C. Scheidenberger, H.J. Schött, D.A. Shaughnessy, M.A. Stoyer, P. Thörle-Pospiech, K. Tinschert, N. Trautmann, J. Uusitalo, and A.V. Yeremin. *Eur. Phys. J. A* ***52****, 116 (2016).*

[89] Yu.Ts. Oganessian. *J. Phys. G: Nucl. Part. Phys* ***34****, R165 (2007).*

[90] W.D. Myers and W.J. Świątecki. *Nucl. Phys. A* ***601****, 141 (1996).*

[91] K. Morita, K. Morimoto, D. Kaji, T. Akiyama, S. Goto, H. Haba, E. Ideguchi, K. Katori, H. Koura, H. Kudo, T. Ohnishi, A. Ozawa, T. Suda, K. Sueki, F. Tokanai, T. Yamaguchi, A. Yoneda, and A. Yoshida. *J. Phys. Soc. Jpn.* ***73****, 043201 (2007).*

[92] G. Neyens. *Rep. Prog. Phys.* ***66****, 633 (2003).*

[93] N.J. Stone. *Atomic Data and Nuclear Data Tables* ***90****, 75 (2005).*

[94] K. Siwek-Wilczyńska and J. Wilczyński. *Phys. Rev. C* ***69****, 024611 (2004).*

[95] A.M. Stefanini, L. Corradi, A.M. Vinodkumar, Y. Feng, F. Scarlassara. G. Montagnoli, S. Beghini, and M. Bisogno. *Phys. Rev. C* ***62****, 014601 (2000).*

[96] K. Nishio, S. Mitsuoka, I. Nishinaka, H. Makii, Y. Wakabayashi, H. Ikezoe, K. Hirose, T. Ohtsuki, Y. Aritomo, and S. Hofmann. *Phys. Rev. C* ***86****, 034608 (2012).*

[97] W.D. Myers and W.J. Świątecki. *Phys. Rev. C* ***62****, 044610 (2000).*

[98] M. Beckerman, M. Salomaa, A. Sperduto, J. D. Molitoris, and A. DiRienzo. *Phys. Rev. C* ***25****, 837 (1982).*

[99] G. Münzenberg, S. Hofmann, F. Heßberger, W. Reisdorf, K. Schmidt, J. Schneider, P. Armburster, C. Sham, and B. Thuma. *Z. Phys. A* ***300****, 107 (1981).*

[100] K. Hagino. *arXiv:1803.02036v1.*

[101] G. Henning, T.L. Khoo, A. Lopez-Martens, D. Seweryniak, M. Alcorta, M. Asai, B.B. Back, P.F. Bertone, D. Boilley, M.P. Carpenter, C.J. Chiara, P. Chowdhury, B. Gall, P.T. Greenlees, G. Grdal, K. Hauschild, A. Heinz, C.R. Hoffman, R.V.F. Janssens, A.V. Karpov, B.P. Kay, F.G. Kondev, S. Lakshmi, T. Lauritsen, C.J. Lister, E.A. McCutchan, C. Nair, J. Piot, D. Potterveld, P. Reiter, A.M. Rogers, N. Rowley, and S. Zhu. *Phys. Rev. Lett.* ***113****, 262505 (2014).*

[102] D.J. Hinde. *Nuclear Physics News* ***28****, 1 (2018).*

Title: Uncertainty analysis:Towards more accurate predictions for the synthesis of superheavy nuclei.

Keywords: Superheavy nuclei, Uncertainty analysis, Nuclear collisions, Liquid-drop model, Regression analysis, Macroscopic-microscopic model.

The nuclear reaction theories describing the synthesis of superheavy nuclei are not firmly established. Although, the basic qualitative features of fusion-evaporation have reached a consensus, the quantitative predictions of the available models are still unsatisfactory. The production cross-section is the product of the capture cross-section, the formation probability and survival probability. Previous studies have shown that the dominating part of the remaining discrepancies came from our inability to properly constrain the formation probability. The main goal of this thesis is to theoretically constrain this quantity. This is achieved by examining the uncertainties in the capture cross-section and the survival probability using regression analysis. The fission barrier being the most influential factor in survival probability calculations, it is assumed to be the only source of uncertainties. Since the fission barrier is the difference between the ground-state and saddle-point masses, we started investigating the uncertainties in the liquid drop model. Based on this analysis we have refined a method to constrain the shell correction energies. To determine the uncertainties in the fission barriers, a simplified phenomenological macroscopic-microscopic model was used. The uncertainties in the capture step were determined using a model based on a parametrization of the barrier distribution. From the propagation of the uncertainties in the capture cross-section and fission barrier, the constraints on the formation probability were determined. Separately, the effects of inertia on the formation probability were investigated using perturbation theory and a new mechanism reducing fusion hindrance was described as a shift in the initial condition within the Smoluchowski approximation. Additionally, based on this approach, an explanation for the phenomenological energy dependent parametrization of the injection point was found.

Titre: Analyse d'incertitude : Vers des prédictions plus précises pour la synthèse des noyaux superlourds.

Mots-clés: Noyaux superlourds, Analyse d'incertitude, Collisions nucléaires, Modèle de la goutte liquide, Analyse de régression, Modèle microscopique-macroscopique.

Les théories de réaction nucléaire décrivant la synthèse des noyaux superlourds ne sont pas fermement établies. Bien qu'un consensus existe sur les caractéristiques qualitatives de la fusion-évaporation, les prédictions quantitatives des modèles disponibles sont encore insatisfaisantes. La section efficace de production est le produit de la section efficace de capture, de la probabilité de formation et de la probabilité de survie. Des études antérieures ont établi que la partie dominante des divergences restantes provenait de notre incapacité à contraindre correctement la probabilité de formation. L'objectif principal de cette thèse est de contraindre théoriquement cette quantité. Celui-ci a été atteint en examinant les incertitudes associées à la section efficace de capture ainsi qu'à la probabilité de survie par le biais de l'analyse de régression. La barrière de fission étant le facteur le plus influent dans les calculs de probabilité de survie, on supposera qu'elle est la seule source de ses incertitudes. Et puisque la différence entre les masses du fondamental et du point-selle définit la barrière de fission, nous avons commencé par étudier les incertitudes d'un modèle de type goutte liquide afin d'obtenir les incertitudes sur les masses. Sur la base de cette analyse, nous avons affiné une méthode permettant de contraindre les énergies de correction de couches. Afin de déterminer les incertitudes sur les barrières de fission, un modèle microscopique-macroscopique simplifié a été utilisé. Les incertitudes sur la phase de capture ont été obtenues à l'aide d'un modèle basé sur une paramétrisation de la distribution de barrières. Les contraintes portant sur la probabilité de formation ont été ensuite déduites à partir de la propagation des incertitudes sur la section efficace de capture et sur la barrière de fission. Par ailleurs, les effets de l'inertie sur la probabilité de formation ont été étudiés en utilisant la théorie des perturbations et un nouveau mécanisme réduisant l'entrave à la fusion a été décrit comme un décalage de la condition initiale dans l'approximation de Smoluchowski. Enfin, sur la base de cette approche, une explication de la dépendance en énergie du point d'injection phénoménologique a été obtenue.